

EDITORS

Aravind Dasari | James Njuguna

Food Packaging

Energy Scavenging

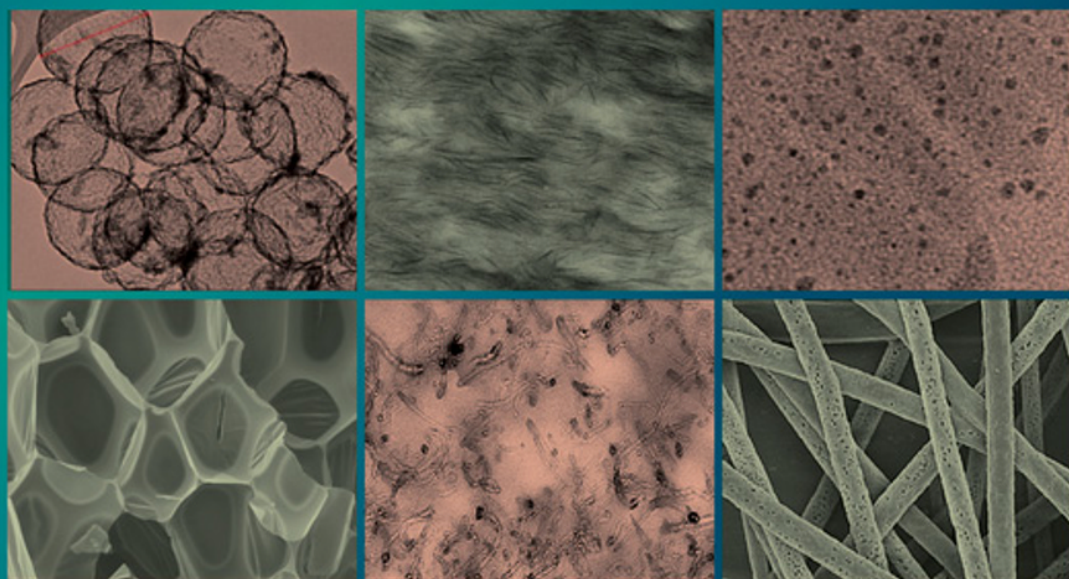
Biodegradability

Thermal Barriers

Sensing

Optical Properties

Functional and Physical Properties of Polymer Nanocomposites



WILEY

Functional and Physical Properties of Polymer Nanocomposites

Functional and Physical Properties of Polymer Nanocomposites

Edited by

ARAVIND DASARI

*School of Materials Science & Engineering, Nanyang
Technological University, Singapore*

and

JAMES NJUGUNA

*Institute for Innovation, Design and Sustainability,
School of Engineering, Robert Gordon University, UK*

WILEY

This edition first published 2016
© 2016 John Wiley & Sons, Ltd

Registered Office

John Wiley & Sons, Ltd, The Atrium, Southern Gate, Chichester, West Sussex, PO19 8SQ, United Kingdom

For details of our global editorial offices, for customer services and for information about how to apply for permission to reuse the copyright material in this book please see our website at www.wiley.com.

The right of the author to be identified as the author of this work has been asserted in accordance with the Copyright, Designs and Patents Act 1988.

All rights reserved. No part of this publication may be reproduced, stored in a retrieval system, or transmitted, in any form or by any means, electronic, mechanical, photocopying, recording or otherwise, except as permitted by the UK Copyright, Designs and Patents Act 1988, without the prior permission of the publisher.

Wiley also publishes its books in a variety of electronic formats. Some content that appears in print may not be available in electronic books.

Designations used by companies to distinguish their products are often claimed as trademarks. All brand names and product names used in this book are trade names, service marks, trademarks or registered trademarks of their respective owners. The publisher is not associated with any product or vendor mentioned in this book.

Limit of Liability/Disclaimer of Warranty: While the publisher and author have used their best efforts in preparing this book, they make no representations or warranties with respect to the accuracy or completeness of the contents of this book and specifically disclaim any implied warranties of merchantability or fitness for a particular purpose. It is sold on the understanding that the publisher is not engaged in rendering professional services and neither the publisher nor the author shall be liable for damages arising herefrom. If professional advice or other expert assistance is required, the services of a competent professional should be sought.

The advice and strategies contained herein may not be suitable for every situation. In view of ongoing research, equipment modifications, changes in governmental regulations, and the constant flow of information relating to the use of experimental reagents, equipment, and devices, the reader is urged to review and evaluate the information provided in the package insert or instructions for each chemical, piece of equipment, reagent, or device for, among other things, any changes in the instructions or indication of usage and for added warnings and precautions. The fact that an organization or Website is referred to in this work as a citation and/or a potential source of further information does not mean that the author or the publisher endorses the information the organization or Website may provide or recommendations it may make. Further, readers should be aware that Internet Websites listed in this work may have changed or disappeared between when this work was written and when it is read. No warranty may be created or extended by any promotional statements for this work. Neither the publisher nor the author shall be liable for any damages arising herefrom.

Library of Congress Cataloging-in-Publication data applied for

ISBN: 9781118542323

A catalogue record for this book is available from the British Library.

Set in 10/12.5pt Times by SPi Global, Pondicherry, India

Contents

<i>List of Contributors</i>	ix
<i>Preface</i>	xi
1 Introduction	1
<i>Aravind Dasari and James Njuguna</i>	
References	5
2 Three-dimensional Microstructural Characterization of Polymer Nanocomposites by Electron Tomography	7
<i>Florent Dalmas and Lucian Roiban</i>	
2.1 Introduction	7
2.2 3D Observation at the Nanoscale	8
2.2.1 Imaging with Electrons	8
2.2.2 Principles of Transmission ET	10
2.3 Application to Polymer Matrix Nanocomposites	13
2.4 3D Image Analysis and Quantification	19
2.5 Conclusion and Prospects	23
References	25
3 Polymer Nanocomposites for Food Packaging Applications	29
<i>Shiv Shankar and Jong-Whan Rhim</i>	
3.1 Introduction	29
3.2 Polymer Nanocomposite	31
3.2.1 Types of Polymer	31
3.2.2 Types of Nanofillers	32
3.3 Preparation of Nanocomposites	34
3.4 Characterization Methods of Polymer Nanocomposite Films	36
3.5 Types of Polymer Nanocomposite Packaging	36
3.5.1 Rigid Packaging	37
3.5.2 Nylon-Based Packaging Materials	38
3.5.3 Biodegradable Packaging	39
3.5.4 Flexible Packaging	39

3.5.5	Active Packaging	40
3.5.6	Intelligent/Smart Packaging	43
3.5.7	Nanocoating	44
3.5.8	Edible Coating/Packaging Films	45
3.5.9	Other Types of Packaging	45
3.6	Properties of Polymer Nanocomposites	46
3.6.1	Mechanical Properties	46
3.6.2	Barrier Properties	46
3.6.3	Chemical Resistance Properties	46
3.6.4	Biodegradation Properties	47
3.6.5	Other Properties	48
3.7	Conclusion	49
	Acknowledgments	50
	References	50
4	Polymer Nanocomposites Biodegradation	57
	<i>Kikku Fukushima and Giovanni Camino</i>	
4.1	Introduction	57
4.2	Biodegradation of Polymers and Their Nanocomposites	59
4.2.1	Standards for Environmentally Biodegradable Polymers	59
4.2.2	Mechanisms of Polymer Biodegradation	61
4.2.3	Biodegradation of Polymers from Natural Resources and Their Nanocomposites	63
4.2.4	Biodegradation of Polymers from Fossil Origins and Their Nanocomposites	74
4.3	Summary	81
	References	84
5	Functional Fibers Produced Using Electrospinning Techniques for Energy Scavenging Applications	93
	<i>Avinash Baji and Yiu-Wing Mai</i>	
5.1	Introduction	93
5.2	Principle of Electrospinning	95
5.3	Fabrication of Aligned Fibers	96
5.4	Fabrication of Ferro/Piezoelectric Organic Fibers	97
5.5	Fabrication of Ferro/Piezoelectric Inorganic Fibers	99
5.6	Fabrication of Fibers Filled with Reinforcements	100
5.7	Characterization of Ferro/Piezoelectric Behavior of Electrospun Fibers	102
5.8	Piezoresponse of Electrospun Fibers	103
5.9	Nanogenerators Based on Electrospun Fibers	106

5.10	Energy Harvesters Based on Electrospun Fibers	107
5.11	Force/Pressure Sensors	108
5.12	Multifunctional Inorganic Fibers	109
5.13	Magnetoelectric Inorganic Fibers	112
5.14	Future Directions	114
	Acknowledgments	115
	References	115
6	Magnetic Properties of Polymer Nanocomposites	119
	<i>Paolo Allia, Marco Sangermano and Alessandro Chiolerio</i>	
6.1	Introduction	119
6.2	Preparation of Magnetic NPs and Its Influence on the Properties of NCs	120
	6.2.1 Top-down versus Bottom-up Approach to Synthesis	120
	6.2.2 Considerations Regarding Homogeneity and Interactions	121
6.3	Anhysteretic Properties and Interparticle Interactions	124
6.4	Hysteretic Properties	127
6.5	Nanocomposites Exhibiting Magnetoelectric Properties	131
6.6	Applications	132
	References	135
7	Optical Properties of Polymer Nanocomposites	139
	<i>Ignazio Roppolo, Marco Sangermano and Alessandro Chiolerio</i>	
7.1	Introduction	139
7.2	Photoluminescence and Related Applications	140
	7.2.1 Nanocomposite with Quantum Dots	141
	7.2.2 Transition Metal Nanocomposites	143
	7.2.3 Rare-Earth Polymer Nanocomposites	143
7.3	Light Emission in Polymer Nanocomposites: From Science to Applications	145
7.4	Transparency and Adsorbance in Polymer Nanocomposite	152
	References	154
8	Bismuth-Based Nanomaterials and Platforms for Sensing and Biosensing Applications	159
	<i>Miquel Cadevall, Josep Ros, and Arben Merkoçi</i>	
8.1	General Properties and Applications of Bismuth	159
8.2	BiNPs Synthesis	161
	8.2.1 Chemical Methods	161
	8.2.2 Physical Methods	164
8.3	Bi-Based Modifications and Composites for (Bio)sensing Platforms	167
	8.3.1 Chemical Sensing	167
	8.3.2 Biosensing Applications	169

viii *Contents*

8.4	Conclusions	173
	Acknowledgments	173
	References	174
9	High-Temperature-Resistant Polymer Nanocomposites	183
	<i>Indraneel S. Zope and Aravind Dasari</i>	
9.1	Background	183
9.2	Representative High-Performance Polymer Nanocomposites	187
9.2.1	Polyethersulfone Nanocomposites	187
9.2.2	Polyimide Nanocomposites	192
9.2.3	Polyetherimide Nanocomposites	196
9.3	Applications of High-Temperature Polymers and their Nanocomposites	198
	Acknowledgments	200
	References	200
	<i>Index</i>	203

List of Contributors

Paolo Allia, Applied Science and Technology Department, Politecnico di Torino, Italy

Avinash Baji, Engineering Product Development (EPD) Pillar, Singapore University of Technology and Design (SUTD), Singapore

Miquel Cadevall, Catalan Institute of Nanoscience and Nanotechnology (ICN2), Campus UAB, Spain; and The Barcelona Institute of Science and Technology, Campus UAB, Spain

Giovanni Camino, Applied Science and Technology Department, Politecnico di Torino, Italy

Alessandro Chiolerio, Center for Space Human Robotics, Istituto Italiano di Tecnologia, Italy

Florent Dalmas, MATEIS (Matériaux: Engénierie et Science), CNRS/INSA de Lyon, France

Aravind Dasari, School of Materials Science & Engineering, Nanyang Technological University, Singapore

Kikku Fukushima, Applied Science and Technology Department, Politecnico di Torino, Italy

Yiu-Wing Mai, Centre for Advanced Materials Technology (CAMT), School of Aerospace Mechanical and Mechatronic Engineering, The University of Sydney, Australia

Arben Merkoçi, Catalan Institute of Nanoscience and Nanotechnology (ICN2), Campus UAB, Spain; and The Barcelona Institute of Science and Technology, Campus UAB, Spain

James Njuguna, Institute for Innovation, Design and Sustainability, School of Engineering, Robert Gordon University, UK

Jong-Whan Rhim, Department of Food Engineering and Bionanocomposite Research Institute, Mokpo National University, Korea

Lucian Roiban, MATEIS (Matériaux: Engénierie et Science), CNRS/INSA de Lyon, France

Ignazio Roppolo, Center for Space Human Robotics, Istituto Italiano di Tecnologia, Italy

Josep Ros, Department of Chemistry, Universitat Autònoma de Barcelona, Spain

Marco Sangermano, Applied Science and Technology Department, Politecnico di Torino, Italy

Shiv Shankar, Department of Food Engineering and Bionanocomposite Research Institute, Mokpo National University, Korea

Indraneel S. Zope, School of Materials Science & Engineering, Nanyang Technological University, Singapore

Preface

Polymer-based nanocomposites have been studied extensively for almost three decades. However, the key questions remain as follows: Have they made in-roads into the spectrum of applications dominated by micro-composites? Have they found completely different sets of applications and opened up new possibilities? Qualitatively, the superiority of polymer-based nanocomposites compared to their micro-counterparts is often attributed to the availability of a large number of nanoparticles with huge interfacial areas and confinement of polymer matrix chains at the nano-level. Another facet that is often highlighted is nanoparticles' 'size-dependent functionality'. The community still believes that these characteristics of the nano-reinforcements, if fully exploited, can impart multi-functional properties to polymers.

Despite their huge potential, final outcomes are not entirely positive which is clearly reflected in their limited commercial applicability. Mechanical properties, for instance, are still dominated by the matrix. Some of the problems associated include processing, dispersion/distribution of nanoparticles in a matrix, surface modification and compatibility among the different phases, controlled micro- to nano-structures and preserving the surface activity of nanoparticles. Moreover, it is still unclear as to what extent the interface between nanoparticles and matrix influences the properties. Even the catalytic activity of clay nanoplatelets (montmorillonite) in influencing the time to ignition and other parameters during combustion of a polymer/clay nanocomposite is vague. More often than not, poor characterization and analysis of the materials and/or processes are to be blamed for the confusion and contradictory results.

Further, accommodating their disposal (end of life) is challenging from both scientific/technical and socio-economic perspectives. This is due to the dramatic direct/indirect impacts exerted on our eco-system. Nonetheless, looking at the bright side, polymer nanocomposites have opened up completely novel possibilities in different functional applications ranging from biomedical to energy storage. In this book, we cover a range of functional and physical properties of these materials, with basics as well as advanced and in-depth knowledge on these properties. These include gas/water barrier, anti-microbial (Chapter 3), biodegradability (Chapter 4), energy scavenging (Chapter 5), magnetic (Chapter 6), optical (Chapter 7), biosensing (Chapter 8), and thermal properties (Chapter 9). Chapter 2 is dedicated towards a three-dimensional microstructural characterization of nanocomposites.

We are grateful to our authors (contributors) for their continued support and patience. Their views and ideas on different aspects of polymer nanocomposites are truly insightful. Permissions to reproduce many figures in this book from various publishers and authors are much appreciated.

Aravind Dasari (Singapore)
James Njuguna (United Kingdom)
October 2015

1

Introduction

Aravind Dasari¹ and James Njuguna²

¹*School of Materials Science & Engineering, Nanyang Technological University, Singapore*

²*Institute for Innovation, Design and Sustainability, School of Engineering, Robert Gordon University, UK*

In the early 1960s, polymer composites are in the spotlight and this field is treated as a new template for prototyping high-performance materials for exploration in different applications. In the past two decades, polymer nanocomposites took the limelight away from conventional polymer-based composites due to their promising potential. One facet that is often highlighted as a reason for their dominance is their ‘size-dependent functionality’. Auffan *et al.* [1] concluded that there is a critical size that is considerably smaller than 100 nm at which properties of particles change. They identified this critical size of about 20–30 nm by relating the exponential increase in the number of atoms localized at the surface to the size of nanoparticles (Figure 1.1). This excessive increase in surface energy of nanoparticles results in crystallographic changes [1, 2], and subsequently effects their interfacial reactivity [3, 4].

Even size dependence of optical and electronic properties as well as bactericidal effects is well reported [5–7]. Silver nanoparticles, for instance, show highest bactericidal effect in the 1–10 nm range, where there are more highly reactive {111} surfaces [6]. These nanoparticles penetrate cell membranes of bacteria to strongly interact with sulphur- and phosphorus-containing compounds. In the process, they release toxic silver ions. In fact, this suggests that particle dissolution is another parameter that is size-dependent. Solubility, although dependent on solvent properties, is also dependent on solute (nanoparticles) properties like specific surface area (in turn, surface energy and interfacial reactivity),

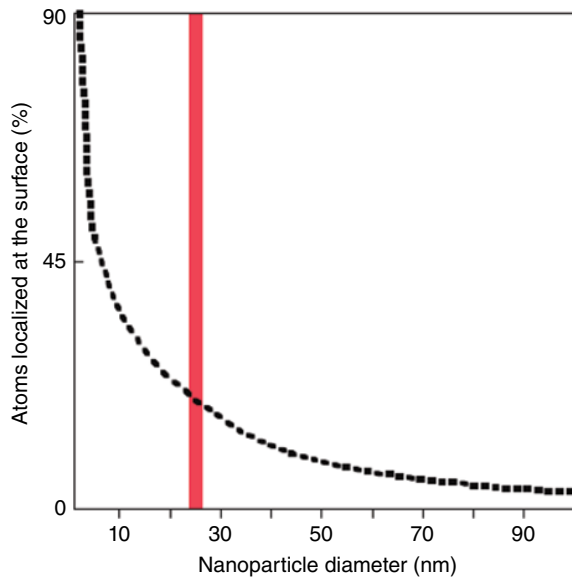


Figure 1.1 Percentage of atoms localized at the surface of a nanoparticle as a function of its diameter. Grey line indicates the boundary below which non-bulk properties emerge. Auffan et al. [1]. Reproduced with permission of Nature Publishing

surface morphology, and dispersion state [8]. More interestingly, these properties are manipulated by changing interactions between them and organic ligands. An example is the use of alkylamines as capping ligands in the control of the size and shape of ruthenium nanoparticles (spherical or rod-like) [9]. Another example is boehmite. By controlling the pH and ionic strength of the synthesis medium, 100-nm-sized fibres (or rods) and even 10–25-nm-sized diamond-shaped particles are formed [1, 4]. Importantly, fibres have (100) as lateral faces and (010) basal planes; and diamond-shaped particles are with (101) lateral faces.

The above discussions suggest that the presence of nanoparticles in a polymer system provides an opportunity to alter many of the base properties of the system. The extent of alteration and the potential of these materials to exhibit superior properties are dependent on two major aspects: interface between polymer and matrix and confinement of polymer matrix chains at the nano-level.

1. **Interface:** It is generally believed that interface is a region with altered chemistry, altered polymer chain mobility, and altered crystallinity [10]. Figure 1.2 shows a schematic of interface region in two systems: micro-composites and nanocomposites [11]. With the same volume fraction of filler, the higher radius of curvature of nanoparticles ensures that more polymer is involved in the interfacial regions. This huge interfacial area created by well-dispersed nanoparticles is shown to influence the surrounding polymer matrix for several radii of gyration [12], fundamentally influencing the glass transition temperature, T_g and mechanical properties of the matrix. This suggests the importance

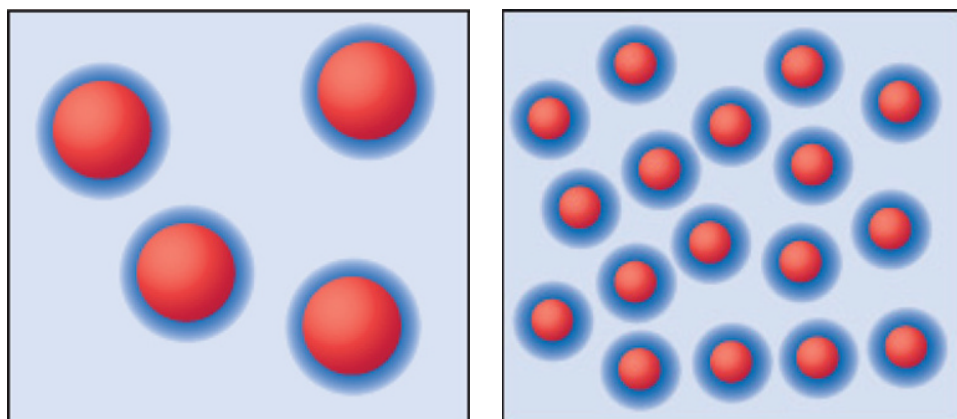


Figure 1.2 Interfacial regions in polymer micro- and nanocomposites. Particles are coloured red, interfacial regions blue and the rest is polymer matrix (in light blue). Schadler [11]. Reproduced with permission of Nature Publishing (See insert for color representation of the figure)

of having a greater degree of control on the interface in polymer nanocomposites. Changes in T_g are particularly important, not only because they yield insights into the fundamental changes in polymer chain dynamics, but also because the associated gains in thermal stability are critical. With many nanoparticles (particularly those with high aspect ratio), results showed that a noticeable change in T_g occurred only when inter-particle distances are less than 500 nm [13]. As an example, Figure 1.3 shows changes in T_g for some polymer nanocomposites (based on graphene and carbon nanotubes) [14]. Though this number (500 nm) is qualitative and subjective (and much larger than that predicted by theory [15]), it indicates that inter-particle spacing is important in influencing intrinsic properties of a polymer.

2. **Nanoscale confinement of polymer chains:** It is known that under conditions of nanoscopic confinement, conformation of chains and segmental mobility are highly affected, suppressing the conventional spherulitic superstructures and resulting in growth of structures with specific crystal orientations. These concepts of confinement/restricted mobility in well-defined geometries and different dimensions versus crystallization have been the subject of many investigations [16–18]. Various reasons are considered for the formation of interfacial zones ranging from chemisorption (e.g. interaction of polar groups with inorganic fillers), to geometric confinement.

Geometric (spatial) confinement specifically hypothesizes that nanoparticles like carbon nanotubes might be treated as macromolecules as their diameters are similar to the radius of gyration of a polymer. Their highly curved surfaces result in strong geometric confinement (by allowing preferential orientation of lamellae) even if (lattice) matching between polymer chain and the filler (graphitic sheet) is absent. This is termed ‘soft epitaxy’ [19, 20]. While in the case of large diameter particles, as the surface curvature is small, the polymer behaves as if it is on a flat surface and, therefore, require crystallographic lattice matching for preferential lamellae organization. The behaviour of large-diameter carbon fibres and

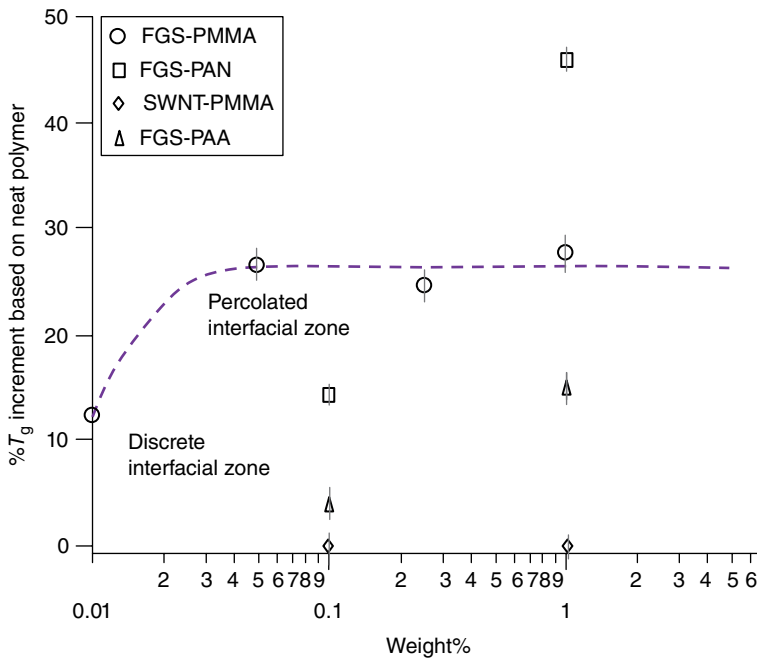


Figure 1.3 Changes in T_g for some selected polymer nanocomposites. FGS, functionalized graphene sheets produced by rapid thermal expansion of completely oxidized graphite oxide; PAA, poly(acrylic acid); PAN, poly(acrylonitrile); PMMA, poly(methyl methacrylate); SWNTs, single-walled carbon nanotubes. Adapted from Ref. [14]

small-diameter carbon nanotubes is shown in Figure 1.4. However, there are many other studies that reported the absence of soft epitaxy despite a uniform dispersion of nanoparticles with sizes similar to or less than individual lamellae. This suggests the complexity in analysing an interface as it is affected by even the slightest change of shape, size and surface modification (influencing the surface energy) of the particles along with their dispersion/inter-particle distances.

Regardless of these discrepancies about interfacial zones, it is rather more important to identify whether their presence would enhance the filler-polymer interfacial strength and ultimately result in improved mechanical properties. Though mostly positive results are reported in the literature on stiffness and strength of polymer nanocomposites, toughness/ductility is often dramatically reduced (in line with the scaling/dimension arguments) [21]. Nevertheless, their promising potential is realized, in particular with functional and physical properties. On this positive note, in this book, we cover a range of functional and physical properties of these materials, with basics as well as advanced and in-depth knowledge on various facets of these properties. These include optical, magnetic, thermal, energy scavenging, biosensing, gas/water barrier, anti-microbial, and biodegradability. As discussed earlier, it is also important to understand how the

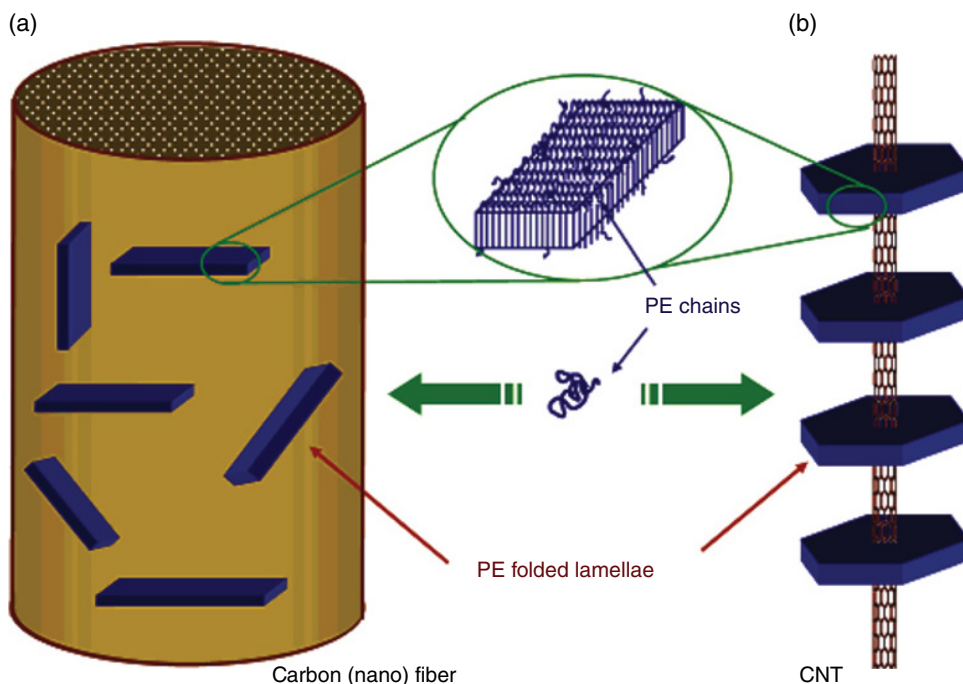


Figure 1.4 Schematic of size-dependent soft epitaxy mechanism. (a) For large-diameter carbon fibres, polymer lamellae will be randomly orientated on the fibre surface, and (b) for small-diameter carbon nanotubes, soft epitaxy dictates the orientation of polymer chains. Li et al. [20]. Reproduced with permission of Elsevier

nanoparticles are dispersed and distributed (inter-particle spacing) in a polymer matrix as many intrinsic properties of polymers are influenced by this. Therefore, to kick-start the proceedings, an entire chapter is dedicated towards three-dimensional microstructural characterization of nanocomposites.

References

- (1) M Auffan, J Rose, JY Bottero, GV Lowry, JP Jolivet, MR Wiesner, Towards a definition of inorganic nanoparticles from an environmental, health and safety perspective, *Nature Nanotechnology* **4** (2009) 634–641.
- (2) R Nagarajan (2008). Nanoparticles: building blocks for nanotechnology. In: *Nanoparticles: synthesis, stabilization, passivation, and functionalization*, Vol. **996**: American Chemical Society, Washington, DC. pp 2–14.
- (3) R Lamber, S Wetjen, NI Jaeger, Size dependence of the lattice parameter of small palladium particles, *Physical Review B* **51** (1995) 10968–10971.
- (4) JP Jolivet, C Froidefond, A Pottier, C Chanéac, S Cassaignon, E Tronc, P Euzen, Size tailoring of oxide nanoparticles by precipitation in aqueous medium. A semi-quantitative modelling, *Journal of Materials Chemistry* **14** (2004) 3281–3288.

6 Functional and Physical Properties of Polymer Nanocomposites

- (5) BJ Ash, A Eitan, LS Schadler (2004). Polymer nanocomposites with particle and carbon nanotube fillers. In: SE Lyshevski (Ed.), *Dekker Encyclopedia of Nanoscience and Nanotechnology*, CRC Press, Boca Raton, FL, pp. 2917–2930.
- (6) JR Morones, JL Elechiguerra, A Camacho, K Holt, JB Kouri, JT Ramírez, MJ Yacaman, The bactericidal effect of silver nanoparticles, *Nanotechnology* **16** (2005) 2346–2353.
- (7) KL Kelly, E Coronado, LL Zhao, GC Schatz, The optical properties of metal nanoparticles: the influence of size, shape and dielectric environment, *Journal of Physical Chemistry B* **107** (2003) 668–677.
- (8) P Borm, FC Klaessig, TD Landry, B Moudgil, J Pauluhn, K Thomas, R Trottier, S Wood, Research strategies for safety evaluation of nanomaterials, part V: role of dissolution in biological fate and effects of nanoscale particles, *Toxicology Science* **90** (2006) 23–32.
- (9) C Pan, K Pelzer, K Philippot, B Chaudret, F Dassenoy, P Lecante, MJ Casanove, Ligand-stabilized ruthenium nanoparticles: synthesis, organization, and dynamics, *Journal of American Chemical Society* **123** (2001) 7584–7593.
- (10) PC Ma, JK Kim (2011). *Carbon nanotubes for polymer reinforcement*. CRC Press, Boca Raton, FL. pp.115–168.
- (11) LS Schadler, Nanocomposites: model interfaces, *Nature Materials* **6** (2007) 257–258.
- (12) VA Harmandaris, KC Daoulas, VG Mavrantzas, Molecular dynamics simulation of a polymer melt/solid interface: local dynamics and chain mobility in a thin film of polyethylene melt adsorbed on graphite, *Macromolecules* **38** (2005) 5796–5809.
- (13) P Rittigstein, RD Priestley, LJ Broadbelt, JM Torkelson, Model polymer nanocomposites provide an understanding of confinement effects in real nanocomposites, *Nature Materials* **6** (2007) 278–282.
- (14) T Ramanathan, AA Abdala, S Stankovich, DA Dikin, M Herrera-Alonso, RD Piner, DH Adamson, HC Schniepp, X Chen, RS Ruoff, ST Nguyen, A AksayI, RK Prud'Homme, LC Brinson, Functionalized graphene sheets for polymer nanocomposites, *Nature Nanotechnology* **3** (2008) 327–331.
- (15) T Desai, P Koblinski, SK Kumar, Molecular dynamics simulations of polymer transport in nanocomposites, *Journal of Chemical Physics* **122** (2005) 134910.
- (16) E Woo, J Huh, YG Jeong, K Shin, From homogeneous to heterogeneous nucleation of chain molecules under nanoscopic cylindrical confinement, *Physical Review Letters* **98** (2007) 136103.
- (17) PA Weimann, DA Hajduk, C Chu, KA Chaffin, JC Brodil, FS Bates, Crystallization of tethered polyethylene in confined geometries, *Journal of Polymer Science Part B: Polymer Physics* **37** (1999) 2053–2068.
- (18) M Steinhart, P Goring, H Dernaika, M Prabhakaran, U Gosele, Coherent kinetic control over crystal orientation in macroscopic ensembles of polymer nanorods and nanotubes, *Physical Review Letters* **97** (2006) 027801.
- (19) L Li, CY Li, C Ni, Polymer crystallization-driven, periodic patterning on carbon nanotubes, *Journal of American Chemical Society* **128** (2006) 1692–1699.
- (20) L Li, B Li, MA Hood, CY Li, Carbon nanotube induced polymer crystallization: the formation of nanohybrid shish-kebabs, *Polymer* **50** (2009) 953–965.
- (21) AH Windle, Two defining moments: a personal view by Prof. Alan H. Windle, *Composites Science and Technology* **67** (2007) 929–930.

2

Three-dimensional Microstructural Characterization of Polymer Nanocomposites by Electron Tomography

Florent Dalmas and Lucian Roiban

MATEIS (Matériaux: Ingénierie et Science), CNRS/INSA de Lyon, France

2.1 Introduction

Nowadays, polymer-based nanocomposites are widely used in designed products for mechanical, optical, thermal, or electrolytic applications. Such macroscopic properties are known to be driven by one specific feature: the huge interfacial area developed by nanofillers [1–5]. As a consequence, the microstructure of the material, mainly characterized by the geometry of the nanofillers and their dispersion within the polymer matrix, is one of the key parameters. Thus, one of the most challenging points for the understanding of structure–properties relationships in nanocomposites, is the development of meaningful and effective tools for multiscale morphological characterization and quantification with a nanoscopic resolution.

Transmission electron microscopy (TEM) only provides two-dimensional (2D) projections of a three-dimensional (3D) sample of a given thickness. As a consequence of these limitations, the interpretation of such images is not unambiguous. On the contrary, electron tomography (ET) generates 3D images with a nanometer-scale resolution from tilt series

of 2D projections [6]. Although the first paper using tomography techniques in TEM in order to study polymeric materials was published as early as 1988 by Spontak *et al.* [7], ET recently emerged as an efficient tool to get a detailed and realistic description of nanostructured polymeric systems [8–15]. For instance, substantial further progresses on the microstructural analysis of block copolymers [16, 17] or polymeric nanocomposites [9, 11, 14, 15, 18, 19] have been achieved during the past decade using this technique.

In this chapter, we will, in a first time, briefly recall the principle of electron imaging modes and TEM. Then, several examples of applications of ET to polymer nanocomposites will be presented and discussed, considering the obtained contrast and resolution in the volume. Finally, the issue of 3D image analysis and quantification will be addressed.

2.2 3D Observation at the Nanoscale

2.2.1 Imaging with Electrons

The big advantage of working with electrons in an electron microscope is the high resolving power (up to the atomic scale) that can be reached thanks to the small wavelength of the electron beam (order of magnitude of 1 p.m., depending on the accelerating voltage, e.g., 2.5 p.m. at 200 kV). In this chapter, we will focus on TEM where electrons for imaging are collected below the sample (the image is formed in transparency by electrons transmitted through the sample as illustrated in Figure 2.1a). Generically, by TEM it is understood that the transmitted image is formed employing a parallel (or quasi-parallel) electron beam. In several electron microscopes, it is possible to record a scanning TEM (STEM) image; this imaging mode is formed by focusing and scanning the electron beam at the surface of the sample. The image is recorded by detectors collecting the electrons scattered at different angles (see Figure 2.1b). Electron–matter interactions are responsible for the contrast in electron microscopy imaging. The involved physical phenomena are many and various [20], and so are the acquisition modes in electron microscopes. Figure 2.1 schematically sums up the multiple signals and operating modes available in a (S)TEM. Several books are available describing in detail the principles, experimental, and instrumental methodologies in electron microscopy; the reader is invited to refer to this literature for a complete presentation of these techniques (see, e.g., Refs. [20] and [21]). Conventionally, TEMs are mostly used in the “bright field” (BF) mode when the central part of the transmitted electron beam is selected for imaging (see Figure 2.1a). In this mode, the contrast in the image can be related to the absorption of electrons (so-called mass-thickness contrast) and to the diffraction of the electron beam for crystalline materials. For these crystalline materials, a “dark field” (DF) imaging mode can be set up by selecting a diffraction spot for image formation, highlighting thus one specific type of crystallographic planes in the image (not represented in the figure). The image is recorded either on a film or using a camera located below the sample. Alternatively, the image can also be formed by STEM by collecting electrons below by an annular detector. Furthermore, a contrast mainly due to the atomic number of the material phases can be obtained by selecting the electrons scattered at high angles with an annular detector. This mode is called “high-angle annular DF” (HAADF) (Figure 2.1b). It is worth mentioning here that all recorded images are projections of the sample along the optical axis.

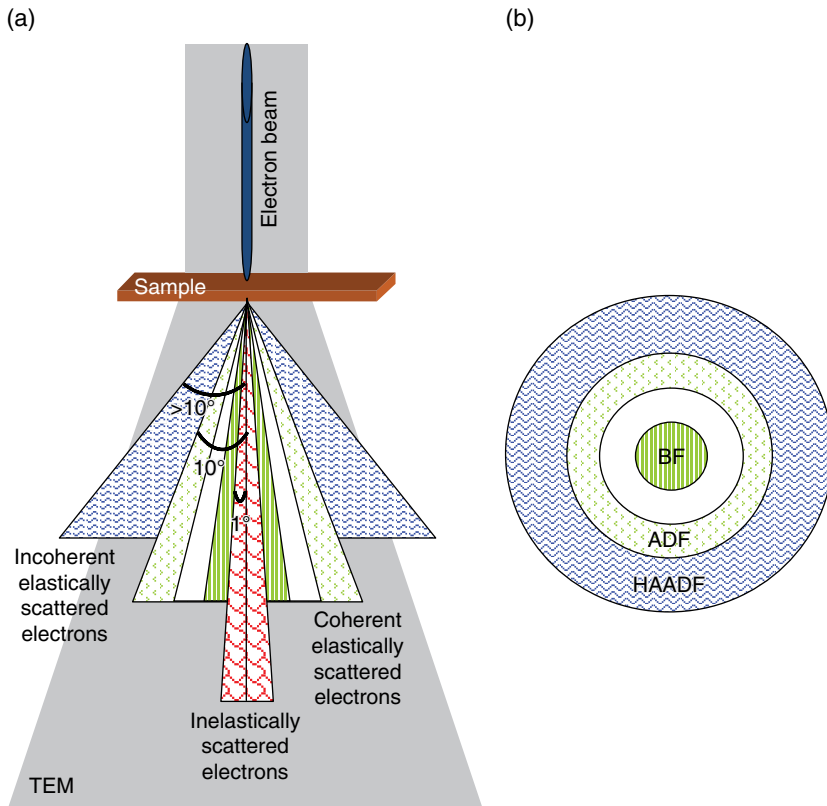


Figure 2.1 (a) The gray-filled area intuitively describes the image formation in conventional TEM mode; the image is recorded on a film or by a digital camera. The textured areas describe the angle distribution of scattered electrons in relation to the type of interactions involved with the sample. (b) Geometry of the annular detectors used in STEM mode: BF, bright field; ADF, annular dark field; and HAADF, high angle ADF. Basically, the ADF and HAADF are the same detectors, the imaging mode being selected by changing the camera length

In addition to structural observation, the electron beam also provides chemical information through two types of spectroscopy: Energy-dispersive X-ray spectroscopy (EDX) and electron energy loss spectroscopy (EELS). These techniques are based on inelastic electron–matter interactions. For EDX, the emitted X-ray photons are collected and their energy is related to the chemical nature of the ionized atoms in the sample. For EELS analysis, inelastic scattered electrons are collected below the sample, and the quantity of energy that was lost through the sample mainly provides information about the chemical nature of the atoms and their ionization state. This last technique is better suited to light-element chemical analysis.

Both spectroscopies allow creating chemical maps of the sample either in STEM by acquiring a spectrum point by point in the sample (“data cube” acquisition), or in TEM by

recording an image formed by electrons with a specific energy loss corresponding to the ionization edge or a plasmonic vibration of a given chemical element (imaging mode called “EFTEM”—energy-filtered TEM).

2.2.2 Principles of Transmission ET

The term “tomography” comes from the Greek words *tomos*=thin and *graphein*=to write. Nowadays, based on the Radon’s theory [22, 23], tomography techniques consist in the volume observation of an object using its projections. The transmission T, also called tilted tomography, can be divided into three major steps: image acquisition, data treatment (projection alignment and volume reconstruction), and data segmentation (quantification and volume visualization). These different steps are schematized in Figure 2.2 and detailed in the following text.

First, data for tomographic observation consist in series of projections acquired at different tilt angles in one imaging modes available on the microscope. Nowadays, such acquisitions can be automated within tilt angles ranging up to $\pm 80^\circ$, depending on the sample geometry,

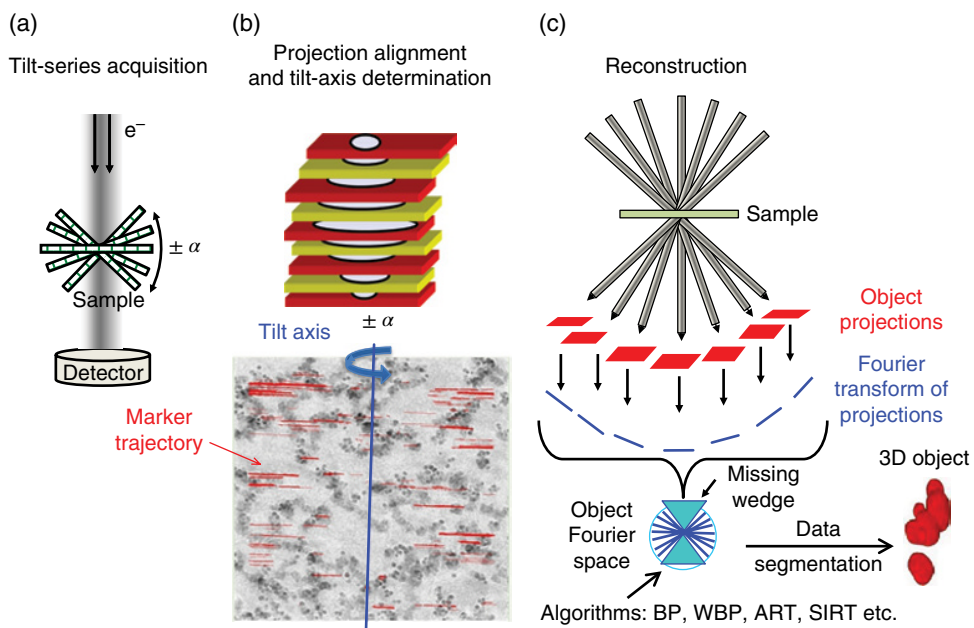


Figure 2.2 The different steps of electron tomography: (a) acquisition of tilted projections over a tilt angle range of $\pm \alpha$, the image can be recorded by a camera or can be computed using a detector; (b) alignment of projections and correction of the tilt axis, image rotation, and magnification by tracking fiducial markers over the full projection series; and (c) the volume reconstruction represented by the Fourier space of the object. Reconstruction algorithms are employed to calculate the volume. Then, obtained volume is segmented by selecting the gray levels resulting in a three-dimensional representation of the object of interest

the sample-holder, and microscope configurations. The sample movements and focus variation between successive projections, due to mechanical imperfections of the goniometer, require an important attention during the acquisition. If the microscope is well calibrated and the sample is at the eucentric height, the image tracking and focalization are performed in an automatic way. Thus, once the tilt projection series is recorded, a rigorous alignment of all the projections in a unique system of coordinates is required. To do so, fiducial markers (consisting in well-identified points in the microstructure or additional gold nanospheres) can be automatically detected and tracked over the entire tilt series. The projections alignment procedure allows, as well, to correct several parameters such as the position of the tilt axis, the tilt angle values, the rotation of the images, and the magnification difference due to the focus variation. Obtaining a well-aligned and corrected tilt series is of importance to get a fine contrasted volume.

Then, the next step is the volume calculation (see Ref. [24] for a recent review of calculation methods). The object reconstruction can be computed using analytical or iterative algorithms [6, 24]. Among the analytical methods, the back projection (BP) is the most commonly used method. The principle of BP can be illustrated by considering the theorem of the central section, which stipulates that the Fourier transform of each projection of an object is a cross section in the Fourier space of the object, oriented perpendicular to the projection direction and with a thickness equal to the invert of the object diameter [25]. By adding all the cross sections, the Fourier space of the object can be filled. Coming back in the real space the volume of the analyzed object is obtained (see Figure 2.2). BP is a fast and easy-to-implement calculation method. However, the obtained volume is usually blurred. This effect can be explained by the fact that in the Fourier space, low frequencies (points near the center of the Fourier space) are more densely sampled than high frequencies (points located on the edge of the Fourier space). To compensate this heterogeneity in the sampling of the Fourier space, each point can be weighted according to its distance from the center of the Fourier space [25]. This method is called weighted BP (WBP). Alternative iterative methods were proposed to ameliorate the quality of the reconstruction. In these methods, the difference between the calculated volume and the initial object (constituted by all the experimental projections) defines the convergence criteria of the algorithm. The simultaneous iterative reconstruction technique (SIRT) [26] and the algebraic reconstruction technique (ART) [27] are the most commonly used techniques. SIRT compares simultaneously all the projections calculated from the BP reconstructed volume to the experimental ones; whereas in ART, the reconstruction is corrected while comparing each calculated projection to the experimental one corresponding to the same tilt angle. These methods are slower and more difficult to implement (among other parameters, the choice of the number of iterations and convergence criteria is crucial for the reconstruction quality), but they lead to more accurate reconstructed volumes, also called tomograms.

Nevertheless, the reached resolution in the reconstructed volumes is usually anisotropic. Indeed, the Radon's theory is based on an infinite number of projections acquired all around the sample (i.e., with tilt angles of $\pm 90^\circ$). Unfortunately, because of the small gap of the pole piece and the shade of the sample-holder at high tilt angle, the tilt angles are very often limited in a TEM ($\pm\alpha$); the rotation of the sample is thus not complete and a "missing

wedge” remains in the data (see Figure 2.2). This induces a loss of resolution in the z direction parallel to the electron beam [6]. First, the resolution depends on the geometrical characteristics of the sample: the thinner the sample, the more resolved the volume. Anyway, in a Cartesian system of coordinates, the volume has the resolution of the projections in the y direction (corresponding to the sample-holder or tilt-axis direction). In the x direction, the resolution is driven by the total number of acquired projections, N . The volume is less resolved in the z direction where it is directly related to the maximum tilt angle, α . Figure 2.3 illustrates this artifact on an aggregate of silica (Si) nanoparticles in a polystyrene (PS) matrix. One can observe the artificial elongated shape of the Si nanospheres in the z direction, resulting in a merging of the sphere in this direction. As an example, using traditional

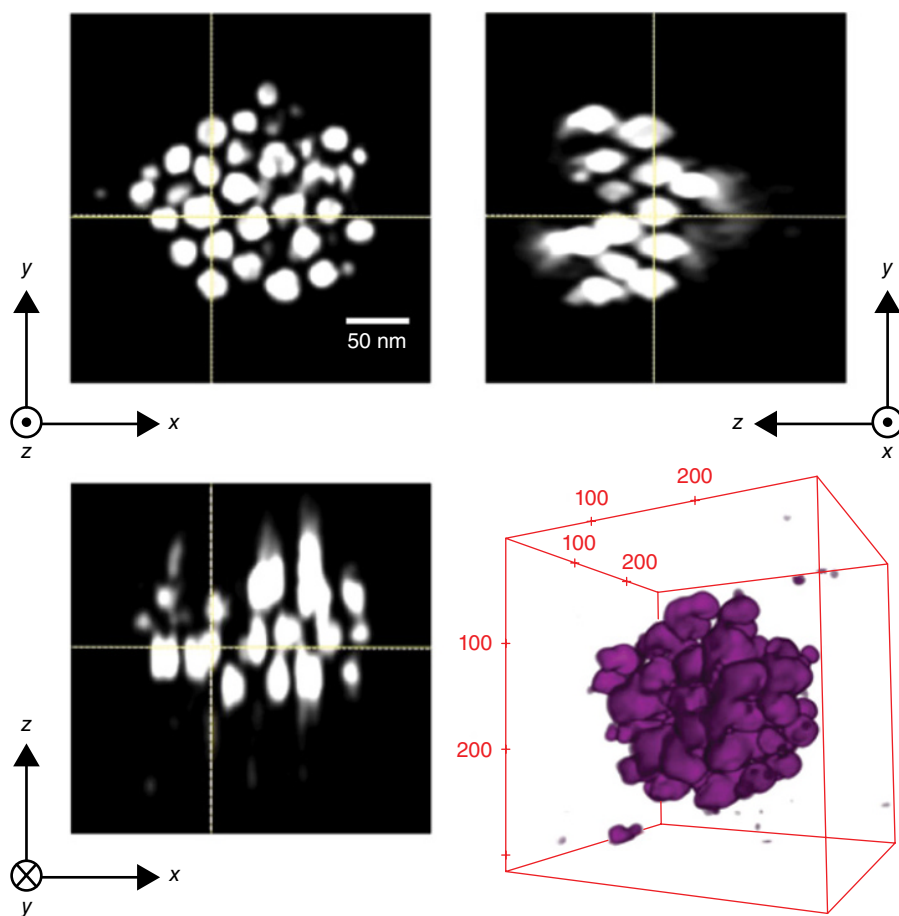


Figure 2.3 ET of aggregated silica nanoparticles in a polystyrene matrix: 3D rendering and corresponding orthogonal digital slices of the reconstructed volume (acquired at $\pm 60^\circ$ and computed using SIRT with 20 iterations). Dalmás et al. [18]. Reproduced with permission of American Chemical Society

mathematical treatments [6], the resolution can be estimated, in Figure 2.3, to be 1, 3.9, and 6.2 nm in the y , x , and z directions, respectively.

To better visualize and quantify all 3D characteristics of the sample, the volumes are segmented by selecting the gray levels representing the different components of the microstructure. However, the accurate quantification of the volume is strongly limited because of the missing information. Different strategies have been recently considered to solve this issue. From an experimental point of view, needle-like TEM samples have been, for instance, processed by focused ion beam (FIB) technique, allowing a complete rotation of the sample and avoiding any missing angular observation [28, 29]. Multiple-axis tomography has also been developed [17, 30]. By acquiring several tilt series at various tilt axes, it reduces the “missing wedge” to a “missing cone,” which decreases the elongation in the z direction in reconstructed volumes. On the other hand, several teams have developed new reconstruction algorithms in order to improve the reliability of the reconstruction [24, 31–35]. Generally speaking, these algorithms are based on the knowledge of prior information on the reconstructed objects. For instance, the discrete ART (DART) assumes that the volume consists in discrete objects that match one grey level [31]. The “compressed sensing” numerical method extended by Leary *et al.* [33] for ET is based on the reconstruction of a signal “sparse” in known small domains. More reliable reconstructed volume with minimized artifacts usually observed in ET (streaking, object blurring, or elongation) can be thus obtained from such numerical approaches since the raw tilt series consist in sufficiently contrasted well-defined objects with a discrete gray-level range.

2.3 Application to Polymer Matrix Nanocomposites

In the past decade, transmission ET has been applied to polymer matrix nanocomposites filled with different types of inorganic nanoparticles (nanoplatelets, nanospheres, or nanotubes) [9, 11–15, 18, 19, 36–41]. First, a good contrast between inorganic particles and an organic matrix was achieved by conventional BF-TEM. For instance, as illustrated in Figure 2.4, the 3D microstructure of ionic aggregates in Zn-neutralized sulfonated PS (SPS-Zn) ionomers was characterized by ET, using BF-TEM imaging and SIRT algorithm with 20 iterations for the reconstruction [8]. Ionomer properties are governed by the formation of ionic aggregates within the materials that can act as crosslinking nodes and/or can be considered as stiff fillers. The morphology of such aggregates was found to be influenced by the process of the material. Tomographic analysis was carried out on two different SPS-Zn films prepared either by hot-pressing (HP) or by solvent-casting (C). Figure 2.4 displays the reconstructed volume obtained for HP SPS-Zn film. As usual in ET volume rendering, the reconstructed volumes are segmented in Figure 2.4 in order to only highlight the features of interest (here, the Zn-rich aggregates) by thresholding the image gray levels so that the polymer matrix becomes transparent. In addition, in order to analyze the 3D microstructure in more details, orthogonal cross sections of the reconstructed tomograms are also shown. A better contrast is obtained in such digital slices than in conventional TEM, helping considerably in the analysis of the spatial organization of the ionic aggregates.

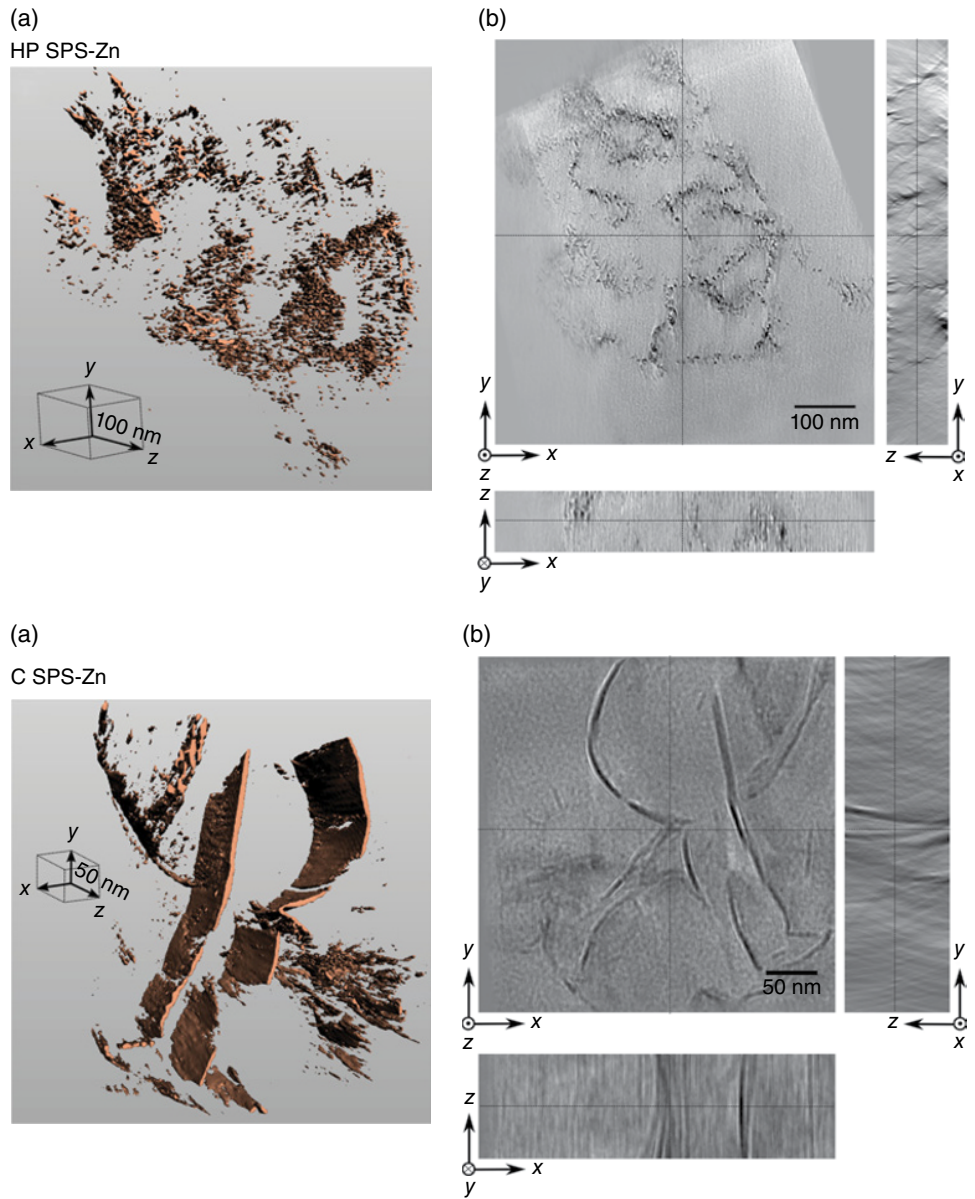


Figure 2.4 (a) Surface rendering of the ET 3D reconstruction and (b) corresponding digital orthogonal slice images of the HP SPS-Zn (above) and C SPS-Zn (below) samples after surface rendering of the Zn-rich phase (BF-TEM imaging, SIRT reconstruction with 20 iterations). Dalmas and Leroy [8]. Reproduced with permission of American Chemical Society

An almost spherical shape (typical diameter of 5 nm) can be observed for the ionic aggregates in Figure 2.4, heterogeneously dispersed within the PS matrix. On the other hand, very large ionic aggregates dispersed within the polymer matrix can be observed in Figure 2.4 for the C SPS-Zn sample. These aggregates obviously present a nanoplatelet shape with a thickness of about few nanometers and length, hundreds of nanometers (as deduced from Figure 2.4). In this study, ET allowed unambiguously observing ionic aggregate morphology and highlighted the influence of the process on the final microstructure.

The dispersion of PS-grafted spherical Si nanoparticles in a PS matrix was also successfully investigated using the same conventional ET procedure [18]. Depending on the R ratio between the molar mass of the grafted PS chains and the matrix ones, various microstructures were observed as shown in Figure 2.5. A procedure for the segmentation of the tomograms was optimized in order to isolate the nanoparticles within the volume. As R increases, the microstructure was found to gradually evolve from a densely aggregated structure to a homogeneous dispersion of individual particles.

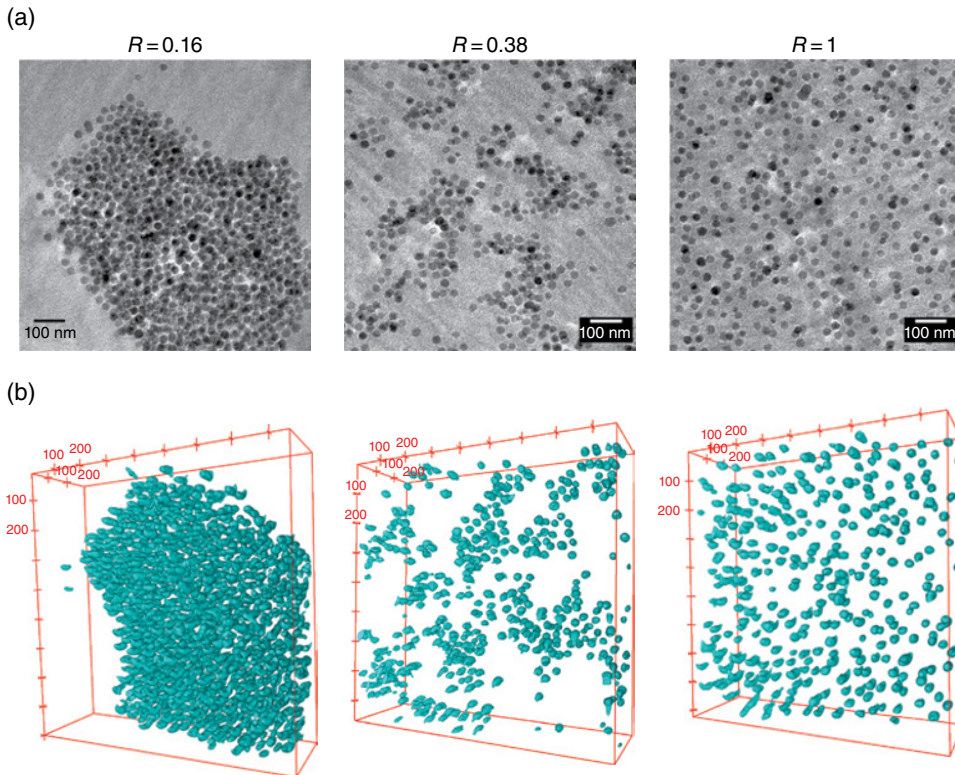


Figure 2.5 (a) TEM image at tilt angle 0° and (b) 3D rendering of the segmented volume for polystyrene/polystyrene nanocomposites filled with grafted silica nanoparticles with $R=0.16$, 0.38 , and 1 (BF-TEM imaging, SIRT reconstruction with 20 iterations). Dalmás et al. [18]. Reproduced with permission of American Chemical Society

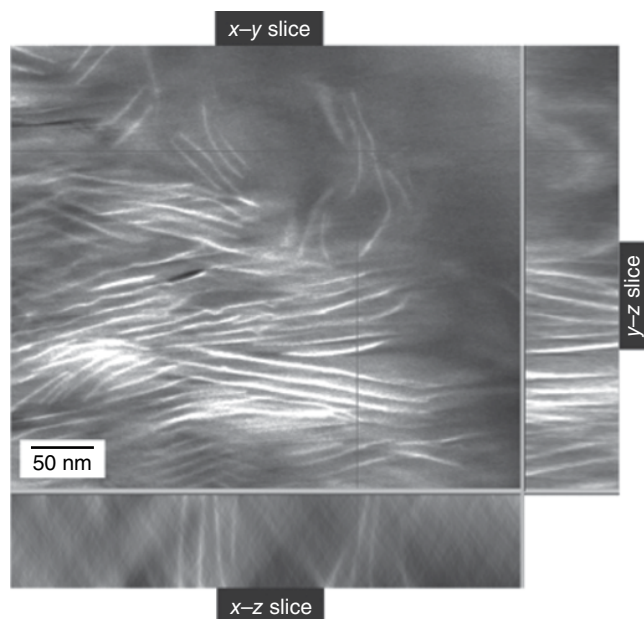


Figure 2.6 Orthogonal view of ET reconstructed volume of an epoxy/layered silicate nanocomposite (HAADF-TEM imaging, SIRT reconstruction). Drummy *et al.* [19]. Reproduced with permission of American Chemical Society

In their study, Lu *et al.* discussed the influence of electron imaging mode on the quality of the reconstructed volume [15]. They compared volumes obtained on carbon black (CB)-filled polymer nanocomposites by BF-TEM and ADF-STEM. As it is commonly utilized, they showed that in BF-STEM, a slight defocusing of the image is necessary to get enough contrast in the tomograms for accurately segmenting the CB phase. By inducing phase contrast, underfocus increases the contrast at the interface between CB particles and polymer matrix. However, the CB volume fraction extracted from the volumes was found to be much larger than the known experimental concentration and distortion of the particle size was observed. On the other hand, ADF-STEM images are collected in focus and formed through incoherent signal collection. Volumes obtained by ADF-STEM showed fewer artifacts and were more reliable for quantification. Drummy *et al.* investigated epoxy/layered silicate nanocomposites by HAADF-STEM tomography [19]. They highlighted that the Z-contrast provided by HAADF-STEM is much more efficient for observation of 1-nm-thick clay nanoplatelets in a polymer matrix than conventional BF-TEM (see Figure 2.6). Here again, a defocus is used in BF-TEM to create phase contrast. However, in addition to the low image contrast, the defocus increases the apparent thickness of silicate layers mainly because of the appearance of Fresnel fringes parallel to the layers. On the other hand, the contrast in HAADF-STEM increases with the local variation of atomic number and is free from any artifact due to defocus, sample thickness, or diffraction effects in the peculiar case of crystalline nanoparticles.

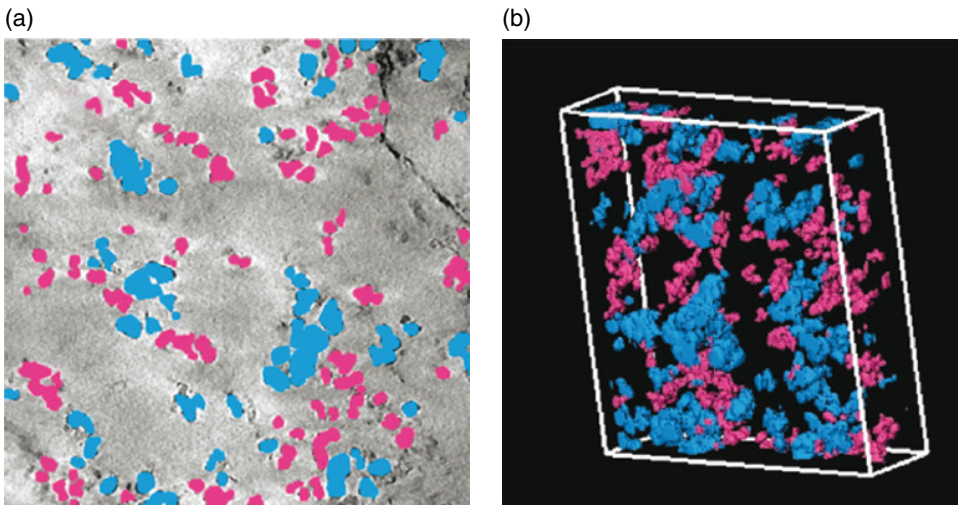


Figure 2.7 (a) Segmentation of CB (blue) and Si nanoparticles (red) in a digital slice and (b) in the 3D reconstruction of the CB-Si/natural rubber system. Box size is $726\text{ nm} \times 726\text{ nm} \times 107\text{ nm}$ (EFTEM imaging, WBP reconstruction). Jinnai *et al.* [11]. Reproduced with permission of American Chemical Society (See insert for color representation of the figure)

Jinnai *et al.* applied EFTEM tomography to ternary systems made of a rubbery matrix filled with CB and Si nanoparticles [11]. Conventional TEM imaging does not allow significantly differentiating both kinds of particles in the 3D reconstruction because of the weak difference in electron density between CB and Si. They managed to solve this issue by acquiring tilt series through EFTEM imaging mode. As recalled previously, EFTEM allows a chemical mapping of the microstructure by collecting electrons with a particular energy loss, ΔE . In this study, Si-mapped projections were recorded at every tilt angle with a filtering window at $\Delta E = 99\text{ eV}$, corresponding to the L-edge of Si. As reproduced in Figure 2.7, the Si nanoparticles and then, by deduction, the CB particles were selectively segmented in the volumes. Such experiments allow the authors to conclude that both CB and Si nanoparticles formed aggregates that consist of only one type of particles, as it can be deduced from Figure 2.7 where no mixed aggregate is visible.

Using also ETEM, Gass *et al.* took advantage, in their study, of the difference in plasmon energy that exists between the EELS spectra of multi-walled carbon nanotubes (MWNTs) and nylon 6,6 [39]. By recording EFTEM tilt series for both plasmon energies (22 eV for MWNTs and 28 eV for nylon 6,6), a reconstruction was computed from the “ratio images” in order to increase the contrast between both carbonaceous phases in the tomograms. Figure 2.8 shows an example of what can be obtained with such a method on a nylon/MWNTs nanocomposite. The enhanced contrast allows obviously identifying the nylon matrix, MWNTs, and holes from the microstructure.

As previously discussed, the “missing wedge” artifact in ET is mainly due to the design of the sample and the sample-holder. Indeed, in most of the studies previously presented,

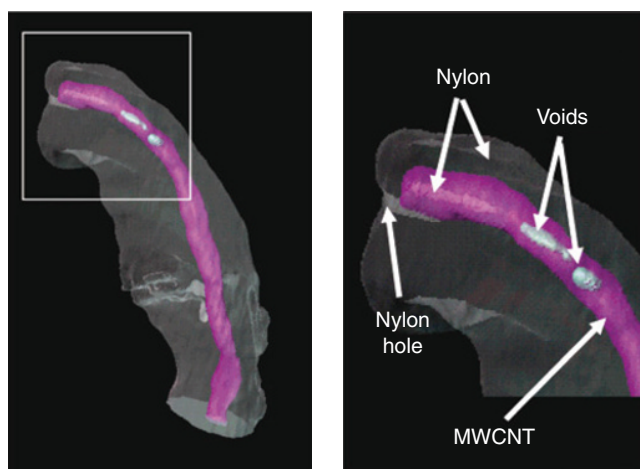


Figure 2.8 Surface render of the nanotube (purple) and nylon (gray) from the tomographic reconstruction of the plasmon ratio 28 eV/22 eV. The nylon that has filled the top end of the nanotube is shaded in light purple. A hole that occurs in the nylon can be seen just under the top end of the nanotube, and the voids within the nanotube are represented by pale green (EFTEM imaging, SIRT reconstruction). Gass *et al.* [39]. Reproduced with permission of American Chemical Society (See insert for color representation of the figure)

thin slices of the sample (typically between 100 and 200 nm thick) are sectioned by ultramicrotomy either at room or cryo temperature, depending on the T_g of the matrix. The slices are then deposited on a TEM grid. Such configuration strongly limits the available tilt angle range in the microscope because of shading effect from the sample-holder or the TEM grid at high tilt angle. Moreover, because of the parallelogram shape of the sample, the projected thickness increases with the tilt of the sample, resulting in a loss of contrast and focus at high tilt angle. Recent advances on FIB technique lead several groups to propose new design of samples for ET acquisitions. For instance, Kawase *et al.* prepared needle-shaped specimen of nanocomposites filled with zirconia nanoparticles, with a diameter of around 100–200 nm using FIB. Once attached on a modified sample-holder and inserted in the microscope column, such a specimen allows for a full $\pm 90^\circ$ rotation, avoiding any missing wedge effect. Examples of reconstructed volumes are shown in Figure 2.9 where no elongation artifact can be observed. In the same study, the authors showed that, by limiting the tilt angle, α , in the reconstruction of the same tilt series, the contrast between zirconia nanoparticles and the polymer matrix become worse. Furthermore, as α decreases, the elongation of the needle shape and the nanoparticles in the tomograms becomes more and more pronounced and the calculated zirconia volume fraction is even higher than the known composition of the sample. Nevertheless, this type of nanomachining becomes more difficult for soft materials, very sensitive to ionic beam damages and induced heating.

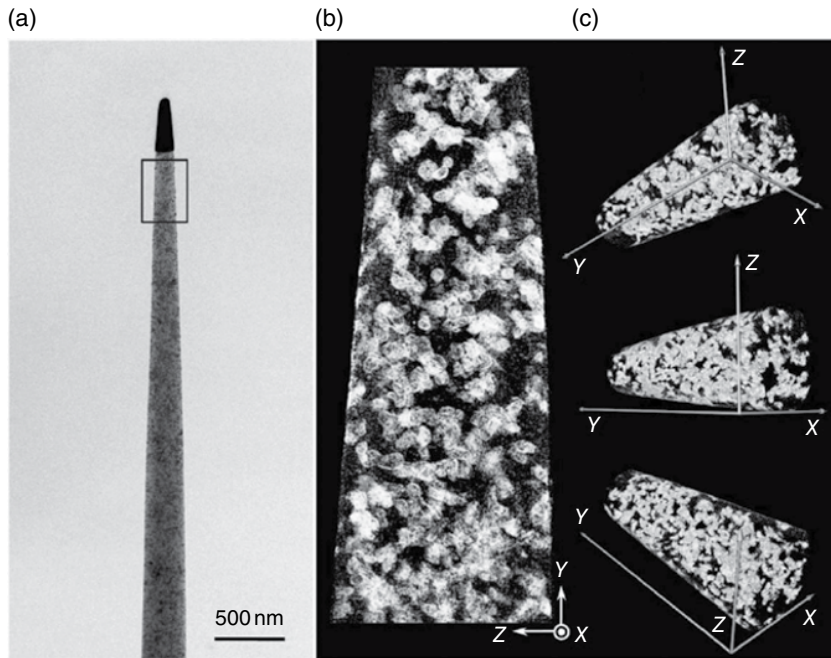


Figure 2.9 (a) TEM pictures of needle-shaped nanocomposites containing zirconia nanoparticles (the rectangle indicated the area subjected to ET experiments); (b) volume render; and (c) surface render of the reconstructed volume at different viewing angles (BF-TEM imaging, WBP reconstruction). Kawase *et al.* [29]. Reproduced with permission of Elsevier

2.4 3D Image Analysis and Quantification

3D image analysis is the next important step for a complete description and quantification of the material microstructure. Beyond the calculation of the filler volume fraction or the particle volume distribution, it is thus of importance to develop numerical tools in order to extract relevant microstructural parameters from 3D. However, before image analysis, the main critical point is the segmentation of the volume allowing individualizing the objects of interest (e.g., pores, particles, or aggregates) from the background (matrix signal) with the best signal-to-noise ratio. This usually implies precise investigation on a prior image pretreatment routine made of successive filters or image calculation (e.g., median filter, watershed process, Gaussian blur, and opening/closure) [42].

Several studies focus on the quantification of shape, size, and spatial distribution of objects in segmented volumes [38, 43–47]. For example, Thiedmann *et al.* recently proposed a method to measure, from ET images, size and coordination of densely packed CdSe nanoparticles in nanocomposites for solar cell application [46]. By assuming a spherical shape for the particles, they analyzed the interconnected conductive pathway within

the volume for a given electron hopping distance. For very anisotropic nanofillers, their orientation within the matrix is an important parameter that tunes the macroscopical properties of the materials (e.g., a percolating path of nanoparticles can be induced, leading to mechanical and electrical specific behavior). Nichioka *et al.* evaluated the 3D orientation of clay nanoplatelets in nanocomposites by fitting each platelet by an equivalent ellipsoid and analyzing its three semi-axis orientation [37]. From image treatment and analysis software such as ImageJ [48], several measurements can be implemented based on plugins available from the user community. For instance, one of the functions of the BoneJ plugin allows calculating the three orthogonal principal axes and moments of inertia around those axes of segmented objects [49]. Anisotropic nanocomposites were prepared by dispersing magnetic nanoparticles (γ - Fe_2O_3) in a PS matrix through a solvent casting way under a constant magnetic field of variable intensity [50]. Using this plugin, Figure 2.10 illustrates measurements of the 3D orientation of nanoparticle aggregates from ET of nanocomposites prepared under a magnetic field. One can easily observe that the magnetic field induces a preferential orientation of the nanoparticles. Indeed, without magnetic field, the points are almost randomly distributed, whereas a concentration of points for $\theta \approx 0^\circ$ and $60^\circ < \phi < 80^\circ$ is seen when a 600G magnetic field is applied during the solvent evaporation.

As soon as the filler geometry is well known, the elongation artifact inherent to the TEM tomography can be avoided by generating 3D dispersions of equivalent objects from the experimental reconstructed volumes. Morphological parameters can be then extracted from such model microstructures. Such an approach was applied to nanocomposites made of a PS matrix filled with PS-grafted silica nanoparticles (see ET observations in Figure 2.5) [18]. The obtained tomograms were pretreated using the 3D tools of the ImageJ software [48]. In a first step, in order to reduce noise in the image and to enhance the edge of the objects, a 3D median filter was applied, followed by a slice-by-slice 2D background subtraction.

Then, in order to overcome the elongation artifact and the artificial merging of the nanoparticles in the z direction, as illustrated in Figure 2.3, a watershed filter was applied to individualize the silica nanoparticles. To this end, a 3D minimum filter was first applied with a radius of 4.75 nm (i.e., 5 pixels) after binarization of the volume. Such a filter results in an erosion of the particles over a thickness of 4.75 nm. As the particle mean radius is about 13 nm, this first step allows isolating the center of each particle and reducing the noise in the tomograms. Then, the coordinates of the particle centroids can be easily found by using the “3D object counter” plugin [51] from ImageJ and used as seeds in the watershed process. The nanoparticles are then individualized and separated in the segmented volume. Finally, the volume of each individualized particles was measured and, by dispersing spherical objects with the same volume at the nanoparticle centroid coordinate, a model-equivalent microstructure was generated (see Figure 2.11a and b).

Then, a quantitative image analysis approach was developed based on a 3D Voronoi tessellation using the open source software library developed by Rycroft [52]. A precise analysis of the nanoparticle local environment was extracted from this method through the identification of the closest neighbors of each particle (see Figure 2.11c and d). The quality

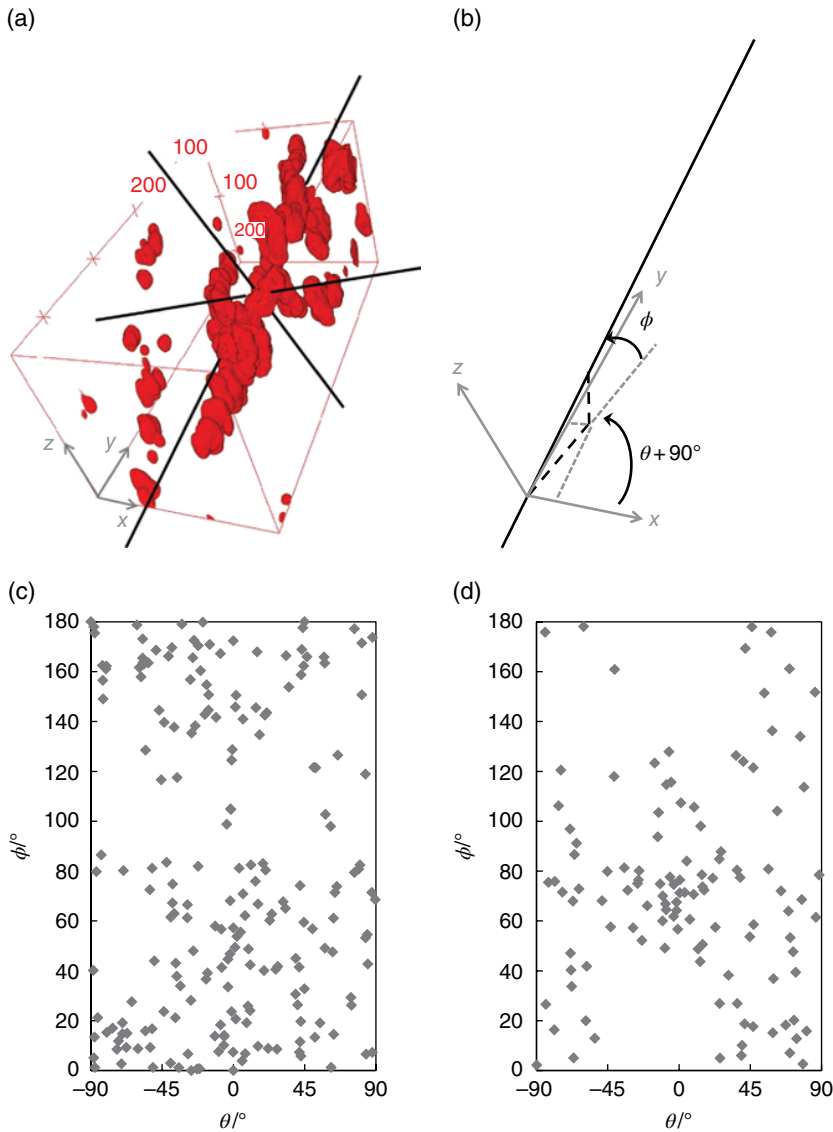


Figure 2.10 (a) ET of an anisotropic aggregate of $Y-Fe_2O_3$ nanoparticles within a polystyrene matrix showing the orientation of principal axes (box scale is given in nanometer) and (b) definition of the polar coordinates, ϕ and θ , in the volume coordinate system $(x; y; z)$. Measured orientation distribution of segmented aggregates in $PS/Y-Fe_2O_3$ nanocomposites prepared by solvent casting either without (c) or with (d) a magnetic field $B=600G$

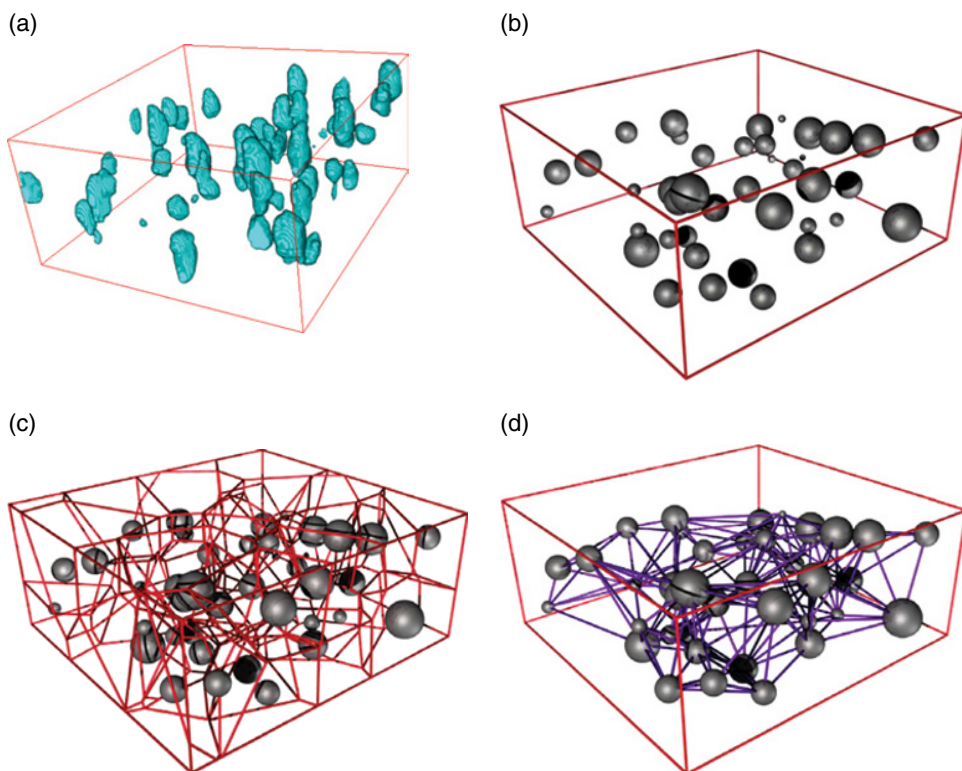


Figure 2.11 (a) ET observation of silica nanoparticles: 3D rendering of the volume after watershed treatment and segmentation, (b) equivalent 3D dispersion of polydisperse spheres, (c) Voronoi cells tessellated from each sphere, and (d) close neighbor identification

of the dispersion could quantitatively be discussed from statistical measurements of the interparticle distance, the number of closest neighbors, and the local density (Φ_{local} , defined as the ratio between the nanoparticle volume and the volume of its surrounding Voronoi cell).

For instance, the dispersion state of the nanoparticles within the PS matrix can then be directly quantified through the local density distribution in the whole volume. Indeed, the Voronoi cell described, for a particle, the area of direct influence with its first neighbors and is an indicator of its local environment. The plot of the full width at half maximum (FWHM) of the Φ_{local} distributions (Figure 2.12) highlights the microstructural transition from densely aggregated nanoparticles to a homogeneous random dispersion as R increases. The case where $R=0.38$ being a critical point in this transition. The FWHM almost follow an R^{-1} decrease from 17 vol% (i.e., a wide distribution revealing a large-scale heterogeneous dispersion) to 2–3 vol% (close to the 5 vol% macroscopical particle loading) for randomly distributed particles. For low R values, the aggregation of the particle was related to a collapse of the grafted chains, resulting from the entropic expulsion of the free PS

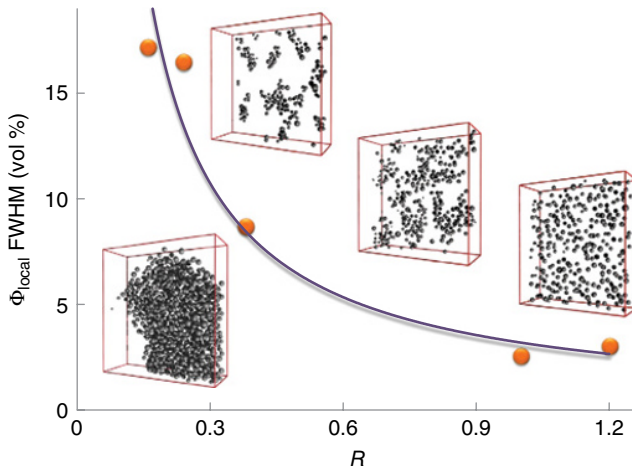


Figure 2.12 Evolution of the full width at half maximum (FWHM) of the local volume fraction distribution with the R ratio in polystyrene nanocomposites filled with 5 vol% silica nanoparticles. The equivalent model microstructures are shown for $R=0.16, 0.24, 0.38,$ and 1.0 . Dalmas *et al.* [18]. Reproduced with permission of American Chemical Society

chains from the smaller grafted ones. For higher R values, the free chains can swell the grafted ones, thereby creating repulsive interparticle interactions and favoring the particle dispersion.

2.5 Conclusion and Prospects

In the past 20 years, ET emerged as a very efficient tool, becoming easier and easier to implement in a TEM. The use of ET in the study of microstructure/properties relationships in polymer nanocomposites gives access to the third dimension in TEM samples, thus eliminating any ambiguity in microstructural interpretation and allowing for a complete description of the morphology and dispersion of nanoparticles in the polymer matrix. Nevertheless, ET always involves the optimization of a complex compromise between imaging mode, contrast, specimen design (e.g., sample thickness and maximum tilt angle), beam-induced damage, and image resolution (see, e.g., the recent paper of Chen *et al.* [53]); it is even more complicated when applied to electron beam-sensitive materials such as polymers. A new challenge in ET would be the development of a “low-dose” ET technique, based on quick recording of tilt series coupled with post-image corrections, in order to minimize the electron dose received by the sample throughout the acquisition and to prevent induced damages.

Beyond the volume viewing of the microstructure at the nanoscale, morphological parameters can be extracted from ET in order to get a quantitative characterization of the structure and to give input parameters for simulation or modeling approaches. At this point,

the segmentation step becomes very crucial in order to accurately highlight and individualize the features of interest in the microstructure. Then, 3D image analysis tools devoted to ET have to be developed, taking into account artifacts inherent to ET (anisotropic resolution, contrast interpretation, etc.).

However, nanocomposite microstructure is very often complex and hierarchically organized at different scales (nanoparticles, agglomerates, aggregates, percolating network, etc.). Thus, new developments for tomographic observation of larger volume with a nanoscale resolution of such multiscale materials are of interest. For instance, several teams investigated the advantage of the high focus depth that can be reached in STEM imaging mode when applied to ET on thick samples (around several micrometers) [14, 54]. Alternatively, recent advances in the development of dual beam microscope coupling an FIB with an SEM open new alternatives for 3D microstructural characterization at a larger scale [55]. By successively milling cuts in a selected area of the sample with the FIB, a “slice-by-slice” observation can be recorded with the SEM. Figure 2.13 illustrates the potential of this technique on a silica nanoparticle/Poly(dimethyl siloxane) (PDMS)

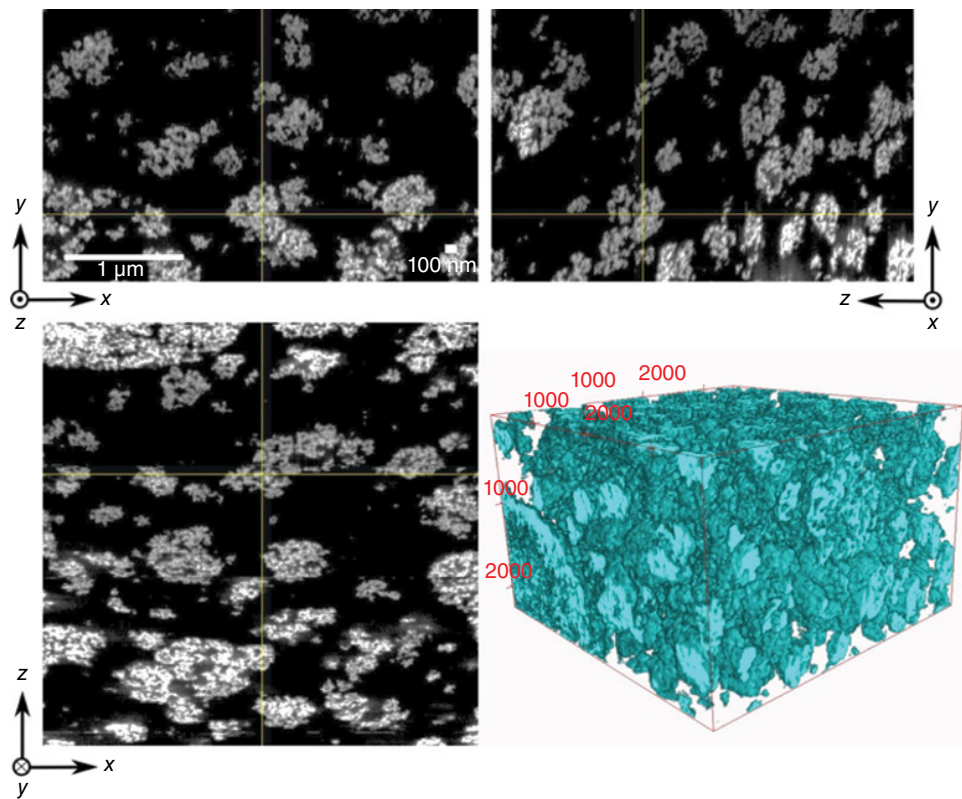


Figure 2.13 FIB/SEM tomography on a silica-filled PDMS nanocomposites: 3D reconstruction and corresponding digital orthogonal slice images (low loss backscattered electrons imaging)

nanocomposite (see Ref. [5] for more information on the material). A volume of several cubic micrometers is observed and highlights the 3D dispersion of the nanoparticle aggregates. The nanoparticle resolution is lost, but the aggregate morphology can be characterized and, for instance, the absence of a percolation network in this case can be deduced. When coupled with ET, FIB/SEM tomography allows a full 3D observation of the filler dispersion from the nanoparticle itself up to larger aggregates. Nevertheless, here again polymer materials can require specific preparation of the sample, and all the soft materials are not suited to this technique because of strong damages that can be induced by the FIB (see, e.g., Figure 2.13 where the shrinking of the PDMS sample under the FIB creates an artificial flattening of the aggregates in the milling direction, z).

References

- (1) G.P. Baeza, A.-C. Genix, C. Degrandcourt, L. Petitjean, J. Gummel, M. Couty, and J. Oberdisse, Multiscale filler structure in simplified industrial nanocomposite silica/SBR systems studied by SAXS and TEM. *Macromolecules*, **46**, 317–329 (2012).
- (2) C. Chevigny, F. Dalmas, E. Di Cola, D. Gigmes, D. Bertin, F. Boué, and J. Jestin, Polymer-grafted-nanoparticles nanocomposites: dispersion, grafted chain conformation, and rheological behavior. *Macromolecules*, **44**, 122–133 (2011).
- (3) J. Jancar, J.F. Douglas, F.W. Starr, S.K. Kumar, P. Cassagnau, A.J. Lesser, S.S. Sternstein, and M.J. Buehler, Current issues in research on structure/property relationships in polymer nanocomposites. *Polymer*, **51**, 3321–3343 (2010).
- (4) N. Jouault, P. Vallat, F. Dalmas, S. Saïd, J. Jestin, and F. Boué, Well-dispersed fractal aggregates as filler in polymer–silica nanocomposites: long-range effects in rheology. *Macromolecules*, **42**, 2031–2040 (2009).
- (5) D. Le Strat, F. Dalmas, S. Randriamahefa, J. Jestin, and V. Wintgens, Mechanical reinforcement in model elastomer nanocomposites with tuned microstructure and interactions. *Polymer*, **54**, 1466–1479 (2013).
- (6) P.A. Midgley and M. Weyland, 3D electron microscopy in the physical sciences: the development of Z-contrast and EFTEM tomography. *Ultramicroscopy*, **96**, 413–431 (2003).
- (7) R.J. Spontak, M.C. Williams, and D.A. Agard, Three-dimensional study of cylindrical morphology in a styrene-butadiene-styrene block copolymer. *Polymer*, **29**, 387–395 (1988).
- (8) F. Dalmas and E. Leroy, New insights into ionic aggregate morphology in zn-neutralized sulfonated polystyrene ionomers by transmission electron tomography. *Macromolecules*, **44**, 8093–8099 (2011).
- (9) Y. Ikeda, A. Katoh, J. Shimanuki, and S. Kohjiya, Nano-structural observation of in situ silica in natural rubber matrix by three dimensional transmission electron microscopy. *Macromolecular Rapid Communications*, **25**, 1186–1190 (2004).
- (10) H. Jinnai, Y. Nishikawa, R.J. Spontak, S.D. Smith, D.A. Agard, and T. Hashimoto, Direct measurement of interfacial curvature distributions in a bicontinuous block copolymer morphology. *Physical Review Letters*, **84**, 518 (2000).
- (11) H. Jinnai, Y. Shinbori, T. Kitaoka, K. Akutagawa, N. Mashita, and T. Nishi, Three-dimensional structure of a nanocomposite material consisting of two kinds of nanofillers and rubbery matrix studied by transmission electron microtomography. *Macromolecules*, **40**, 6758–6764 (2007).
- (12) H. Jinnai and R.J. Spontak, Transmission electron microtomography in polymer research. *Polymer*, **50**, 1067–1087 (2009).
- (13) H. Jinnai, R.J. Spontak, and T. Nishi, Transmission electron microtomography and polymer nanostructures. *Macromolecules*, **43**, 1675–1688 (2010).

- (14) J. Loos, E. Sourty, K. Lu, B. Freitag, D. Tang, and D. Wall, Electron tomography on micrometer-thick specimens with nanometer resolution. *Nano Letters*, **9**, 1704–1708 (2009).
- (15) K. Lu, E. Sourty, R. Guerra, G. Bar, and J. Loos, Critical comparison of volume data obtained by different electron tomography techniques. *Macromolecules*, **43**, 1444–1448 (2010).
- (16) S. Akasaka, T. Okamoto, T. Osaka, T. Matsushita, and H. Hasegawa, 3D analysis of the lattice defects in the gyroid network structure of a block copolymer/homopolymer blend—the line-like defects in the gyroid network structure. *European Polymer Journal*, **47**, 651–661 (2010).
- (17) H. Sugimori, T. Nishi, and H. Jinnai, Dual-axis electron tomography for three-dimensional observations of polymeric nanostructures. *Macromolecules*, **38**, 10226–10233 (2005).
- (18) F. Dalmás, N. Genevaz, M. Roth, J. Jestin, and E. Leroy, 3D dispersion of spherical silica nanoparticles in polymer nanocomposites: a quantitative study by electron tomography. *Macromolecules*, **47**, 2044–2051 (2014).
- (19) L.F. Drummy, Y.C. Wang, R. Schoenmakers, K. May, M. Jackson, H. Koerner, B.L. Farmer, B. Mauryama, and R.A. Vaia, Morphology of layered silicate-(NanoClay-) polymer nanocomposites by electron tomography and small-angle X-ray scattering. *Macromolecules*, **41**, 2135–2143 (2008).
- (20) D.B. Williams and C.B. Carter, *Transmission Electron Microscopy*, Springer, New York, 1996.
- (21) C. Esnouf, *Caractérisation microstructurale des matériaux: Analyse par les rayonnements X et électronique*, PPUR Presses polytechniques, Lausanne, Switzerland 2011.
- (22) J. Radon, Über die Bestimmung von Funktionen durch ihre Integralwerte längs gewisser Mannigfaltigkeiten. *Berichte ueber die Verhandlungen der Saechsischen Akademie der Wissenschaften zu Leipzig, Mathematisch – Physische Klasse*, **69**, 262 (1917).
- (23) M. Radermacher, Radon transform techniques for alignment and three-dimensional reconstruction from Radon projections. *Scanning Microscopy*, **11**, 171–177 (1997).
- (24) J.-J. Fernandez, Computational methods for materials characterization by electron tomography. *Current Opinion in Solid State and Materials Science*, **17**, 93–106 (2013).
- (25) G.L. Zeng, Image reconstruction a tutorial. *Computerized Medical Imaging and Graphics*, **25**, 97–103 (2001).
- (26) P. Gilbert, Iterative methods for the three-dimensional reconstruction of an object from projections. *Journal of Theoretical Biology*, **36**, 105–117 (1972).
- (27) R. Gordon, R. Bender, and G. Herman, Algebraic reconstruction techniques (ART) for three-dimensional electron microscopy and X-ray photography. *Journal of Theoretical Biology*, **29**, 471–481 (1970).
- (28) M. Kato, N. Kawase, T. Kaneko, S. Toh, S. Matsumura, and H. Jinnai, Maximum diameter of the rod-shaped specimen for transmission electron microtomography without the “missing wedge”. *Ultramicroscopy*, **108**, 221–229 (2008).
- (29) N. Kawase, M. Kato, H. Nishioka, and H. Jinnai, Transmission electron microtomography without the “missing wedge” for quantitative structural analysis. *Ultramicroscopy*, **107**, 8–15 (2007).
- (30) S. Lanzavecchia, F. Cantele, P.L. Bellon, L. Zampighi, M. Kreman, E. Wright, and G.A. Zampighi, Conical tomography of freeze-fracture replicas: a method for the study of integral membrane proteins inserted in phospholipid bilayers. *Journal of Structural Biology*, **149**, 87–98 (2005).
- (31) K.J. Batenburg, S. Bals, J. Sijbers, C. Kübel, P.A. Midgley, J.C. Hernandez, U. Kaiser, E.R. Encina, E.A. Coronado, and G. Van Tendeloo, 3D imaging of nanomaterials by discrete tomography. *Ultramicroscopy*, **109**, 730–740 (2009).
- (32) B. Goris, T. Roelandts, K.J. Batenburg, H. Heidari Mezerji, and S. Bals, Advanced reconstruction algorithms for electron tomography: from comparison to combination. *Ultramicroscopy*, **127**, 40–47 (2013).
- (33) R. Leary, Z. Saghi, P.A. Midgley, and D.J. Holland, Compressed sensing electron tomography. *Ultramicroscopy*, **131**, 70–91 (2013).
- (34) T. Roelandts, K.J. Batenburg, E. Biermans, C. Kübel, S. Bals, and J. Sijbers, Accurate segmentation of dense nanoparticles by partially discrete electron tomography. *Ultramicroscopy*, **114**, 96–105 (2012).

- (35) D. Wolf, A. Lubk, and H. Lichte, Weighted simultaneous iterative reconstruction technique for single-axis tomography. *Ultramicroscopy*, **136**, 15–25 (2014).
- (36) A. Kato, Y. Isono, K. Nagata, A. Asano, and Y. Ikeda, Study on Polymeric Nano-Composites by 3D-TEM and Related Techniques, in *Transmission Electron Microscopy Characterization of Nanomaterials*, C.S.S.R. Kumar (Ed), Springer, Berlin/Heidelberg, 2014.
- (37) H. Nishioka, K.-I. Niihara, T. Kaneko, J. Yamanaka, T. Inoue, T. Nishi, and H. Jinnai, Three-dimensional structure of a polymer/clay nanocomposite characterized by transmission electron microtomography. *Composite Interfaces*, **13**, 589–603 (2006).
- (38) S. Kohjiya, A. Katoh, T. Suda, J. Shimanuki, and Y. Ikeda, Visualisation of carbon black networks in rubbery matrix by skeletonisation of 3D-TEM image. *Polymer*, **47**, 3298–3301 (2006).
- (39) M.H. Gass, K.K.K. Koziol, A.H. Windle, and P.A. Midgley, Four-dimensional spectral tomography of carbonaceous nanocomposites. *Nano Letters*, **6**, 376–379 (2006).
- (40) S. Kohjiya, A. Katoh, J. Shimanuki, T. Hasegawa, and Y. Ikeda, Three-dimensional nano-structure of in situ silica in natural rubber as revealed by 3D-TEM/electron tomography. *Polymer*, **46**, 4440–4446 (2005).
- (41) H. Uchida, J.M. Song, S. Suzuki, E. Nakazawa, N. Baba, and M. Watanabe, Electron tomography of nafion ionomer coated on pt/carbon black in high utilization electrode for PEFCs. *The Journal of Physical Chemistry B*, **110**, 13319–13321 (2006).
- (42) J. Ohser and K. Schloditz, *3D Images of Materials Structures*, Wiley-VCH Verlag GmbH, Weinheim, 2009.
- (43) H. Friedrich, J.R.A. Sietsma, P.E. de Jongh, A.J. Verkleij, and K.P. de Jong, Measuring location, size, distribution, and loading of NiO crystallites in individual SBA-15 pores by electron tomography. *Journal of the American Chemical Society*, **129**, 10249–10254 (2007).
- (44) C.J. Gommers, K. de Jong, J.-P. Pirard, and S. Blacher, Assessment of the 3D localization of metallic nanoparticles in Pd/SiO₂ cogelled catalysts by electron tomography. *Langmuir*, **21**, 12378–12385 (2005).
- (45) M. Li, S. Ghosh, O. Richmond, H. Weiland, and T.N. Rouns, Three dimensional characterization and modeling of particle reinforced metal matrix composites: Part I: Quantitative description of microstructural morphology. *Materials Science and Engineering: A*, **265**, 153–173 (1999).
- (46) R. Thiedmann, A. Spettl, O. Stenzel, T. Zeibig, J.C. Hindson, Z. Saghi, N.C. Greenham, P.A. Midgley, and V. Schmidt, Networks of nanoparticles in organic/inorganic composites: algorithmic extraction and statistical analysis. *Image Analysis and Stereology*, **31**, 27–42 (2012).
- (47) L.Y. Yi, K.J. Dong, R.P. Zou, and A.B. Yu, Radical tessellation of the packing of ternary mixtures of spheres. *Powder Technology*, **224**, 129–137 (2012).
- (48) W.S. Rasband, ImageJ, U. S. National Institutes of Health, Bethesda, Maryland, USA, <http://imagej.nih.gov/ij/>, 1997–2015.
- (49) M. Doube, M.M. Klosowski, I. Arganda-Carreras, F.P. Cordelières, R.P. Dougherty, J.S. Jackson, B. Schmid, J.R. Hutchinson, and S.J. Shefelbine, BoneJ: free and extensible bone image analysis in ImageJ. *Bone*, **47**, 1076–1079 (2010).
- (50) A.-S. Robbes, F. Cousin, F. Meneau, F. Dalmas, F. Boué, and J. Jestin, Nanocomposite materials with controlled anisotropic reinforcement triggered by magnetic self-assembly. *Macromolecules*, **44**, 8858–8865 (2011).
- (51) S. Bolte and F.P. Cordelières, A guided tour into subcellular colocalization analysis in light microscopy. *Journal of Microscopy*, **224**, 213–232 (2006).
- (52) C.H. Rycroft, VORO++: a three-dimensional Voronoi cell library in C++. *CHAOS*, **19**, 041111 (2009).
- (53) D. Chen, H. Friedrich, and G.D. With, On resolution in electron tomography of beam sensitive materials. *The Journal of Physical Chemistry C*, **118**, 1248–1257 (2013).
- (54) H. Jinnai and X. Jiang, Electron tomography in soft materials. *Current Opinion in Solid State and Materials Science*, **17**, 135–142 (2013).
- (55) L. Holzer and M. Cantoni, Review of FIB-tomography, in *Nanofabrication using focused ion and electron beams: principles and applications*. Oxford University Press, NY. ISBN, 559201222 (2011).

3

Polymer Nanocomposites for Food Packaging Applications

Shiv Shankar and Jong-Whan Rhim

*Department of Food Engineering and Bionanocomposite Research Institute,
Mokpo National University, Korea*

3.1 Introduction

The prime functions of food packaging are extending the shelf life of packaged food materials by preventing unfavorable changes caused by microbial spoilage, chemical contaminants, temperature change, oxygen, moisture, light, external force, and maintaining the quality and safety of food products from the time of production to the time of consumption. The packaging performs the aforementioned functions by creating proper physicochemical conditions for products and acts as a barrier for gases, water vapor, light, and microorganisms not only to maintain the food quality and safety but also to enhance the shelf life of the packaged food products. Besides basic properties like mechanical, optical, and thermal properties, the food packaging material must prevent microbial growth and contamination, hinder gains or loss of moisture, and act as a barrier against water vapor permeability, oxygen, carbon dioxide, and other volatile compounds such as flavors [1, 2]. Food packaging is not practiced merely as a container, but it also works as a protective barrier with various advanced functions. In addition, the demands of innovative packaging materials are ever increasing to meet the consumer need for higher quality food with safety, convenience, and sustainability. In this sense, food packaging industry is a dynamic and futuristic, which gives birth to sweep up or evolve novel technology.

Nanotechnology is an interdisciplinary science for the creation of useful/functional materials, devices or systems by controlling at least one dimension of the matter on the nanometer-length scale and the development of new phenomena and physical, chemical, and biological properties (Figure 3.1). The material properties change with the size of particles decreasing to the nanometer scale because of the large surface-to-volume ratio. For example, a particle of 30 nm diameter has about 5% of its atoms on its surface; however with 10 nm diameter, the number of surface atoms changes to almost 15%; while for the particle size of 3 nm in diameter have nearly 50% of its atoms on the surface. As a result, the surface area, total surface energy, and reactivity increase [3]. Many industries have known the possible benefits of nanotechnology, and commercial products have already been fabricated in the electronics, communication, energy production, medicine, and the food industry (Figure 3.1). Among the various existing nanotechnologies, polymer nanocomposite has attracted most attention in the food packaging industry.

Although, extensive researches are being undertaken at industry and academic levels, polymer nanotechnology in food packaging is still in the developmental phase. For the growth of polymer nanotechnology in food packaging at advanced level, it is important to glare at the complete life cycle of the packaging (from raw material extraction and production to usage and administration), integrating and balancing cost, performance, health, and

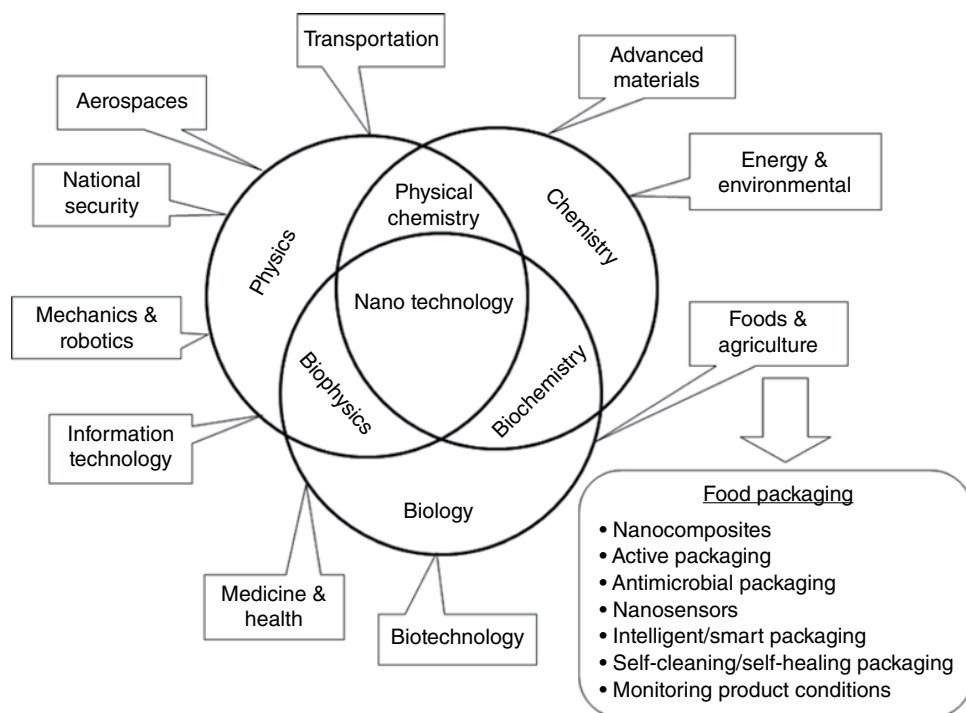


Figure 3.1 Application areas of nanotechnology in various multidisciplinary science and industries with food packaging application

environmental considerations. The high point of multidisciplinary research is required in polymer nanocomposite in food packaging to overcome the barriers like safety, technology, regulation, standardization, trained workforce, and technology transfer in order to achieve the benefit for commercial products in the global market. Moreover, owing to the enormous growth application potential of polymer nanocomposite in food packaging, the emerging technology will be a hub of new employment opportunities because of degradable and ecofriendly nature [4].

The polymer nanocomposite packaging has a great potential as an innovative food packaging technology to maintain the food quality and safety, and to extend the shelf life of the packaged food products. In view of considering the aforementioned points, this chapter is focused on the composition, preparation, characterization, and application of polymer nanocomposite materials in the food packaging areas.

3.2 Polymer Nanocomposite

Polymer nanocomposite is a multiphase hybrid solid material that contains one of the phases as nanoscale fillers that have at least one dimension in less than 100 nm distributed within a polymer matrix [5]. Owing to the nanometer-sized particles dispersed in the polymer matrix, these nanocomposites exhibit prominently enhanced mechanical, thermal, optical, and physicochemical properties, compared with the pure polymer or conventional composites (microscopic) with very low filler loading, typically 5 wt% or below. Plenty of studies have shown a positive impact on barrier properties of polymer nanocomposite after reinforcing with nanofillers. The nanocomposite packaging materials have a high potential as an advanced food packaging technology for maintaining the overall quality of foods and extension of the shelf life of the packaged food products [4, 6–8]. Polymer nanocomposites are mainly composed of the polymer matrix, nanofillers, plasticizers, and compatibilizers.

3.2.1 Types of Polymer

The polymers for the preparation of nanocomposites can be classified as follows, and it is summarized in Figure 3.2 [9, 10]:

1. **Natural biopolymers:** carbohydrates like starch, cellulose, chitosan, alginate, agar, and carrageenan, proteins like soy protein, corn zein, wheat gluten, gelatin, collagen, whey protein, and casein.
2. **Chemically synthesized biodegradable polymers:** poly(L-lactide) (PLA), poly(glycolic acid) (PGA), poly(ϵ -caprolactone) (PCL), poly(butylene succinate) (PBS), and poly(vinyl alcohol) (PVOH), etc.
3. **Microbial polyesters:** poly(hydroxyalkanoates) (PHAs), poly(β -hydroxybutyrate) (PHB), and poly(3-hydroxybutyrate-*co*-3-hydroxyvalerate) (PHBV), etc.
4. **Nonbiodegradable polymers:** nylon, polyamide, polyurethane, polyethylene terephthalate, polyolefins, etc.

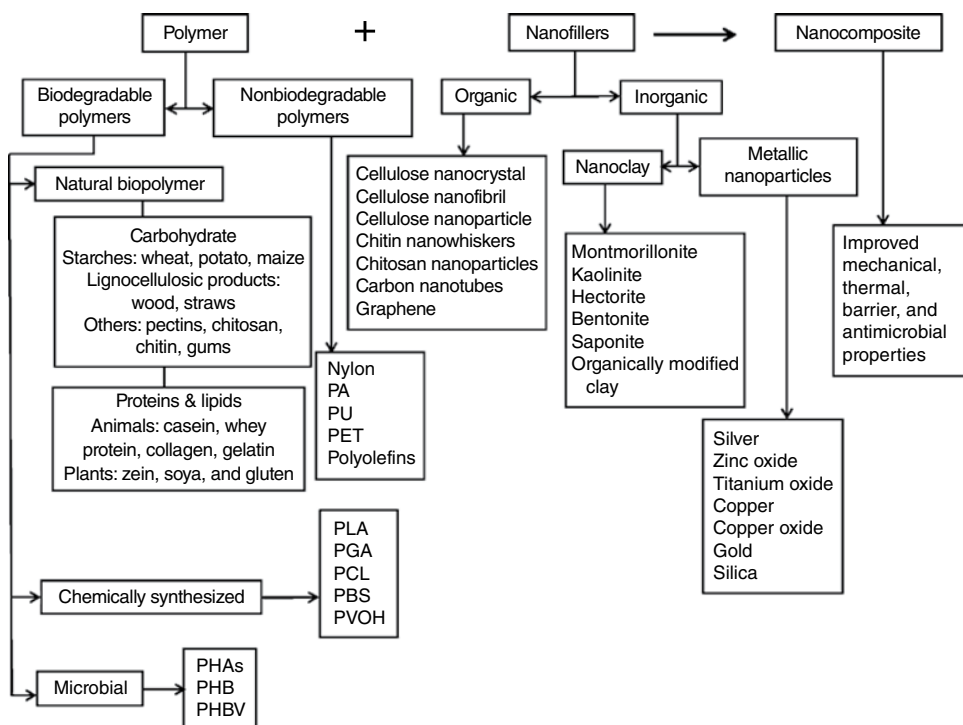


Figure 3.2 Composition and sources for the components of polymer nanocomposite

3.2.2 Types of Nanofillers

The classification of nanofillers depends on the source and types of materials and dimension. On the basis of source, the nanofillers can be either organic or inorganic materials.

3.2.2.1 Organic Nanofillers

These include cellulose nanoparticles, cellulose nanowhiskers, cellulose nanofibrils, chitin nanofibrils, starch nanocrystals, etc.

1. **Cellulose:** Cellulose is the most abundant naturally available polymers in the universe, and it is progressively being used for the preparation of composites with other polymers [11]. Cellulose is a semicrystalline linear chain of polysaccharide composed of β -1,4-linked glucopyranose units. The intermolecular hydrogen bonds in the cellulose chain form bundles of filaments, which consist of highly ordered crystalline and disordered amorphous regions. The crystalline domains can be isolated in nanoscale with highly ordered and regular rod-like nanocrystals, after getting rid of the amorphous regions by acid hydrolysis, which is called cellulose nanofiber, crystalline nanocellulose, or nanowhisker [12]. The production of nanosized cellulose and their application in nanocomposite materials have been gaining increasing attention due to the profound improvement of mechanical and barrier properties of the nanocomposites. The improved

properties of nanocomposite are mainly caused by the high strength and stiffness combined with low weight, as well as biodegradability, biocompatibility, and renewability of nanosized cellulose [13]. Compared with microcellulose, nanocellulose are more useful as reinforcing in polymers because the well-dispersed nanosized fibers with high surface area form a percolated network connected by hydrogen bonds with the polymer matrix [14]. In addition, nanocellulose can be attained from cheap and abundantly available renewable natural resources such as wood, plants, vegetables, and other agricultural residues and their processing wastes [15]. The properties of nanocellulose depend on the isolation method and the source of the nanofibers [16].

2. **Chitin:** Chitin is the second most abundant biopolymer on the earth. Chitin is a linear polysaccharide, made up of β -(1–4)-linked 2-acetamido-2-deoxy-D-glucopyranose units [17]. Chitin can be obtained from fungi, crustaceans (e.g., crabs, lobsters, and shrimps), insects, the radula of mollusks, and cephalopods (squids and octopuses) [17, 18]. Chitin upon acid hydrolysis can form crystalline nanofibrils and nanowhiskers, which have been recently explored in nanotechnology applications. Reinforcement of chitin nanofibrils in carrageenan polymer matrix resulted in increase in mechanical, barrier, and antimicrobial properties of carrageenan films [19].

3.2.2.2 Inorganic Nanofillers

These include metal or metal oxide nanoparticles (silver, copper, zinc, titanium, etc.) and clay (montmorillonite, saponite, hectorite, etc.).

1. **Metal or metal oxide nanoparticles:** Metallic and metal oxide nanoparticles are most promising for antimicrobial food packaging applications as they show strong antimicrobial activity because of their large surface area-to-volume ratio and high specificity [20]. The antibacterial properties of metallic nanoparticles, such as silver, copper, and zinc nanoparticles, have attracted considerable attention in food packaging as well as in biomedical and biotechnological applications [21]. Metal or metal oxide nanoparticles could be synthesized by various techniques, which is summarized in Figure 3.3.
2. **Clay nanoparticles:** Although, various nanoparticles have been recognized as potential nanofillers to improve polymer performance, the layered silicate clays, such as montmorillonite (MMT), saponite, and hectorite, have been extensively explored due to their low cost, easy availability, substantial enhancement properties, and relatively simple steps of processing. These clay layers consist of two coordinated tetrahedral silicon atoms, combined with octahedral sheet of either aluminum or magnesium hydroxide [4, 8]. The clay layer is approximately 1 nm thick, and the lateral dimensions may vary from a few nanometers to several micrometers or even larger, which depend on the method of preparation, the source of the clay, and the types of layered silicate [22].

For the formation of successful polymer–clay nanocomposites, it is essential that the clay nanoparticles be compatible with the polymer matrix and homogeneously distributed through the polymer matrix. In general, natural layered silicates possess Na^+ or K^+ on the surface, which makes the surface hydrophilic and, consequently, they are only miscible with hydrophilic polymers. To make silicates miscible in hydrophobic polymers, the hydrophilic silicate surfaces should be converted to a hydrophobic using exchange reaction with

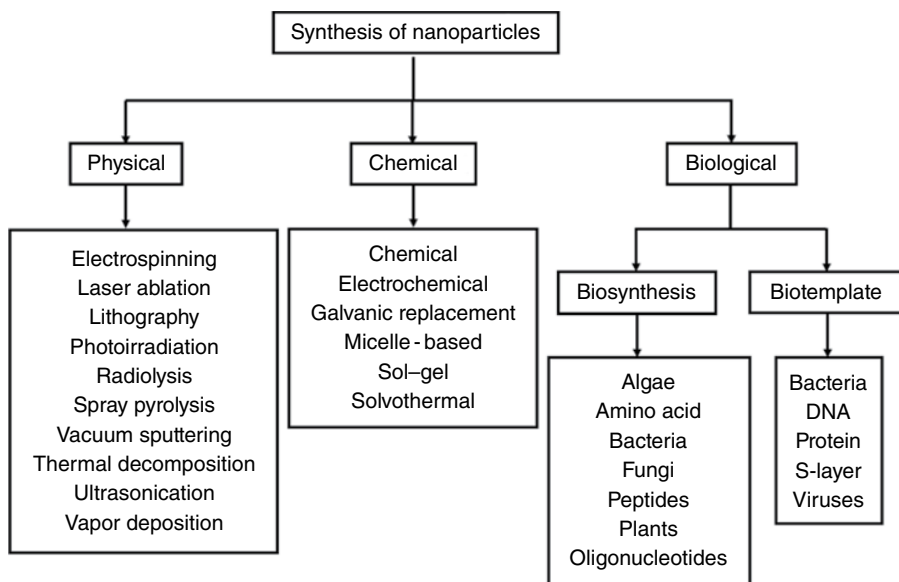


Figure 3.3 Various sources for the preparation of metal and metal oxide nanoparticles

various organic cations. The surface energy of the silicate surface lowers by organic cations that result in a larger interlayer spacing, which enables better-intercalated nanocomposite formation. In addition, the functional groups present on organic cations react with the polymer and improve the interaction between the silicates and the polymer matrix [23–25].

3.3 Preparation of Nanocomposites

The homogeneous dispersion of nanofillers within a polymeric matrix is the primary step to obtain the enhanced properties of nanocomposites. These nanofillers have a high tendency for self-agglomeration due to the hydroxyl groups present on the surface of nanofillers. The interparticle interactions of nanofillers can cause aggregation during the preparation of the nanocomposite resulted in the loss of the nanoscale dimension, which limits the potential use of them. Different strategies are employed during the nanocomposite film formation to minimize the agglomeration of nanofillers. The different methods of polymer nanocomposite film preparation are as follows:

1. **Solvent casting method:** In this method, a polymer is dissolved in an organic solvent or water at room temperature or by heating. Particles, with particular dimensions, are then added to the solution. The film forming solution can be cast onto a glass plate to make a thin film. When the solvent evaporates, it creates a thin film of composite material consisting of the particles together with the polymer. This process involves three basic steps for film forming: solubilization, casting, and drying [26].

2. **Thermocompression method:** In this method, the polymer is thermally compacted between preheated two stainless steel plates lined with aluminum foil. A high pressure of about 10000psi (68.9MPa) is applied for 3–5 min. The films are peeled from the aluminum foil layers after cooling in the air to room temperature [26].
3. **In-situ intercalative polymerization method:** This process involves the physical mixing of the clay mineral with the selected monomer. Thereafter, monomers intercalate within the interlayer and stimulate delamination. The polymerization initiated by a number of ways to form linear or cross-linked polymer matrices. The pre-swelling of clay mineral is required for dispersion, intercalation, and exfoliation of long-chain alkylammonium ion of clay [27].
4. **Solution intercalation method:** In this method, the clay is pre-swollen in a solvent and the polymer (intercalant) is dissolved in the solvent separately. Thereafter, both solutions are combined, where the polymer chains intercalate and displace the solvent within the interlayer of the clay. This method is suitable for the intercalation of polymers with low or no polarity into a layered structure and facilitates the production of thin films with polymer-oriented clay intercalated layers. This technique has been widely used to produce intercalated nanocomposites with water-soluble biopolymers [5, 28].
5. **Melt intercalation method:** In this method, the polymer and clay are added together above the melting temperature of the polymer; they may be held under shear, or at the same temperature for some time period, or other conditions to encourage intercalation or exfoliation of the clay. The melt intercalation is the most appealing approach because of its compatibility with current polymer processing equipment, its versatility, and its environmentally benign character due to the absence of solvents [5, 28]. The highest mechanical reinforcement effect of organic nanofillers is attained when unmodified nanofillers having hydroxyl groups are used for reinforcement.

When the layered silicate clays are mixed with a polymer, three types of composites are commonly obtained (Figure 3.4): (i) immiscible tactoid, (ii) intercalated, and (iii) exfoliated

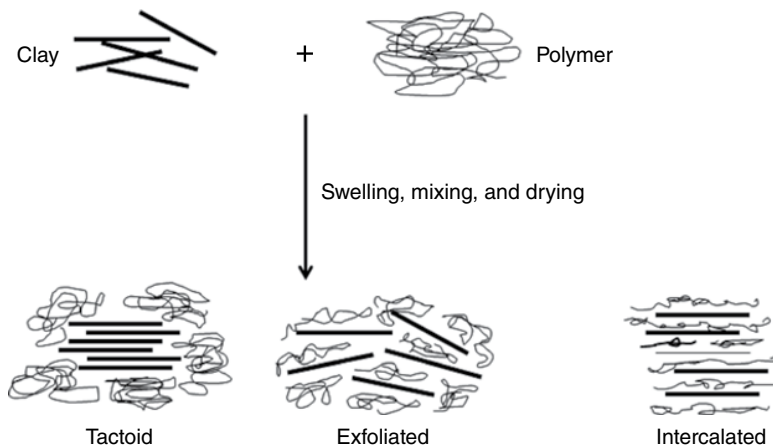


Figure 3.4 Preparation methods of polymer/clay nanocomposites and their molecular arrangement

structures [6, 10]. In immiscible tactoids, complete clay particles are dispersed within the clay matrix, and the polymer cannot intercalate into the galleries of clay layers. The properties of such composites are similar to that of polymer composites reinforced by macroparticles. Intercalation and exfoliation produce two ideal nanoscale composites. In an intercalated nanocomposite, often, a single polymer chain is inserted into the gallery of clay layers and forms alternate polymer layers and clay platelets. The silicate layers are completely delaminated from each other and are well dispersed in an exfoliated nanocomposite. The exfoliated nanocomposite has been shown to exhibit the most significant improvements in physical properties. The formation of intercalation or exfoliation depends on the type of clay and the processing conditions [24].

3.4 Characterization Methods of Polymer Nanocomposite Films

The microstructure and surface morphology of polymer nanocomposites are characterized by scanning electron microscopy (SEM) and transmission electron microscope (TEM). TEM allows a qualitative understanding of the spatial distribution, internal structure, and dispersion of the nanofillers within the polymer matrix. Whereas, chemical compositions of films are determined by energy-dispersive X-ray spectroscopy (EDX) analysis. The crystallinity, crystallite size, and composite structures such as tactoid, intercalated, or exfoliated structures of polymer nanocomposite and polymer/clay composite can be determined using XRD measurements. The functional group and chemical changes due to the interaction of polymer with nanofillers can be determined by Fourier transform infrared spectroscopy (FTIR). It shows the vibration peaks in a particular frequency for a specific chemical group. In addition, a number of analytical techniques have been used to characterize the polymer nanocomposites films including atomic force microscopy (AFM), thermogravimetric analysis (TGA), and nuclear magnetic resonance (NMR).

3.5 Types of Polymer Nanocomposite Packaging

The reinforcement of nanofillers in the polymer matrix has been explored for the significant enhancement in performance properties of nanocomposites for potential applications in food packaging, such as processed meat products, cheese, bakery products, confectionery, food grains, boil-in-bag foods, fruit juices and dairy products, and for the manufacture of carbonated beverage and beer bottles [29]. There are various reports available on potential applications of nanocomposites in the food packaging sector (Figure 3.5). However, they are mostly focused on nanocomposites made from thermoset or thermoplastic polymers. Moreover, the use of nanocomposite as food packaging materials is limited because of the relatively high production cost and less feasibility for mass production. In addition, the concern about the food product safety emerging from consumer and government about use of nanomaterials as packaging materials.

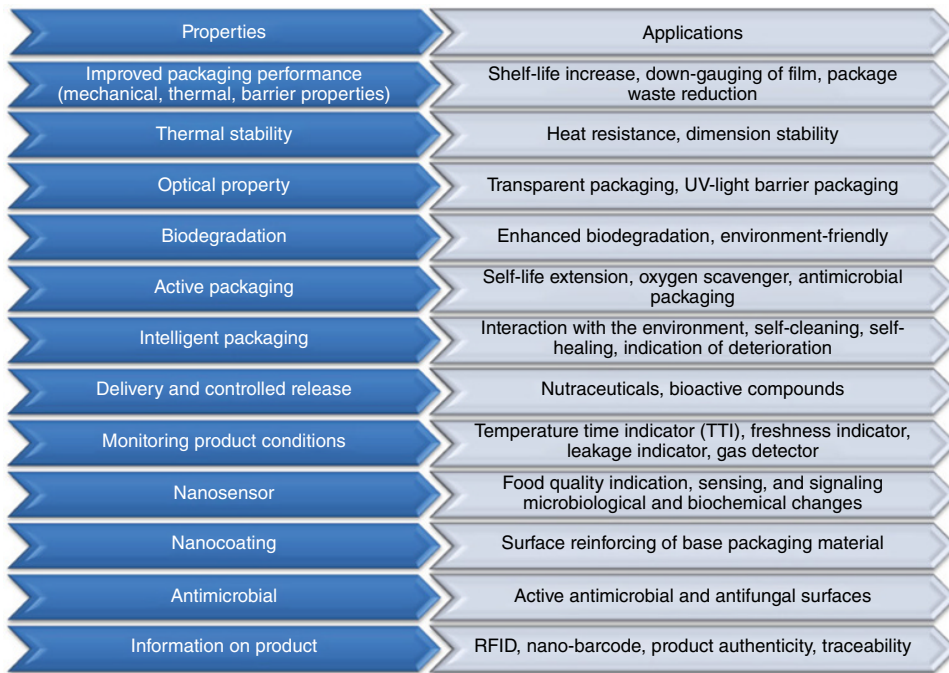


Figure 3.5 Properties and potential application of polymer nanocomposite in food packaging

3.5.1 Rigid Packaging

The packaging material's resistance to gas intrusion like oxygen and water vapor and retention of gasses like CO_2 and aroma are the primary limiting factors for the shelf life of many foods and beverages. The migration of CO_2 out of carbonated beverage bottles could reduce the shelf life by making the beverage become flat. However, oxygen migrating into beer bottles reacts with the beer and make it stale. In both cases, the best solution to the problem is providing a barrier to the movement of molecules through the polymer matrix comprising the package. Considerable improvements in gas barrier properties of nanocomposites have been explored in the food packaging industry, and some of them are commercially available already. Polymer nanocomposites with different nanofillers have been developed for improved gas and water vapor barrier properties. The packaging materials for applications in beer bottles, carbonated beverages, and thermoformed containers are multilayer nanocomposites for rigid food packaging. The typical food packaging materials with multilayer structures are shown in Figure 3.6. The first type of packaging consists of only polymer that can be a barrier for gas or water vapor molecules. The second type is a passive barrier, in which the middle layer is reinforced with nanocomposite film with enhanced barrier property. The third type is an active barrier packaging materials composed of gas (O_2) scavenger incorporated into the polymer. The fourth type is the combination of passive and active barrier.

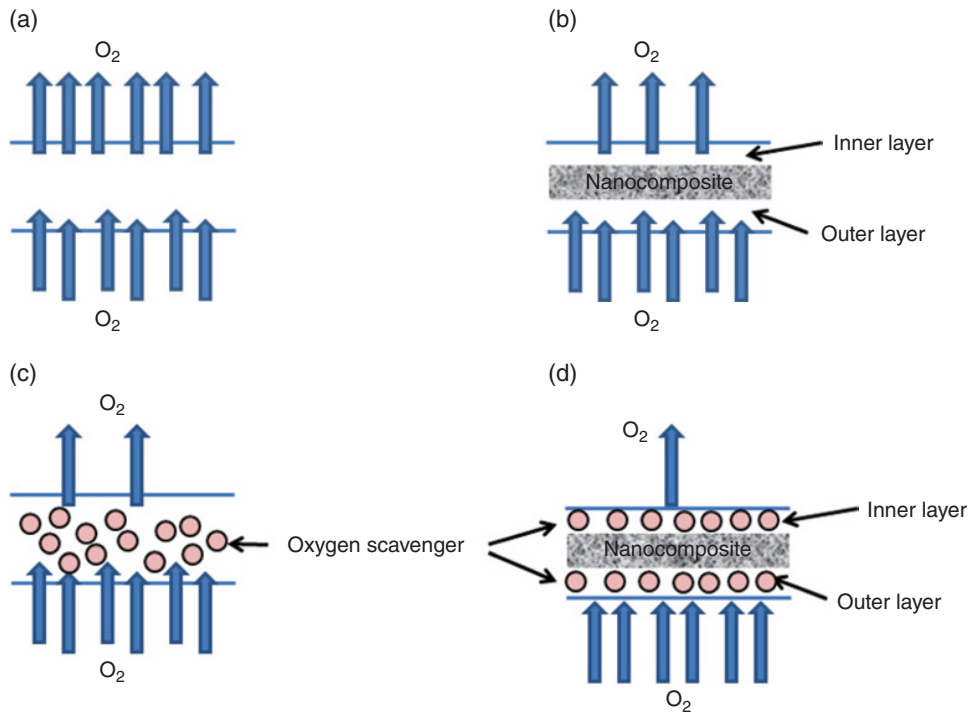


Figure 3.6 Diagrammatic representation of the structures of multilayer nanocomposite for oxygen (O_2) barrier packaging: (a) neat polymer film without barrier, (b) nanocomposite layer as passive barrier, (c) oxygen scavengers as active barrier, and (d) mixture of active (oxygen scavenger) and passive (nanocomposite) barrier

3.5.2 Nylon-Based Packaging Materials

1. **Polyamide 6** or thermoform nylon is one of the most widely used plastic material to produce laminated films, sheets, and bottles, because it is cheap, transparent, strong, tough, and thermoformable over a broad range of temperatures and chemicals, but it is more permeable to gasses and water vapor. Thermoformed nylons are used for packing meat and cheese. Nylons are often used as coextrusion with other plastic materials, providing both strength and toughness to the structure. Development of nanocomposite with nylon and clay has been tried in order to improve gas and water vapor barrier properties.
2. **Nylon-6** nanocomposite (Durethan®, Bayer Polymers) is known to have better properties than simple polyamide 6 and a barrier for the gasses and water vapor, as well as maintaining excellent transparency. The nanoparticles influence the crystallization of the plastic, acting as nuclei for the crystallization of the polymer, resulting in improving the light transmission through the film.

Honeywell produces three types of nylon-6 nanocomposite: (i) Aegis™: OX, (ii) HFX, and (iii) CDSE with high oxygen barrier properties for plastic beer bottles, hot-fill bottles,

and carbonated soft drink bottle, respectively. Nylon-6 nanocomposites showed an oxygen barrier properties approximately four times higher than pristine nylon-6 [30].

Nylon-MXD6 is a crystalline polyamide of meta-Xylenediamine and adipic acid, which is widely used in multilayer food packaging applications [31]. Mitsubishi Gas Chemical Company and Nanocor jointly developed MXD6 (trade name: Imperm™), which is semi-aromatic nylon in nanocomposite form with high gas barrier properties. In addition, they also produce a nanocomposite of multilayer PET and clay platelets in MXD6 nylon under the trade name “M9” [32]. Imperm is used in food and beverage packaging to increase the shelf life of carbonated beverages. Their CO₂ retention capability determines their shelf life. The multilayered PET bottles blended with nanocomposite have been used for the packaging carbonated beverages to minimize the carbon dioxide loss from the drinks and the oxygen ingress into the bottles, thus maintaining the quality and extending the shelf life of the drinks. Moreover, the resultant bottles are both lighter and stronger than glass bottles and are less likely to shatter.

3.5.3 Biodegradable Packaging

Various types of biodegradable food packaging films are developed using biopolymers. The nanofillers from renewable resources have been used to increase the water vapor barrier property. Reinforcement of chitin nanofibrils in carrageenan biopolymer increased the mechanical property and decreased the water vapor permeability of nanocomposite films [19]. The water vapor permeability of carrageenan biopolymer also decreased when it was reinforced with paper mulberry pulp nanocellulose [11]. Rhim and Wang [33] reinforced clay into carrageenan biopolymer to increase the water vapor barrier property and mechanical properties of nanocomposite. Kanmani and Rhim [34] mixed nanoclay into gelatin matrix to improve the mechanical and water vapor barrier properties.

3.5.4 Flexible Packaging

Flexible packaging materials are bags, pouches, envelopes, wraps, and sachets, which are made of materials such as film, foil, or paper sheeting that, when filled and sealed, acquire pliable shape. Some packaging materials contain metal layers and container that can be replaced by nanocomposites to flexible pouches or rigid plastic structures. Packaging films with metal layers increase the amount of solid waste in the environment after their disposal. Many current packaging materials are multilayered, which are unrecyclable, but nanocomposite polymers could help reduce packaging waste and would allow efficient recycling. The prime goal in using polymer nanocomposite is to moderate the amount of solid waste associated with the current packaging as well as to lower the costs by savings material.

Nylon-MXD6 is explored as potential substitutes for foil-based packaging materials in food supply chain nowadays. Nylon-MXD6/clay nanocomposites can enhance mechanical properties of the polymer in addition to gas barrier properties. Thellen *et al.* [35] reported the enhanced oxygen barrier properties of nylon-MXD6/clay nanocomposites decrease in film elongation while improving the tear resistance of the films. Nylon-MXD6/clay nanocomposites showed 4.5, 2.0, and 2.3 times, lower OTR, CO₂ TR, and WVTR, respectively,

than those of the neat nylon-MXD6 [36]. Nanocomposite films with improved barrier properties and superior mechanical strength provide an opportunity to reduce the environmental load occurred by currently used packaging materials.

3.5.5 Active Packaging

It refers to the techniques concerned with substances that absorb oxygen, carbon dioxide, moisture, ethylene, flavors/odors, and those that release antioxidants, carbon dioxide, flavor, and antimicrobial agents (Figure 3.7). It can remove undesirable flavor and tastes and also improve the smell or color of the packed food. Active packaging materials interact with the packed food and the environment surrounding the food and plays an active role in extending the shelf life of packaged food or improving safety or sensory properties, however, maintaining the quality of the food [37, 38]. The dynamic packaging technologies have been modernized to provide more dependable quality, food safety and also to minimize package-related environmental contamination and disposal problems [39]. The expansion in active packaging has led to advances in many regions, including antioxidant activity, antimicrobial activity, controlled respiration rates, and water vapor permeability. Other active packaging technologies include carbon dioxide absorber/emitters, odor absorbers, ethylene absorber, and aroma emitters. Among these techniques, oxygen scavengers, moisture absorbers, and antimicrobial packaging constitute more than 80% of the market today [40].

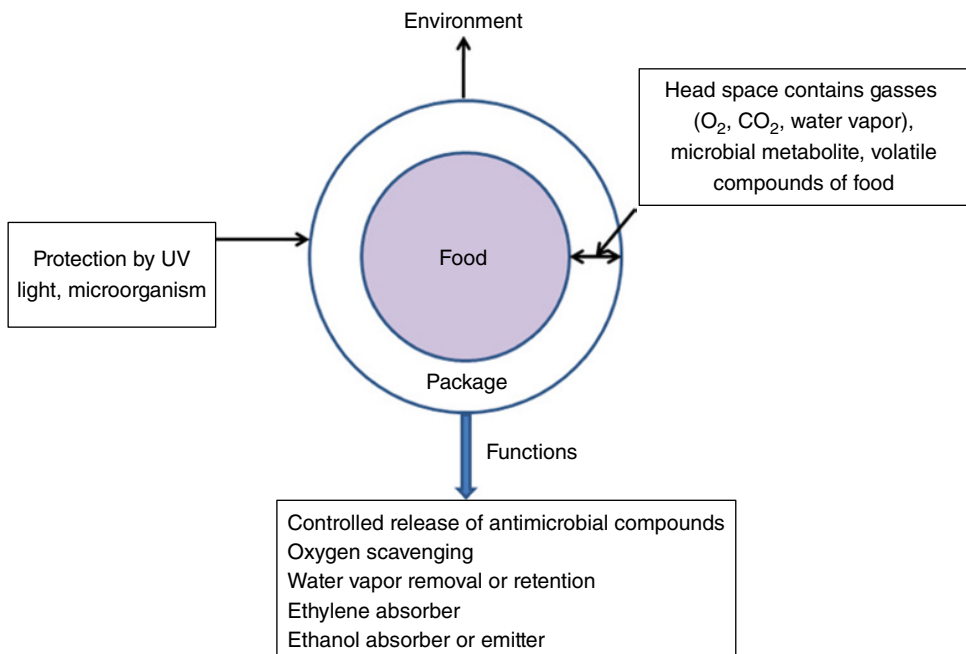


Figure 3.7 Functions of active packaging to improve self-life of packaged food

1. **Oxygen barrier/oxygen scavenging:** The presence of oxygen in the packaged foods causes many harsh reactions such as color changes, nutrient losses, microbial growth, and off-flavor development. In addition to these, it also considerably affects the ethylene production and respiration rate in vegetables and fruits. Although O₂-sensitive food has been packed using passive barrier packaging materials such as high-barrier packaging materials with multilayered structures containing ethylene vinyl alcohol copolymers or aluminum foil [41] or barrier nanocomposite [42], the passive method cannot completely remove the oxygen (Figure 3.6). The oxygen may remain in the head space or dissolve in the food or permeate into the container wall. To overcome such problem, recently, an active packaging method using oxygen scavenger systems has been developed to reduce the residual oxygen in the package; however, the risk of anaerobic pathogenic bacterial growth will be high.

Oxygen scavenger can be used in sealed small sachets that are inserted into the package or fixed by adhering to the inner wall of the package materials. Although, this technology is well implanted, there are some problems associated with this method like the accidental consumption of the contents of the sachets and the difficulty in recycling such sachets. Polymer nanocomposite could be applied as an alternative to solve such problems [43]. Aegis® OX is a commercially developed resin with oxygen-scavenging potential, which is a mixture of active barrier (nylon) and passive oxygen scavengers (nanocomposite clay particles) to enhance the barrier properties against oxygen, carbon dioxide, and aroma. Janjarasskul *et al.* [44] produced edible and biodegradable biopolymer film of whey protein and ascorbic acid with oxygen scavenging activity. Xiao *et al.* [45] developed oxygen scavenger films by blending different polymers with TiO₂ nanoparticles. The nanocomposite films with oxygen scavenger activity could be used as active packaging materials for oxygen-sensitive food products.

2. **Carbon dioxide emitter/absorber:** The foods such as meat and poultry require a high concentration of carbon dioxide (CO₂) levels (10–80%) in order to inhibit the surface microbial growth and to extend the shelf life. The removal of oxygen from the package creates a partial vacuum resulting in collapsing of flexible packaging. Therefore, the simultaneous release of carbon dioxide from inserted sachets, which consume oxygen, is desirable. Such systems could be developed by ferrous carbonate or a mixture of sodium bicarbonate and ascorbic acid [46]. Calcium hydroxide, potassium hydroxide, sodium hydroxide, calcium oxide, and silica gel can be used in carbon dioxide absorbers sachets, in order to remove carbon dioxide during storage and prevent bursting of the package [46]. The commonly used CO₂ scavenger is calcium hydroxide, which reacts with CO₂ in the presence of high moisture to form calcium carbonate. But the disadvantage in using calcium hydroxide is that it irreversibly scavenges the CO₂ from the package headspace resulting in depletion of CO₂, which is always not needed [47].
3. **Ethylene absorber:** Ethylene is a plant hormone that has physiological effects on fresh fruit and vegetables. It is also known as ripening hormone. It accelerates the respiration rate, resulting in maturity and senescence as well as softening and ripening of fruits. In addition, ethylene accumulation causes yellowing of green vegetables and is responsible for various postharvest disorders in fresh fruits and vegetables. The accumulation of ethylene in the packaged food should be avoided to increase the shelf life and maintain the quality of packaged food. Various ethylene absorbing substances are reported, but

the efficiency of the materials is difficult to substantiate because of inadequate documentation. Owing to the photocatalytic properties of titanium oxide (TiO_2), it has been exploited for the removal of ethylene vapor and delayed the ripening of climacteric fruits. Unlike conventional ethylene scavenger, TiO_2 has the unlimited ethylene scavenging capacity, because TiO_2 is not being consumed in the reaction. Maneerat and Hayata [48] developed polypropylene films coated with TiO_2 for ethylene gas removal of packaged horticultural products. They compared the efficacy of micro ($\sim 5 \mu\text{m}$) versus nano ($\sim 7 \text{nm}$) TiO_2 particles and found the higher ethylene scavenging efficacy with nano TiO_2 .

- 4. Antimicrobial packaging:** Antimicrobial nanocomposite packaging is one of the most promising smart packaging systems that assist in prolonging the shelf life of food by putting down or inhibiting spoilage and pathogenic microorganisms that contaminate foods [20]. Polymer nanocomposite food packaging material with antimicrobial properties is particularly useful because of the high surface-to-volume ratio of nanofillers and also because it enhances surface reactivity of the nanosized antimicrobial agents compared to bulk counterpart, making them able to inactivate or kill microorganisms [7]. Antimicrobial packaging films are produced by blending antimicrobial materials to the polymeric matrix during the polymer processing. Polymer nanocomposite materials have been investigated for antimicrobial activity as a growth inhibitors [49], antimicrobial agents [50], antimicrobial carriers [51], or antimicrobial food packaging films [20]. Metal and metal oxide nanoparticles are one of the widely used nanomaterials for antimicrobial food packaging applications as they show intense antimicrobial activity owing to their large surface area and high specificity. The antibacterial properties of metal and their oxide nanoparticles, such as silver, copper, titanium, and zinc nanoparticles have attracted considerable attention not only in the food packaging field but also in biomedical and biotechnological applications [20, 52–54]. Among these, nanocomposite of silver nanoparticles (AgNPs) and biopolymers such chitosan [55], agar [7], and gelatin [34] exhibited strong antimicrobial activity against both, Gram-positive and Gram-negative bacteria. Due to strong antimicrobial activity of copper nanoparticles [52], it has attracted the attention of researchers for its application in food packaging. Copper-based nanomaterials possess low cost of source materials, insignificant sensitivity to human tissues, and highly sensitive to microorganisms as compared to silver [52, 56]. Shankar *et al.* [20] developed the nanocomposite of agar polymer and six different types of nanoparticles and reported high antimicrobial activity against Gram-positive and Gram-negative foodborne pathogens. Metal oxides such as TiO_2 , ZnO , and MgO have also been exploited for the preparation of antimicrobial packaging films due to their potent antimicrobial activity with high stability [34, 57, 58]. Excitingly, polymer nanocomposite films made with organically modified nanoclay have been known to have profound antimicrobial activity [55, 59]. Rhim *et al.* [55] prepared chitosan/clay nanocomposite films mixed with two different types of nanoclay, which showed the antimicrobial activity against pathogenic microorganisms. They found that the nanocomposite film prepared with the organically modified MMT (Cloisite® 30B) exhibited antimicrobial activity against Gram-positive bacteria such as *Listeria monocytogenes* and *Staphylococcus aureus*, while the natural MMT did not show any antimicrobial activity. Although

chitosan itself has long been recognized as an antimicrobial against a wide variety of microorganisms, Hong and Rhim [50] demonstrated the strong antimicrobial activity organically modified clays and concluded that the antimicrobial activity of the chitosan/clay nanocomposite is mainly due to the quaternary ammonium salt of organically modified nanoclay (Cloisite 30B).

Applications like antioxidant releasing, color containing, light absorbing/regulation, antifogging and antisticking, suitable microwave heating, gas permeable/breathable, and insect-repellant package films developed by polymer nanocomposites are expected to find increased attention in the future [39].

3.5.6 Intelligent/Smart Packaging

Intelligent or smart packaging contains an external or internal indicator to provide information and monitor the quality of the packaged food or its surrounded environment to predict or to decide the safety and shelf life [60]. The features of intelligent packaging can be used to access the efficiency and reliability of active packaging systems; they have distinctively different concept. Intelligent/smart packaging devices can sense and provide information about the properties and function of packaged food. Moreover, they can provide assurances of pack integrity, product safety and quality, and tamper evidence. The properties of intelligent packaging are used in product authenticity, product traceability, and antitheft. It alerts a consumer to contamination of pathogens, to identify pathogenic bacterial contamination and harmful chemicals or degradation of products caused by food deterioration, indicate food quality, and initiate self-healing. Intelligent packaging devices include sensors, gas sensing dyes, time-temperature indicators, physical shock indicators, microbial growth indicators, and tamper proof, antitheft, and anti-counterfeiting technologies [29, 61]. Polymer nanocomposite paves the way for the development of packaging systems that monitor the condition of packaged goods to provide information during transport and storage. Various bioactive nanocomposite materials like nanosensors, nanostructure indicators, antigen-detecting biosensors, and DNA-based biochips are developed using the high activity of enzymes, antibodies, microorganisms, or some physicochemical reactions to identify specific reactions. A sensor is defined as a device used to locate, detect, or quantify energy or matter and give a signal for the detection or measurement of a physical or chemical property changes. The sensors contain two basic functional units: a receptor that transforms physical or chemical information into a form of energy, and a transducer used to measure the transformed energy and produce analytical signal. A biosensor is a device incorporating a biological sensing element either intimately connected to or integrated within a transducer [61]. Various nanomaterials, such as gold nanoparticles [62], carbon nanotubes [63], magnetic nanoparticles, and quantum dots [64] are used for the preparation of effective biosensors because of their unique physical, chemical, optical, magnetic, and electrochemical properties with high sensitivity and specificity for the detection of the targeting compounds [65]. Biosensors can be incorporated into polymer films or other packaging materials to detect pesticides, allergens, toxins, pathogens, temperature

changes, residual oxygen, leakages, etc. [65, 66]. The method using bio-analytical sensors offers several advantages, including rapid and high-throughput detection, simplicity and cost-effectiveness, reduced power requirements, and easier recycling.

Freshness indicators are used to indicate directly the quality of the packaged food [67]. A signal of microbiological quality could be a result of a reaction between the indicator and the metabolites produced during the growth of the microorganisms in the product. Most of the freshness indicators are based on an indicator tag color change due to the presence of microbial metabolites produced during the growth of microorganisms, giving a clear visible signal of whether the food is fresh or not.

3.5.7 Nanocoating

Coatings are mostly continuous layers formed on the base packaging materials. Plastic films metalized with aluminum have been used as gas barriers and light barriers and as decorative films. The aluminum layer is laid down by vacuum deposition techniques and is typically a few nanometers thick. This metal layer is sandwiched in a multilayer film construction to prevent corrosion, scratching, and abrasion that would spoil the optical properties of the food packaging.

Metallic oxide nanoparticles such as TiO_2 , MgO , ZnO , and Al_2O_3 , and metallic nanoparticles such as Ag are widely used to produce nanocoatings on polymeric films, metallic surface, or paperboard. Various novel properties of nanocoating materials such as optical, mechanical, chemical, electronic, magnetic, and thermal properties are properly used in some industries including the packaging industry. A variety of production and precipitation methods of nano-thin films or nanocoatings are industrially used, which include physical vapor deposition, chemical vapor deposition, electronic precipitation/electronic coating, sol-gel process, electrodeposition, rotating coating, spray coating, and self-assembling [68].

High-barrier nanocoatings consisting of hybrid organic-inorganic nanocomposite coatings by sol-gel process [69] are being developed for oxygen-diffusion barriers for plastics such as PET. The coatings are produced through atmospheric plasma technology using dielectric barrier discharges. The coatings have been reported to be very efficient at keeping out oxygen and retaining carbon dioxide, and can rival traditional active packaging technologies such as oxygen scavengers.

Coatings containing nanomaterials are used to create corrosion-resistant, scratch-resistant, antireflective or antimicrobial surfaces. Nanoscale silicate and alumina particles have been found to increase the scratch and abrasion resistance of coatings without interfering with the transparencies [70]. Applerot *et al.* [71] prepared ZnO-coated glass using an ultrasonic irradiation method, and they demonstrated a significant antibacterial effect against both Gram-positive and Gram-negative bacteria of the glass slide coated with a low level of ZnO coating (as low as 0.13%, mean diameter of ZnO nanocrystals of 300 nm). TiO_2 -coated orientated polypropylene films showed potent antibacterial activity against *Escherichia coli* and reduced the microbial contamination on the surface of cut lettuce, reducing the risk of microbial growth [72]. Bio-hybrid nanocomposite (chitosan and bentonite nanoclay)

coated on argon-plasma-activated LDPE-coated paper had improved barrier properties against water vapor, oxygen, grease, and ultraviolet (UV)-light transmission [73]. The coating materials were classified as “generally recognized as safe” (GRAS) and the total migration was in the permitted range ($\leq 6 \text{ mg/dm}^2$) of legislation; the multilayer-coated films were suggested as safe and environmentally sound alternatives for synthetic barrier packaging materials. The antimicrobial activity of AgNPs has been exploited by developing non-cytotoxic coating for methacrylic thermosets using lactose-modified chitosan and AgNPs [74]. Such biocompatible antimicrobial polymeric films containing antimicrobial AgNPs may have real potential for using as an antimicrobial active packaging material. Self-cleaning smart nanocoatings that destroy bacteria, isolate pathogens, or fluoresce under certain conditions are under development [75].

3.5.8 Edible Coating/Packaging Films

Biodegradable materials derived from food ingredients such as polysaccharides, proteins, and lipids are edible and have attracted significant interest in recent years due to their potential abilities to replace traditional plastics and act as food contact edible films and/or coatings. An edible/biodegradable film is one that is typically produced from food-derived ingredients in a thin layer using wet or dry manufacturing processes to do so. The resulting film should be a free standing film for wrapping of food stuffs or could be used between food components for separation. In contrast, edible coatings are materials that can be applied directly to the surfaces of food products by dipping, spraying, or panning. Edible packaging formats can be consumed with, or as part of, the food product in question, but they may fulfill other functions, such as acting as carriers for targeted food additives (antimicrobial agents, antioxidants, flavorings, etc.). Edible films and coatings may also be used to inhibit migration of oxygen, carbon dioxide, and moisture to improve the mechanical integrity or handling characteristics of the food. Preparation of biodegradable and edible films involves the use of at least one film-forming agent (macromolecule): polysaccharides, proteins and lipids, a solvent, and plasticizer. Hydrocolloids (proteins and polysaccharides) are the most widely investigated biopolymers in the field of edible coatings and edible films.

3.5.9 Other Types of Packaging

The most rudimentary method to protect food products against temperature fluctuations experienced an unintentional break of cold chain during storage and distribution of refrigerated or frozen foods is in using the insulating packaging materials. However, most insulating packaging materials are bulky, and they usually add significant package weight and volume. As a new type of insulating materials, nanostructured foams that are significantly thinner than conventional materials for the same thermal properties, have been developed as an alternative for the bulky traditional insulating materials. Addition of nanoscale nucleating agents in foams results in smaller cell size and higher cell density, along with improving the performance of the foam [76].

3.6 Properties of Polymer Nanocomposites

For the packaging applications of polymer nanocomposites, the performance properties such as mechanical, barrier, optical, thermal, biodegradation, antimicrobial, and other functional properties ought to be evaluated. The properties of polymer nanocomposites are closely related to their microstructure. Substantial improvements in the properties were found with various polymer/nanofillers nanocomposites, which are mainly attributed to the high interfacial area between nanofillers and polymer matrices.

3.6.1 Mechanical Properties

Formation of nanocomposites with organoclays and organic nanofillers (cellulose nanoparticles, cellulose nanowhiskers, cellulose nanofibrils, chitin nanofibrils, etc.) has shown pronounced improvement in the mechanical properties of different polymers even with a low level of filler loading (<5 wt%). It has been frequently observed that mechanical properties such as tensile strength, elongation at break, and Young's modulus of nanocomposites are strongly dependent on the concentration of nanofillers used. Various reports on the mechanical properties of polymer nanocomposites have been documented [7, 19, 20, 24, 33, 34]. The enhancement in mechanical properties of polymer nanocomposites can be ascribed to the high rigidity and aspect ratio of nanofillers together with the good affinity through interfacial interaction between the polymer matrix and dispersed nanofillers.

3.6.2 Barrier Properties

Polymer nanocomposites have excellent barrier properties against gasses (e.g., O₂ and CO₂), water vapor, and UV light. Studies have shown that such reduction in UV light, gas, and water vapor permeability of nanocomposites strongly depends on the types of nanofillers, size of nanofillers, and structure of the nanocomposites. The increase in the gas and water vapor barrier properties of polymer nanocomposite films is believed to be because of the presence of highly dispersed nanofillers with large aspect ratios in the polymer matrix which are impermeable to water molecules [77, 78]. The gas and water vapor molecule travel through the film to follow a tortuous path through the polymer matrix surrounding the nanofillers particles as schematically shown in Figure 3.8, thereby increasing the effective path length for diffusion. The enhanced gas and water vapor barrier properties of nanocomposites make them attractive and useful in food packaging applications.

3.6.3 Chemical Resistance Properties

It is necessary to evaluate the performance and the suitability of biopolymers stored with common food packaging solutions as a function of time, because some food products release some chemicals that may have weak or strong acid characteristics. The absorption and interaction of chemical compounds released from food may affect the final mechanical properties of polymer used for packaging [79]. Generally, the chemical resistance tested is necessary to measure the tensile strength, elongation at break, and modulus of elasticity of sample submerged in weak (acetic acid) and strong (hydrochloric) acid

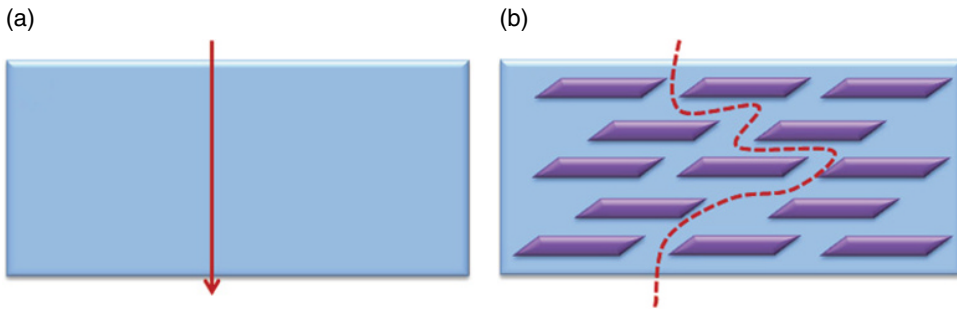


Figure 3.8 The path length of the gas and water vapor through (a) neat polymer and (b) polymer nanocomposite films

solutions as a function of time at ambient temperature (23°C) and at lower temperature used for food storage [79].

3.6.4 Biodegradation Properties

There is a research effort throughout the world to develop eco-friendly and totally biodegradable polymers as a waste management option for food packaging materials in the environment. Biodegradation is a degradation of polymer or materials activated by the action of microorganisms such as bacteria, fungi, and algae. Biodegradation of polymers may occur by hydrolysis, enzyme-catalyzed hydrolysis, ionization, solubilization, or microbial degradation either alone or in combination with one another [80]. Natural polymers (i.e., proteins, polysaccharides, and lipids) are degraded in the biological systems by oxidation and hydrolysis [81]. Biodegradable polymers degrade into biomass, carbon dioxide, and methane. In the case of synthetic polymers, microbes utilize the carbon backbone of the polymer as a carbon source. Biodegradation of polymers in general occurs in two distinct steps, that is, depolymerization and mineralization. The bio-nanocomposite packaging materials are expected to be degraded in the environment in a short time span after being discarded.

Biodegradable polymers are of three different types: (i) the mixtures of synthetic polymers and substances that can be easily digested by microorganisms (natural polymers such as polysaccharide, protein, and lipid); (ii) synthetic materials with groups that are susceptible to microbial hydrolysis, for example, polycaprolactone; and (iii) the polyesters from bacterial sources. The most famous biodegradable polymers are polyethylene oxide, polylactide, poly(ϵ -caprolactone) (PCL), poly(3-hydroxybutyrate), polyglycolic acid, and thermoplastic proteins [82]. Biodegradable polymers can be composted with organic wastes and applied to the soil to enrich the fertility of the land. The use of conventional plastics causes harm to animals; however, the use of biodegradable polymers not only reduces the harms to animals but also decreases the labor cost for the removal of plastic wastes from the surroundings. Since, biodegradable polymers degrade naturally, their decomposition helps increase the longevity and stability of landfills by reducing the volume of garbage and they could be recycled to useful oligomers and monomers by microbial

and enzymatic processing [82]. In general, the biodegradability of biopolymer films is known to be significantly improved after formation of nanocomposite with nanoclays and other nanofillers. Tetto *et al.* [83] first tested the biodegradability of nanocomposites based on PCL and reported that the PCL/clay nanocomposites showed improved biodegradability compared to pure PCL. They explained that such an improved biodegradability of PCL in clay-based nanocomposites might be due to the catalytic role of the organoclay during the biodegradation process. The degradation of PLA is reported to occur by uptake of water, followed by hydrolysis of ester bonds, fragmentation into oligomer, solubilization of oligomer fragments, diffusion of soluble oligomers, and finally mineralization into CO₂ and H₂O [84]. Sinha *et al.* [85] suggested that the enhanced biodegradability of PLA nanocomposite films is ascribed to the existence of terminal hydroxyl groups in the clay layers. Maiti *et al.* [86] found significant improvement in thermal and mechanical properties of PHB/clay nanocomposites as compared to the neat polymer. The enhanced rate of biodegradation of PHB was found with low crystallinity nanocomposite films. Sasmal *et al.* [87] also observed the faster rate of degradation of soy protein-based nanocomposite films than the pure soy protein films. In contrast, Lee *et al.* [88] found the rate of biodegradability of PBS/organoclay nanocomposite films decreased compared to the neat PBS film. In addition, the higher loading of nanoclay reduces the biodegradability of the nanocomposite. They related the contradictory results of lower degradability with the improved barrier properties of the nanocomposites, which hinder microorganisms to diffuse in the bulk of the film through more tortuous paths. Similarly, Wu and Wu [89] also reported a decrease in the degradation rate of the PLA/chitosan-organically modified MMT nanocomposite films. Hong and Rhim [50] demonstrated that the reduced biodegradability of PBS/Cloisite 30B nanocomposite was attributed to the antimicrobial action of the organoclay modified with a quaternary ammonium group. They suggested that the degree of biodegradation of bio-nanocomposites can be controlled by the nature of the layered silicates or the presence of surface modifying chemicals (quaternary ammonium cations). This property can be properly used for the development of bio-nanocomposite packaging materials with fine-tuning the biodegradation rate.

3.6.5 Other Properties

Polymer nanocomposites showed significant improvement in other polymer properties also that are useful for packaging application such as transparency, light weight, UV-light barrier, and thermal and dimensional stability. Polymer nanocomposite films show the clarity similar to pristine polymer materials when the nanofillers are small in size and well distributed through the polymer matrix. The clay platelets with a size lower than the visible light wavelength do not hinder light's passage, and the polymer nanocomposite films are transparent. However, the evenly distributed clay platelets as intercalated or exfoliated through the polymer matrix have a high UV light barrier property [90]. Shankar *et al.* [20] reported that the agar/copper nanoparticle bio-nanocomposite films exhibited high UV light barrier activity without sacrificing the transparency of the agar film. Nanocomposite packaging materials with such optical properties (transparency and UV-barrier properties)

could be utilized for transparent UV-light barrier materials for food packaging or coatings. Some of the applications of nanocomposite films are wrapping for processed meats, cheese, confectionery, cereals, fruit juice, and dairy products. Some other applications include packing material for beer and carbonated drink bottles, multilayer films and containers, and paper coatings.

Moreover, thermal properties of polymer nanocomposite films are crucial for the large-scale processing of thermoforming films at an elevated temperature without shrinkage after processing of food packaging materials. The thermal and dimensional stabilities of biopolymer films can be improved by incorporating nanocomposites with nanofillers, such as layered silicate clays, cellulose nanofibers, metallic nanoparticles, and chitin nanofibrils [11, 19]. The dimensional stability of polymer/nanofillers nanocomposites has been recognized to be enhanced owing to a higher modulus and lower thermal expansion coefficient of the nanofillers than the polymer matrix [91].

Generally, the incorporation of nanofillers into the biopolymer matrix is found to enhance thermal stability because the dispersed crystalline nanofillers act as an insulator for heat transfer and a barrier for mass transfer to the volatile products generated during thermal decomposition, and the nanofillers also serve as shields for the polymer from the action of oxygen, dramatically increasing the thermal stability under oxidative conditions [22]. Rao [92] showed a slight increase in melting point in a solution intercalated gelatin-based nanocomposite with an increase in the clay content, using DSC. Hedenqvist *et al.* [93] reported a 5–10°C increase in glass transition temperature of whey protein-based nanocomposite films made using a solution intercalation method. Sinha *et al.* [94] reported HDT of PLA-based nanocomposite films increased from 76 to 111°C as the MMT content increased to 7%. Rhim and Wang [33] observed the increased thermostability of nanocomposite films prepared with κ -carrageenan and AgNPs and organically modified clay mineral (Cloisite 30B). Shankar *et al.* [20] demonstrated an increase in thermostability of agar nanocomposite films after incorporation of copper nanoparticles. However, Reddy and Rhim [11] reported that the thermostability of agar nanocomposite film decreased after blending with paper–mulberry pulp nanocellulose.

The nanofillers may have two functions in thermal stability of nanocomposites: (i) a barrier effect, which improve the thermal stability; and (ii) a catalytic effect toward the degradation of the polymer matrix which would decrease the thermal stability [95]. Therefore, thermal stability of polymer nanocomposites depend on temperature and types and concentration of nanofiller for the preparation of nanocomposite films [22].

3.7 Conclusion

The successful use of the polymer nanocomposite has stimulated new research on the development of nanocomposites based on polymers as a matrix. Various polymers have been tested to develop nanocomposites by mixing with layered silicate nanoclays, metal or metal oxide nanoparticles, and organic nanofillers. Polymer nanocomposites exhibited increased mechanical and gas barrier properties and decreased water sensitivity without

sacrificing transparency or biodegradability after nanofillers incorporation. These properties improvements are attained at low nanofiller content (<5 wt%) compared to that of conventional fillers (in the range of 10–50%). For these reasons, nanocomposites are far lighter in weight than conventional composite materials, making them economical with other materials for specific applications in the food packaging industry. Polymer nanocomposites have an enormous potential for expanding the use of polymers to make it partially or completely biodegradable. The application of nanocomposites has expanded the use of biopolymer-based plastic packaging materials. It will help minimize the packaging waste in the environment and preserve the food for a long time by enhancing its shelf life. In addition, inorganic nanoparticles may be used to introduce multiple functionalities like antioxidants, antimicrobials, and controlled release of functionally active compounds. Using these technologies, some commercial products have already appeared in the market, while many others are currently being under development. In the forthcoming decade, nanotechnology will allow the packaging industry to provide more satisfactory packaging systems to respond to the ever-increasing demand of both consumers and food manufacturers for producing high-quality food, maintaining food safety, enhancing shelf life, and providing intelligent functions with convenient use. Polymer nanocomposite packaging materials appear to have a ravishing future for a wide range of applications in the food packaging industries including innovative, active, and intelligent food packaging with multifunctional properties.

Acknowledgment

Support from the Center for Intelligent Agro-Food Packaging (the Agriculture Research Center program of the Ministry for Food, Agriculture, Forestry and Fisheries, Korea) is acknowledged.

References

- (1) K. Marsh and B. Bugusu, Food packaging—Roles, materials, and environmental issues, *J. Food Sci.*, **72**, R39–R55 (2007).
- (2) S. J. Lee and A. T. M. M. Rahman, Intelligent packaging for food products, in *Innovations in Food Packaging*, 2nd ed., J. H. Han (Ed), pp. 171–212, Elsevier Academic Press, San Diego, CA (2014).
- (3) M. Mariano, N. E. Kissi, and A. Dufresne, Cellulose nanocrystals and related nanocomposites: Review of some properties and challenges, *J. Polym. Sci. B Polym. Phys.*, **52**, 791–806 (2014).
- (4) C. Silvestre, D. Duraccio, and S. Cimmino, Food packaging based on polymer nanomaterials, *Prog. Polym. Sci.*, **36**, 1766–1782 (2011).
- (5) R. S. Sinha and M. Bousmina, Biodegradable polymers and their layered silicate nanocomposites: In greening the 21st century materials world, *Prog. Mater. Sci.*, **50**, 962–1079 (2005).
- (6) J. W. Rhim and P. K. W. Ng, Natural biopolymer-based nanocomposite films for packaging applications, *Crit. Rev. Food Sci. Nutr.*, **47**, 411–433 (2007).
- (7) J. W. Rhim, L. F. Wang, and S. I. Hong, Preparation and characterization of agar/silver nanoparticles composite films with antimicrobial activity, *Food Hydrocoll.*, **33**, 327–335 (2013).

- (8) T. V. Duncan, Application of nanotechnology in food packaging and food safety: Barrier materials, antimicrobials and sensors, *J. Colloid Interface Sci.*, **363**, 1–24 (2011).
- (9) A. M. Clarinval and J. Halleux, Classification of biodegradable polymers, in *Biodegradable Polymers for Industrial Applications*, R. Smith (Ed), pp. 3–31, Woodhead Publishing Ltd., Cambridge, UK (2005).
- (10) P. Bordes, E. Pollet, and L. Avérous, Nano-biocomposites: Biodegradable polyester/nanoclay systems, *Prog. Polym. Sci.*, **34**, 125–155 (2009).
- (11) J. P. Reddy and J. W. Rhim, Characterization of bionanocomposite films prepared with agar and paper-mulberry pulp nanocellulose, *Carbohydr. Polym.*, **110**, 480–488 (2014).
- (12) M. M. de Souza Lima and R. Borsali, Rodlike cellulose microcrystals: Structure properties and applications, *Macromol. Rapid Commun.*, **25**, 771–787 (2004).
- (13) B. L. Peng, N. Dhar, H. L. Liu, and K. C. Tam, Chemistry and applications of nanocrystalline cellulose and its derivatives: A nanotechnology perspective, *Can. J. Chem. Eng.*, **89**, 1191–1206 (2011).
- (14) A. Khan, T. Huq, R. A. Khan, B. Ried, and M. Lacroix, Nanocellulose-based composites and bioactive agents for food packaging, *Crit. Rev. Food Sci. Nutr.*, **54**, 163–174 (2014).
- (15) D. Klemm, F. Kramer, S. Moritz, T. Lindström, M. Ankerfors, D. Gray, and A. Dorris, Nanocelluloses: A new family of nature-based materials, *Angew. Chem. Int. Ed.*, **50**, 5438–5466 (2011).
- (16) M. A. S. S. Azizi, F. Alloin, and A. Dufresne, A review of recent research into cellulosic whiskers, their properties and their application in nanocomposite field, *Biomacromolecules*, **6**, 612–626 (2005).
- (17) R. A. A. Muzzarelli, Chitin nanostructures in living organisms, in *Chitin Formation and Diagenesis, Topics in Geobiology*, N. S. Gupta (Ed), pp. 1–34, Springer, Netherlands (2011).
- (18) R. A. A. Muzzarelli, J. Boudrant, D. Meyer, N. Manno, M. DeMarchis, and M. G. Paoletti, Current views on fungal chitin/chitosan, human chitinases, food preservation, glucans, pectins and inulin: A tribute to Henri Braconnot, precursor of the carbohydrate polymers science, on the chitin bicentennial, *Carbohydr. Polym.*, **87**, 995–1012 (2012).
- (19) S. Shankar, J. P. Reddy, J. W. Rhim, and H. Y. Kim, Preparation, characterization, and antimicrobial activity of chitin nanofibrils reinforced carrageenan nanocomposite films, *Carbohydr. Polym.*, **117**, 468–475 (2015).
- (20) S. Shankar, J. Chorachoo, L. Jaiswal, and S. P. Voravuthikunchai, Effect of reducing agent concentrations and temperature on characteristics and antimicrobial activity of silver nanoparticles, *Mater. Lett.*, **137**, 160–163 (2014).
- (21) S. V. Kyriacou, W. J. Brownlow, and X. H. N. Xu, Using nanoparticle optics assay for direct observation of the function of antimicrobial agents in single live bacterial cells, *Biochemistry*, **43**, 140–147 (2004).
- (22) S. Pavlidou and C. D. Papispyrides, A review on polymer-layered silicate nanocomposites, *Prog. Polym. Sci.*, **33**, 1119–1198 (2008).
- (23) J. W. Rhim, Effect of clay contents on mechanical and water vapor barrier properties of agar-based nanocomposite films, *Carbohydr. Polym.*, **86**, 691–699 (2011).
- (24) J. W. Rhim, S. B. Lee, and S. I. Hong, Preparation and characterization of agar/clay nanocomposite films: The effect of clay type, *J. Food Sci.*, **76**, N40–N48 (2011).
- (25) P. Kumar, K. P. Sandeep, S. Alavi, V. D. Truong, and R. E. Gorga, Effect of type and content of modified montmorillonite on the structure and properties of bio-nanocomposite films based on soy protein isolate and montmorillonite, *J. Food Sci.*, **75**, N46–N56 (2010).
- (26) J. W. Rhim, A. K. Mohanty, S. P. Singh, and P. K. W. Ng, Effect of the processing methods on the performance of polylactide films: Thermocompression versus solvent casting, *J. Appl. Polym. Sci.*, **101**, 3736–3742 (2006).
- (27) P. V. Coveney, J. L. W. Griffin, M. Watkinson, A. Whiting, and E. S. Boek, Novel non-exfoliated clay-nanocomposite materials by in situ co-polymerisation of intercalated monomers: A combinatorial discovery approach, *Mol. Simul.*, **28**, 295–316 (2002).

- (28) F. Xie, P. J. Halley, and L. Averous, Bio-nanocomposites based on starch, in *Nanocomposites with Biodegradable Polymers*, V. Mittal (Ed), pp. 234–260, Oxford University Press, New York (2011).
- (29) M. Smolander and Q. Chaudhry, Nanotechnologies in food packaging, in *Nanotechnologies in Food*, Q. Chaudhry, L. Castle, and R. Watkins (Eds), pp. 86–101, Royal Society of Chemistry Publishing, Cambridge, UK (2010).
- (30) A. Brody, Nano, nano: Food packaging technology, *Food Technol.*, **57**, 52–54 (2003).
- (31) A. Ammala, Nylon-MXD6 resins for food packaging, in *Multifunctional and Nanoreinforced Polymers for Food Packaging*, J. M. Lagarón (Ed), pp. 243–260, Woodhead Publishing Ltd., Cambridge, UK (2011).
- (32) C. Sanchez, B. Julian, P. Belleville, and M. Popall, Applications of hybrid organic–inorganic nanocomposites, *J. Mater. Chem.*, **15**, 3559–35912 (2005).
- (33) J. W. Rhim and L. W. Wang, Preparation and characterization of carrageenan-based nanocomposite films reinforced with clay mineral and silver nanoparticles, *Appl. Clay Sci.*, **97–98**, 174–181 (2014).
- (34) P. Kanmani and J. W. Rhim, Physical, mechanical and antimicrobial properties of gelatin based active nanocomposite films containing AgNPs and nanoclay, *Food Hydrocoll.*, **35**, 644–652 (2014).
- (35) C. Thellen, S. Schirmer, J. A. Ratto, B. Finnigan, and D. Schmidt, Co-extrusion of multilayer poly(m-xylene adipimide) nanocomposite films for high oxygen barrier packaging applications, *J. Membr. Sci.*, **340**, 45–51 (2009).
- (36) T. Lan and Y. Liang, Commercial development of nanocomposite packaging, in *Packaging Nanotechnology*, A. K. Mohanty, M. Misra, and H. S. Nalwa (Eds), pp. 299–304, American Scientific Publishers, Stevenson Ranch, CA (2009).
- (37) A. Scully, Active packaging, in *The Wiley Encyclopedia of Packaging Technology*, 3rd ed, K. L. Yam (Ed), pp. 2–9, John Wiley & Sons, Inc., Hoboken, NJ (2009).
- (38) L. Vermeiren, F. Devlieghere, M. van Beest, N. de Kruijf, and J. Debevere, Developments in active packaging of foods, *Trends Food Sci. Technol.*, **10**, 77–86 (1999).
- (39) M. Ozdemir and J. D. Floros, Active food packaging technology, *Crit. Rev. Food Sci. Nutr.*, **44**, 185–193 (2004).
- (40) D. K. R. Robinson and M. J. Morrison, Nanotechnologies for food packaging: Reporting the science and technology research trends; Report for the ObservatoryNANO, August 2010. Available at: www.observatorynano.eu (accessed on December 22, 2015).
- (41) J. M. Lagaron, R. Catalá, and R. Gavara, Structural characteristics defining high barrier properties in polymeric materials, *Mater. Sci. Technol.*, **20**, 1–7 (2004).
- (42) V. Teixeira, J. Carneiro, P. Carvalho, E. Silva, S. Azevedo, and C. Batista, High barrier plastics using nanoscale inorganic films, in *Multifunctional and Nanoreinforced Polymers for Food Packaging*, J. M. Lagarón (Ed), pp. 285–315, Woodhead Publishing Ltd., Cambridge, UK (2011).
- (43) M. Imran, A. M. Revol-Junelles, A. Martyn, E. A. Tehrani, M. Jacquot, M. Linder, and S. Desobry, Active food packaging evolution: Transformation from micro- to nanotechnology, *Crit. Rev. Food Sci. Nutr.*, **50**, 799–821 (2010).
- (44) I. Janjarasskul, K. Tananuwong, and J. M. Krochta, Whey protein film with oxygen scavenging function by incorporation of ascorbic acid, *J. Food Sci.*, **76**, E561–E568 (2011).
- (45) E. L. Xiao, A. N. M. Green, S. A. Haque, A. Mills, and J. R. Durrant, Light driven oxygen scavenging by titania/polymer nanocomposite films, *J. Photochem. Photobiol. A Chem.*, **162**, 253–259 (2004).
- (46) J. P. Kerry, M. N. O’Grady, and S. A. Hogan, Past, current and potential utilization of active and intelligent packaging systems for meat and muscle-based products: A review, *Meat Sci.*, **74**, 113–130 (2006).
- (47) R. Ahvenainen, *Novel Food Packaging Techniques*, Woodhead Publishing Limited., Cambridge, UK (2003).

- (48) C. Maneerat and Y. Hayata, Gas-phase photocatalytic oxidation of ethylene with TiO₂-coated packaging film for horticultural products, *Trans. ASABE*, **51**, 163–168 (2008).
- (49) N. Cioffi, L. Torsi, N. Ditaranto, G. Tantillo, L. Ghibelli, L. Sabbatini, T. Bleve-Zacheo, M. D'alessio, P. G. Zambonin, and E. Traversa, Copper nanoparticle/polymer composites with antifungal and bacteriostatic properties, *Chem. Mater.*, **17**, 5255–5262 (2005).
- (50) S. I. Hong and J. W. Rhim, Antimicrobial activity of organically modified nanoclays, *J. Nanosci. Nanotechnol.*, **8**, 5818–5824 (2008).
- (51) L. Bi, L. Yang, G. Narsimhan, A. K. Bhunia, and Y. Yao, Designing carbohydrate nanoparticles for prolonged efficacy of antimicrobial peptide, *J. Control. Release*, **150**, 150–156 (2011).
- (52) S. Shankar and J. W. Rhim, Effect of copper salt and reducing agents on characteristics and antimicrobial activity of copper nanoparticles, *Mater. Lett.*, **132**, 307–311 (2014).
- (53) S. Shankar, L. Jaiswal, R. S. L. Aarna, and R. G. S. V. Prasad, Synthesis, characterization, *in vitro* biocompatibility, and antimicrobial activity of gold, silver and gold silver alloy nanoparticles prepared from *Lansium domesticum* fruit peel extract, *Mater. Lett.*, **137**, 75–78 (2014).
- (54) S. Shankar, X. Teng, and J. W. Rhim, Properties and characterization of agar/CuNP bionanocomposite films prepared with different copper salts and reducing agents, *Carbohydr. Polym.*, **114**, 484–492 (2014).
- (55) J. W. Rhim, S. I. Hong, H. M. Park, and P. K. W. Ng, Preparation and characterization of chitosan-based nanocomposite films with antimicrobial activity, *J. Agric. Food Chem.*, **54**, 5814–5822 (2006).
- (56) J. J. Hostynek and H. I. Maibach, Copper hypersensitive: Dermatologic aspects, *Dermatol. Ther.*, **17**, 328–333 (2004).
- (57) A. Emamifar, M. Kadivar, N. Shahedi, and S. Soleimani-Zad, Effect of nanocomposite packaging containing Ag and ZnO on inactivation of *Lactobacillus plantarum* in orange juice, *Food Control*, **22**, 408–413 (2011).
- (58) L. Zhang, Y. Jiang, Y. Ding, N. Daskalakis, L. Jeuken, M. Povey, A. J. O'Neill, and D. W. York, Mechanistic investigation into antibacterial behaviour of suspensions of ZnO nanoparticles against *E. coli*, *J. Nanopart. Res.*, **12**, 1625–1636 (2010).
- (59) X. Wang, Y. Du, J. Yang, X. Wang, X. Shi, and Y. Hu, Preparation, characterization and antimicrobial activity of chitosan/layered silicate nanocomposites, *Polymer*, **47**, 6738–6744 (2006).
- (60) K. L. Yam, P. T. Takhistov, and J. Miltz, Intelligent packaging: Concepts and applications, *J. Food Sci.*, **70**, R1–R10 (2005).
- (61) X. Zhang, Q. Guo, and D. Cui, Recent advances in nanotechnology applied to biosensors, *Sensors*, **9**, 1033–1053 (2009).
- (62) J. Fu, B. Park, G. Siragusa, L. Jones, R. Tripp, and Y. Zhao, An Au/Si hetero-nanorod based biosensors for *Salmonella* detection, *Nanotechnology*, **19**, 1–7 (2008).
- (63) D. Cui, F. Tian, S. R. Coyer, J. Wang, B. Pan, F. Gao, R. He, and Y. Zhang, Effects of antisense-myc-conjugated single-walled carbon nanotubes on HL-60 cells, *J. Nanosci. Nanotechnol.*, **7**, 1639–1646 (2007).
- (64) P. Dallas, J. Tucek, D. Jancik, M. Kolar, A. Panacek, and R. Zboril, Magnetically controllable silver nanocomposite with multifunctional phosphotriazine matrix and high antimicrobial activity, *Adv. Funct. Mater.*, **20**, 2347–2354 (2010).
- (65) N. Sanvicens, C. Pastells, N. Pascual, and M. P. Marco, Nanoparticle-based biosensors for detection of pathogenic bacteria, *Trends Anal. Chem.*, **28**, 1243–1252 (2009).
- (66) D. Restuccia, U. G. Spizzirri, O. I. Parisi, G. Girillo, M. Curcio, F. Iemma, F. Puoci, G. Vinci, and N. Picci, New EU regulation aspects and global market of activated and intelligent packaging for food industry applications, *Food Control*, **21**, 1425–1435 (2010).
- (67) M. Smolander, The use of freshness indicators in packaging, in *Novel Food Packaging Techniques*, R. Ahvenainen (Ed), pp. 127–143, Woodhead Publishing Ltd., Cambridge, UK (2003).
- (68) M. Aliofkhaezrai, Synthesis, processing and application of nanostructured coatings, in *Nanocoatings: Size Effects in Nanostructured Films*, Springer-Verlag, Berlin (2011).

- (69) A. Garland, *Nanotechnology in Plastics Packaging: Commercial Applications in Nanotechnology*, pp. 14–63, Pira International Limited, Leatherhead (2004).
- (70) S. Selke, Nanotechnology and packaging, in *The Wiley Encyclopedia of Packaging Technology*, 3rd ed., K. L. Yam (Ed), pp. 813–818, John Wiley & Sons, Inc., Hoboken, NJ, 2009.
- (71) G. Applerot, N. Perkas, G. Amirian, O. Girshevitz, and A. Gedanken, Coatings of glass with ZnO via ultrasonic irradiation and a study of its antibacterial properties, *Appl. Surf. Sci.*, **256**, 53–58 (2009).
- (72) C. Chawengkijwanich and Y. Hayata, Development of TiO₂ powder-coated food packaging film and its ability to inactivate *Escherichia coli in vitro* and in actual test, *Int. J. Food Microbiol.*, **123**, 288–292 (2008).
- (73) J. Vartiainen, M. Tuominen, and K. Nättinen, Bio-hybrid nanocomposite coatings from sonicated chitosan and nanoclay, *J. Appl. Polym. Sci.*, **116**, 3638–3647 (2010).
- (74) A. Travan, E. Marsich, I. Donati, M. Benicasa, M. Giazzon, L. Felisari, and S. Paoletti, Silver-polysaccharide nanocomposite antimicrobial coatings for methacrylic thermosets, *Acta Biomater.*, **7**, 337–346 (2011).
- (75) J. O. Carneiro, V. Texeira, P. Carvalho, and S. Azevedo, Self-cleaning smart nanocoatings, in *Nanocoatings and Ultra-Thin Films*, A. S. H. Makhlof and I. Tiginyanu (Eds), pp. 397–413, Woodhead Publishing Ltd., Cambridge, UK (2011).
- (76) L. M. Sherman, Chasing nanocomposites, *Plast. Technol.*, **50**, 56–61 (2004).
- (77) B. Xu, Q. Zheng, Y. Song, and Y. Shanguan, Calculating barrier properties of polymer/clay nanocomposites: Effects of clay layers, *Polymer*, **47**, 2904–2910 (2006).
- (78) G. Choudalakis and A. D. Gotsis, Permeability of polymer/clay nanocomposites: A review, *Eur. Polym. J.*, **45**, 967–984 (2009).
- (79) R. Auras, S. P. Singh, and J. J. Singh, Evaluation of oriented poly(lactide) polymers vs. existing PET and oriented PS for fresh food service containers, *Packag. Technol. Sci.*, **18**, 207–216 (2005).
- (80) I. J. Chin and S. Uematsu, Biodegradation of polymeric systems, in *Nanocomposites with Biodegradable Polymers*, V. Mittal (Ed), pp. 28–57, Oxford University Press, New York (2011).
- (81) K. Leja and G. Lewandowicz, Polymer biodegradation and biodegradable polymers: A review, *Pol. J. Environ. Stud.*, **19**, 255–266 (2010).
- (82) H. T. Liao and C. S. Wu, Preparation and characterization of ternary blends composed of polylactide, poly(ϵ -caprolactone) and starch, *Mater. Sci. Eng.*, **515**, 207 (2009).
- (83) J. A. Tetto, D. M. Steeves, E. A. Welsh, and B. E. Powell, Biodegradable poly(ϵ -caprolactone)/clay nanocomposites, Annual Technical Conference on Society of Plastics Engineers, pp. 1628–1632 (1999).
- (84) S. J. de Jong, E. R. Arias, D. T. S. Rijkers, C. F. Van Nostrum, J. J. Kettenes-van den Bosch, and W. E. Hennik, New insights into the hydrolytic degradation of poly(lactic acid): Participation of the alcohol terminus, *Polymer*, **42**, 2795–2802 (2001).
- (85) R. S. Sinha, K. Yamada, M. Okamoto, and K. Ueda, Biodegradable polylactide/montmorillonite nanocomposites, *J. Nanosci. Nanotechnol.*, **3**, 503–510 (2003).
- (86) P. Maiti, C. A. Batt, and E. P. Giannelis, New biodegradable polyhydroxybutyrate/layered silicate nanocomposites, *Biomacromolecules*, **8**, 3393–3400 (2007).
- (87) A. Sasmal, P. L. Nayak, and S. Sasmal, Degradability studies of green nanocomposites derived from soy protein isolate (SPI)-furfural modified with organoclay, *Polym. Plast. Technol. Eng.*, **48**, 905–909 (2009).
- (88) S. R. Lee, H. M. Park, H. Lim, T. Kang, X. Li, W. J. Cho, and C. S. Ha, Microstructure, tensile properties, and biodegradability of aliphatic polyester/clay nanocomposites, *Polymer*, **43**, 2495–2500 (2002).
- (89) T. M. Wu and C. Y. Wu, Biodegradable poly(lactic acid)/chitosan-modified montmorillonite nanocomposites: Preparation and characterization, *Polym. Degrad. Stab.*, **91**, 2198–2204 (2006).

- (90) H. Fischer, Polymer nanocomposites: From fundamental research to specific applications, *Mater. Sci. Eng. C*, **23**, 763–772 (2003).
- (91) P. J. Yoon, T. D. Fornes, and D. R. Paul, Thermal expansion behavior of nylon 6 nanocomposites, *Polymer*, **43**, 6272–6741 (2002).
- (92) Y. Q. Rao, Gelatin-clay nanocomposites of improved properties, *Polymer*, **48**, 5369–5375 (2007).
- (93) M. S. Hedenqvist, A. Backman, B. Gällstedt, R. H. Boyd, and U. W. Gedde, Morphology and diffusion properties of whey/montmorillonite nanocomposites, *Compos. Sci. Technol.*, **66**, 2350–2359 (2006).
- (94) R. S. Sinha, K. Yamada, M. Okamoto, and K. Ueda, New polylactide-layered silicate nanocomposites. 2. Concurrent improvements of materials properties, biodegradability and melt rheology, *Polymer*, **44**, 857–866 (2003).
- (95) C. Zhao, H. Qin, F. Gong, M. Feng, S. Zhang, and M. Yang Mechanical, thermal and flammability properties of polyethylene/clay nanocomposites, *Polym. Degrad. Stab.*, **87**, 183–189 (2005).

4

Polymer Nanocomposites Biodegradation

Kikku Fukushima and Giovanni Camino

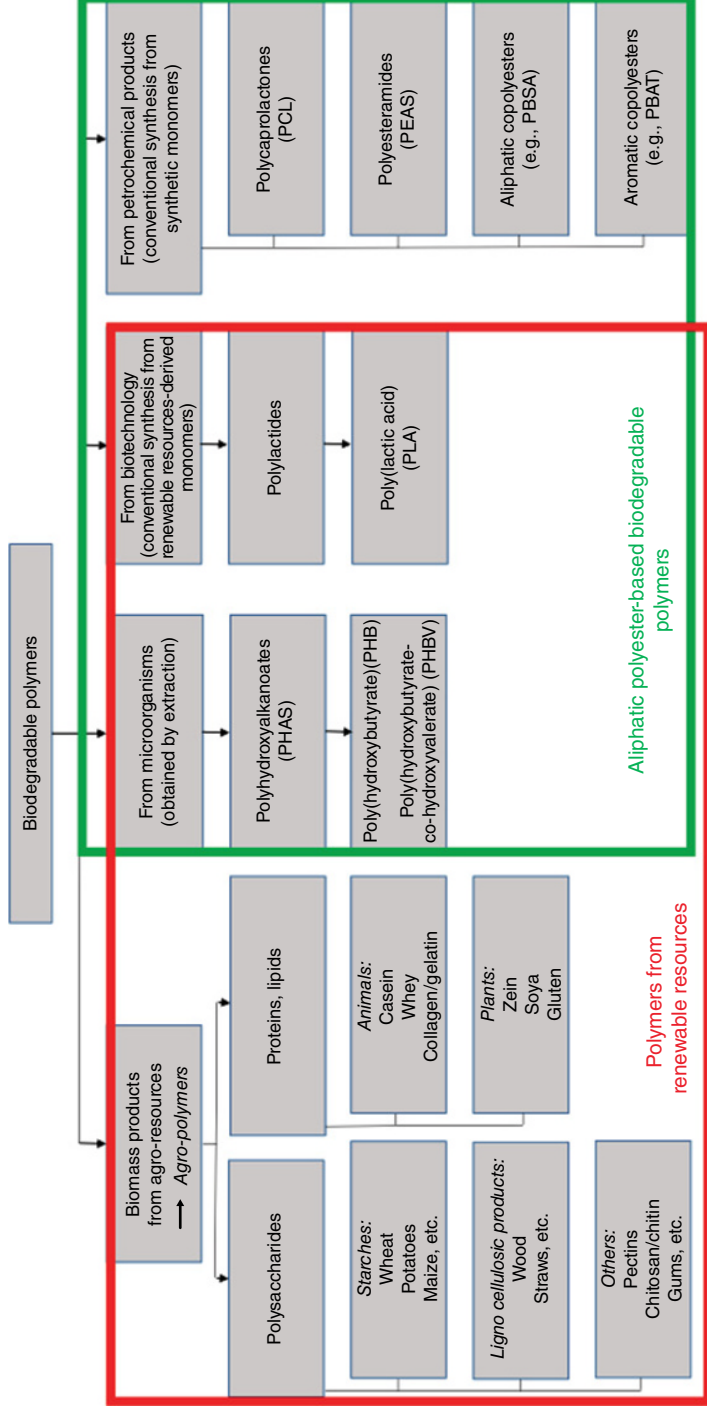
Applied Science and Technology Department, Politecnico di Torino, Italy

4.1 Introduction

In recent years, the obtainment of polymers that may fully degrade in the environment has been the topic of many researches. These polymers (often called “biodegradable polymers”) can be mainly classified according to their origin into three groups as shown in Table 4.1: natural polymers from biomasses, polymers produced either by microorganisms or by biotechnology applied to agricultural products, and polymers synthesized from crude oil.

Since these materials can be degraded in different environmental conditions, they represent an interesting alternative route to common nondegradable polymers for short-life range applications (packaging, agriculture, etc.). Nevertheless, until now, most of these degradable polymers are costly compared to conventional polymers, and they are sometimes too weak for practical use. Therefore, to extend their applications, materials have been formulated with nano-sized fillers, which could bring a large range of improved thermal, physical, and mechanical properties, thus making them fully competitive with common plastics.

Table 4.1 Classification of main biodegradable polymers



Bordes et al. [1]. Reproduced with permission of Elsevier.

The resulting nanocomposites often referred to as “nano-biocomposites” have been the subject of some publications. These works have reported the developments obtained in preparation, characterization, properties, crystallization behavior, and melt rheology of these biodegradable polymer/nanoparticle systems during the past decade; however, concerning their process of degradation in the environment, this has been scarcely studied. Indeed, at the present day, there is a low understanding of the effect of nanoparticles on the polymer environmental degradation process, being this one of the most important key questions concerning the possible use of biodegradable polymer-based nanocomposites for environmental applications.

In this way, some research works have reported a catalytic effect of clays on the biodegradation or hydrolytic degradation of different biodegradable polyesters, due to the high hydrophilicity of these nanoparticles. However, other works reported that nanoclays can retard the degradation of aliphatic polyesters during either biodegradation or hydrolytic degradation, attributing this effect to the enhanced barrier properties of the layered silicate nanocomposites. On the other hand, it has also been reported that the degradation of nanocomposites seems to depend directly on the architecture and physical properties of the polymer matrix and on the degradation conditions (temperature of the medium, pH, humidity, presence of some specific microorganisms, etc.).

The aim of this work is to summarize the most relevant published literature of the past decade about the environmental degradation process of different polymers with current interest in biodegradable polymers applications, and the effect of nanoparticles on their degradation process. This chapter will cover the main processes of environmental (bio) degradation (hydrolysis, oxidation, and composting) reported for polymers and nanocomposites. The polymer matrices in study include those as of natural, renewable as of fossil origins. Considerations to several possible variables in the polymer degradation process, such as polymer matrix and nanoparticles types, degradation medium and conditions of degradation, and prospective conclusions, will be proposed.

4.2 Biodegradation of Polymers and Their Nanocomposites

4.2.1 Standards for Environmentally Biodegradable Polymers

Materials based on biodegradable polymers of Table 4.1 are generally classified as follows [2]:

1. Renewable resource-based polymer materials: these polymers are either synthesized naturally from plants and animals, or entirely synthesized from renewable resources. This class includes starch, cellulose, proteins, chitosan, poly lactic acid (PLA) and polyhydroxyalkanoates (PHAs).
2. Petroleum-based polymer materials: these polymers are synthesized from petroleum resources but are biodegradable at the end of their functionality. Polycaprolactone (PCL) and poly(butyleneadipate-*co*-terephthalate) (PBAT) are included in this category.

3. Polymer materials from mixed sources: these are made from combinations of polymers belonging to the two aforementioned categories: they include poly(trimethylene terephthalate) (PTT), thermosets, and blends.

General definitions of biodegradable polymers have been proposed by standardization authorities:

- ISO 472 (1988): a plastic designed to undergo a significant change in its chemical structure under specific environmental conditions resulting in the loss of some properties that may vary as measured by standard test methods appropriate to the plastic for the application in a period of time that determines its classification. The change in the chemical structure results from the action of naturally occurring microorganisms.
- ASTM (1996): a degradable plastic in which the degradation results from the action of naturally occurring microorganisms such as bacteria, fungi, and algae.
- CEN (1993): degradable material in which the degradation results from the action of microorganisms, and ultimately the material is converted to water, carbon dioxide and/or methane, and a new cell biomass.
- BPS Japan (1994): polymeric materials that are changed into lower-molecular-weight compounds where at least one step in the degradation process is through metabolism in the presence of naturally occurring organisms.

These standards provide the achievement of the level of biodegradation of polymer systems needed for specific final applications; however, the mechanism of material degradation cannot be accessed through these normatives. Furthermore, the development of biodegradable polymers has been beset by misinterpretation of the way in which nature deals with its waste products. In particular, the importance of abiotic processes has not been given sufficient emphasis in the process of bioassimilation. Consequently, existing international standards for biodegradable polymers tend to be based on folklore rather than scientific evidence since they ignore completely the environmental role of abiotic chemistry [3].

In general, the most important factor in determination of biodegradation is the proper selection of the test procedure based on the nature of plastic and the climatic conditions of the environment [4]. Several test methods to assess the potential biodegradability of plastics have been developed, and accordingly biodegradation can be characterized by weight loss, or by change in tensile strength, or in dimensions, or in chemical and physical properties, or change in molecular weight and molecular weight distribution or by carbon dioxide production, or bacterial activity in soil. The most recognized degradation media and conditions proposed are Ref. [4] as follows:

- *Soil burial method*: biodegradation test is performed under natural conditions or laboratory conditions. Sample with definite weight and dimension is buried in specific depth in the soil for different time intervals. After a specified time, the sample is taken out of soil and thoroughly rinsed with distilled water following immersion in distilled water, and after that it is dried at 50°C for 24h in a vacuum oven. The sample is then allowed to equilibrate to ambient temperature and humidity for at least 24h before measurement. In one study, starch plastic films buried in a forest soil have developed rapid colonization

(15 days later) by fungal hyphae and showed degradation of the starch granules on the films [4].

- *Compost method*: the definite weight of the dry plastic is subjected to the mixture of definite amount of mature compost and then incubated at 58°C with maintained moisture content at 65%. Biodegradation is measured based on the amount of material carbon converted to gaseous carbon dioxide. The nature of the compost affects the degree of degradation. Unexpected trends have been reported for the biodegradation of plastics in the compost stored at -20, 4, and 20°C for different periods. The shape of the plastic sample and additives in the compost affect the plastic degradation in the compost [4].
- *Pure culture method*: specific bacteria and fungi can be applied for the degradation of polymers. In laboratory conditions, isolated microorganism strain has been allowed for sufficient growth in different nutrient media. In pure culture method, pre-weighed sterilized films are aseptically added to sterilized culture medium and films in culture medium are incubated with shaking for 24h before inoculation to ensure asepsis. The culture medium is inoculated with spores from a specific microorganism and is incubated with shaking at 125 rpm for 4 weeks at optimal growth temperature for the selected microorganism. The sample is weighed after washing with 70% ethanol and drying at 45°C until equilibrated. Each of the different films is then compared with the corresponding uncultured material [4].
- *Aerobic degradation in the presence of sewage sludge*: due to the enriched environment of sewage sludge, microbes present here are more diverse in composition than other disposed methods encountered [5]. In laboratory conditions, samples have been inoculated with sewage microbes. Gaseous CO₂ and CH₄ are monitored by headspace analysis using GC/MS.

4.2.2 Mechanisms of Polymer Biodegradation

The understanding and consideration of the biodegradation mechanisms are essential for the design and development of novel biodegradable polymers. In the environment, polymeric materials are subjected to degradation by biological, chemical, and/or physical (mechanical) actions [6]. In living organisms generally, biodegradation involves successive chemical reactions, such as hydrolysis, oxidation/reduction with or without the aid of enzymes depending on the environment conditions. Biological action is represented by enzymatic reactions [6].

According to Matsumura [6], biodegradable polymers are generally degraded through two steps: primary degradation and ultimate biodegradation. Primary degradation is the main chain cleavage forming low-molecular-weight fragments (oligomers) that can be assimilated by the microbes. Molecular weight reduction is mainly caused by hydrolysis or oxidative chain scission. Hydrolysis involves environmental water with the aid of an enzyme or under nonenzymatic conditions (abiotic). In latter case, autocatalysis, heat, or catalytic metals are often responsible for the hydrolysis rate. Oxidative scission occurs mainly by combined action of oxygen, a catalytic metal, ultraviolet (UV) light, or an enzyme. It should be noted that the polymer chain can also be cleaved by mechanical stress

such as bending, pressing, or elongation. The low-molecular-weight fragments thus produced are then incorporated into microbial cells for further assimilation to produce carbon dioxide, water, and microbial cells/metabolic products under aerobic conditions. Under anaerobic conditions, methane is mainly produced in place of carbon dioxide and water.

4.2.2.1 *Polymer Chain Scission*

Polymer chain bond scission can occur in two ways: at chain ends (exogeneous scission) or at random (endogeneous) along the chain [6]. In the former case, a water-soluble monomer/oligomer is generally liberated into the reaction media, and the rate of molecular weight reduction of the residual polymer is low. Whereas when the polymer chain is randomly cleaved, the molecular weight and mechanical properties of the remaining polymer quickly decrease.

4.2.2.2 *Degradation Site*

In general, amorphous regions are more susceptible to degradation by both enzymatic and nonenzymatic hydrolysis than crystalline ones. This is ascribed to the ease of water penetration into the amorphous region. There are two main degradation mechanism types found in polymer materials depending on the main degradation site: surface degradation (erosion) and bulk degradation [6]. Surface degradation occurs when the hydrolytic degradation rate of the material surface in contact with water containing catalytic substances such as alkalis and enzymes is much higher than the diffusion rate of water molecules or of catalytic substances within the material. In such a case, the hydrolytic degradation seemingly occurs solely on the material surface because the hydrolytic degradation rate is much higher on the surface than at the core [7]. According to Tsuji [8], the bulk degradation mechanism can be divided into at least three stages: (i) initial hydration or water absorption of materials, (ii) gradual decrease in molecular weight without weight loss, and (iii) weight loss through the formation and dissolution of water-soluble oligomers and monomers.

Some structural or external factors can determine the predominant hydrolytic degradation mechanism of the sample. For example, when the material thickness becomes larger than a critical value, the hydrolytic degradation mechanism can change from bulk to surface erosion [9]. In such cases, hydrolysis-formed oligomers and monomers with a high catalytic effect are trapped and accumulated in the core part of the materials [10], resulting in an accelerated hydrolytic degradation in the core part (core-accelerated bulk erosion).

4.2.2.3 *Degradation via Hydrolysis*

Most of the polymers, such as polyesters, polyanhydrides, polycarbonates, and polyamides are mainly degraded by hydrolysis into low-molecular-weight oligomers at the primary degradation stage with subsequent microbial assimilation in the biodegradation process [6]. Hydrolytic degradation is divided into two types: catalytic and non-catalytic hydrolysis; subsequently, catalytic degradation is divided into external and internal catalytic degradation. The former includes enzymatic degradation by hydrolase enzymes (i.e., depolymerase, lipase, esterase, and glycohydrolase), and by non-enzymatic catalysts (i.e., alkaline

metal and soil acids in the environment). Internal catalytic degradation involves autocatalysis by the terminal carboxyl groups of the polymer chain. In general, it has been reported that enzymatic hydrolysis accompanies nonenzymatic degradation [6].

4.2.2.4 Various Degradation Mechanisms

Different degradation mechanisms than hydrolysis have been found in some biodegradable polymers. Such mechanisms include oxidative cleavage by a radical mechanism, this degradation being the main mechanism found for non-hydrolysable polymers, such as polyolefins, natural rubber, and polyurethanes (PUs) [6]. In many cases, hydrolysis and oxidation normally occur simultaneously in environmental degradation of polymers [6].

4.2.3 Biodegradation of Polymers from Natural Resources and Their Nanocomposites

4.2.3.1 Polysaccharides

Starch Starch is a widely used bioplastic that is actually a storage polysaccharide in plants. It is composed of both linear and branched polysaccharides known as amylose and amylopectin, respectively [2]. Amylose is crystalline, constitutes nearly 20% of starch, and is soluble in hot water. Amylopectin is insoluble in boiling water; but in their use in foods, both fractions are readily hydrolyzed at the acetal link by enzymes [11].

Although it is possible to make useful products from thermoplastic starch (TPS) alone, extreme moisture sensitivity of starch leads to limited practical application. Therefore, the reality in commercialization of starch-based plastics involves blending of TPS with other polymers such as PLA, PHB, PCL, PBS, and PBAT [2]. In either form, the fraction of starch in the mixture that is accessible to enzymes has been reported to be degraded by either, or both, amylases and glucosidases. The starch molecule has two important functional groups, the —OH group that is susceptible to substitution reactions and the C—O—C acetal bond that is susceptible to chain breakage [11].

A few studies have investigated the effect of particles and/or nanoparticle on the biodegradation of starch polymers. Jalalvandi *et al.* [12] studied the effect of montmorillonite (MMT) nanoparticles on the biodegradation trend in compost of films based on polylactic acid (PLA), tapioca starch, glycerol, and maleic anhydride (MA) prepared by using a twin screw extruder. They found that the addition of MMT improved the water barrier property and accelerated the rate of biodegradation. They ascribed this phenomenon to the fact that nano-sized MMT particles could disturb the continuity of PLA/starch chains, forming pathways for microorganisms to enter and attack the polymer chain, and thus increasing the biodegradation rate.

On the other hand, Heydari *et al.* [13] studied soil burial tests for up to 6 months, the biodegradation of corn starch/glycerol/Na-MMT nanocomposites prepared by casting method. They found that the increase in Na-MMT content decreased biodegradability of starch polymer matrix; while the presence of glycerol increased it. This effect of nanoparticle's content was attributed to interactions between starch and Na-MMT that further prevented enzymatic attack on the biopolymer. In addition, the films with higher initial contact

angle and lower water solubility revealed slower biodegradation. Domka *et al.* [14] studied the biodegradation process of foils based on starch, glycerin as plasticizer, and three different nanofillers (kaolin, montmorillonite, and bentonite) in a compost made of leaves and cooking (vegetable and fruit) waste placed on a special wooden platform ensuring air access ($T \sim 0.5\text{--}8.5^\circ\text{C}$ depending on the temperature of the surroundings), and in garden soil ($T \sim 2\text{--}11^\circ\text{C}$). Similar to Heydari *et al.* [13], they found that nanoparticles induced a delaying effect on the degradation of starch-based polymer matrix. They reported that starch-based foils showed different rates of biodegradation depending on their composition, being the pure starch foil (with no plasticizer or filler): the one that presented the highest biodegradation rate in compost and in soil. The foil with glycerin as a plasticizer (starch + glycerin) presented higher rates of biodegradation as compared to nanocomposites, but lower than pure starch matrix. Interestingly enough, the addition of bentonite brought higher rates of biodegradation as compared to its analogous based on MMT and kaolin, and this was attributed to its lower dispersion level in the polymer matrix, according to mechanical analysis.

Cellulose and Chitosan Cellulose, chitosan, and chitin are among the most abundant natural biopolymers, which are inexpensive, renewable, and biodegradable. The major challenge for their sustainability is their poor moisture resistance at high humidity conditions; however, incorporation of nanostructured materials with high aspect ratio as reinforcements has been found to significantly reduce water permeability compared to virgin matrix [15].

Cellulose is an abundant and ubiquitous natural polymer. It is the major structural component of plant cells and is found throughout nature. This linear polymer is composed of D-glucose subunits linked by 1,4-glycosidic bonds forming cellobiose molecules [11]. Cellulose can appear in crystalline forms as well as in amorphous form, with the latter being more susceptible to enzymatic degradation [16]. Microorganisms capable of degrading cellulose produce a battery of enzymes with different specificities. Cellulases hydrolyze the 1,4-glycosidic linkages of cellulose. Traditionally, they are divided into two classes referred to as endoglucanases and cellobiohydrolases. Endoglucanases can hydrolyze internal bonds (preferably in cellulose amorphous regions) releasing new terminal ends. Cellobiohydrolases act on the existing or endoglucanase-generated chain ends [11].

The importance of cellulose nanocomposites have arisen from the unique properties of cellulose nanomaterials such as structural stability against various processing windows and excellent mechanical properties in terms of Young's modulus (about 138 GPa) compared to other lignocellulosic natural fibers (35–45 GPa for flax fiber) [17]. In this case fibrillated cellulose has nano size and is the nanofiller. In other cases, cellulose is used as the polymer matrix not the filler, obtaining that, in general, cellulose nanocomposites made using renewable resource-based biopolymers exhibit superior thermal, mechanical, and barrier properties with minimum reinforcement (~ 5 wt.%) compared to macroreinforcements with the added advantages of recyclability and biodegradability [2].

Methyl cellulose (MC) has been recently found as a potential polymer to be used as environmental friendly product, especially as coating or mulching film, because of its large

availability, low cost, and easy processability [18]. However, due to its high biodegradability, it can be used only in limited applications. In this way, it has been found that the addition of nanoreinforcements in the pristine polymer could increase the length of the tortuous path, obstruct the diffusion of microorganisms in the bulk of the film, and bring a decrease of the biodegradability rate [19]. Rimdusit *et al.* [18] investigated the effect of MMTs and glutaraldehyde (GA) contents on the biodegradability, physical, thermal, and mechanical properties of MC/MMT nanocomposite films prepared by solution intercalation and cross-linked MC films (by using GA as a chemical cross-linking reagent and hydrochloric acid as a catalyst in an aqueous solution). They performed biodegradation test in compost and by measuring the amount of CO₂ evolved from the biodegradation process (according to a modified version of the standard ASTM D5988). They also found that according to the quantitative study of net CO₂ evolution from pure MC, nanocomposite and cross-linked films, a higher amount of CO₂ was obtained for pure MC as compared to nanocomposites and cross-linked films, indicating that addition of MMT and cross-linking delayed the biodegradation of MC films. They attributed this decrease of biodegradability for MC/MMT nanocomposites to the interaction and adhesion of MC and layered silicate surfaces of MMT, which could restrict segmental motions at the interface. They suggested that a part of MC chains could be hidden by silicate layers on the surface of the film, which forced the degraders to diffuse into the bulk of the film through a more tortuous path, and therefore, hindered polymer biodegradation. They also related a decreased water permeability of nanocomposites and cross-linked samples as a possible cause for the decrease of their biodegradability, making the transport of water from the surface into the material bulk more difficult.

Regarding chitin and chitosan, the interest in these materials is driven by their unique properties such as renewable, biocompatible, biodegradable, and non-toxic with excellent adsorption properties [2]. Chitin is an abundantly available natural polysaccharide and is the supporting material in many invertebrate animals such as insects and crustaceans. The monomers in chitin are 2-acetamido-2-deoxy- β -D-glucoses that are connected by β (1 \rightarrow 4) linkages, and this polymer is degraded by chitinase. The deacetylated chitin is known as chitosan, and commercial chitosans have around 50–90% deacetylation degree [20]. Chitosan is a semicrystalline polymer whose crystallinity depends on the extent of deacetylation [2]. Chitosan fibers have been used as wound-dressing materials and absorbable sutures, and they have a great interest in biomedical applications [2]. At the same time, chitosan has also been found to have antimicrobial characteristics, thus presenting a great potential in packaging applications [21]. Furthermore, it has been reported to be able to form a barrier against moisture, oxygen, and CO₂ [22]. Concerning the biodegradation of these polymers, the enzymes that have been investigated in detail are strains of *Serratia marcescens*, which have been reported to be able to convert chitin to monomers and oligomers [23, 24]. Chitinolytic enzymes from fungi (*Trichoderma*) have also been investigated [25], which seem to degrade chitin to *N*-acetyl-D-glucosamine almost exclusively. The biodegradation of their nanocomposites has also been recently studied. Fengwei-Xie *et al.* [22] studied the effect of fully delaminated non-modified (MMT-Na⁺) and organo-modified (OMMT-Ch) MMT particles (2.5–5 wt.% filler content) on the mechanical

properties and biodegradability in compost of plasticized chitosan-based materials prepared by thermomechanical kneading and by using glycerol as plasticizer. They found that the plasticized chitosan-based nanobiocomposites showed drastically improved mechanical properties compared to neat chitosan due to high clay dispersion levels, and that the biodegradation rate of the polymer matrix was slightly increased by the addition of unmodified nanoclay, but practically unaffected by addition of organo-modified particles.

Similar results were observed by Xu *et al.* [26] during their biodegradation studies on acetylated chitosan films. They observed that the biodegradation of plasticized chitosan samples was considerably fast and without notorious differences upon addition of nanoclays. The addition of organo-modified MMTs did not considerably affect the biodegradation rate of plasticized chitosan matrix, even if they expected that exfoliated clay could create a tortuous path for oxygen permeation and water absorption, and thus delay the rate of polymer biodegradation. On the other hand, unmodified nanoclay samples showed a slight increase in their relative degree of biodegradation compared to pure chitosan matrix, and probably due to the inherent microstructural defects in the MMT-Na⁺ samples, making easier the water absorption process during degradation.

Recently, Gaurav *et al.* [27] studied the thermal and mechanical properties, and biodegradability in soil (30–35°C), of nanocomposites based on an esterified cellulose derivative blended with chitosan and reinforced with surface functionalized nanoclay (0–10 wt.%). They reported enhanced mechanical properties due to the addition of nanoparticles as well as a general increase in the rate of biodegradation and water uptake with higher nanoparticle contents. In specific, they found that chitosan was more biodegradable than cellulose as the hydroxyl groups in the latter are replaced by ester groups. The blends showed a retarded initial, but thereafter the biodegradation was higher than either cellulose or chitosan. The addition of nanoparticles lowered the biodegradation up to 4% nanoparticle loading, probably due to interactions between cellulose and chitosan with the amine groups of modified nanoparticles that restricted the segmental motion at the interface, causing the effective path length and diffusion time to increase (similar observations were reported by Rindusit *et al.* [28] during the biodegradation of methylcellulose–MMT composites); however, beyond 4% nanoparticle loading, the blends exhibited higher degradation rates than for lower clay loadings. The addition of increased modified nanoparticles seemed to induce large amorphous regions, and these regions were easily accessible during degradation process. A similar observation was reported by Wu and Wu [29] who observed higher biodegradation rates for nanocomposites with 6 wt.% MMT content than with 3 wt.% clay loading. They also explained these results assuming that the water uptake level was considerably high in nanocomposites with clay contents higher than 4%.

4.2.3.2 *Proteins*

A protein is a random copolymer of different amino acids. Based on the origin, proteins can be classified as plant proteins (e.g., soy, canola and wheat protein) and animal proteins (e.g., gelatin and casein). Generally, proteinoous biomaterial can be defined as a stable three-dimensional (3D) polymeric network that is strengthened by hydrophobic

interactions and hydrogen bonding [2]. Although, both animal- and plant-based proteins are used in designing many nonfood applications, these proteins plastics have not progressed significantly toward commercialization at a large scale [2].

Gelatin Gelatin is an edible, biodegradable, and renewable biopolymer produced from the partial denaturation of collagen, a by-product of meat processing [30] or from the pharmaceutical industry [31], with film-forming properties appropriate for the production of biopackaging materials [32]. Like most protein-based materials, gelatin films show excellent oxygen and aroma barrier properties as well as fairly good mechanical properties [32]; however, these films tend to be moisture sensitive [33]. At high relative humidity, gelatin films swell due to their hydrophilic nature, lose their dimensional stability, and decrease their mechanical and barrier properties, limiting their application in direct contact with foodstuffs with high water. Apart from these applications, due to its almost identical composition to that of natural collagen [34], it has been explored as scaffolding materials for many tissue engineering applications; however, its poor mechanical properties in wet state limit its application as a structural biomedical material [35]. The most reported attempts to reinforce gelatin materials include vapor cross-linking [36], orientation techniques [37], and compounding with natural fibers [31] or with nano-sized particles [38, 39].

Research data on the biodegradability of gelatin-based materials and bionanocomposites have been reported [30, 40, 41]. Gelatin is susceptible to the action of enzymes (proteases), which are present in a variety of microorganisms [42]. Some studies highlighted the effect of chemical modifications on the rate and extension of gelatin biodegradation in different environments such as lake and river waters [30] and soil [40] under laboratory conditions. Results revealed that the rate and extension of biodegradation depended on the type of cross-linking reagent and on the cross-linking density. Apostolov *et al.* [43] found that developed laminates based on cross-linked or uncross-linked gelatin reinforced with linen and silk fabrics suffered a degradation level of enzymatic degradation similar to gelatin or gelatin-based materials [44].

Martucci *et al.* [45] studied the biodegradation in soil (pH 6.1, $T=40^{\circ}\text{C}$, ASTM D2216) of three-layer gelatin films composed of sodium MMT—plasticized gelatin (inner layer) and dialdehyde starch (DAS) cross-linked gelatin films plasticized with 30 wt.% glycerol (outer layers). Soil burial testing demonstrated that cross-linking and the compounding with unmodified clay delayed the overall extent of gelatin biodegradation due to some resistance to attack by microorganisms. They found that cross-linking and nanoparticles had an effect in depressing polymer biodegradation during soil burial due to some restriction in water and/or microorganism diffusion through the bulk material. Similarly, Zhuang *et al.* [46] indicated that *in vitro* degradation tests of intercalated nanocomposites of gelatin/MMT/chitosan, prepared via solution casting, showed that nanocomposites had a lower degradation rate than gelatin/chitosan blends. Nistor *et al.* [47], also reported that the presence of some MMTs (Dellite 67G and Cloisite 93A) could delay the hydrolytic biodegradation rate of collagen-based hydrogels, due to a superior collagenase resistance in nanocomposites compared to hydrogels without nanoparticles.

Wheat Gluten Among biosourced polymers, proteins such as wheat gluten are natural heteropolymers constituted by different amino acids, which offer a large spectrum of chemical functionalities and, thus, various polymer network structures [48, 49]. Wheat gluten is a by-product of the wheat starch industry available at a reasonable price and displaying functional properties interesting for packaging or agricultural applications. Wheat gluten is mainly constituted of two main storage proteins: gliadins and glutenins. These gluten proteins can undergo disulfide interchange upon heating, which leads to the formation of a 3D macromolecular network [50]. Owing to good thermoplastic properties, wheat gluten can be processed by extrusion at temperature as low as 60°C in the presence of hydrophilic plasticizers [51]. Besides the application of thermal and chemical treatments, the creation of a nanocomposite structure through the introduction of layered silicates constitutes another promising route to modulate properties of wheat gluten materials [52]. Wheat gluten-based nanocomposites are commonly prepared using either a solvent (casting) or a thermo-molding process, and it has been shown that the introduction of unmodified MMT led to a significant decrease in water sensitivity, water vapor permeability, together with an increase in rigidity and resistance of wheat gluten-based materials [52].

Domenek *et al.* [53] have demonstrated the high biodegradability and non-ecotoxicity of wheat gluten-based materials. Even if covalent cross-linking induced by thermal treatments allowed to significantly improve in water resistance and mechanical properties of wheat gluten-based materials [54], it was shown that the biodegradability was not affected when this is evaluated in a liquid medium (modified Sturm test) [53]. Nevertheless, under composting conditions, Zhang *et al.* [55] have recently reported that the biodegradability of wheat gluten-based materials can be affected by chemical modification.

Chevillard *et al.* [56] investigated the influence of nanoclays (unmodified sodium MMT and organically modified MMT) on the biodegradability through respirometric experiments and water sensitivity of wheat gluten-based materials by focusing on a better understanding of multi-scale relationships between biodegradability, water transfer properties, and structure of resulting materials. Respirometric experiments showed that the rate of biodegradation of wheat gluten-based materials was slowed down by adding unmodified MMT (HPS) without affecting the final biodegradation level, whereas the presence of an organically modified MMT (C30B) did not significantly influence the biodegradation pattern. Three hypotheses were proposed to explain how the presence of MMT could slow down biodegradation patterns of wheat gluten-based materials: (i) a reduced water adsorption capacity of the materials in the presence of such fillers; (ii) the establishment of interactions between MMT and the matrix, resulting in a lower availability for the matrix to be biodegraded; and/or (iii) the presence of a tortuous path induced by the nanodispersion of layered silicates leading to a slower diffusion of penetrants. In the case of organically modified MMT- (C30B) based nanocomposites, no change in the biodegradation pattern was observed based on the three hypotheses proposed before, considering the insignificant changes in water sensitivity of polymer obtained by addition of C30B, the poor chemical compatibility between C30B and wheat gluten matrix, and the low dispersion achieved for C30B. Contrarily, the presence of unmodified MMT (HPS) led to a significant reduction in biodegradation rate, result consistent with the good affinity between HPS and wheat gluten

matrix, and with the decrease in liquid water adsorption level and high dispersion/exfoliation level of HPS nanoclays achieved for HPS nanocomposites. They concluded that molecular/macromolecular compatibility between clay layers and wheat gluten matrix, that is, the ability of both components to establish interactions appeared as the key parameter governing the nanostructure, the liquid water sensitivity, and, as a result, the biodegradation process.

4.2.3.3 Polyesters

Biodegradable polyesters can be grouped according to their synthetic methods, biological synthesis, and chemical synthesis. Microbially produced biopolyesters are exclusively based on polyhydroalkanoic acid policondensates. Chemically synthesized polyesters include the polycondensates of diols with dibasic acids and of hydroxy acids. These polyesters are equally biodegraded by hydrolysis at the ester bonds to produce low-molecular-weight intermediates during the initial degradation stage [6].

Polyesters Produced by Microorganism or by Plants

Polyhydroxyalkanoates PHAs are the family of biopolyesters that are totally synthesized by microorganisms from various substrates as carbon sources. This group of polymers has diverse structures and display properties accordingly. Over 150 different types of PHAs, that is homopolymers and copolymers, can be synthesized by employing different bacterial species and growth conditions. Polyhydroxybutyrate (PHB) and poly(hydroxybutyrate-*co*-hydroxyvalerate) (PHBV) are the most well-known polymers of the PHA family [2].

PHAs are renewable, biodegradable, and biocompatible; also the properties of the PHBV copolymer can be easily tailored by varying the valerate content. PHAs are very sensitive to processing conditions and exhibit a very narrow processing window. Under higher shears, they display rapid reduction in the molecular weight due to chain cleavage, and pose problems during most of the polymer processing operation. Additives, blends, and composites are the most studied ways to overcome these problems [2].

The diversity of PHA's properties makes it suitable for wide-range applications including packaging, fibers, and biomedical uses [57]. Researchers are working toward improving PHA's mechanical, biodegradation, and morphological properties in order to broaden its applicability in various industries. For example, blending PHBV with PCL [58], PLA [59], starch [60], fibers [61], and nanoclays has been studied for this purpose.

The *in vitro* degradation of PHB and PHBV under physiological conditions has been reported to be very slow [62]. Under accelerated conditions (high temperature and/or acidic/basic pH), the degradation seems to proceed through a molecular weight decrease, and when the molecular weight is sufficiently low a weight loss is observed; almost all the mechanical strength is lost and the remaining polymer breaks down into small fragments [63]. There is no agreed explanation as to how the copolymer composition affects the hydrolysis rate. It has been suggested that it is the crystallinity rather than the composition that affects the hydrolysis rate [64].

The bacterially produced poly (hydroxyalkanoates) are quite resistant to moisture, but they have been found to be rapidly biodegraded by a wide range of microorganisms [63]. Actually, PHAs can be completely degraded to carbon dioxide and water through an aerobic bacterial action [6]. The biodegradation of PHAs has been demonstrated in natural environments such as soil and sea water, and the rate of biodegradation of PHA seems to be dependent on environmental conditions such as temperature, moisture, pH, nutrient supply, and those related to the PHA materials themselves, such as monomer composition, crystallinity, additives, and surface area [6].

The biodegradation mechanism of PHB has been reported to begin with its depolymerization by HB depolymerase to produce the R-3-Hydroxybutyric acid (R-3-HB oligomers) [6], the latter is further depolymerized by oligomer hydrolase to R-3HB monomer. R-3-HB is dehydrogenated with NAD^+ into acetoacetic acid, which follows esterification with CoA-SH to produce acetoacetyl-CoA by the action of acetoacetyl-CoA synthase with the aid of ATP. The acetoacetyl-CoA is then degraded into acetyl-CoA by β -ketothiolase. This compound successively enters the tricarboxylic acid (TCA) cycle to be transformed into carbon dioxide and water under aerobic conditions [6]. This enzymatic hydrolysis of PHB has also been reported as a heterogeneous erosion process proceeding from the surface, where polymer chains are degraded initially by *endo*-scissions (randomly throughout the chain) and then by *exo*-scissions (from the chain ends) [63]. This results in subsequent surface erosion and weight loss. The average molecular weight and molecular weight distribution seem changeless during enzymatic degradation because of the highly selective surface degradation, together with the removal and dissolution of low molecular weight degradation products from the polymer matrix into the surrounding environment [63]. A preferential enzymatic attack of the amorphous phase of PHB has also been reported [65], and it has been found that in the initial stages of degradation only amorphous material is consumed, but later, however, both amorphous and crystalline regions can be degraded without preference [66]. The polymer structure seems to affect the enzymatic degradation, for instance, a large number of HV units in the PHBV copolymer seems to reduce the extent of enzymatic degradation [63].

Concerning the biodegradation of PHA-based nanocomposites, Maiti *et al.* [67] reported the biodegradability of PHB and its organically modified layered silicate (OMLS) nanocomposites in compost. They obtained a retardation of biodegradation of PHB because of the improvement of the barrier properties of the matrices after nanocomposites preparation with OMLS; however, they did not present any permeability results. Interestingly enough, contrary results have been reported for PHB microcomposites. Peterson *et al.* [68] found that microcomposites based on PHA (BiopolTM) with different wood fiber mass fractions degraded faster than pure BiopolTM in an activated sludge soil at 40°C. Composites with 25 wt.% fiber loading exhibited considerably higher weight losses as compared to the unreinforced polymer over the same degradation time. The authors concluded that these natural fibers were acting as conduits for bacterial attack, allowing easier access to the material and therefore faster biodegradation. Mohanty *et al.* [69] also found that biodegradation of alkali-treated and acrylonitrile-grafted fiber BiopolTM microcomposites was higher than found for unreinforced BiopolTM under the same degradation conditions.

Polyesters Synthesized from Bio-derived Monomers and Their Nanocomposites

Poly(lactic Acid) PLA is perhaps the most frequently used polyester in biomedical applications due to its many favorable characteristics, for example, high strength and biocompatibility, as well as alternative to traditional commodity plastics due to an increased environmental concern related to the use of non-biodegradable polymers in everyday life [63]. The melt processing and physical properties of PLA are similar to those of conventional polymers; indeed in many aspects, the properties of PLA lie between those of crystalline polystyrene and polyethylene terephthalate (PET) [63], making possible its use as a commodity polymer for general applications. Among the most important applications reported for PLA are those especially focused as disposable material such as food packaging, diapers, and contaminated hospital waste, which sometimes are not suitable for collecting and recycling. PLA polymers can be also extensively used in a broad variety of medical applications: bioresorbable surgical sutures, dental implants, bone screws and plates, and controlled drug delivery [63].

In general, commercial PLA grades are copolymers of poly(L-lactic acid) and poly(D,L-lactic acid), which are produced from L-lactides and D,L-lactides, respectively. The ratio of L-enantiomers to D,L-enantiomers is known to affect the properties of PLA [70], in particular its crystallinity with a maximum of nearly 30% for the semicrystalline systems. Until now, almost all the efforts reported in order to improve the properties of PLA have been focused on the semicrystalline material (e.g., D-content <6%) presenting a melting and a glass transition temperature around 215°C and 55–58°C, respectively.

It has been reported that PLA has a high degree of stability under normal conditions of use and storage, and can be rapidly biodegraded after use, such as in a compost [71]. The hydrolytic degradability of PLA in a buffer solution has been extensively studied, and the biodegradation of PLA has also been confirmed, even if PLA degraders have a limited distribution and are rather scarce in the environment compared with those that degrade PHB, PCL, and PBS [6]. In natural environments, the main PLA degradation proceeds in a two-step reaction. During the primary degradation step, PLA undergoes nonenzymatic hydrolysis, which is both temperature- and humidity-dependent. During the secondary degradation step where the M_w decreases to 10 000–20 000, microorganisms present in the soil begin to digest the lower-molecular-weight oligomer and lactic acid, producing carbon dioxide and water [63].

The first report of microbial degradation of PLA was done in 1997 [72] by using an *Amycolatopsis* strain, then it has been found that PLA degraders are widely distributed within this genus due to the fact that most strains of these actinomycetes exhibit a silk fibroin degrading ability (in addition to a PLA degrading ability) and that L-alanine and L-lactic acid present stereochemical similarity [6]. PLA-degrading enzymes seem to selectively cleave the α -ester bond of the L-isomer as the L-alanine unit of silk fibroin (protein) [73], this could partially explain why L-Lactic acid units have been reported to be preferentially degraded than D-lactic acid units [74]. Interestingly enough, it has been reported that some purified PLA depolymerases isolated from *Amycolatopsis* strains exhibit a degrading activity on PLA, casein and fibroin, but not on PCL and PHB [75], making clear this very selective process of enzymatic degradation. At the same time, PLA-degrading *Bacillus*

strains have also been isolated from compost [76], and other enzymes such as tissue esterases, pronases, and bromelain have also been found to be able to affect PLA degradation. In general, PLA-degrading enzymes seem to be a protease-type enzyme that recognizes L-Lactic acid unit of PLA [77].

Degradation rate of PLA can be controlled by blending PLA with additives, plasticizers, and inorganic fillers. Layered silicate nanoclays, such as MMTs, have been the most extensively studied nanoparticles in PLA nanocomposites in terms of mechanical, thermal, fire retardancy, and crystallization behavior [78], especially when these are organically modified clays due to the achievement of intercalated and exfoliated nanocomposites [79]. However, biodegradation and hydrolytic degradation of PLA in the presence of layered silicate clays has been investigated to a lower extent.

Concerning the effects of the filler type combined with the effect of polymer crystallinity and degradation temperature, recently Zhou *et al.* [78] reported the hydrolytic degradation over a temperature range of 50–70°C of semicrystalline and amorphous PLA with unmodified and organically modified MMTs, observing that the pH of the nanofillers and their hydrophilicity change upon treatment with organo-modifiers, thus increasing PLA degradation rate; by contrast, this value was lower for microcomposites than for the unfilled polymer, possibly because of the reduction of the polymer carboxyl group autocatalytic effect through neutralization reaction with the hydrophilic alkaline filler. They found that bulk hydrolytic degradation apparently starts from the interface between polymer and fillers, resulting in significant morphological differences between nanocomposites, microcomposites, and neat polymer. Paul *et al.* [80] tested the effect of clay type on the hydrolytic degradation in buffered solution of PLA and PLA/organoclay nanocomposite films prepared by using three different types of organoclays: Cloisite Na⁺, Cloisite 30B, and Cloisite 25A. They found that the degradability of PLA nanocomposites was enhanced compared to the neat PLA and also found that among the nanoclays tested, the more hydrophilic the filler, the more pronounced the degradation.

Concerning biodegradability, the major problem reported with PLA matrix is the slow rate of biodegradation as compared to the rate of waste accumulation. Despite the considerable amount of reports concerning the enzymatic degradation of PLA and various PLA blends, there are not extensive studies on the compost degradability of PLA [35]. Ray and Okamoto [81] studied the biodegradation in compost of neat PLA and three organically modified layered silicate nanocomposites: PLA/qC18Mica4, PLA/C18MMT4, and PLA/qC18MMT4. They found that within 1 month, both M_w and weight loss were almost the same level for PLA and nanocomposites. However, after this induction time, a sharp change occurred in the weight loss of PLA/qC18MMT4 nanocomposite, which within 2 months was completely degraded. Ray *et al.* [82] also conducted a respirometric test to study the degradation of the PLA and its organically modified layered silicate nanocomposites in a compost environment. They found a faster CO₂ evolution for several PLA-based nanocomposites, indicating a catalytic effect of these clays in the PLA biodegradation; while other nanocomposites presented the same level to that obtained for neat PLA. They concluded that the differences in the PLA trend of degradation observed upon clay addition were related to the different types of used clays, resulting in a different mode of attack on the

PLA matrix of the test samples that could be due to the presence of different types of surfactants and pristine layered silicates. Since PLA is an aliphatic polyester, it is probable that addition of different types of clays resulted in a different mode of disruption of some of the ester linkages.

Nieddu *et al.* [83] also reported similar results on enhanced biodegradation of PLA-based nanocomposites prepared with five different types of nanoclays and different levels of clay content. They measured the degree of biodegradation of PLA nanocomposite films by measuring both the amount of lactic acid released and weight change of the sample materials during hydrolytic degradation in blood plasma incubated at 37°C. They found that the degradation rate of nanocomposites was more than 10 times (when measured the lactic acid release) or 22 times (when measured the weight change) higher than that of neat PLA. During the hydrolytic degradation of PLA and PLA nanocomposites, the formation of lactic acid oligomers obtained from the chain scission of PLA increased the carboxylic acid end-groups concentration, and these carboxylic groups are known to catalyze the degradation reaction; thus, since the hydrolytic degradation of PLA is a self-catalyzed and self-maintaining process, they proposed that hydrolysis of PLA can be affected by not only such structural factors as stereo-structure, molar mass and their distribution, crystallinity, and purity but also by the hydrophilicity and dispersion of fillers.

In a previous work [84], we also observed that the addition of two organo-modified MMTs (Cloisite 30B and Nanofil 804) increased the hydrolytic degradation rate in compost (at 40°C) of PLA matrix at room temperature because of the presence of hydroxyl groups belonging to the silicate layers of these clays, thus allowing an easier permeability of water into polymer matrix, this phenomenon being particularly evident for Cloisite 30B due to its higher dispersion in PLA as compared to Nanofil 804. Similarly, in a subsequent work [85], we found that addition of MMT and fluoro-hectorite nanoparticles accelerated the degradation process of PLA in compost at 40°C, degradation particularly accelerated by the highest dispersed nanoparticle in the polymer matrix and at higher clay contents. This phenomenon was attributed to catalysis by the hydroxyl groups belonging to the silicate layers surface and/or to their organic modifier.

However, contrasting results have been found by using different conditions of degradation, different PLA grades, or nanoparticles with different chemical structure. In this way, in a recent work [86] we found that the addition of nanoparticles (5 wt.% of modified MMT—CLO30B—or fluorohectorite—SOM MEE—and unmodified sepiolite—SEPS9) in PLA can have contrasting effects on its hydrolytic degradation (pH 7, 37, and 58°C) depending on the clay dispersion level in the polymer matrix, polymer crystallization level, and degradation temperature. In more detail, it was found that the addition of CLO30B and SEPS9 delayed the degradation of PLA at 37°C due to their inducing PLA crystallization effect and/or to their high water uptake, reducing the amount of water available for polymer matrix hydrolysis. The presence of SOM MEE also induced polymer crystallization, but it was found to catalyze hydrolysis of PLA. The differences in the degradation trend of PLA/SOM MEE as compared to PLA/CLO30B and PLA/SEPS9 were related to a probably higher water uptake of CLO30B and SEPS9 in the nanocomposites as compared to neat PLA and SOM MEE in PLA/SOM MEE. Water segregation between CLO30B layers and

SEPS9 pores was associated to the delayed polymer degradation due to a reduced amount of water, available for hydrolysis, in the polymer matrix. This effect should be probably reduced in the case of PLA/SOM MEE due to lower hydrophilic properties of the fluoromica SOM MEE. The degradation of PLA at 58°C was found to be significantly faster than at 37°C due to more extensive microstructural changes and molecular rearrangements allowing a higher water absorption into the polymer matrix. Contrasting to degradation at 37°C, the presence of any nanoparticle did not significantly affect the degradation trend of PLA at 58°C, achieving similar molecular weight decreases for all the studied materials, and probably related to the fact that at this temperature of degradation (around glass transition temperature of PLA), the high polymer chain mobility and water absorption in the specimens resulted in an extensive degradation of both low- and high-molecular-weight molecules, minimizing the effect of polymer crystallinity clay nature and aspect ratio on the polymer degradation.

Interestingly enough, in another study [87] we found that the presence of sepiolite nanoparticles partially delayed the bulk degradation of PLA in compost at 58°C, and due to a possible preventing effect of these particles on polymer chain mobility and/or PLA/enzymes miscibility. In this way, the presence of the sepiolite particles could reduce the high polymer chain mobility in the bulk material at this “high” degradation temperature acting as cross-linking entanglements and presenting a lower water absorption in the polymer matrix and a lower compost enzymes/polymer miscibility as compared to neat PLA, thus resulting in a lower extent of degradation for this system. Similar results were also obtained during the biodegradation in compost at 58°C of PLA-based nanocomposites with three different types of fumed nanosilica [88], observing that at this temperature of degradation of all PLA samples were considerably fast degraded, but with a protection action of silica toward the early degradation stages of PLA. In conclusion, in our studies, the biodegradation in compost of PLA-based nanocomposites at 40°C (below polymer T_g) [84] was shown to be catalyzed for the most dispersed nanoclay, due to the presence of terminal hydroxylated edge groups of the silicate layers able to accelerate the bulk hydrolysis of the polymer ester groups. The different effect of nanoparticles observed at 58°C of degradation could be attributed to the degradation mechanism of PLA (from the bulk to the surface), so that different clay dispersion had different influences in the degradation trend. We may hypothesize that also in this case, given the same degradation mechanism, the polymer/filler interaction is such that a delaying effect is observed upon the addition of sepiolite and nanosilica. In general, PLA hydrolysis in the presence of nanoparticles seems to be a complex phenomenon depending on degradation temperature, nature and dispersion of filler, and polymer crystallinity.

4.2.4 Biodegradation of Polymers from Fossil Origins and Their Nanocomposites

4.2.4.1 Aliphatic Polyesters from Fossil Origins

Polybutylene Succinate Poly(butylene succinate) (PBS) is generally obtained by direct polymerization of succinic acid and 1,4-butanediol as it is a simple process that produces high-molecular-weight polymers [89]. Currently, there are efforts to obtain succinic acid

by using biological feedstocks such as corn starch, corn steep liquor, whey, cane molasses, glycerol, lignocelluloses, cereals, and straw hydrolysates [2]. It has been reported that PBS readily undergoes degradation in any environment [90] and that microbes degrade the main polymer chain into small fragments via enzymatic hydrolysis [6]. Several PBS-degrading microbes has been isolated, such as *Amycolatopsis* sp. HT-6 and *Bacillus* strain TT96, obtaining that water-soluble 1,3-butanediol, 4-hydroxy *n*-butyrate and succinic acid, are temporarily accumulated during PBS degradation [6].

Concerning the biodegradation of PBS nanocomposites, Sinha Ray *et al.* [91, 92] reported the biodegradability of neat PBS and nanocomposites in two different modes: under compost and under soil field. In compost, they observed that several cracks appeared in nanocomposites preliminary, indicating an improved biodegradability of nanocomposites as compared to pure PBS given that this kind of fracture could have an advantage for biodegradation because it should be easy to mix with compost and create much more surface area for further attack by microorganisms. However, after conducting GPC measurements of recovered samples from compost, it was observed that the extent of molecular weight loss was almost the same for all samples, concluding that MMT or alkylammonium cations, as well as other properties, had no effect on the biodegradability of PBS. Similar behavior was observed during the degradation of PBS and nanocomposites in soil.

Lee *et al.* [20] prepared melt intercalated PBS/organoclay (Cloisite 30B) nanocomposites films with different content of nanoclay and performed soil compost test. They found that the rate of biodegradability of the nanocomposite was decreased compared to the pristine polymer (PBS) and the more loading of nanoclay incorporated, the lower the biodegradability of the nanocomposite was observed. They attributed such result to the improved barrier properties of the nanocomposites developed by the intercalated clays with high aspect ratio, which hinder microorganisms to diffuse in the bulk of the film through more tortuous paths. Rhim *et al.* [93] supported this delayed biodegradation of PBS by addition nanoparticles due to a strong antimicrobial activity of organoclays (Cloisite 30B) against food poisoning bacteria, especially against Gram-positive bacteria, and they suggested that the antimicrobial action was attributable to the quaternary ammonium groups in the modified organoclay. Later, Hong and Rhim [94] proved that the same organoclay (Cloisite 30B) has a strong bactericidal activity against Gram-positive bacteria and bacteriostatic activity against Gram-negative bacteria, which was caused by the quaternary ammonium groups in the organoclay. They concluded that the retarded biodegradability of PBS/Cloisite 30B nanocomposite observed by Lee *et al.* [19] was attributed to the antimicrobial action of the organoclay modified with the quaternary ammonium groups.

Phua *et al.* [95] prepared biodegradable nanocomposites from PBS and organo-MMT (OMMT) in the presence of MA-grafted PBS (PBS-*g*-MA) as compatibilizer. Similar to Lee *et al.* [19], they found that PBS nanocomposites showed lower biodegradability than that of neat PBS due to improved barrier properties, and that the extent of biodegradation was greatly dependent on the OMMT dispersion in PBS matrix, where agglomerations at high OMMT loading diminished the barrier effects.

Polycaprolactone PCL is a linear polyester manufactured by ring-opening polymerization of ϵ -caprolactone. This is a semicrystalline polymer with a degree of crystallinity around 50%. It has rather low glass transition temperature ($T_g = -60^\circ\text{C}$) and melting point ($T_m = 60^\circ\text{C}$) [35]. The PCL chain is flexible and exhibits high elongation at break and low modulus. Its physical properties and commercial availability make it very attractive not only as a substitute material for nondegradable polymers for commodity applications but also as a specific plastic of medical and agricultural areas [96]. The main drawback of PCL is its low melting point, which can be overcome by blending it with other polymers [97] or by cross-linking processes resulting in enhanced properties for wide range of applications [98].

PCL has been blended with various polymers, for example, PVC [99], PET [100], polyvinyl alcohol (PVA) [97], and PE [101] as well as blended and copolymerized with PLA [102, 103], PHB [104, 105], and poly (1,5-dioxepan-2-one) (PDXO) [106, 107]. However, in most cases the mechanical properties or the degradability were reduced compared to the homopolymer.

In general, PCL is a relatively stable material against abiotic hydrolysis, but it has been reported that it can be easily degraded in many different environments, for example, in pure fungal cultures [108, 109], in compost [110, 111], in active sludge [111], by enzymes [112], and in soil [113]. The proposed biodegradation mechanism is started by the hydrolysis of the polymer chain to 6-hydroxyhexanoic acid, an intermediate of ω -oxidation and then β -oxidation to acetyl-CoA, which can then undergo further degradation in the TCA cycle [6]. The molecular weight decreases during biodegradation, and is accompanied by a broadening of the molecular weight distribution [114]. The degree of crystallinity of PCL increases with the degradation, indicating preferential degradation in amorphous regions [115].

Contrary to PLA, it has been shown that the biodegradation of PCL proceeds by rapid weight loss through surface erosion with minor reduction of the molecular weight in contrast to its abiotic hydrolysis, which proceeds by a reduction in molecular weight combined with minor weight loss. It has been demonstrated that the erosion of PCL proceeds in the vicinity of chain ends [116]. Eldsäter *et al.* [111] studied the surface erosion of PCL films in compost, in anaerobic sludge, and by *Aspergillus fumigates*. The degradation in compost resulted in parallel grooves or cracks, while incubation with *A. fumigates* produced a spherulitic erosion pattern. Similar results were obtained by Benedict *et al.* in their study on incubation of PCL with *Aspergillus sp.*, *Penicillium funiculosum*, *Chaetomium globosum*, and a *Fusarium sp.* [114]. They achieved that the PCL degradation rate was controlled by degree of crystallinity, obtaining a faster degradation in the amorphous regions.

The degradation of PCL-based nanocomposites have been scarcely studied until now; and similar to PLA-based nanocomposites, few works existing in the literature are mostly concentrated on layered silicates. Tetto *et al.* [117] first reported results on the biodegradability of nanocomposites based on PCL in biotic aqueous medium. They reported that the PCL/organically modified layered silicate nanocomposites showed improved biodegradability compared to neat PCL, which was attributed to a catalytic role of the clays in the

polymer biodegradation mechanism. Tetto *et al.* [117] have prepared PCL/modified clay-based nanocomposites via both *in situ* polymerization and twin screw extrusion methods. They found 50% mineralization of PCL/clay in 50 days in soil as compared to 10% for the pure PCL film.

On the other hand, Maiti *et al.* [67] reported the biodegradation of PCL-based nanocomposites in compost, and showed that PCL biodegradability was depressed upon clay addition, probably because of an improvement of the barrier properties. In a previous work [118], we studied the biodegradation of PCL and nanocomposites based on organically modified MMTs (Cloisite 30B and Nanofil 804) at 5 wt.% loading degraded in a commercial compost at 40°C. We found that the biodegradation of PCL in compost proceeded through an inhomogeneous surface mechanism and that the addition of the nanoclays partially delayed the rate of polymer degradation probably due to a more difficult pathway for microorganisms in order to attack the PCL ester groups, being this phenomenon significantly evident for the highest dispersed clay in the polymer matrix (Cloisite 30B). Considering that the degradation seems to proceed from the surface to the interior of the sample, as shown in this work by optical microscopy and Fourier transform infrared spectroscopy (FTIR)-ATR analysis, it is possible to suppose that nanoclay layers can play a barrier role toward microbial attack on PCL ester groups, for example, slowing down the diffusion of enzymes into the polymer matrix. On the other hand, it has been reported that the presence of clays increases the hydrophilicity of the polymer matrix thus increasing the amount of water at equilibrium in the material, which should increase rate of hydrolysis. Furthermore, barrier to diffusion in nanocomposites [35] also reduces loss of oligomers that catalyze PCL hydrolysis through chain-end hydroxyl groups. To rationalize these results and considerations, we can assume that adhesion of PCL and/or of enzymes macromolecules to clay layers, when they are finely dispersed in the polymer matrix, could prevent or partially hinder macromolecular conformations suitable for hydrolysis catalysis. This effect, which is bound to be polymer dependent, could explain why the same nanoclays show an accelerating effect on PLA biodegradation carried out in the same conditions [84]. Indeed, in the case of PCL the higher delaying effect was observed upon the addition of Cloisite 30B, possibly because of its higher dispersion level in the polymer as compared to Nanofil 804.

In further studies, we observed that the addition of 5 wt.% of sepiolite nanoparticles [87] and fumed silica nanoparticles [88] did not show a considerable influence on the degradation trend of PCL in compost at 40°C. Taking into account the preferential surface degradation of PCL matrix, it is possible to suggest that the fumed silica and sepiolite particles did not play a barrier role toward polymer microbial attack or water diffusion rate into the material due to their lower aspect ratio (for fumed silica) or needle-like morphology (for sepiolite) as compared to the layered silicate morphology of MMTs, thus allowing the scission of the PCL ester groups and even a slight acceleration of the degradation process upon addition of both particles due to their high surface silanol groups (Si—OH) concentration. These differences were not encountered in the case of PLA [87, 88] most probably because of the different biodegradation mechanism of the two polymers.

4.2.4.2 *Aromatic Polyesters from Fossil Origins*

Polybutylene Adipate-co-Terephthalate The biodegradable polyesters developed up to now do not always sufficiently exhibit mechanical and thermal properties; however, these properties can be sometimes improved by incorporating aromatic units into the main chain of the aliphatic polyesters in ratios at which the biodegradability of the resulting copolymers may not be decreased [6]. One of the most studied and used aromatic polyesters for industrial applications is PBAT. PBAT is flexible and has a higher elongation at break than most biodegradable polyesters, such as PLA, and therefore is more suitable for food packaging and agricultural films. PBAT has been reported to degrade into various aliphatic and aromatic oligomers by the action of the microorganism *Thermomonospora fusca*, and at the end of this biodegradation, adipic acid, terephthalic acid, and 1,4-butanediol can be detected [119]. The morphologies and physical properties of nanocomposites of PBAT have been already studied [120]; however, few publications have reported on the biodegradability of these PBAT nanocomposites.

Someya *et al.* [121] tested the effect of biodegradability of PBAT-based nanocomposites prepared by melt blending with two different types of layered silicates, that is, non-modified MMT and octadecylamine-modified MMT (ODA-M). Biodegradability was investigated through aerobic tests in soil (15–30°C) and in an aqueous medium with activated sludge (25°C, pH 7.4, standard JIS K6950). They found that the biodegradability of PBAT in soil itself is not so high, PBAT/ODA-M nanocomposites showed even lower weight losses than PBAT during degradation, whereas PBAT/MMT microcomposites exhibited higher weight losses than the control PBAT. Similarly, the biodegradability test in aqueous medium, by determining biochemical oxygen demand (BOD), showed a promotion of the biodegradation in PBAT/MMT microcomposites due to the highly hydrophilic character of the non-modified MMT, whereas the addition of ODA-M showed a delaying effect on the biodegradation rate of PBAT. The lowering of the biodegradability for PBAT/ODA-M composites was related to the more hydrophobic nature of ODA-M than non-modified MMT and to its finely dispersion level with large aspect ratios in the PBAT matrix which forced enzymes or water diffusion in the bulk of the film through more tortuous paths. Similarly, Mohanty *et al.* [122] found that the biodegradability rate of PBAT bionanocomposite hybrids with non-modified and modified layered silicates was increased only by addition of Na+MMT and due to its higher hydrophilic nature.

In a recent work [123], it was reported that the hydrolytic degradation of PBAT and nanocomposites with 10 wt.% of organically modified MMT, hectorite, and unmodified sepiolite in phosphate-buffered solution (pH 7.0 at 37°C) seemed to proceed mainly from the interior of the samples and the diffusion rate of degradation products was relatively slow. Important decreases of viscosity for all samples degraded in buffered solution were observed after 8 weeks (around 40%), indicating an effective process of polymer degradation in these hydrolytic conditions; however, it was observed that addition of nanoparticles tended to reduce slightly the polymer matrix degradation but only in the early degradation stages; afterward, the presence of nanoparticles did not affect significantly the degradation level of the PBAT matrix. This protection action of nanoparticles in the early

degradation stages was related to the high concentration of clay hydroxyl groups in all nanocomposites able to confer a higher water uptake by these materials as compared to unfilled PBAT. Nevertheless, prolonged studies on the hydrolytic degradation of these PBAT nanocomposites should be performed in order to know the general effect of nanoparticles in the last stages of PBAT degradation.

4.2.4.3 Polyvinyl Alcohols

PVA is the largest, synthetic, water-soluble polymer produced in the world based on volume [6]. It exists only as a polymer; a monomer has not yet been isolated. PVA has been used for many industrial applications such as paper processing, textile sizing and finishing adhesives and binders, dispersant, and molded products [35]. The prominent properties of PVA may include its biodegradability in the environment, because the polyvinyl-type polymer consisting of a carbon-carbon main chain is hardly biodegradable [124]. The nature of PVA as a truly biodegradable synthetic vinyl polymer was repeatedly and intensively assessed. Nevertheless, the occurrence of specific PVA-degrading microorganisms in the environment appears to be uncommon and, in most cases, is strictly associated with PVA-contaminated environments [125]. Suzuki *et al.* [126] reported that *Pseudomonas boreopolis* microbes can degrade PVA. Similar PVA-degrading microbes have also been found, such as *Pseudomonas vesicularis*, *Alcaligenes faecalis* KK314, *Bacillus megaterium*, and *Pseudomonas* sp. 113P3 [6]. Additionally, anaerobic biodegradation of PVA has been confirmed; however, considerably longer times are needed to degrade PVA under anaerobic conditions compared to aerobic ones [6].

Two PVA biodegradation mechanisms have been proposed: a random-type attack and a terminal unzipping depolymerization process of the polymer chains [127]. The generally accepted biodegradation mechanism occur via a two-step reaction by oxidation (dehydrogenation) of the hydroxyl group followed by hydrolysis [6]. The initial step is the specific oxidation of 1,3-hydroxyl groups, mediated by oxidase- and dehydrogenase-type enzymes, to give β -hydroxyketone as well as 1,3-diketone moieties. The latter groups are susceptible to carbon-carbon bond cleavage promoted by specific β -diketone hydrolase, giving rise to the formation of carboxyl and methyl ketone end groups [125]. Enzymatic random end-cleavage of PVA chains does not appear to be appreciably affected by polymer structural features, such as degree of polymerization and HD, at least while these features are in the 80–100% range. However, a positive influence on the hydrophobic character (e.g., residual acetyl group content) of the polymeric substrates on the activity of specific PVA-dehydrogenase was demonstrated. The ultimate biological fate of PVA appears to be largely dependent on the environment it degraded. Accordingly, high levels of biodegradation were observed in aqueous environments, whereas moderate or negligible microbial attacks were repeatedly achieved in soil and compost [125]. Possible explanations to these last observations have been related to the absence or scarce occurrence of PVA-degrading microorganisms in soil and compost environments, as well as strong interactions of PVA matrix with the organic and inorganic components of environmental solid matrices, thus limiting the ability of enzymes to cleave the PVA chains, and to degrade extensively in these degradation media [125].

PVA nanocomposites have showed a broad range of improved physical properties (i.e., mechanical properties and moisture sensitivity) and other advantageous characteristics at acceptable cost as compared to pure PBAT. The addition of nanoparticles could realize PBAT-based materials with a great variety of improved property profiles, and they could even be able to compete, both in price and in performance, with other synthetic polymer materials in different applications [128]. However, regarding biodegradability of these nanocomposites, a few data have been published in the literature, and those that are available generally report a decrease in the biodegradation rate of PVA upon addition of nanoparticles.

Spiridon *et al.* [129] studied the enzymatic degradation of some MMT-containing nanocomposites of PVA with starch (through some determinations of mass loss, FT-IR spectroscopy, and optical microscopy), and obtained that nanoparticles hindered the enzymatic degradation of PVA. Taghi Taghizadeh *et al.* [130] studied the effect of PVA, carboxy MC (CMC), and sodium MMT clay (MMT-Na) content within starch (S) blends on the rate and extent of starch enzymatic hydrolysis using enzymes α -amylase and cellulase. The results of this study revealed that blends with MMT-Na content of 5 wt.% exhibited a significantly reduced rate and extent of hydrolysis. The results suggest that this could be attributed to interactions between PVA/S/CMC and MMT-Na that further prevented enzymatic attack on the remaining PVA/MMT-Na phases within the blend. The highest hydrolysis reaction rate was obtained for PVA/S/CMC and the lowest enzymatic degradation rate was observed for sodium MMT-containing nanocomposites of PVA/CMC with starch. In a subsequent work, Taghi Taghizadeh *et al.* [131] obtained similar conclusions during their study on the effect of PVA and sodium MMT clay content within the TPS blends on the rate and extent of starch enzymatic hydrolysis using enzyme α -amylase.

Finally, Abbasi [132] investigated the effect of PVA and nano-SiO₂ particles within TPS blends on the rate and extent of starch enzymatic hydrolysis using enzymes α -amylase and amyloglucosidase. Similar to Taghi Taghizadeh *et al.* [130, 131], they found that blends with 5 wt.% of nano-SiO₂ particles exhibited a significantly reduced rate and extent of polymer hydrolysis, attributing these results to interactions between polymers and nano-SiO₂ particles able to prevent an enzymatic attack on the remaining polymer phases within the blend.

4.2.4.4 *Polyurethanes*

PUs are widely used in various industrial fields because they possess a wide range of properties to suit many requirements. Some of the applications of this polymer include foams, elastomers, poromerics, paints, fibers, fabric coatings, adhesives, and sealants [133]. Conventional PU is produced using toxic diisocyanate, which is derived from the even more toxic phosgene, and it is generally resistant to biodegradation [134]. One of the main reasons why homo PUs are resistant to biodegradation may be due to the complexity of the urethane moieties. Simple and high-molecular-weight PUs without hydrolysable linkages, such as ester or carbonate linkages, are generally resistant to biodegradation; however, recently the molecularly pure and biodegradable diurethane moiety as a hard segment has been combined by enzymatically hydrolysable carbonate or ester linkages to produce novel

biodegradable polycarbonate/ester urethanes [6]. In this way, it has been reported [6, 135] that microbial degradation of polyester–urethanes first occurs by hydrolysis of ester bonds by esterases or lipases, and then proceeds with the degradation of oligomeric urethane segments. In parallel, it has been reported that low-molecular-weight urethane oligomers can be hydrolyzed by some microorganisms and the hydrolytic reaction can be catalyzed by some esterases [136]. Another possible mechanism of biodegradation proposed for PUs, other than hydrolysis, has been oxidation. For instance, it has been reported that poly (carbonate urethane) can undergo a slight degradation via oxidation reactions [6].

Nanocomposites composed of PU and nanoparticles (specially layered silicates) have been widely investigated [137–139]. These nanocomposites have shown advanced properties, such as mechanical properties [140], water vapor permeability [139], and water permeability [141]. Concerning the biodegradation of PU nanocomposites, Dutta *et al.* [142] studied the biocompatibility of epoxy modified *Mesua ferrea* L. seed oil (MFLSO)-based PU nanocomposites with different clay loadings (1–5 wt.%). They reported that their biodegradation studies revealed a 5–10-fold increase in biodegradation rate for nanocomposites compared to the pristine polymers. Rodrigues Da Silva *et al.* [143] studied the *in vitro* biodegradation for 4 months of biodegradable PUs based on PCL and/or poly(ethylene glycol) as soft segments and biodegradable PUs containing MMT nanoparticles. FTIR results indicated that hard segments of the biomaterials were preserved during biodegradation, but the ester bonds of the PCL incorporated into the soft segments were hydrolytically broken. Similar to Dutta *et al.* [142], they found higher rates of weight loss for nanocomposites than pure polymer matrix during degradation, concluding a catalytic effect of nanoparticles on the polymer degradation process.

Betingyte *et al.* [144] investigated the effects of different crystallographic modifications of calcium carbonate (CaCO_3) particles (2–6 wt.% filler content) on the melt flow, mechanical properties, and hydrolytic degradation (25°C), recycled low-temperature poly(ϵ -caprolactone)-based PU (rTPU). They found that the hydrolytic degradation of rTPU was slightly accelerated upon addition of CaCO_3 particles due to their hydrophilic structure.

4.3 Summary

Research and development in polymeric nanocomposites have shown potential applications in several industrial applications, given that nanoparticles have proportionally larger surface area and significant aspect ratio than their microscale counterparts, which promotes the development of mechanical, thermal, and barrier properties. Nevertheless, the possible effects of nanoparticles on the biodegradation of nanocomposites are still unclear and need to be studied. In general, it has been reported in the literature that the incorporation of clays in biopolymers could accelerate their biodegradability in compost; however, in this work we could observe that this is not an iron rule obtaining that nanoparticles can bring different effects on the polymer degradation trend depending on: the degradation mechanism of neat polymer, degradation conditions, filler nature, and dispersion level into the polymer.

It is of interest to recognize that the mechanism of polymer degradation seems to be one of the most (or the most) important factors to predict the effect of some nanoparticles on the biodegradation trend of the polymer matrix. In parallel, this biodegradation mechanism seems to be mainly affected by the chemical structure of the polymer and by the environmental conditions of degradation (such as: temperature and microorganisms/enzymes present in the degradation medium).

Most of the biopolymers used for several industrial applications have been reported to be mainly biodegraded by hydrolysis reaction, such as polyesters (PHAs, PLA, PCL, PBAT, PBS); polysaccharides (starch, cellulose, chitin, chitosan); proteins-based materials (gelatine, collagen, wheat gluten); and modified PUs with hydrolysable linkages such as ester or carbonate linkages. At the same time, this hydrolytic reaction is catalyzed by enzymes/microorganisms present in the medium or simply by specific degradation conditions, such as higher temperatures. At this point, it seems that, according to our review, the level of this catalyzing effect on the hydrolytic degradation process can define mainly if the polymer matrix will predominantly degrade by a bulk degradation mechanism or by a preferentially surface degradation mechanism; and these last two mechanisms together with the nature/size and dispersion of nanoparticles seem to affect importantly the effect of nanoparticles on the polymer degradation trend.

In more detail, when the polymer degradation mainly occurs through a hydrolytic bulk mechanism (which is normally characterized by a two-step reaction: nonenzymatic hydrolysis as primary degradation step, and then an enzymatically catalyzed degradation only after a considerably reduction of molecular weight), the addition of hydrophilic nanoparticles generally increases the polymer biodegradation rate because of the presence of hydroxyl groups belonging to the nanoparticles, which increase the hydrophilicity of the polymer matrix, the amount of water at equilibrium in the material, and finally the rate of polymer hydrolysis. This phenomenon is particularly evident for the highest dispersed nanoparticles in the polymer matrix or for the most hydrophilic nanoparticles. A similar trend can be also prognosticated through the abiotic hydrolytic degradation of these nanocomposites. Some examples found in the literature are nanocomposites based on polymer matrices with a limited distribution of catalytic degraders in the degradation environment under study, but susceptible to hydrolysis, such as PBAT, modified PU with hydrolysable linkages, and PLA (at degradation temperatures below its glass transition temperature).

On the other hand, when the degradation mainly occurs through a hydrolytic surface erosion mechanism (which is generally characterized by a rapid weight loss through surface erosion with minor reduction of the molecular weight, the appearance of grooves or cracks even at the first stages of degradation, and in polymers that can be easily degraded in many different environments, even if some of them can be relatively stable against abiotic hydrolysis), the addition of the nanoclays (hydrophilic or not) can generally delay the rate of polymer degradation probably due to a more difficult pathway for microorganisms in order to attack the polymer cleavage groups (esters in the case of polyesters), this phenomenon being significantly evident for the highest dispersed nanoparticles in the polymer matrix, or for those with high surface area. Considering that this kind of degradation seems to mainly proceed from the surface to the interior of the sample, it is possible to suppose

that nanoparticles can play a barrier role toward microbial attack on polymer cleavage groups, for example, slowing down the diffusion of enzymes into the polymer matrix. On the other hand, it has been reported that the presence of clays increases the hydrophilicity of the polymer matrix, thus increasing the amount of water at equilibrium in the material, which should increase the rate of hydrolysis. Furthermore, barrier to diffusion in nanocomposites also reduces loss of oligomers that catalyze polymer hydrolysis through chain-end hydroxyl groups. To rationalize these results and considerations, we can assume that adhesion of polymer and/or of enzymes macromolecules to nanoparticles, when they are finely dispersed in the polymer matrix, could prevent or partially hinder macromolecular conformations suitable for hydrolysis catalysis. Interestingly enough, it is possible to find in the literature that in this kind of degradation trend, although nanocomposites can present a lower biodegradation rate compare to pure polymer matrix, microparticles and low-dispersed nanoparticles or particles with relatively low aspect ratio did not play an important barrier role toward polymer microbial attack or water diffusion rate into the material, thus allowing the scission of the polymer cleavage groups and even accelerating the polymer degradation process in the case of hydrophilic particles. It is important to highlight that in this kind of biodegradation, given that the enzymatic factor seems to predominate the polymer degradation trend, the toxic nature of nanoparticles could play an important role in the polymer degradation process, observing that addition of nanoparticles with a strong antimicrobial effect can considerably delay the degradation. This kind of degradation can be generally found in nanocomposites based on proteins (gelatine, collagen), polysaccharides (cellulose, chitosan, starch, wheat gluten), PHAs, PBS, and PCL.

Interestingly enough, even if the bulk-hydrolytic (bio)degradation of PLA ($T < 40^{\circ}\text{C}$) has been extensively reported to be catalyzed by nanoparticles, it has been found that PLA can be predominantly degraded by a mechanism of surface erosion and that hydrophilic or non-hydrophilic nanoparticles can delay (or at least not significantly affect) the polymer degradation at degradation temperatures around or higher than its glass transition temperature ($T \geq 58^{\circ}\text{C}$). Same observations have been found during the abiotic degradation of PLA at these elevated temperatures, suggesting that the higher degradation temperature is the main catalyzer of its hydrolytic degradation under abiotic and biotic conditions. In this case, at these temperatures, the degradation of PLA proceeds significantly faster than at lower temperatures due to more extensive microstructural changes and molecular rearrangements allowing a higher water absorption into the polymer matrix; and the presence of nanoparticles can reduce the polymer chain mobility in the bulk material, presumably due to a lower water absorption in the polymer matrix and possibly a lower enzymes/polymer miscibility as compared to neat PLA.

On the other hand, there are other polymer matrices that biodegrade mainly via other mechanism than hydrolysis, such as PVAs that seem to degrade first via oxidation (dehydrogenation) of the hydroxyl groups followed by hydrolysis. PVA is hardly biodegradable in the environment due to its carbon-carbon main chain and also due to the uncommon occurrence of specific PVA-degrading microorganisms in natural environments. The presence of nanoparticles tends to decrease the biodegradability rate of PVA probably because nanoparticles can presumably hinder polymer cleavage groups for enzymatic degradation

by PVA-dehydrogenases. However, more studies should be done to confirm this and the effect of nanoparticles on the oxidation process of other polymers should be further studied.

Finally, it is possible to conclude that the study of the biodegradation mechanisms of polymers can importantly contribute to predict the effect of nanoparticles on the general degradation trend of biodegradable polymers. It is possible to say that the preliminary conclusions proposed here are supported for an extent literature; however, further studies should be done in order to know clearly how the biodegradability of nanocomposites can be finely tuned through a proper choice of polymer matrix and nanoparticles.

References

- (1) P. Bordes, E. Pollet, L. Avérous, Nano-biocomposites: biodegradable polyester/nanoclay systems, *Progress in Polymer Science*, **34**, 125–55, (2009).
- (2) M. Murali Reddy, S. Vivekanandhan, M. Misra, S.K. Bhatia, A.K. Mohanty, Biobased plastics and bionanocomposites: current status and future opportunities, *Progress in Polymer Science*, **38**, 1653–89, (2013).
- (3) G. Scott, Standards for environmentally biodegradable plastics, in *Biodegradable polymers for industrial applications*, R. Smith (Ed), CRC Press LLC, Boca Raton, FL, 2000.
- (4) B. Singh, N. Sharma, Mechanistic implications of plastic degradation, *Polymer Degradation and Stability*, **93**, 561–84 (2008).
- (5) T. Ishigaki, Y. Kawagoshi, M.I.M. Fujita, Biodegradation of a polyvinyl alcohol starch blend plastic film, *World Journal of Microbiology and Biotechnology*, **15**, 321–7 (1999).
- (6) S. Matsumura, Mechanism of biodegradation, in *Biodegradable polymers for industrial applications*, R. Smith (Ed), CRC Press LLC, Boca Raton, FL, 2000.
- (7) H. Tsuji, Polyesters, 3, in *Biopolymers*, Y. Doi and A. Steinbuechel (Eds), vol. **4**, Wiley-VCH Verlag GmbH, Weinheim, 2002.
- (8) H. Tsuji, Poly(lactic acid), in *Synthesis, structures, properties, processing, and applications*, R. Auras, L.T. Lim, S.E.M. Selke, H. Tsuji (Eds), John Wiley & Sons, Inc., Hoboken, NJ, 2010.
- (9) F. von Burkert, L. Schedl, A. Goepferich, Why degradable polymers undergo surface erosion or bulk erosion, *Biomaterials*, **23**, 4221 (2002)
- (10) M. Li, M. Vert, Biodegradation of Aliphatic Polyesters in *Biodegradable polymers: principles and applications*, G. Scott and D. Gilead (Eds), Chapman & Hall, Cambridge, UK, 71–131 (1995).
- (11) G. Madras. Enzymatic degradation of polymers, in *Biodegradable polymers for industrial applications*, R. Smith (Ed), CRC Press LLC, Boca Raton, FL, 2000.
- (12) E. Jalalvandi, R.A. Majid, T. Ghanbari, H. Ilbeygi, Effects of montmorillonite (MMT) on morphological, tensile, physical barrier properties and biodegradability of polylactic acid/starch/MMT nanocomposites, *Journal of Thermoplastic Composite Materials*, **28**, 496–509 (2013).
- (13) A. Heydari, I. Alemzadeh, M. Vossoughi, Influence of glycerol and clay contents on biodegradability of corn starch nanocomposites, *International Journal of Engineering, Transactions B: Applications*, **27**, 203–14, (1994).
- (14) L. Domka, A. Malicka, K. Jagła, A. Kozak, Biodegradation of starch-modified foil in natural conditions. *Polish Journal of Environmental Studies*, **18**, 191–5 (2009).
- (15) E.M. Teixeira, D. Pasquini, A.A.S. Curvelo, E. Corradini, M.N. Belgacem, A. Dufresne, Cassava bagasse cellulose nanofibrils reinforced thermoplastic cassava starch. *Carbohydrate Polymers*, **78**, 422–31, (2009).
- (16) P. Béguin and J.P. Aubert, The biological degradation of cellulose. *FEMS Microbiology Reviews*, **13**, 25, (1994).

- (17) I. Siró and D. Plackett, Microfibrillated cellulose and new nanocomposites materials: a review, *Cellulose*, **17**, 459–94 (2010).
- (18) S. Rimdusit, S. Jingjid, S. Damrongsakkul, S. Tiptipakorn, T. Takeichi, Biodegradability and property characterizations of methyl cellulose: effect of nanocompositing and chemical crosslinking, *Carbohydrate Polymers*, **72**, 444–55 (2008).
- (19) S.R. Lee, H.M. Park, H.L. Lim, T. Kang, X. Li, W.J. Cho, Microstructure, tensile properties, and biodegradability of aliphatic polyester/clay nanocomposites, *Polymer*, **43**, 2495–500 (2002).
- (20) J.K. Francis Suh and H.W. T. Matthew, Application of chitosan-based polysaccharide biomaterials in cartilage tissue engineering: a review, *Biomaterials*, **21**, 2589–98 (2000).
- (21) P.K. Dutta, S. Tripathi, G.K. Mehrotra, J. Dutta, Perspectives for chitosan based antimicrobial films in food applications, *Food Chemistry*, **114**, 1173–82 (2009).
- (22) D. Fengwei Xie, V.P. Martino, P. Sangwan, C. Way, G.A. Cash, E. Pollet, K.M. Dean, P.J. Halley, L. Avérous, Elaboration and properties of plasticised chitosan-based exfoliated nanobiocomposites, *Polymer*, **54**, 3654–62 (2013).
- (23) T. Watanabe, K. Kimura, T. Sumiya, N. Nikaidou, K. Suzuki, M. Suzuki, M. Taiyoji, S. Ferrer, M. Regue, Genetic analysis of the chitinase system of *Serratia marcescens* 2170, *Journal of Bacteriology*, **179**, 7111–7117 (1997).
- (24) P.A. Aloise, M. Lumme, C.A. Haynes, in *Chitin Enzymology*, R.A. Muzarrelli (Ed.), N-Acetyl-D-glucosamine production from chitin-waste using chitinases from *Serratia marcescens*, Vol. 2, Atec Edizioni, Grottammare, 581–594 (1996).
- (25) M. Lorito, in *Trichoderma and Gliocladium 2*, G.E. Harman and C.P. Kubicek (Eds), Taylor and Francis, Chitinolytic Enzymes and Their Genes, London (1998).
- (26) J. Xu, S.P. McCarthy, R.A. Gross, D.L. Kaplan, Chitosan film acylation and effects on biodegradability, *Macromolecules*, **29**, 3436–40 (1996).
- (27) A. Gaurav, A. Ashamol, M.V. Deepthi, R.R. N. Ailaja, Biodegradable nanocomposites of cellulose acetate phthalate and chitosan reinforced with functionalized nanoclay: mechanical, thermal, and biodegradability studies, *Journal of Applied Polymer Science*, **125**, E16–E26 (2012).
- (28) S. Rimdusit, S. Jingjid, S. Damrongsakkul, S. Tiptipakorn, T. Takeichi, Biodegradability and property characterizations of Methyl Cellulose: Effect of nanocompositing and chemical crosslinking, *Carbohydrate Polymers*, **72**, 444–455 (2008).
- (29) T. Wu, C. Wu, Biodegradable poly(lactic acid)/chitosan-modified montmorillonite nanocomposites: Preparation and characterization, *Polymer Degradation and Stability*, **91**, 2198–2204 (2006).
- (30) R.D. Patil, P.G. Dalev, J.E. Mark, E. Vassileva, S.J. Fakirov, Biodegradation of chemically modified gelatin films in lake and river waters, *Applied Polymer Science*, **76**, 29–37 (2000).
- (31) E. Chiellini, P. Cinelli, A. Corti, E.R. Kenawy, Composite films based on waste gelatin: thermal–mechanical properties and biodegradation testing, *Polymer Degradation and Stability*, **73**, 549–55 (2001).
- (32) A. Jongjareonrak, S. Benjakul, W. Visessanguan, T. Prodpran, M. Tanaka, Characterization of edible films from skin gelatin of brown stripe red snapper and big eye snapper, *Food Hydrocolloids*, **20**, 492–501 (2006).
- (33) P. Hernández-Muñoz, A. López-Rubio, J.M. Lagarón, R. Gavara, Formaldehyde cross-linking of gliadin films: effects on mechanical and water barrier properties, *Biomacromolecules*, **5**, 415–21 (2004).
- (34) W.F. Harrington and P.H. Von Hippel, The structure of collagen and gelatin, *Advances in Protein Chemistry*, **16**, 1–138 (1961).
- (35) S. Sinha Ray and M. Bousmina, Biodegradable polymers and their layered silicate nanocomposites: in greening the 21st century materials world, *Progress in Materials Science*, **50**, 962–1079 (2005).
- (36) S. Fakirov, Z. Sarac, T. Anbar, B. Boz, I. Bahar, M. Evstatiev, A.A. Apostolov, J.E. Mark, A. Kloczkowski, Mechanical properties and transition temperature of crosslinked oriented gelatine II. Effect of orientation and water content on transition temperatures, *Colloid and Polymer Science*, **275**, 307–14 (1997).

- (37) A. Bigi, S. Panzavolta, N. Roveri, Hydroxyapatite-gelatin films: a structural and mechanical characterization, *Biomaterials*, **19**, 739–44 (1998).
- (38) J.P. Zheng, P. Li, Y. L. Ma, K.D. Yao, Gelatin/montmorillonite hybrid nanocomposite. 1. Preparation and properties, *Journal of Applied Polymer Science*, **86**, 1189–94 (2002).
- (39) J.F. Martucci, A. Vazquez, R.A. Ruseckaite, Nanocomposite based on gelatin and montmorillonite. Morphological and thermal studies, *Journal of Thermal Analysis and Calorimetry*, **89**, 117–22 (2007).
- (40) J.F. Martucci, R.A. Ruseckaite, Tensile properties, barrier properties and biodegradation in soil of compression—molded gelatin-dialdehyde starch films, *Journal of Applied Polymer Science*, **112**, 2166–78 (2009).
- (41) T.H. Goswami, M.M. Maiti, Biodegradability of gelatin–PF resin blends by soil burial method, *Polymer Degradation and Stability*, **61**, 355–9 (1998).
- (42) C. Abrusci, D. Marquina, A. Del Amo, T. Corrales, F. Catalina, A viscometric study of the biodegradation of photographic gelatin by fungi isolated from cinematographic films, *International Biodeterioration & Biodegradation*, **58**, 142–9 (2006).
- (43) A.A. Apostolov, S. Fakirov, M. Evstatiev, J. Hoffmann, K. Friederich, Biodegradable laminates based on gelatin, 1. Preparation and mechanical properties, *Macromolecular Materials and Engineering*, **287**, 693–7 (2002).
- (44) M. Boyanova, N. Stambolieva, A.A. Apostolov, S. Fakirov, Dissolution and enzymatic degradation studies before and after artificial ageing of silk or linen reinforced gelatin laminates, *Macromolecular Materials and Engineering*, **288**, 407–11 (2003).
- (45) J.F. Martucci and R.A. Ruseckaite, Biodegradation of three-layer laminate films based on gelatin under indoor soil conditions, *Polymer Degradation and Stability*, **94**, 1307–13, (2009).
- (46) H. Zhuang, J.P. Zheng, H. Gao, K. De Yao, In vitro biodegradation and biocompatibility of gelatin/montmorillonite-chitosan intercalated nanocomposites, *Journal of Materials Science: Materials in Medicine*, **18**, 951–7 (2007).
- (47) M.T. Nistor, C. Vasile, A.P. Chiriac, L. Tarțău, Biocompatibility, biodegradability, and drug carrier ability of hybrid collagen-based hydrogel nanocomposites, *Journal of Bioactive and Compatible Polymers*, **28**, 540–56 (2013).
- (48) B. Cuq, N. Gontard, S. Guilbert, Proteins as agricultural polymers for packaging production, *Cereal Chemistry*, **75**, 1–9 (1998).
- (49) H. Angellier-Coussy, V. Guillard, C. Guillaume, N. Gontard, Wheat gluten-based materials for food packaging, in *Multifunctional and nanoreinforced polymers for food packaging*, J.M. Lagaron (Ed), Woodhead Publishing Limited, Cambridge, UK (2011).
- (50) J.D. Schofield, R.C. Bottomley, M.F. Timms, M.R. Booth, The effect of heat on wheat gluten and the involvement of sulfhydryl-disulfide interchange reactions, *Journal of Cereal Science*, **1**, 241–53 (1983).
- (51) A. Redl, M. H. Morel, J. Bonicel, B. Vergnes, S. Guilbert, Extrusion of wheat gluten plasticized with glycerol: influence of process conditions on flow behavior, rheological properties, and molecular size distribution, *Cereal Chemistry*, **76**, 361–70 (1999).
- (52) H. Angellier-Coussy, S. Torres-Giner, M.H. Morel, N. Gontard, E. Gastaldi, Functional properties of thermoformed wheat gluten/montmorillonite materials with respect to formulation and processing conditions, *Journal of Applied Polymer Science*, **107**, 487–96 (2008).
- (53) S. Domenek, P. Feuilloley, J. Gratraud, M.H. Morel, S. Guilbert, Biodegradability of wheat gluten based bioplastics, *Chemosphere*, **54**, 551–9 (2004).
- (54) H. Angellier-Coussy, E. Gastaldi, N. Gontard, V. Guillard, Influence of processing temperature on the water vapour transport properties of wheat gluten based agromaterials, *Industrial Crops and Products*, **33**, 457–61 (2011).
- (55) X. Zhang, Y. Gozukara, P. Sangwan, D. Gao, S. Bateman, Biodegradation of chemically modified wheat gluten-based natural polymer materials, *Polymer Degradation and Stability*, **95**, 2309–17 (2010).

- (56) A. Chevillard, H. Angellier-Coussy, B. Cuq, V. Guillard, N. Gontard, E. Gastaldi, How the biodegradability of wheat gluten-based agromaterial can be modulated by adding nanoclays, *Polymer Degradation and Stability*, **96**, 2088–97 (2011).
- (57) Y. Doi, *Microbial polyesters*, Wiley-VCH Verlag GmbH, New York, 1990.
- (58) Y. Chun, W. Kim, Thermal properties of poly (hydroxybutyrate-co-hydroxyvalerate) and poly (ϵ -caprolactone) blends, *Polymer*, **41**, 2305–8 (2000).
- (59) M.R. Nanda, M. Misra, A.K. Mohanty, The effects of process engineering on the performance of PLA and PHBV blends, *Macromolecular Materials and Engineering*, **296**, 719–28 (2011).
- (60) M. Avella, M. Errico, Preparation of PHBV/starch blends by reactive blending and their characterization, *Journal of Applied Polymer Science*, **77**, 232–236 (2000).
- (61) S. Singh, A. Mohanty, Wood fiber reinforced bacterial bioplastic composites: fabrication and performance evaluation, *Composites Science and Technology*, **67**, 1753–63 (2007).
- (62) Y. Kanetsawa, Y. Doi, Hydrolytic degradation of microbial poly(3-hydroxybutyrate-co-3-hydroxyvalerate) fibers, *Makromolekulare Chemie, Rapid Communications*, **11**, 679–682 (1990).
- (63) M. Hakkarainen, Aliphatic Polyesters: Abiotic and Biotic Degradation and Degradation Products, in *Advances in Polymer Science*, Ann-Christine Albertsson (Ed), vol. **157**, Springer-Verlag, Berlin/Heidelberg, pp. 113–38 (2002).
- (64) S.J. Holland, A.M. Jolly, M. Yasin, B.J. Tighe, Polymers for biodegradable medical devices: II. Hydroxybutyrate-hydroxyvalerate copolymers: hydrolytic degradation studies, *Biomaterials*, **8**, 289–295 (1987).
- (65) G. Tomasi, M. Scandola, B.H. Briese, D. Jendrossek, Enzymatic Degradation of Bacterial Poly(3-hydroxybutyrate) by a Depolymerase from *Pseudomonas lemoignei*, *Macromolecules*, **29**, 507–513 (1996).
- (66) A. Spyros, R. Kimmich, B.H. Briese, D. Jendrossek, H NMR Imaging Study of Enzymatic Degradation in Poly(3-hydroxybutyrate) and Poly(3-hydroxybutyrate-co-3-hydroxyvalerate). Evidence for Preferential Degradation of the Amorphous Phase by PHB Depolymerase B from *Pseudomonas lemoignei*, *Macromolecules*, **30**, 8218–8225 (1997).
- (67) P. Maiti, C.A. Batt, E.P. Giannelis, Renewable plastics: synthesis and properties of PHB nanocomposites, *Polymeric Materials Science and Engineering*, **88**, 58–9 (2003).
- (68) S. Peterson, K. Jayaraman, D. Bhattacharyya, Forming performance and biodegradability of wood fibre-Biopol[®] composites, *Composites Part A: Applied Science*, **33**, 1123–34 (2002).
- (69) A.K. Mohanty, M.A. Khan, G. Hinrichsen, Surface modification of jute and its influence on performance of biodegradable jute-fabric/Biopol[®] composites, *Composites Science and Technology*, **60**, 1115–24 (2000).
- (70) J.L. Feijoo, L. Cabedo, E. Giménez, J.M. Lagaron, J.J. Saura, Development of amorphous PLA-montmorillonite nanocomposites, *Journal of Materials Science*, **40**, 1785–1788 (2005).
- (71) N. Kawashima, S. Ogawa, S. Obuchi, M. Matsui, T. Yagi, Polylactic acid: LACEA, in *Biopolymers 4, polyesters III*, Y. Doi and A. Steinbüchel (Eds), Wiley-VCH Verlag GmbH, Weinheim, 2002.
- (72) H. Pranamuda, Y. Tokiwa, H. Tanaka, Polylactide degradation by an *Amycolaptopsis* sp., *Applied and Environmental Microbiology*, **63**, 1637–40, (1997).
- (73) Y. Tokiwa, A. Jarerat, Biodegradation of poly(l-lactide), *Biotechnology Letters*, **26**, 771–7 (2004).
- (74) R.T. MacDonald, S.P. McCarthy, R.A. Gross, Enzymatic degradability of poly(lactide): effects of chain stereochemistry and material crystallinity, *Macromolecules*, **29**, 7356–61 (1996).
- (75) K. Nakamura, T. Tomita, N. Abe, Y. Kamio, Purification and characterization of an extracellular poly(L-lactic acid) depolymerase from a soil isolate, *Amycolaptopsis* sp strain K104-1, *Applied and Environmental Microbiology Letters*, **129**, 39–42 (2001).
- (76) K. Sakai, H. Kawano, A. Iwami, M. Nakamura, M. Moriguchi, Isolation of a thermophilic poly-L-lactide degrading bacterium from compost and its enzymatic characterization, *Journal of Bioscience and Bioengineering*, **92**, 298–300 (2001).

- (77) M. Vert, Polyglycolide and copolyesters with lactide, in *Biopolymers 4, polyesters III*, Y. Doi and A. Steinbüchel (Eds), Wiley-VCH Verlag GmbH, Weinheim, 2002.
- (78) Q. Zhou, M. Xanthos, Nanoclay and crystallinity effects on the hydrolytic degradation of polylactides, *Polymer Degradation and Stability*, **93**, 1450–1459 (2008).
- (79) B. Pukánszky, Interfaces and interphases in multicomponent materials: past, present, future, *European Polymer Journal*, **41**, 645–662 (2005).
- (80) M.A. Paul, C. Delcourt, M. Alexandre, P. Degée, F. Monteverde, P. Dubois, Polylactide/montmorillonite nanocomposites: study of the hydrolytic degradation, *Polymer Degradation and Stability*, **87**, 535 (2005).
- (81) S. Sinha Ray, M. Okamoto, Biodegradable Polylactide and Its Nanocomposites: Opening a New Dimension for Plastics and Composites, *Macromolecular Rapid Communications*, **24**, 815–840 (2003).
- (82) S. Sinha Ray, K. Yamada, M. Okamoto, A. Ogami, K. Ueda, New Polylactide/Layered Silicate Nanocomposites. 3. High-Performance Biodegradable Materials, *Chemistry of Materials*, **15**, 1456–1465 (2003).
- (83) E. Nieddu, L. Mazzucco, P. Gentile, T. Benko, V. Balbo, R. Mandrile, G. Ciardelli, Preparation and biodegradation of clay composite of PLA, *Reactive & Functional Polymers*, **69**, 371–9 (2009).
- (84) K. Fukushima, C. Abbate, D. Tabuani, M. Gennari, G. Camino, Biodegradation of poly(lactic acid) and its nanocomposites, *Polymer Degradation and Stability*, **94**, 1646–55 (2009).
- (85) K. Fukushima, D. Tabuani, M. Arena, M. Gennari, G. Camino, Effect of clay type and loading on thermal, mechanical properties and biodegradation of poly(lactic acid) nanocomposites, *Reactive and Functional Polymers*, **73**, 540–9 (2013).
- (86) K. Fukushima, D. Tabuani, M. Dottori, I. Armentano, J.M. Kenny, G. Camino, Effect of temperature and nanoparticle type on hydrolytic degradation of poly(lactic acid) nanocomposites, *Polymer Degradation and Stability*, **96**, 2120–9 (2011).
- (87) K. Fukushima, D. Tabuani, C. Abbate, M. Arena, L. Ferreri, Effect of sepiolite on the biodegradation of poly(lactic acid) and polycaprolactone, *Polymer Degradation and Stability*, **95**, 2049–56 (2010).
- (88) K. Fukushima, D. Tabuani, C. Abbate, M. Arena, P. Rizzarelli, Preparation, characterization and biodegradation of biopolymer nanocomposites based on fumed silica, *European Polymer Journal*, **47**, 139–52 (2011).
- (89) G.Q. Chen, M.K. Patel, Plastics derived from biological sources: present and future: a technical and environmental review, *Chemical Reviews*, **112**, 2082–99 (2012).
- (90) R. Ishioka, E. Katakuni, Y. Ichikawa, Aliphatic polyesters: bionolle, in *Biopolymer, 4, polyesters III, applications and commercial products*, Y. Doi and A. Steinbüchel (Eds), Wiley-VCH Verlag GmbH, Weinheim, 2002.
- (91) S. Sinha Ray, K. Okamoto, M. Okamoto, Structure–property relationship in biodegradable poly (butylene succinate)/layered silicate nanocomposites, *Macromolecules*, **36**, 2355–67 (2003).
- (92) K. Okamoto, S. Sinha Ray, M. Okamoto, New poly (butylene succinate)/layered silicate nanocomposites. 2. Effect of organically modified layered silicates on morphology, materials properties, melt rheology, and biodegradability, *Journal of Polymer Science Part B: Polymer Physics*, **41**, 3160–70 (2003).
- (93) J.W. Rhim, S.I. Hong, H.M. Park, P.K.W. Ng, Preparation and characterization of chitosan-based nanocomposite films with antimicrobial activity, *Journal of Agricultural and Food Chemistry*, **54**, 5814–22 (2006).
- (94) S.I. Hong, J.W. Rhim, Antimicrobial activity of organically modified nanoclays, *Journal for Nanoscience and Nanotechnology*, **8**, 5818–24 (2008).
- (95) Y.J. Phua, N.S. Lau, K. Sudesh, W.S. Chow, Z.A. Mohd Ishak, Biodegradability studies of poly(butylene succinate)/organo-montmorillonite nanocomposites under controlled compost soil conditions: effects of clay loading and compatibiliser, *Polymer Degradation and Stability*, **97**, 1345–54 (2012).

- (96) A. Nakayama, N. Kawasaki, Y. Maeda, I. Arvanitoyannis, S. Aiba, N. Yamamoto, Study of biodegradability of poly(δ -valerolactone-co-L-lactide)s, *Journal of Applied Polymer Science*, **66**, 741–748 (1997).
- (97) C. De Kesel, C. Vander Wauven, C. David, Biodegradation of polycaprolactone and its blends with poly(vinylalcohol) by micro-organisms from a compost of house-hold refuse, *Polymer Degradation and Stability*, **55**, 107–113 (1997).
- (98) R.W. Rees, in *Encyclopedia of polymer science and engineering*, J.E. Mark (Ed), John Wiley & Sons, Inc., New York, 1985.
- (99) M.M. Coleman, J. Zarian, Fourier-transform infrared studies of polymer blends. II. Poly(ϵ -caprolactone)–poly(vinyl chloride) system, *Journal of Polymer Science: Polymer Physics Edition*, **17**, 837–850 (1979).
- (100) E. Chiellini, A. Corti, A. Giovannini, P. Narducci, A.M. Paparella, R. Solaro, Evaluation of biodegradability of poly(ϵ -caprolactone)/poly(ethylene terephthalate) blends, *Journal of Environmental Polymer Degradation*, **4**, 37–50 (1996).
- (101) L. Tilstra, D. Johnsonbaugh, A test method to determine rapidly if polymers are biodegradable, *Journal of Environmental Polymer Degradation*, **1**, 247–255 (1993).
- (102) H. Tsuji, A. Mizuno, Y. Ikada, Blends of aliphatic polyesters. III. Biodegradation of solution-cast blends from poly(L-lactide) and poly(ϵ -caprolactone), *Journal of Applied Polymer Science*, **70**, 2259–2268 (1998).
- (103) G. Kister, G. Cassanas, M. Bergounhon, D. Hoarau, M. Vert, Structural characterization and hydrolytic degradation of solid copolymers of D,L-lactide-co- ϵ -caprolactone by Raman spectroscopy, *Polymer*, **41**, 925–932 (2000).
- (104) H. Abe, Y. Doi, Y. Kumagai, Synthesis and Characterization of Poly[(R,S)-3-hydroxybutyrate-b-6-hydroxyhexanoate] as a Compatibilizer for a Biodegradable Blend of Poly[(R)-3-hydroxybutyrate] and Poly(6-hydroxyhexanoate), *Macromolecules*, **27**, 6012–6017 (1994).
- (105) H. Abe, Y. Doi, H. Aoki, T. Akehata, Y. Hori, A. Yamaguchi, Physical Properties and Enzymic Degradability of Copolymers of (R)-3-Hydroxybutyric and 6-Hydroxyhexanoic Acids, *Macromolecules*, **28**, 7630–7637 (1995).
- (106) A.C. Albertsson, M. Gruvegård, Degradable high-molecular-weight random copolymers, based on ϵ -caprolactone and 1,5-dioxepan-2-one, with non-crystallizable units inserted in the crystalline structure, *Polymer*, **36**, 1009–1016 (1995).
- (107) A. Löfgren, A.C. Albertsson, Ph. Dubois, R. Jerome, Ph. Teyssie, Synthesis and Characterization of Biodegradable Homopolymers and Block Copolymers Based on 1,5-Dioxepan-2-one, *Macromolecules*, **27**, 5556–5562 (1994).
- (108) R.D. Fields, F. Rodriguez, R.K. Finn, Microbial degradation of polyesters: Polycaprolactone degraded by *P. pullulans*, *Journal of Applied Polymer Science*, **18**, 3571–3579 (1974).
- (109) Y. Oda, H. Asari, T. Urakami, K. Tonomura, Microbial degradation of poly(3-hydroxybutyrate) and polycaprolactone by filamentous fungi, *Journal of Fermentation and Bioengineering*, **80**, 265–269 (1995).
- (110) C.A. Murphy, J.A. Cameron, S.J. Huang, R.T. Vinopal, Fusarium polycaprolactone depolymerase is cutinase, *Applied and Environmental Microbiology*, **62**, 456–460 (1996).
- (111) C. Eldsäter, B. Erlandsson, R. Renstad, A.C. Albertsson, S. Karlsson, The biodegradation of amorphous and crystalline regions in film-blown poly(ϵ -caprolactone), *Polymer*, **41**, 1297–1304 (2000).
- (112) Z. Gan, Q. Liang, J. Zhang, X. Jing, Enzymatic degradation of poly(ϵ -caprolactone) film in phosphate buffer solution containing lipases, *Polymer Degradation and Stability*, **56**, 209–213 (1997).
- (113) V. Toncheva, A. Van Den Bulcke, E. Schacht, J. Mergaert, J. Swings, Synthesis and environmental degradation of polyesters based on poly (ϵ -caprolactone), *Journal of Environmental Polymer Degradation*, **4**, 71–83 (1996).

- (114) C.V. Benedict, J.A. Cameron, S.J. Huang, Polycaprolactone degradation by mixed and pure cultures of bacteria and a yeast, *Journal of Applied Polymer Science*, **28**, 335–42 (1983).
- (115) A.C. Albertsson, I.K. Varma, Aliphatic polyesters, in *Biopolymers 4, polyesters III*, Y. Doi and A. Steinbüchel (Eds), Wiley-VCH Verlag GmbH, Weinheim, 2002.
- (116) F. Lefebvre, C. David, C. Vander Wauven, Biodegradation of polycaprolactone by microorganisms from an industrial compost of household refuse, *Polymer Degradation and Stability*, **45**, 347–353 (1994).
- (117) J.A. Tetto, D.M. Steeves, E.A. Welsh, B.E. Powell, Biodegradable poly(ϵ -caprolactone)/clay nanocomposites, Proceedings of the Technical Conference of the Society of Plastics Engineers: “Plastics Bridging the Millenium”: ANTEC '99, Publisher: Society of Plastics Engineer, **3**, 1628–1632. New York City, May 2–6 (1999).
- (118) K. Fukushima, C. Abbate, D. Tabuani, M. Gennari, P. Rizzarelli, G. Camino, Biodegradation trend of poly(ϵ -caprolactone) and nanocomposites, *Materials Science and Engineering: C*, **30**, 566–74 (2010).
- (119) U. Witt, T. Einig, M. Yamamoto, I. Kleeberg, W.D. Deckwer, R.J. Müller, Biodegradation of aliphatic-aromatic copolyesters: evaluation of the final biodegradability and ecotoxicological impact of degradation intermediates, *Chemosphere*, **44**, 289–99 (2001).
- (120) Y. Someya, Y. Sugahara, M. Shibata, Nanocomposites based on poly(butylene adipate-co-terephthalate) and montmorillonite, *Journal of Applied Polymer Science*, **95**, 386–392 (2005).
- (121) Y. Someya, N. Kondo, M. Shibata, Biodegradation of poly(butylenes adipate-co-butylene terephthalate)/layered-silicate nanocomposites, *Journal of Applied Polymer Science*, **106**, 730, (2007).
- (122) S. Mohanty, S. Nayak, Biodegradable nanocomposites of poly(butylene adipate-co-terephthalate) (PBAT) and organically modified layered silicates, *Journal of Polymers and the Environment*, **20**, 195–207 (2012).
- (123) K. Fukushima, A. Rasyida, M.C. Yang, Characterization, degradation and biocompatibility of PBAT based nanocomposites, *Applied Clay Science*, **80–81**, 291–8, (2013).
- (124) R. Chandra, R. Rustigi, Biodegradable polymers, *Progress in Polymer Science*, **23**, 1273–335 (1998).
- (125) E. Chiellini, A. Corti, S. D'Antone, R. Solaro, Biodegradation of poly (vinyl alcohol) based materials, *Progress in Polymer Science*, **28**, 963–1014 (2003).
- (126) T. Suzuki, Y. Ichihara, M. Yamada, K. Tonomura, Some characteristics of pseudomonas O-3 which utilizes polyvinyl alcohol, *Agricultural and Biological Chemistry*, **37**, 747–56 (1973).
- (127) R. Solaro, A. Corti, E. Chiellini, Biodegradation of poly(vinyl alcohol) with different molecular weights and degree of hydrolysis, *Polymers for Advanced Technologies*, **11**, 873–8 (2000).
- (128) X. Tang, S. Alavi, Recent advances in starch, polyvinyl alcohol based polymer blends, nanocomposites and their biodegradability, *Carbohydrate Polymers*, **85**, 7–16 (2011).
- (129) I. Spiridon, M.C. Popescu, R. Bodârlău, C. Vasile, Enzymatic degradation of some nanocomposites of poly(vinyl alcohol) with starch, *Polymer Degradation and Stability*, **93**, 1884–90 (2008).
- (130) M. Taghi Taghizadeh, N. Sabouri, Study of enzymatic degradation and water absorption of nanocomposites polyvinyl alcohol/starch/carboxymethyl cellulose blends containing sodium montmorillonite clay nanoparticle by cellulase and α -amylase, *Journal of the Taiwan Institute of Chemical Engineers*, **44**, 995–1001 (2013).
- (131) M. Taghi Taghizadeh, Z. Abbasi, Z. Nasrollahzade, Study of enzymatic degradation and water absorption of nanocomposites starch/polyvinyl alcohol and sodium montmorillonite clay, *Journal of the Taiwan Institute of Chemical Engineers*, **43**, 120–4 (2012).

- (132) Z. Abbasi, Water resistance, weight loss and enzymatic degradation of blends starch/polyvinyl alcohol containing SiO₂ nanoparticle, *Journal of the Taiwan Institute of Chemical Engineers*, **43**, 264–8 (2012).
- (133) Y. Duk Kim, S. Chul Kim, Effect of chemical structure on the biodegradation of polyurethanes under composting conditions, *Polymer Degradation and Stability*, **62**, 343–52 (1998).
- (134) Y. Tokiwa, Biodegradation of polyurethanes, in *Biopolymers 9, miscellaneous biopolymers and biodegradation of polymers*, S. Matsumura and A. Steinbüchel (Eds), Wiley-VCH Verlag GmbH, Weinheim, 2003.
- (135) I. Dupret, C. David, M. Colpaert, J.M. Loitz, C. Wauven, Biodegradation of poly(ester-urethane)s by a pure strain of micro-organisms, *Macromolecular Chemistry and Physics*, **200**, 2508–18 (1999).
- (136) T. Ohshiro, M. Shinji, Y. Morita, Y. Takayama, Y. Izumi, Novel L-specific cleavage of the urethane bond of t-butoxycarbonylamino acids by whole cells of *Corynebacterium aquaticum*, *Applied Microbiology and Biotechnology*, **48**, 546–8 (1997).
- (137) A. Cheng, S. Wu, D. Jiang, F. Wu, J. Shen, Study of elastomeric polyurethane nanocomposites prepared from grafted organic-montmorillonite, *Colloid and Polymer Science*, **284**, 1057–61 (2006).
- (138) N. Salahuddin, A. Abo-El-Enein, A. Selim, O. Salah El-Dien, Synthesis and characterization of polyurethane/organo-montmorillonite nanocomposites, *Applied Clay Science*, **47**, 242–8 (2010).
- (139) M.M. Rahman, H.D. Kim, W.K. Lee, Preparation and characterization of waterborne polyurethane/clay nanocomposite: effect on water vapor permeability, *Journal of Applied Polymer Science*, **110**, 3697–705 (2008).
- (140) Y.I. Tien and K.H. Wei, High-tensile-property layered silicates/polyurethane nanocomposites by using reactive silicates as pseudo chain extenders, *Macromolecules*, **34**, 9045–52 (2001).
- (141) G. Rodrigues da Silva, A. Da Silva-Cunha, E. Ayres, R.L. Oréfice, Effect of the macromolecular architecture of biodegradable polyurethanes on the controlled delivery of ocular drugs, *Journal of Materials Science: Materials in Medicine*, **20**, 481–7 (2009).
- (142) S. Dutta, N. Karak, J.P. Saikia, B.K. Konwar, Biocompatible epoxy modified bio-based polyurethane nanocomposites: mechanical property, cytotoxicity and biodegradation, *Bioresource Technology*, **100**, 6391–7 (2009).
- (143) G. Rodrigues da Silva, A. da Silva-Cunha, F. Behar-Cohen, E. Ayres, R.L. Oréfice, Biodegradation of polyurethanes and nanocomposites to non-cytotoxic degradation products, *Polymer Degradation and Stability*, **95**, 491–9 (2010).
- (144) V. Betingytė, K. Žukienė, V. Jankauskaitė, D. Milašienė, K.V. Mickus, A. Gulbinienė, Influence of calcium carbonate fillers on the properties of recycled poly(ϵ -caprolactone) based thermoplastic polyurethane, *Materials Science (MEDŽIAGOTYRA)*, **18**(3), 243–249 (2012).

5

Functional Fibers Produced Using Electrospinning Techniques for Energy Scavenging Applications

Avinash Baji¹ and Yiu-Wing Mai²

¹Engineering Product Development (EPD) Pillar, Singapore University of Technology and Design (SUTD), Singapore

²Centre for Advanced Materials Technology (CAMT), School of Aerospace Mechanical and Mechatronic Engineering, The University of Sydney, Australia

5.1 Introduction

The interest in fabrication of functional materials such as energy harvesting materials has been fueled by the prospects of developing novel, low-powered electronic devices, sensors, actuators, and generators [1–7]. Such energy harvesting materials have the ability to detect changes in force or stress and the ability to convert ambient energy into an electrical output [1, 2, 4, 5]. By scavenging and harvesting the ambient energy, these functional materials can provide permanent power source to an electrical device [8]. Thus, periodic replacement of the electrical device and the use of batteries can be avoided. Several classes of materials and structures have been investigated in recent years, which work on various mechanisms to harvest ambient energy and convert it to other useful forms of energy [1, 7]. For example, researchers have successfully fabricated photovoltaic materials that convert solar/light energy to electrical voltage, piezoelectric materials that convert mechanical to electrical energy, and thermoelectric materials that convert temperature gradients to voltages [3, 9–13].

The most accessible and abundant energy source available is mechanical energy based on vibration or movement. It is estimated that the energy density available with random vibrations with frequency ranging from a few hundreds of hertz to a few kilohertz is between a few microwatts to a few milliwatts per cubic centimeter [14, 15]. This suggests that utilizing this form of energy and harvesting it offers tremendous potential for powering microelectronic devices. Piezoelectric materials are typically used to harvest mechanical energy as they have the ability to convert mechanical energy/vibrations into an electrical energy because of the presence of coupling between their mechanical and electrical domains [16, 17].

Recent studies have shown that the efficiency of the materials to generate voltages in response to stimuli such as light, mechanical stress, or temperature can be tailored by refining or making modifications to its chemistry, processing, or geometric configuration [2, 4, 13, 16]. Their electroactive behavior can be enhanced when they are fabricated in one-dimensional (1D) structures in the form of wires, fibers, needles, tubes, and whiskers. Compared to bulk materials, it is estimated that 1D structures can display 400–500% enhanced piezoelectric effect due to the flexoelectric effect [15]. Furthermore, owing to the large aspect ratio, huge surface area to volume ratio and small thickness of the 1D structures, a significant strain is developed in the structures when a force of few nano-Newton is applied to it [15]. Such 1D functional materials provide an opportunity toward the development of nano-/microelectronic devices and nanogenerators.

A wide range of techniques has been explored to fabricate 1D nanostructures in a reliable and reproducible way [7, 18–20]. Electrospinning has been recognized as a versatile and efficient method for processing such 1D fibrous structures. A key feature of fibers obtained using electrospinning is the orientation of structural elements within the fibers such as crystals and molecular chains [21, 22]. Reduced dimensionality afforded by nanostructured fibers in combination with the orientation of structural elements within the fibers plays a critical role in improving its properties, such as mechanical strength, stiffness, electrical, optical, and magnetic, which have led to the discovery of a new class of functional materials [22, 23]. Recent studies demonstrate that electrospinning can be used as a single-step fabrication technique to produce such piezo/ferro-electric and magnetic fibers [2–5, 13, 16, 17, 24–26]. Additionally, the fibers can be blended with other functional nanoparticles, ceramics, or nanotubes to improve its specific function for applications ranging from sensors to advanced microelectronics [27–29]. In some cases, piezoelectric fibers obtained using electrospinning have been used to develop flexible energy harvesting devices [4, 30]. Such flexible nanogenerators have found immense use for biomedical applications. These flexible nanogenerators can convert biomechanical energy generated from the human body such as breathing, heartbeat, contraction and extension of muscles, or blood flow into electrical energy. This electrical energy can then be used to provide power to devices that are implanted in the body.

More recently, the interest of researchers is centered on tailoring the properties and functions of these nanostructured materials. An intensified research effort and an in-depth understanding of the structure–property response relationship of nanostructured materials can contribute immensely to the progress of electroactive materials for novel applications.

In this chapter, the focus is on recent developments of piezoelectric fibers and multifunctional fibers using electrospinning and their adoption for fabrication of nanogenerators that can convert mechanical vibrations/force into electricity. An introduction to the fundamental concept of electrospinning and the technique for processing of functional fibers is given. In particular, electrospun piezoelectric fibers and their piezoresponse behavior are discussed. Their recent applications to develop novel devices are presented with a few selected examples.

5.2 Principle of Electrospinning

Electrospinning is one of the most efficient nanofiber fabrication techniques. It relies on the application of a strong electrostatic field to produce fibers from viscoelastic polymer solutions [22, 31–34]. Conventional electrospinning setup consists of three main components: a high-voltage power source, a spinneret or a syringe that holds the polymer solution, and a grounded collector on which the fibers are deposited. Figure 5.1a shows the schematic of the conventional electrospinning setup. Functional nanostructured fibers and fiber composites have been obtained by electrospinning different polymeric materials and inorganic materials [29, 32]. When a high voltage (typically 5 kV or higher) is applied to the organic polymer solution or an inorganic precursor solution, an electrostatic field established between the needle tip connected to the spinneret and the grounded collector forces the polymer solution out of the needle [32–34]. Surface tension of the solution acts against the electrostatic force and prevents the polymer droplet from ejecting [33, 34]. Hence, the droplet takes a conical shape, also called the Taylor cone, serving as a jet initiating surface. When a critical voltage is reached, the electrostatic forces acting on the droplet surpasses the surface tension that resists it from dripping. Thus, a jet emanates from the Taylor cone

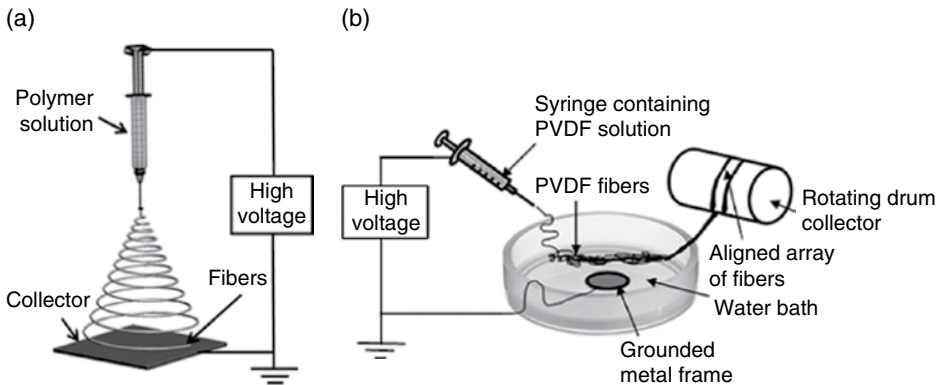


Figure 5.1 (a) Conventional electrospinning setup consisting of a high-voltage source, a syringe, and a metal-grounded collector and (b) modified electrospinning setup that is used to collect aligned fibers. The fibers are deposited on water surface and are wound up on a drum collector

and travels toward the collector [34]. During its trajectory toward the grounded collector, the jet experiences a whipping and chaotic process, elongating in length and shrinking in diameter. Also, the solvent from the traveling jet is evaporated and the polymer is deposited on the collector as nonwoven. Uniaxial stretching of the polymer jet with concomitant reduction in its diameter results in the formation of ultrafine fibers. The size of the fibers and its topography are a function of applied voltage, solution viscosity, solution conductivity, surface tension, flow rate of solution, and distance between the collector and spinneret. Consequently, the desired fiber size and morphology can be obtained by controlling the electrospinning parameters.

5.3 Fabrication of Aligned Fibers

In practice, researchers have modified the conventional electrospinning setup to collect fibers with desired features such as highly aligned fibers. The schematic of one such modified electrospinning setup is shown in Figure 5.1b. Fibers obtained using a conventional electrospinning setup is shown in Figure 5.2a. From the scanning electron microscopy (SEM) image of the fibers, it is evident that the fibers are randomly oriented. In some applications, collecting aligned array of fibers is highly useful, particularly when the fibers are intended for some functional applications. For example, Chang *et al.* [1] demonstrated in their study that the alignment of the fibers improves the energy generation efficiency of the material. Typically, fiber alignment can be obtained by improving the design of the conventional electrospinning setup. The use of rotating collectors in the form of spindle disks, wire drum, or a cylindrical drum have all shown success in controlling the alignment

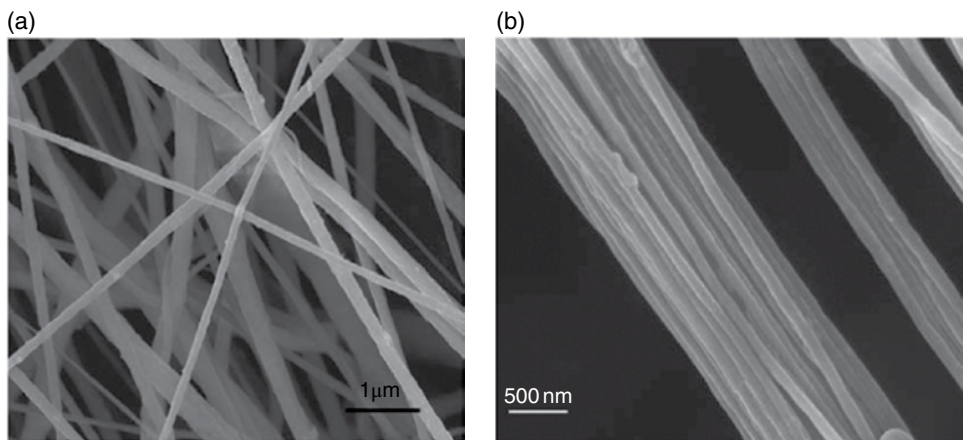


Figure 5.2 (a) SEM image of fibers obtained using conventional electrospinning setup. The fibers are randomly oriented and (b) SEM image of fibers obtained using the modified electrospinning setup. The fibers are deposited on the surface of water and are wound up on a rotational collector. This setup leads to alignment of the fibers

of the fibers during electrospinning [22]. Details of these collection techniques and the physics that leads to fiber alignment have been intensively investigated in our previous study [22]. Additionally, researchers have also looked at exploiting electric fields to obtain alignment by controlling the deposition location of the fibers [35, 36]. A simple approach to align the fibers is to use two parallel electrodes [21, 37]. The electrospun fibers are attracted by the electrodes and are deposited alternating between the left and right sides of the collectors to produce aligned array of fibers.

Recently, aligned fibers are obtained by electrospinning the fibers on the surface of water instead of the conventional stationary grounded collector [23, 38]. In this method, the fibers are directly electrospun onto the surface of water as shown in Figure 5.1b. A grounded metal plate is placed inside the water bath. The fibers are then drawn out from the surface of water using a mechanical roller. The fiber alignment is attributed to the pulling force exerted by the roller that drags the fibers on the water surface. The surface tension pulls together the fibers that are wound onto the drum collector as aligned array of fibers. Figure 5.2b shows representative SEM images of fibers collected using this method, and they have a good degree of macroscopic orientation.

5.4 Fabrication of Ferro/Piezoelectric Organic Fibers

Polyvinylidene fluoride (PVDF) is often used as polymeric piezoelectric material due to its polar crystalline nature [39–44]. The chain configurations in PVDF of trans (*T*) and gauche (*G*) linkages are capable of taking five different crystalline structural forms. Of these forms, the chain configurations of all trans (*TTTT*, β -crystalline structure) and alternate trans gauche (*TG⁺TG⁻*, α -crystalline structure) are most common in PVDF [44–46]. The schematic of the β -crystalline and α -crystalline phases is shown in Figure 5.3.

Typically, the α -phase is nonpolar and the most stable crystalline form, while the β -phase is the most polar crystalline form. The orientation of the CH₂ and CF₂ unit cells evident in Figure 5.3 makes the β -crystalline structure the most polar. However, it is difficult to obtain PVDF free of α -phase and consisting of pure β -phase only. This is attributed to the unique structural arrangement. In case of all trans (*TTTT*) PVDF, fluorine atom has a diameter of 0.270 nm, which is larger than the space of 0.256 nm provided by the carbon chain [47]. Hence, fluorine atoms often overlap with neighboring fluorine atoms. This overlap can be minimized by tilting and rotating neighboring CF₂ groups in the opposite direction. Deflection of the groups relative to their original configuration yields the nonpolar *TG⁺TG⁻*-configuration (α -phase) [47]. This indicates that under normal circumstances, it is easier to obtain PVDF consisting of mainly α -crystals rather than β -crystals. Further, the high crystal lattice energy associated with the β -crystal phase prohibits formation of direct β -phase from the melt [48]. Thus, a typical approach to obtain the β -crystalline phase is by crystal phase transition from the nonpolar (*TG⁺TG⁻*) α -phase.

One approach to transform α -phase of PVDF to β -crystalline phase is by poling the material [45]. Poling consists of electrical poling and mechanical stretching the material at ambient temperature. This process reduces the α -phase content and at the same time

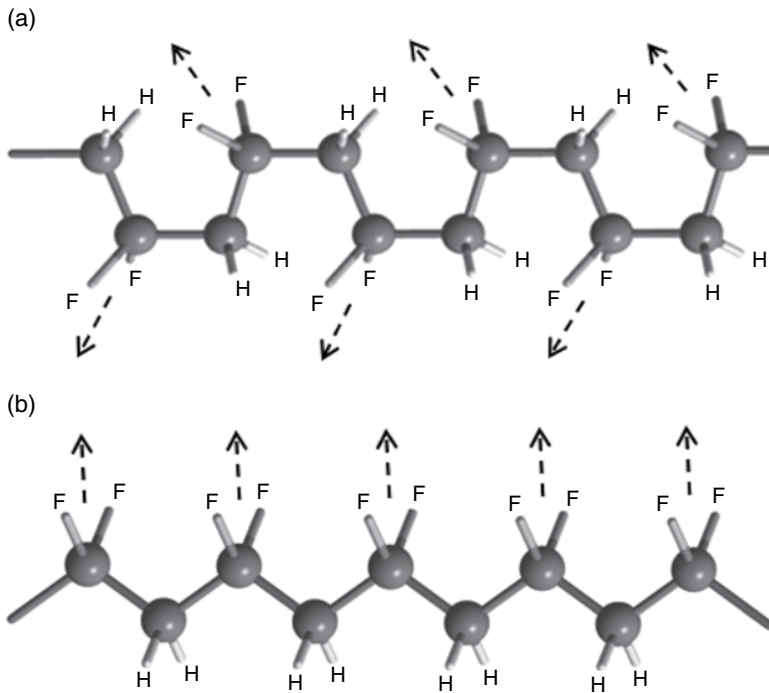


Figure 5.3 Crystal structure of PVDF: (a) α -Phase (alternate trans gauche). The dipoles in this phase point in the opposite direction, and hence the net dipole is zero. (b) β -Phase (all-trans phase). In this crystal phase, the dipoles are oriented and hence this crystalline phase is highly polar

increases the β -phase content within the PVDF. Mechanically stretching PVDF forces the molecular chains to assume the configuration of an extended chain structure. Such extended chain configuration is associated with β -crystals that have all the dipole moments aligned [47, 48]. Similarly, poling the material under a strong electric field orientates the polar axis of the crystallites along the electric field direction. This is known to promote higher spontaneous polarization for the all-trans β -crystals.

More recently, electrospinning has been recognized as an ideal processing technique to promote piezoelectricity within PVDF since PVDF fibers fabricated using electrospinning undergo electrical poling and mechanical stretching in a single step [16, 23]. The extensional forces imparted to produce fibers also stretch the molecular chains and align them along the fiber axis. During this process, the α -crystals of PVDF can be converted to the extended chain configuration (β -crystalline phase). This is attributed to the use of high electrostatic fields during the fiber formation stage as well as thinning and stretching of the polymer jet to obtain PVDF fibers. Furthermore, the use of electric field and mechanical stretching on the polymer jet during electrospinning arranges and aligns the molecular

chains within the fibrous matrix. This also results in the orientation and alignment of the dipoles within the fibers. Electrospun PVDF fibers with tunable piezoelectric and electro-mechanical coupling show tremendous potential for the development of sensors, actuators, and energy generators.

5.5 Fabrication of Ferro/Piezoelectric Inorganic Fibers

Typically, organic polymer fibers are obtained using a single-step electrospinning approach. Studies have successfully used electrospinning to fabricate fibers composed of purely ceramic, metals, or purely carbon phase [9, 17, 49, 50]. Such 1D fibrous structures are expected to display specific properties such as electrical conductivity, piezo/ferroelectricity, ferromagnetic, photocatalytic, photovoltaic, electronic, and photonic properties [13, 51–53]. In this chapter, we focus on fibers that display ferro/piezoelectric and ferromagnetic behaviors and are useful for the fabrication of nanogenerators and energy harvesters. Typically, inorganic fibers like carbon fibers and ceramic fibers are obtained by combining electrospinning with sol–gel process or by utilizing a polymer-based precursor method [49, 50, 54]. These fabrication methods are considered as a two-step approach. The first step involves the preparation of sol–gel precursor solution. The sol solution is then blended with a polymer solution to increase its viscosity for electro-spinning. Once the solutions are mixed, the conventional electrospinning technique is used to obtain fibers consisting of uniformly dispersed precursor materials. In the second step, the fibers are thermally treated in a furnace at an appropriate temperature to remove the polymer and convert the fibers into ceramic fibers.

Using this approach, we successfully fabricated bismuth ferrite (BiFeO_3) and barium titanate (BaTiO_3) fibers. In the case of BiFeO_3 fibers, precursor sol–gel is prepared by adding $\text{Bi}(\text{NO}_3)_3 \cdot 5\text{H}_2\text{O}$ and $\text{Fe}(\text{NO}_3)_3 \cdot 9\text{H}_2\text{O}$ to a solution mixture of 2-methoxyethanol and glacial acetic acid. Then, polyvinylpyrrolidone (PVP) is introduced to a dimethylformamide/ethanol solution mixture. The two solutions are blended together and electrospun to obtain PVP fibers with homogeneously dispersed precursor material. In the subsequent step, the polymer is removed by thermally treating the fibers in a furnace at a suitable temperature and length of time. Thermal treatment results in the formation of fine grained BiFeO_3 structures that yield a fibrous geometry. Figure 5.4a and b shows the SEM and transmission electron microscopy (TEM) images of the as-prepared fibers. The fibers have an average diameter of 170 ± 50 nm and tens of microns in length. A similar approach is used for the fabrication of BaTiO_3 fibers. In this case, the precursor sol–gel for fabrication of BaTiO_3 fibers is obtained by dissolving barium acetate in a solution mixture of titanium isopropoxide and glacial acetic acid. Electrospinning the sol–gel solution blended with the PVP solution followed by thermal annealing yield BaTiO_3 fibers. Figure 5.4c and d shows the SEM and TEM images of the BaTiO_3 fibers obtained. This approach of combining electrospinning with sol–gel techniques has proven a successful method to fabricate various ceramic fibers including zinc oxide, titanium dioxide, etc.

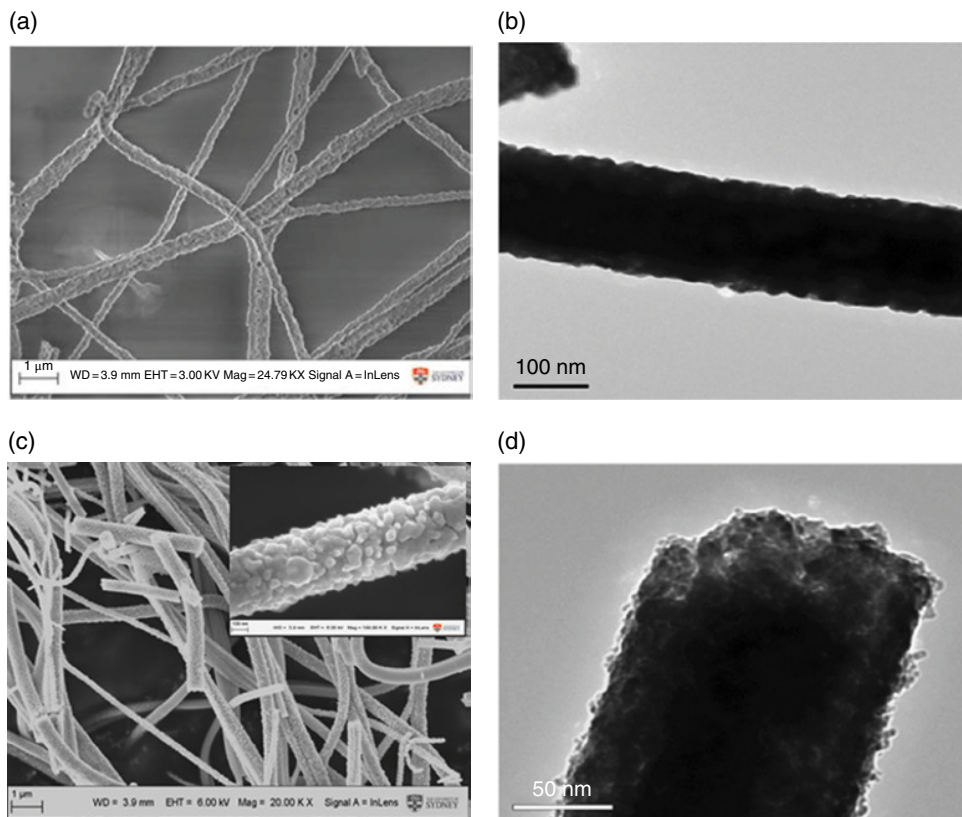


Figure 5.4 (a) SEM image of bismuth ferrite (BiFeO_3) fibers; (b) transmission electron microscopy (TEM) image of BiFeO_3 fiber; (c) SEM image of barium titanate (BaTiO_3) fibers. The inset shows the magnified image of the fibers; and (d) TEM image of BaTiO_3 fiber

5.6 Fabrication of Fibers Filled with Reinforcements

An area of electrospinning which is expanding at a rapid rate is fabrication of polymer fibers filled with nano-reinforcements [55–57]. Electrospinning can be used as a single-step processing technique to obtain reinforced fibers by suspending the nano-reinforcements into the polymer solution prior to electrospinning. Filler inclusion within the fibers is typically obtained by dispersing the fillers directly into the polymer solution prior to the electro-spinning process. Fibers with uniformly dispersed fillers often lead to improvements in their performance due to the unique properties associated with nanoscale features of the fillers.

Some recent studies have shown that the inclusion of nanofillers improves the piezoelectricity of PVDF fibers [28, 47]. The nanofillers within the fiber cause the surrounding PVDF matrix to swell; and swelling of matrix increases its radius of gyration (R_g) [57].

This gives the conformation changes within the PVDF fiber and results in the formation of extended chains that are associated with the electroactivity in the region surrounding the nanofillers [17, 57]. Numerous studies report that polar electroactive β -crystals within PVDF can be enhanced by blending it with external nucleating agents [28]. Consequently, blending PVDF fibers with nanofillers can give rise to novel piezoelectric PVDF fibrous composites that display improved performance and combination of desirable material behavior that cannot be obtained in neat PVDF. Wide varieties of reinforcements are used to not only improve piezoelectricity of PVDF but also increase its mechanical properties, such as strength and stiffness. An interesting case is PVDF composites filled with functional fillers, such as magnetic nanoparticles or carbon nanotubes (CNTs). For example, dispersing magnetic particles such as magnetite, cobalt, iron, or metal oxides within the matrix influences the magnetic properties of the PVDF fibers [57]. Figure 5.5a shows the TEM images of ferroelectric PVDF fibers filled with magnetite nanoparticles. Such composite fibers have tremendous potential in biomedical, electronic, and multiferroic applications.

Besides metal particles, CNTs are commonly used to reinforce electrospun fibrous matrices since they improve mechanical properties, ferroelectricity, and electrical conductivity of the fibers [27, 28, 48, 55]. We and other researchers have conducted extensive work on CNT reinforced electrospun fibers [28, 47, 55]. Typically, the surfaces of CNTs are functionalized with carboxylic acid groups to facilitate uniform dispersion in the polymer solution. Electrospinning this polymer solution with well dispersed CNTs lead to polymer fibers with CNTs embedded within the fiber matrix and aligned along the fiber axis. Figure 5.5b shows a TEM image of CNT-reinforced fiber illustrating that CNTs are embedded and mostly aligned along the fiber-axis direction. The alignment of the CNTs

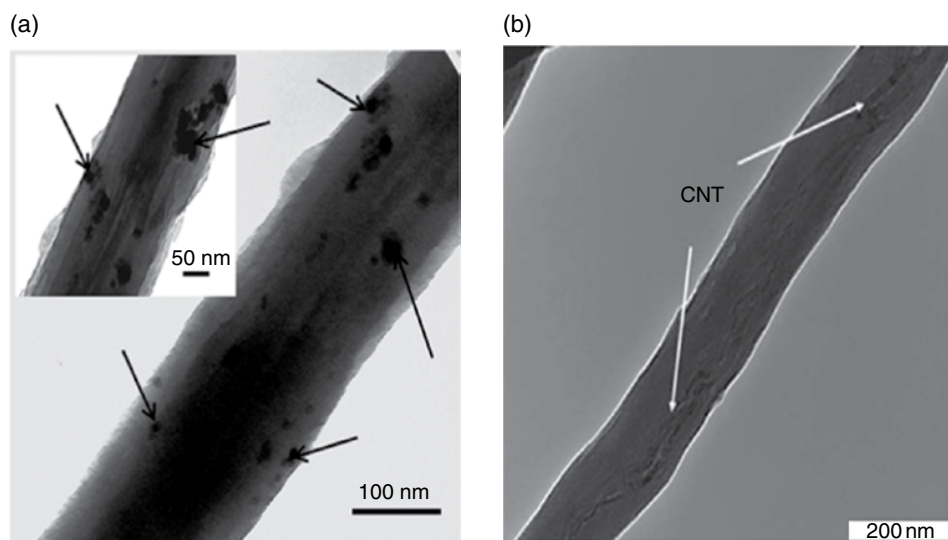


Figure 5.5 (a) TEM image of PVDF fibers reinforced with magnetite nanoparticles. The inset shows the magnified image of the fiber. (b) TEM image of PVDF fiber reinforced with CNT

within the fibers is attributed to the large extensional forces exerted on the polymer jet during electrospinning. The CNTs provide higher surface area for the all-trans (*TTTT*) chains of PVDF to be easily adsorbed when compared to the trans-gauche-trans-gauche (*TG⁺TG⁻*) chains. These all-trans chains of PVDF form the electroactive β -crystalline phase during crystallization, which shows the effect of CNTs on β -phase transformation. This has motivated recent studies to employ magnetic nanoparticles or CNTs as an effective method for nucleation of the β -crystallization phase (electroactive phase) within the PVDF matrix. The use of nanofillers in combination with electrospinning can thus be highly useful to induce the formation of ferroelectric crystals within the fibers.

5.7 Characterization of Ferro/Piezoelectric Behavior of Electrospun Fibers

In recent years, piezoresponse force microscopy (PFM) has been increasingly used to characterize the piezoelectric response of electrospun fibers [13, 16, 17, 25, 26, 58, 59] due to its ability to obtain ferroelectric images of the samples, high resolution, and its insensitivity to sample topography [60–62]. Researchers have successfully used PFM and demonstrated its application for obtaining domain structures of samples, selective poling on ferro/piezoelectric samples, and piezoresponse of samples by hysteresis measurements on localized regions [61, 62]. PFM is particularly useful as it allows local piezoelectric measurements and enables the evaluation of the piezoelectric response of a single fiber [63]. The principle of PFM is based on the detection of surface deformations in the sample that are induced by applied voltages. The local hysteresis loops measured for the fiber gives the piezoelectric response of small ferroelectric domains present in the localized region of the fiber. Information such as coercive voltage, forward and reverse saturation, and remnant response of the fiber can be obtained.

Like an atomic force microscope (AFM) setup, measurements using PFM require the fibers to be deposited on a substrate. Here, a silicon wafer substrate is used and is coated with a thin platinum layer, which acts as one of the electrodes. Following this, a conductive tip that serves as a second electrode is brought into contact with the deposited fiber and a bias voltage is applied such that the localized region on the fiber experiences dimensional changes. When the tip is in contact with the fiber surface and the dipoles in the localized region are parallel to the PFM voltage direction, the deformation in the fiber owing to the piezoelectric behavior is considered as an “in-phase” response. By contrast, when the dipoles in the localized region are in the opposite direction to that of the bias voltage, the “out-of-phase” response is recorded as shifting of the phase by 180° [1]. Hence, sample regions that have c^- domains with their polarization vector oriented downward and normal to the surface will expand when a positive bias voltage is applied. Similarly, sample regions with c^+ domains with their polarization vector oriented upward and normal to surface will contract when a positive bias voltage is applied. The surface oscillations are out of phase with the tip voltage ($\varphi = 180^\circ$) for c^+ domains and their response is opposite to that of the c^- domains. Thus, the phase angle (φ) of the electroelastic response of the sample surface provides information of the polarization direction in the domains under the PFM tip.

However, the measured piezoresponse amplitude provides information on the electromechanical activity of the localized region underneath the PFM tip.

5.8 Piezoresponse of Electrospun Fibers

Fibers that display good piezoresponse show tremendous potential for use in sensing devices and transducers including strain and pressure sensors. In our previous studies, we obtained the voltage-induced deformation of PVDF fiber and PVDF fiber reinforced with barium titanate (BaTiO_3) using PFM and demonstrated that both set of fibers display good piezoelectric and ferroelectric properties [16, 17]. Fibers with BaTiO_3 have a larger diameter than neat PVDF fibers, and a meaningful comparison of their piezoresponse cannot be made. Figure 5.6a shows an AFM image of neat PVDF fiber deposited on

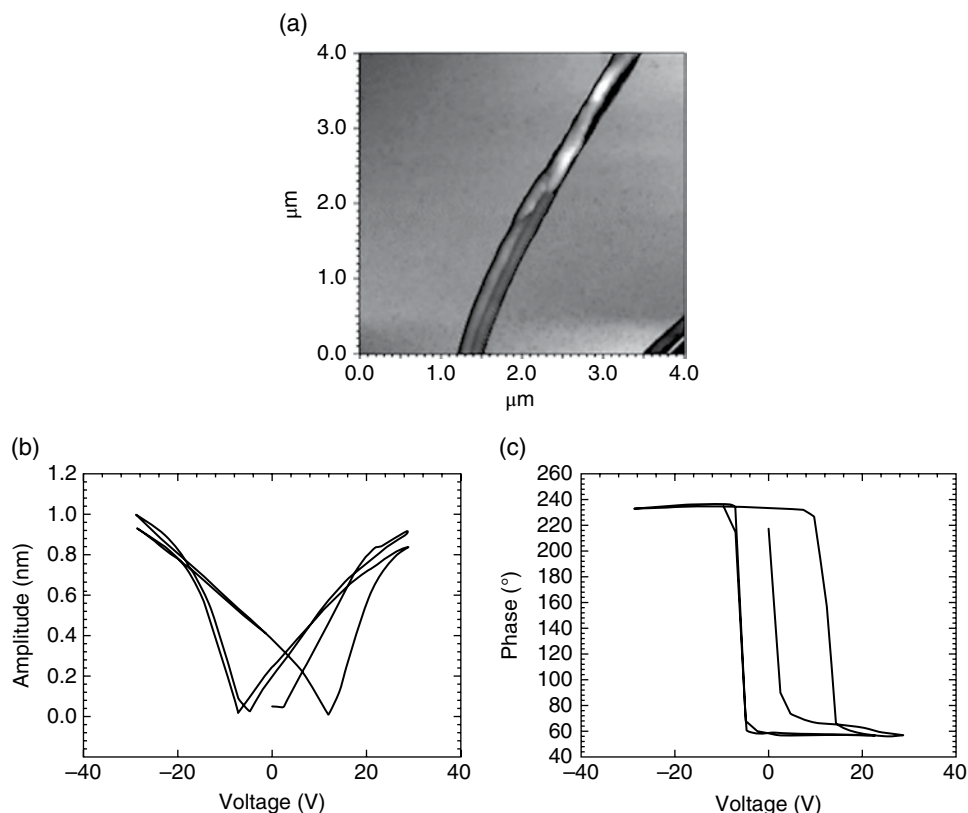


Figure 5.6 (a) Atomic force microscopy (AFM) image of neat PVDF fiber, (b) PFM amplitude–voltage hysteresis loops recorded for neat PVDF fiber, and (c) PFM phase–voltage hysteresis loops recorded for neat PVDF fiber

the Pt-coated silicon wafer substrate. Their corresponding PFM amplitude and PFM phase versus voltage plots are also shown in Figure 5.6a and b, respectively.

For the PVDF/BaTiO₃ fibers, the PFM amplitude and phase images are recorded and shown in Figure 5.7a and b. These images are useful to estimate the piezoresponse of the fiber. They are also helpful in determining the domain structures and local polarization within the PVDF/BaTiO₃ fiber. The high-voltage PFM amplitude image (see Figure 5.7a) obtained for the composite fiber gives an estimate of the deformations induced in the sample. On the other hand, the high-voltage PFM images (see Figure 5.7b) obtained for the composite fiber show clear ferroelectric domains. The phase image in Figure 5.7b shows dark and bright contrast. Using this phase image, we determine that the dark regions of the fibers (see Figure 5.7b) have polarization vector within the sample pointing upward, while the center brighter region has the polarization vector pointing downward. In our study, bright regions in the center of the fiber are attributed to the presence of BaTiO₃ phase in the core region of the fiber. It is known that BaTiO₃ has piezoelectric coefficients that have opposite signs compared to PVDF. This explains why the center region of the fiber is brighter compared to the rest of the fiber in the phase image. Piezoreponse of the sample, that is, amplitude versus voltage and phase versus voltage loops (see Figure 5.7c and d) are conducted to determine the ferroelectric switching and piezoelectric electromechanical behavior of the PVDF/BaTiO₃ fibers.

In samples (neat PVDF and PVDF/BaTiO₃), the amplitude and phase as a function of voltage are measured immediately after the application of poling pulse. The amplitude versus voltage hysteresis recorded for both set of samples is an indication of deformation induced by electrical voltage. This measured amplitude is proportional to d_{33} and shows the piezoelectric behavior of the fiber samples. Neat PVDF fibers show characteristic “butterfly” hysteresis, which is associated with ferro/piezoelectric materials (see Figure 5.6b). For the PVDF/BaTiO₃ composite fiber, PFM amplitude versus strain shows an asymmetric hysteresis loops (see Figure 5.7c). We attribute this to the difference in strain behavior associated with PVDF and BaTiO₃ phases. Such asymmetric loops have been obtained for ceramic phases such as BaTiO₃ when the applied voltage is not high enough to align all their dipoles. Therefore, we presume in our study that not all dipoles present in the domains of the BaTiO₃ phase are aligned, and hence they do not form one single domain. Nonetheless, the results successfully show the voltage-induced strain behavior of the fibers. It should be pointed out that the amplitude and phase hysteresis loops are recorded for an un-poled fiber. Despite this, the results demonstrate that maximum amplitudes of 1 nm and ~0.22 nm can be obtained for PVDF fiber and PVDF/BaTiO₃, respectively, with a ~30V bias voltage. Similarly, the phase recorded for both neat and composite fibers shows the polarization direction of the dipoles. It is clear that from the phase versus voltage loops recorded for both fibers (see Figures 5.6c and 5.7d), a classic symmetric square-shape loop is obtained. Such symmetric loops that display a 180° domain switching feature when the electric field is reversed demonstrates the presence of in-plane switchable ferroelectric polarization.

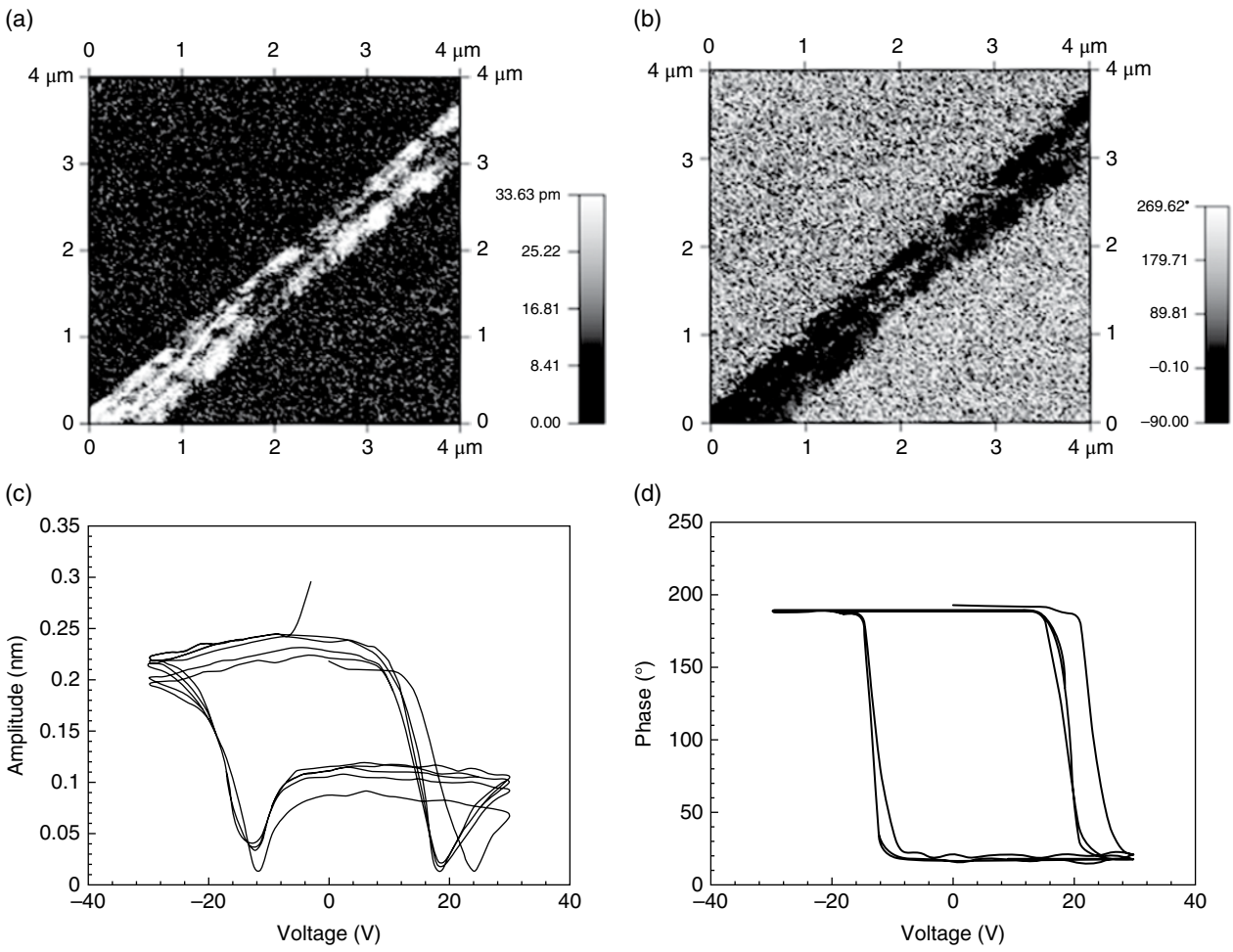


Figure 5.7 (a) PFM amplitude image recorded for PVDF fiber reinforced with BaTiO₃, (b) PFM phase image of the composite fiber, (c) PFM amplitude-voltage hysteresis loops, and (d) PFM phase-voltage hysteresis loops recorded for PVDF fiber reinforced with BaTiO₃

5.9 Nanogenerators Based on Electrospun Fibers

The piezoelectric behavior of PVDF fibers has been exploited for their use as nanogenerators. Chang *et al.* [3] fabricated nanogenerators using electrospun PVDF fibers to convert mechanical energy to electricity with high efficiency. In their study, a single PVDF fiber is deposited across two adjacent electrodes that are placed 100–600 μm apart. These electrodes are placed on top of a flexible plastic substrate (see Figure 5.8). They argue that the dipoles within the fibers are aligned along the fiber axis due to the strong electric field and the stretching forces exerted on the PVDF fibers during electrospinning. A schematic for this process is shown in Figure 5.8. The stretching of the PVDF polymer jet during electrospinning also converts the nonpolar α -crystals consisting of randomly oriented dipoles into polar β -crystalline phase. Due to the presence of the β -crystals, the fiber demonstrates piezoelectricity; and hence when an axial stress is applied by bending the substrate, an electric potential is generated.

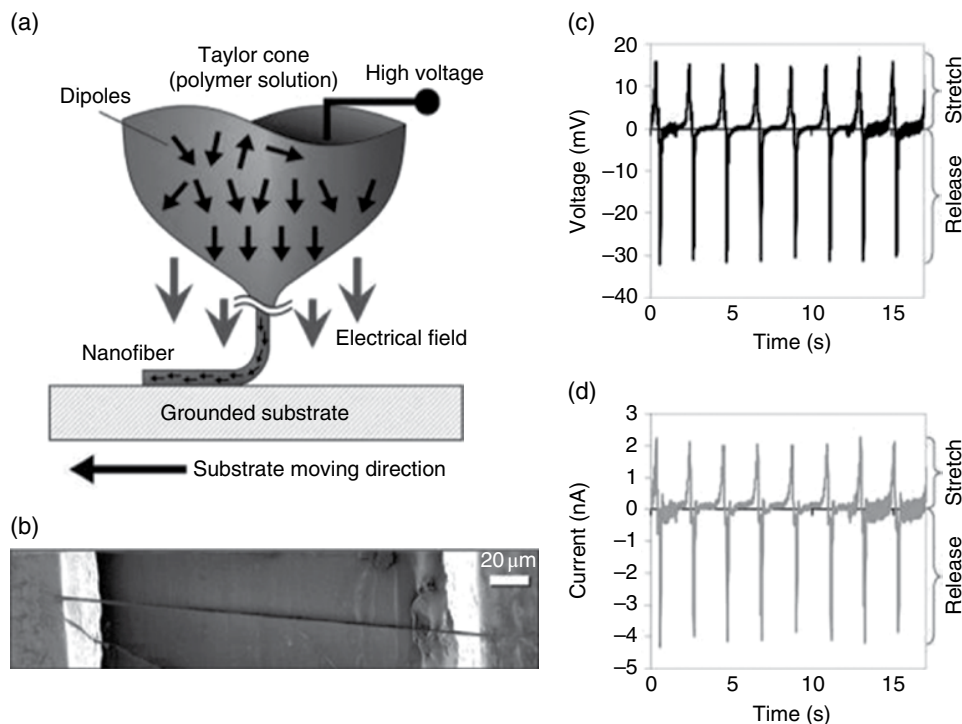


Figure 5.8 (a) Schematic showing application of electrostatic voltage which acts as in situ electrical poling during the electrospinning process that helps align the dipoles within PVDF fibers. (b) SEM image of a single PVDF fiber deposited on top of two electrodes; the electrodes are placed onto of a flexible plastic substrate. (c) Output voltage measured as a function of time. (d) Output current measured as a function of time. Chang *et al.* [3]. Reproduced with permission of American Chemical Society

Figure 5.8 also shows the voltage and current generated using a single PVDF fiber as a nanogenerator. Current and voltage output are obtained by repeatedly stretching and releasing the substrate. The nanogenerator based on a single PVDF fiber generated a voltage of 5–30 mV and a current of 0.5–3 nA. In this case, the piezoelectric constant of the PVDF fiber is negative. This indicates that when the fiber is mechanically stretched along the poling axis, it generates a voltage with polarity in the opposite direction. Chang *et al.* [3] explain that stretching the fiber induces polarization within the fiber, which results in potential difference at the two ends of the nanogenerator. The potential difference is caused by the piezoelectric charges induced within the fiber during the stretching process. The charges present outside the fiber, referred to as “free charges,” flow into the fiber to neutralize the potential generated within the fiber. When the strain in the fiber is maintained, a steady state is reached because the free charges balance the generated charges within the fiber. Thus, the potential reduces to zero. When the fiber is allowed to relax, that is, the mechanical strain is released, the free charges at the ends of the fiber generate an opposite potential. This causes the free charges to gradually flow out in opposite direction and decrease the current to zero. The results demonstrate the potential of using PVDF fibers for converting mechanical energy to electric energy [3]. Naturally, the electrical output can be greatly enhanced with multiple nanofibers deposited in parallel.

5.10 Energy Harvesters Based on Electrospun Fibers

In a similar study, Fang *et al.* [64] showed that non-woven PVDF fibers obtained using electrospinning can also be used for energy harvesting applications. They used needle-less electrospinning to produce fibers in large scale. They demonstrated that the obtained fibers are capable of converting mechanical energy to electrical energy and can be used as a power-generating device [64]. To this end, the non-woven fiber mat is sandwiched between two aluminum foils. Following this step, two flexible plastic sheets with gold coating on their inside surface are placed on the aluminum foils such that the gold coating is in contact with aluminum. In this device, the gold coating serves as electrodes while the flexible plastic film is used as a protective layer. Fang *et al.* [64] illustrated that when this device is subjected to repeated compressive loads, it displays voltage and current output. Each compressive load on the device generated two signals of opposite polarity. One signal is obtained when the fibers are mechanical deformed and the other signal when the deformation in the fibers is recovered. A compressive force of 10 N on the device generates a voltage between 1 and 2.6 V and current output between 1.4 and 4.5 μA . In comparison, bulk commercial PVDF disk specimen displays a maximum voltage of 0.28 V and current output of 0.56 μA [64]. Their results verified the ability of PVDF fibers to convert mechanical energy to electrical energy. The excellent power generation capability of the electrospun PVDF fibers is attributed to the high β -crystalline phase content within the fibers which is ~88%.

5.11 Force/Pressure Sensors

Piezoelectricity in PVDF fibers is acquired during the electrospinning process. The results presented in the previous sections demonstrate the feasibility of using these fibers as energy harvesters and nanogenerators. However, to use electrospun PVDF fibers as sensors and actuators, their piezoelectric properties should be further improved so as to increase their sensitivity. Sensors made from PVDF bulk film have been previously used to detect pressure, test, and characterize fabrics, and monitor human health [65]. However, only limited success has been achieved since the PVDF films must be poled electrically and treated mechanically. Wang *et al.* [65, 66] used electrospinning to obtain PVDF non-woven and fabricate force sensors. The amount of electroactive crystalline phase within the fibers is controlled by adjusting the voltage and flow rate during electrospinning. For example, applied voltage of 12 kV and flow rate of 0.01 ml/min produced PVDF fibers with the highest concentration of β -crystals. The fibers are then used to fabricate force sensor devices. As shown in Figure 5.9a, PVDF non-woven is sandwiched between a flexible electrode and rigid electrode.

The flexible electrode consists of a plastic film that is coated with indium tin oxide (ITO). Similarly, the rigid electrode is obtained by using a small piece of ITO-coated glass. The sensitivity of the fabricated sensors based on PVDF fibers is determined by exerting a force on the surface of the electrodes. The load applied on the sensor is between 0.04 and 0.05 N. Figure 5.9b (top) shows the applied signal in terms of voltage that is equivalent to the applied load. In this case, a load cell is brought in contact with the upper surface

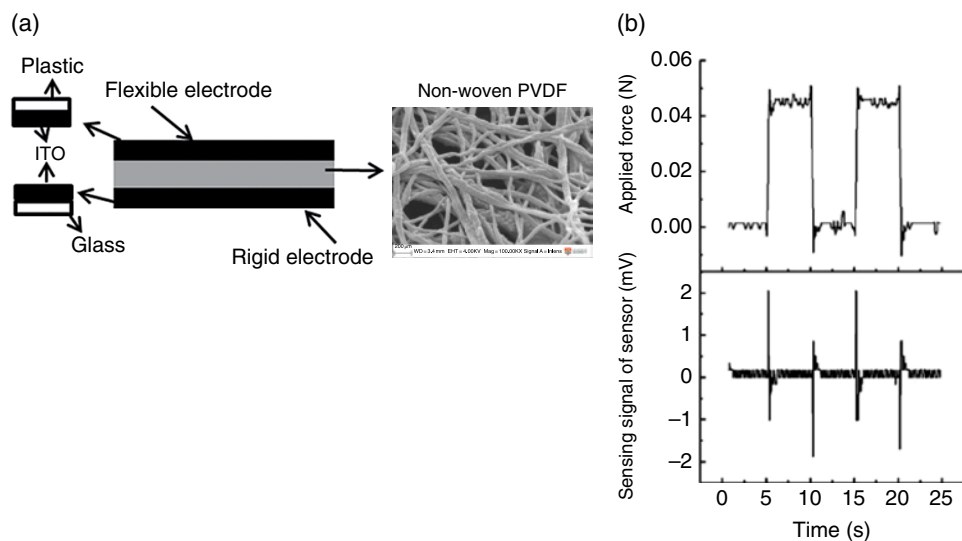


Figure 5.9 (a) Schematic showing the fabrication of a force sensor based on electrospun PVDF fibers and (b) response recorded for the sensor based on PVDF fibers in terms of voltage. Ren *et al.* [66]. Reproduced with permission of John Wiley & Sons

of the sensor and a load is applied. The peak applied load is held for a few seconds and the load cell is retracted back. The corresponding electrical signals generated by the sensor are also shown in Figure 5.9b (bottom). As expected, two peaks are seen in the response signal generated by the sensors. One peak corresponds to the applied force on the sensor by the load cell, while the other peak represents the releasing force. The sensors display good repeatability and dynamic sensitivity [65]. The highest output and sensitivity come from sensors which are fabricated using PVDF fibers with the highest electroactive phase. Hence, these results show tremendous potential of using electrospun PVDF fibers for designing flexible force sensors.

5.12 Multifunctional Inorganic Fibers

Fabrication of inorganic fibers, metal oxide, or fibers composed of purely ceramic phase is an area in electrospinning that has gained tremendous interest [13, 17, 50, 54, 63]. The nanometer-sized 1D structure of the inorganic fibers obtained using electrospinning have the potential to improve different functional properties, for example, magnetic, piezo/ferroelectric, electroluminescence, and photovoltaic [10, 13]. Recently, several studies reported fabrications of nanofibers and/or nanowires composed of zinc oxide, barium titanate, bismuth ferrite, lead zirconate titanate, cadmium sulfide, and gallium nitride and demonstrated that these nanostructures display enhanced piezoelectric properties compared to their bulk counterparts [13, 59, 63]. These 1D nanostructured fibers show great potential for use as nanogenerators that effectively convert low-frequency mechanical energy into electrical energy [59]. Recent breakthrough of piezoelectric fabrics for converting mechanical energy into electric energy using nanofiber-based nanogenerators has opened up possibilities to harvest biomechanical energy created by normal physical motion, such as breathing and walking [5].

In recent work, we demonstrated that electrospinning can be used to fabricate ceramic fibers, such as BiFeO_3 fibers, which display multiferroic properties [13]. For example, the ferro/piezoelectric behaviors of BiFeO_3 (see Figure 5.10) fibers are examined using PFM to reveal their amplitude and phase images. The amplitude image in Figure 5.10a shows the deformation in the sample due to the application of voltage. It provides information on the magnitude of piezoresponse. It is also evident from the phase image in Figure 5.10b that ferroelectric domains exist within the fibers and the direction of the polarization domains is revealed. The voltage-induced deformation is characterized by the amplitude versus voltage hysteresis loops recorded for the fiber shown in Figure 5.10c. The polar domain switching behavior is exhibited in the phase versus voltage hysteresis loops in Figure 5.10d, which support the ferroelectric and piezoelectric behavior of the fibers.

Further, we also characterized their magnetization versus magnetic field behavior. As evident in Figure 5.11, the obtained BiFeO_3 fibers display clear magnetic hysteresis loops; bulk BiFeO_3 does not. Bulk BiFeO_3 is associated with a linear magnetization versus magnetic field (M vs. H) relationship. The linear M versus H relationship is attributed to the weak magnetization and inhomogeneity seen in bulk BiFeO_3 s yielding a leakage current.

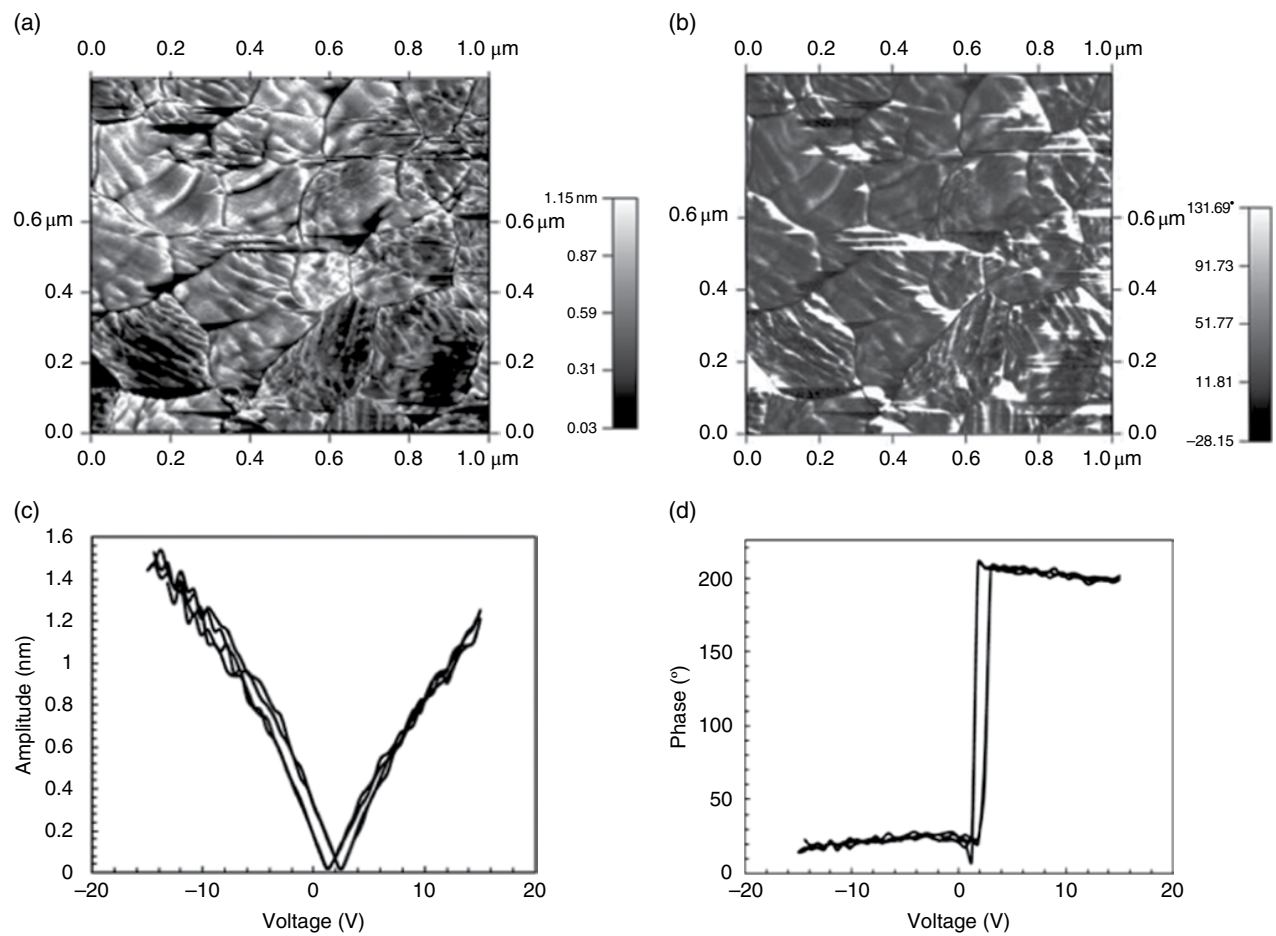


Figure 5.10 (a) PFM amplitude image recorded for BiFeO_3 fiber, (b) PFM phase image of the BiFeO_3 fiber, (c) PFM amplitude–voltage hysteresis loops, and (d) PFM phase–voltage hysteresis loops recorded for BiFeO_3 fiber

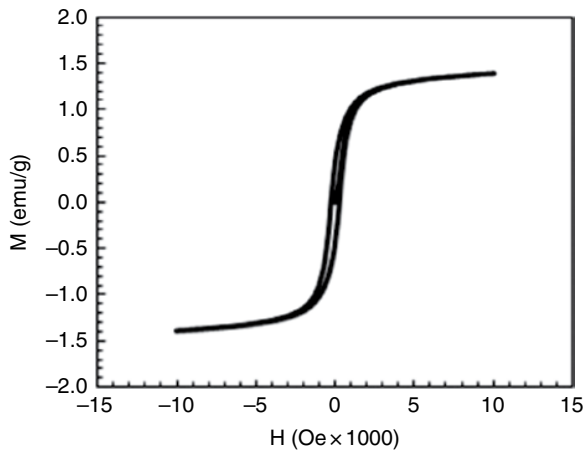


Figure 5.11 Magnetization versus magnetic field hysteresis loops recorded for BiFeO_3 fiber

On the other hand, in our study, we show that electrospun fibers with nanometer-sized particles of BiFeO_3 (see Figure 5.11) have good saturation magnetization. The hysteresis obtained in our fibers is attributed to the size of the BiFeO_3 particles which is ~ 30 nm. This is smaller than the periodicity of helical ordering, which is 62 nm. Hence, the nanoparticles suppress the modulated spin structure, resulting in enhanced magnetization. Figure 5.11 shows the magnetization (M) versus magnetic field (H) hysteresis loops of these fibers. Nonlinear hysteresis behavior is clearly seen in the M versus H loops for the fibers. The coercivity and saturation magnetization of BiFeO_3 fibers is determined from these hysteresis loops to be ~ 250 Oe and ~ 1.5 emu/g, respectively. Such fibers that display ferro/piezoelectric and ferromagnetic characteristics are excellent materials for the fabrication of novel sensors, nanogenerators, actuators, memory storage devices, etc.

Wu *et al.* [59] fabricated lead zirconate titanate nanofibers using electrospinning as wearable nanogenerators. For this purpose, the aligned array of PZT fibers is deposited on flexible polyethylene terephthalate (PET) film that is spin-coated with a poly(dimethylsiloxane) (PDMS) layer. Using a glass slide the fibers are lightly pressed so that they attach themselves to the PDMS layer. Then, gold electrodes are deposited on the end regions of the aligned fiber arrays. The electrodes are subsequently connected to copper wires with silver paste. This ensemble is then packaged with PDMS to protect the fibers and the assembly. In the final step, the flexible nanogenerator is obtained by polarizing the fibers with a 4 kV/mm electric field for 15 min. The performance of the nanogenerator is measured using an open-circuit voltage and short-circuit current. The maximum output voltage and current generated by these fibers reach 6 V and 45 nA, respectively, when the flexible PET is bent and released repeatedly. Each time the PET is bent, the PZT fibers within the device experience a tensile stress and strain in the direction along the fiber axis. Due to this mechanical strain, a piezoelectric potential is recorded at the ends of the fibers. The potential difference across the two ends of the fibers drives the flow of free electrons

from the low to the high potential end via a load in the external circuit. These electrons accumulate at the interface between the fibers and electrodes owing to the insulating property of the PZT fiber that restricts the flow of electrons through them. This explains the generation of output voltage and current whenever the PET is bent. By contrast, when PET is released and allowed to relax, the fibers are not tensioned and the strain disappears. During this stage, there is no potential difference across the fibers. The electrons flow back to the external circuit through the outer load, generating electricity again. The voltage generated by the nanogenerator composed of fibers is sufficient to light a liquid crystal display (LCD) [2, 59]. In a similar study, Chen *et al.* [2] fabricated piezoelectric nanogenerator based on PZT fibers obtained using a sol–gel electrospinning technique. Here, the PZT fibers are deposited on interdigitated platinum electrodes that are separated by 500 μm and a PDMS layer is applied on top of the fibers. The fibers are poled to align the dipoles within the matrix. They show that such nanogenerators are ideal for harvesting biomechanical energy.

5.13 Magnetoelectric Inorganic Fibers

The coexistence of ferroelectric and ferromagnetic orders in BiFeO_3 fibers opens a new way of obtaining magnetoelectric (ME) materials that allow coupling between ferroelectric and ferromagnetic domains. In recent years, ME materials have aroused widespread interest and are becoming one of the future trendy areas of ferroelectrics [67–70]. Such materials have attracted considerable interest due to their potential for applications as multifunctional devices [67, 70]. This desired mechanism enables a variety of potential applications for ME materials, including sensors, transducers, and memory devices that can be electrically written and magnetically read, magnetically controlled piezoelectric devices, etc. ME effect in materials depends on the magnetic-strain-electrical coupling between magnetostrictive and ferroelectric phases [67, 71]. When a magnetic field is applied, the magnetostrictive phase within the material induces a strain in terms of a change in dimension, which in turn transfers the stress to the ferroelectric phase, resulting in an electric polarization. This strong coupling can yield materials that are capable of displaying large ME coefficients. Prashanthi *et al.* [72] used sol–gel and electrospinning techniques to fabricate BiFeO_3 fibers and showed ME coupling of the fibers. Using magnetic force microscopy (MFM), they demonstrated that magnetic domain patterns in the fibers can be controlled by varying the external electric field. Figure 5.12a shows the MFM response of the fibers as a function of displacement. The magnetic domains developed within the fibers in response to the external electric field are shown in Figure 5.12b.

When no external electric field is applied to the fiber, the MFM phase image shows distinct domain structure. However, when an electric field of 5 V is applied to the sample, the change in the magnetic domains structure is noticed. When the external electric field is increased to 10 V, a single domain pattern is obtained as opposed to multiple domain patterns at 5 V. In the next stage, when the external electric field is removed, some magnetic domains are retained within the fiber. They argue that this is a clear indication of electric

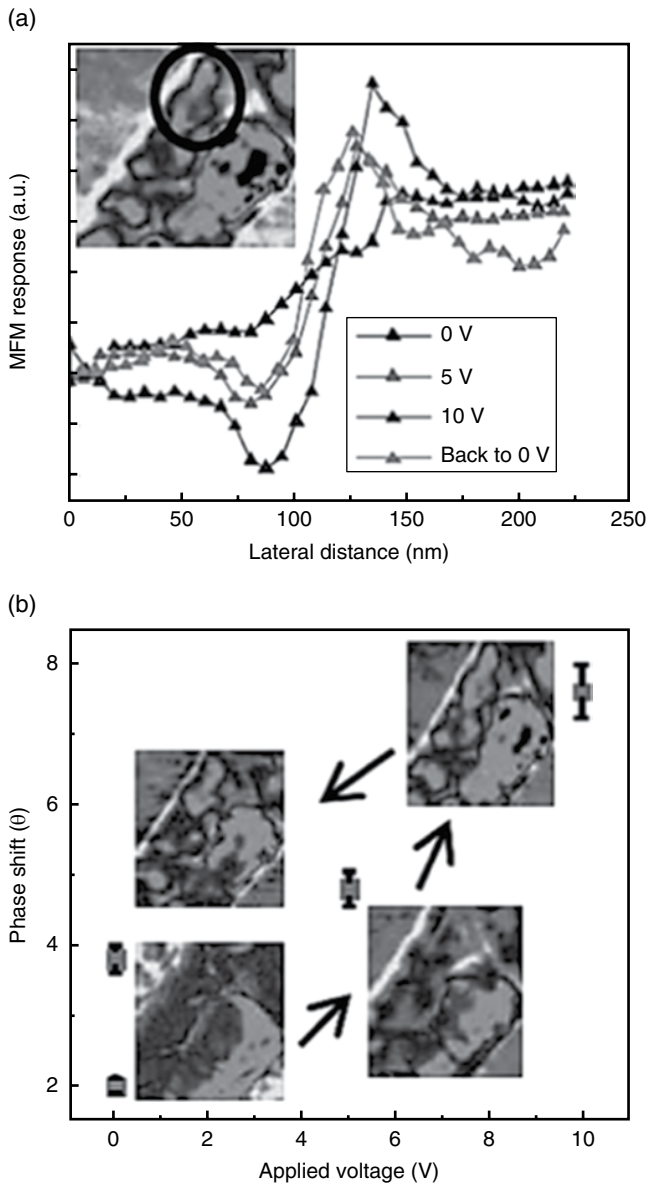


Figure 5.12 (a) Cross-sectional analysis of MFM response recorded for the BiFeO₃ fiber at different applied voltages. The inset shows the region on the fiber where the MFM signal is recorded. (b) MFM phase shift versus applied voltage recorded for the fiber. The corresponding magnetic domains at different applied voltages are also shown. Prashanthi et al. [72]. Reproduced with permission of John Wiley & Sons

field-induced magnetic hysteresis. The equivalent ME coefficient is determined to be $\sim 0.5 \text{ V}/(\text{cm Oe}^{-1})$ using the magnetization values obtained at various applied electric fields. This value is found to be higher than the previous reported value for bulk BiFeO_3 . In a similar study, Xie *et al.* [26] used the sol-gel combined with coaxial electrospinning technique to fabricate core-shell $\text{CoFe}_2\text{O}_4\text{-Pb}(\text{Zr}_{0.52}\text{TiO}_{0.48})\text{O}_3$ nanofibers. The multiferroic properties of these fibers such as the ferromagnetic behavior and ferroelectric response are obtained using magnetic hysteresis and PFM, respectively. The ME coupling is confirmed by measuring the piezoresponse of the fibers in the presence of an external magnetic field with PFM. The external magnetic field provided to the fibers induces ferroelectric domains within the fibers and also influences the ferroelectric switching characteristics of the fibers. Further, they demonstrate that the ME coupling coefficient is $29.4 \text{ V}/(\text{cm Oe}^{-1})$, which is two orders of magnitude higher than its bulk counterpart. Thus, their results demonstrate the possibility of fabricating novel heterogeneous nanostructured materials.

5.14 Future Directions

The results presented in this chapter demonstrate that piezoelectric fibers obtained using the electrospinning technique show tremendous promise for harvesting mechanical energy and converting it to electricity. This concept of using piezoelectric fibers for powering a microelectronic device is a promising concept. Electrospinning is particularly attractive as it is cost-effective and fibers from various materials can be easily fabricated. Furthermore, nanoparticles embedded within the fibrous matrix not only improve the piezoelectricity of the matrix but also broaden the functions of the electrospun fibers. Flexible nanogenerators using both polymer and ceramic fibers can be obtained for integration with implantable devices or other flexible devices. For example, flexible nanogenerators can be integrated with textiles to develop electroactive clothing. Several studies have also used electrospun fibers to fabricate nanogenerators and demonstrated the applications of their prototypes.

The challenge for the researchers is to take this beyond the laboratory and implement their use in practical applications. To realize this potential, it is essential to increase both the energy conversion efficiency and the power density of nanogenerators. Some recent studies have used electrospun PVDF fibers and demonstrated that the electricity generated from the piezoelectric fibers is sufficient to drive active devices such as light emitting diodes. Others have demonstrated that the overall electrical output from a nanogenerator can be amplified by using numerous fibers in series instead of a single fiber. This is encouraging since a modified electrospinning setup (see Section 5.2) can be used to collect aligned array of fibers. However, the power generated from a single fiber should be maximized. Currently, the power generated by a nanogenerator with a single fiber is $\sim 10^{-11} \text{ W}$, not even sufficient to power an electrical watch that requires microwatts.

Results obtained in this chapter also show the feasibility of using electrospinning to obtain ME composites. Research on electrospun ME fibers is still in an early stage and many issues need to be addressed before ME fibers can be used for commercially viable products. Nevertheless, recent work on electrospinning suggested great promise to achieve

novel ME composites. For example, intimate coupling between ferroelectric and ferromagnetic domains in electrospun composite fibers makes electrospinning an ideal processing technique to obtain ME composites capable of displaying electrostatically controllable magnetization. Further, it is possible to control the poling and applied field direction for these fibrous composites, leading to enhancement of ME effects. Composites fabricated using conventional techniques including sintering, microwave sintering and hot pressing are found to exhibit low ME coefficients due to the poor binding between phases, presence of micro-cracks, impurity phases, defects, and high leakage currents. Electrospun 1D composite fibers can be used as novel ME materials for nanoscale devices. The reduced dimensionality of the nanostructured composite fibers will play a critical role on the ME effect, enabling coupling between their ferroelectric and ferromagnetic domains and a strong ME coefficient. Such composites are very attractive for a variety of commercial and industrial products related to microwave devices that require strong coupling to electromagnetic generations, electronic applications such as power generation and conversion, memory storage devices, among others.

Acknowledgments

We would like to thank the Australian Research Council for the financial support of the work reported in this chapter.

References

- (1) J.Y. Chang, M. Dommner, C. Chang, and L.W. Lin, Piezoelectric nanofibers for energy scavenging applications. *Nano Energy*, **1**, 356–371 (2012).
- (2) X. Chen, S.Y. Xu, N. Yao, and Y. Shi, 1.6 V Nanogenerator for mechanical energy harvesting using PZT nanofibers. *Nano Lett.*, **10**, 2133–2137 (2010).
- (3) C.E. Chang, V.H. Tran, J.B. Wang, Y.K. Fuh, and L.W. Lin, Direct-write piezoelectric polymeric nanogenerator with high energy conversion efficiency. *Nano Lett.*, **10**, 726–731 (2010).
- (4) L. Gu, N.Y. Cui, L. Cheng, Q. Xu, S. Bai, M.M. Yuan, W.W. Wu, J.M. Liu, Y. Zhao, F. Ma, Y. Qin, and Z.L. Wang, Flexible fiber nanogenerator with 209 V output voltage directly powers a light-emitting diode. *Nano Lett.*, **13**, 91–94 (2013).
- (5) B.J. Hansen, Y. Liu, R.S. Yang, and Z.L. Wang, Hybrid nanogenerator for concurrently harvesting biomechanical and biochemical energy. *ACS Nano*, **4**, 3647–3652 (2010).
- (6) Y. Qin, X.D. Wang, and Z.L. Wang, Microfibre-nanowire hybrid structure for energy scavenging. *Nature*, **451**, 809–813 (2008).
- (7) S.R. Anton and H.A. Sodano, A review of power harvesting using piezoelectric materials (2003–2006). *Smart Mater. Struct.*, **16**, R1–R21 (2007).
- (8) H.A. Sodano, D.J. Inman, and G. Park, Comparison of piezoelectric energy harvesting devices for recharging batteries. *J. Intell. Mater. Syst. Struct.*, **16**, 799–807 (2005).
- (9) M.D. Wei, Y. Konishi, H.S. Zhou, M. Yanagida, H. Sugihara, and H. Arakawa, Highly efficient dye-sensitized solar cells composed of mesoporous titanium dioxide. *J. Mater. Chem.*, **16**, 1287–1293 (2006).
- (10) T.M. Razykov, C.S. Ferekides, D. Morel, E. Stefanakos, H.S. Ullal, and H.M. Upadhyaya, Solar photovoltaic electricity: Current status and future prospects. *Sol. Energy*, **85**, 1580–1608 (2011).

- (11) A.I. Hochbaum, R.K. Chen, R.D. Delgado, W.J. Liang, E.C. Garnett, M. Najarian, A. Majumdar, and P.D. Yang, Enhanced thermoelectric performance of rough silicon nanowires. *Nature*, **451**, 163–167 (2008).
- (12) W.S. Liu, X. Yan, G. Chen, and Z.F. Ren, Recent advances in thermoelectric nanocomposites. *Nano Energy*, **1**, 42–56 (2012).
- (13) A. Baji, Y.-W. Mai, Q.A. Li, S.C. Wong, Y. Liu, and Q.W. Yao, One-dimensional multiferroic bismuth ferrite fibers obtained by electrospinning techniques. *Nanotechnology*, **22**, 235702 (2011).
- (14) S. Roundy, E.S. Leland, J. Baker, E. Carleton, E. Reilly, E. Lai, B. Otis, J.M. Rabaey, P.K. Wright, and V. Sundararajan, Improving power output for vibration-based energy scavengers. *IEEE Pervasive Comput.*, **4**, 28–36 (2005).
- (15) X.D. Wang, Piezoelectric nanogenerators—Harvesting ambient mechanical energy at the nanometer scale. *Nano Energy*, **1**, 13–24 (2012).
- (16) A. Baji, Y.-W. Mai, Q. Li, and Y. Liu, Electrospinning induced ferroelectricity in poly(vinylidene fluoride) fibers. *Nanoscale*, **3**, 3068–3071 (2011).
- (17) A. Baji, Y.-W. Mai, Q. Li, and Y. Liu, Nanoscale investigation of ferroelectric properties in electrospun barium titanate/polyvinylidene fluoride composite fibers using piezoresponse force microscopy. *Compos. Sci. Technol.*, **71**, 1435–1440 (2011).
- (18) Z.R.R. Tian, J.A. Voigt, J. Liu, B. McKenzie, M.J. McDermott, M.A. Rodriguez, H. Konishi, and H.F. Xu, Complex and oriented ZnO nanostructures. *Nat. Mater.*, **2**, 821–826 (2003).
- (19) H.J. Zhou and S.S. Wong, A facile and mild synthesis of 1-D ZnO, CuO, and α -Fe₂O₃ nanostructures and nanostructured arrays. *ACS Nano*, **2**, 944–958 (2008).
- (20) J. Wang, C.S. Sandu, E. Colla, Y. Wang, W. Ma, R. Gysel, H.J. Trodahl, N. Setter, and M. Kuball, Ferroelectric domains and piezoelectricity in monocrystalline Pb(Zr,Ti)O₃ nanowires. *Appl. Phys. Lett.*, **90**, 133107 (2007).
- (21) A. Baji, Y.-W. Mai, and S.C. Wong, Effect of fiber diameter on the deformation behavior of self-assembled carbon nanotube reinforced electrospun Polyamide 6,6 fibers. *Mater. Sci. Eng. A: Struct. Mater. Prop. Microstruct. Process.*, **528**, 6565–6572 (2011).
- (22) A. Baji, Y.-W. Mai, S.C. Wong, M. Abtahi, and P. Chen, Electrospinning of polymer nanofibers: Effects on oriented morphology, structures and tensile properties. *Compos. Sci. Technol.*, **70**, 703–718 (2010).
- (23) A. Baji, Y.-W. Mai, X.S. Du, and S.C. Wong, Improved tensile strength and ferroelectric phase content of self-assembled polyvinylidene fluoride fiber yarns. *Macromol. Mater. Eng.*, **297**, 209–213 (2012).
- (24) H. Wu, R. Zhang, X.X. Liu, D.D. Lin, and W. Pan, Electrospinning of Fe, Co, and Ni nanofibers: Synthesis, assembly, and magnetic properties. *Chem. Mater.*, **19**, 3506–3511 (2007).
- (25) S.H. Xie, J.Y. Li, Y.Y. Liu, L.N. Lan, G. Jin, and Y.C. Zhou, Electrospinning and multiferroic properties of NiFe₂O₄-Pb(Zr_{0.52}Ti_{0.48})O₃ composite nanofibers. *J. Appl. Phys.*, **104**, 024115 (2008).
- (26) S.H. Xie, J.Y. Li, Y. Qiao, Y.Y. Liu, L.N. Lan, Y.C. Zhou, and S.T. Tan, Multiferroic CoFe(2)O(4)-Pb(Zr(0.52)Ti(0.48))O(3) nanofibers by electrospinning. *Appl. Phys. Lett.*, **92**, 062901 (2008).
- (27) J.J. Ge, H.Q. Hou, Q. Li, M.J. Graham, A. Greiner, D.H. Reneker, F.W. Harris, and S.Z.D. Cheng, Assembly of well-aligned multiwalled carbon nanotubes in confined polyacrylonitrile environments: Electrospun composite nanofiber sheets. *J. Am. Chem. Soc.*, **126**, 15754–15761 (2004).
- (28) A. Baji, Y.-W. Mai, M. Abtahi, S.C. Wong, Y. Liu, and Q. Li, Microstructure development in electrospun carbon nanotube reinforced polyvinylidene fluoride fibres and its influence on tensile strength and dielectric permittivity. *Compos. Sci. Technol.*, **88**, 1–8 (2013).
- (29) S. Mazinani, A. Ajji, and C. Dubois, Morphology, structure and properties of conductive PS/CNT nanocomposite electrospun mat. *Polymer*, **50**, 3329–3342 (2009).

- (30) Q. Wu, Y.X. Xu, Z.Y. Yao, A.R. Liu, and G.Q. Shi, Supercapacitors based on flexible graphene/polyaniline nanofiber composite films. *ACS Nano*, **4**, 1963–1970 (2010).
- (31) D. Li and Y.N. Xia, Electrospinning of nanofibers: Reinventing the wheel? *Adv. Mater.*, **16**, 1151–1170 (2004).
- (32) Z.M. Huang, Y.Z. Zhang, M. Kotaki, and S. Ramakrishna, A review on polymer nanofibers by electrospinning and their applications in nanocomposites. *Comp. Sci. Technol.*, **63**, 2223–2253 (2003).
- (33) D.H. Reneker, A.L. Yarin, H. Fong, and S. Koombhongse, Bending instability of electrically charged liquid jets of polymer solutions in electrospinning. *J. Appl. Phys.*, **87**, 4531–4547 (2000).
- (34) D.H. Reneker and I. Chun, Nanometre diameter fibres of polymer, produced by electrospinning. *Nanotechnology*, **7**, 216–223 (1996).
- (35) L.S. Carnell, E.J. Siochi, R.A. Wincheski, N.M. Holloway, and R.L. Clark, Electric field effects on fiber alignment using an auxiliary electrode during electrospinning. *Scr. Mater.*, **60**, 359–361 (2009).
- (36) M. Acharya, G.K. Arumugam, and P.A. Heiden, Dual electric field induced alignment of electrospun nanofibers. *Macromol. Mater. Eng.*, **293**, 666–674 (2008).
- (37) A. Baji, Y.-W. Mai, S.C. Wong, M. Abtahi, and X.S. Du, Mechanical behavior of self-assembled carbon nanotube reinforced nylon 6,6 fibers. *Compos. Sci. Technol.*, **70**, 1401–1409 (2010).
- (38) E. Smit, U. Buttner, and R.D. Sanderson, Continuous yarns from electrospun fibers. *Polymer*, **46**, 2419–2423 (2005).
- (39) Z.M. Dang, Y.H. Lin, and C.W. Nan, Novel ferroelectric polymer composites with high dielectric constants. *Adv. Mater.*, **15**, 1625–1629 (2003).
- (40) R.G. Kepler and R.A. Anderson, Ferroelectricity in polyvinylidene fluoride. *J. Appl. Phys.*, **49**, 1232–1235 (1978).
- (41) R. Gregorio and M. Cestari, Effect of crystallization temperature on the crystalline phase content and morphology of poly(vinylidene fluoride). *J. Polym. Sci. B: Polym. Phys.*, **32**, 859–870 (1994).
- (42) L. Priya and J.P. Jog, Poly(vinylidene fluoride)/clay nanocomposites prepared by melt intercalation: Crystallization and dynamic mechanical behavior studies. *J. Polym. Sci. B: Polym. Phys.*, **40**, 1682–1689 (2002).
- (43) A.J. Lovinger, Polymorphic transformations in ferroelectric copolymers of vinylidene fluoride induced by electron-irradiation. *Macromolecules*, **18**, 910–918 (1985).
- (44) A.J. Lovinger, T. Furukawa, G.T. Davis, and M.G. Broadhurst, Crystallographic changes characterizing the curie transition in three ferroelectric co-polymers of vinylidene fluoride and trifluoroethylene: 1. As crystallized samples. *Polymer*, **24**, 1225–1232 (1983).
- (45) A.J. Lovinger, T. Furukawa, G.T. Davis, and M.G. Broadhurst, Crystallographic changes characterizing the curie transition in three ferroelectric co-polymers of vinylidene fluoride and trifluoroethylene: 2. Oriented or poled samples. *Polymer*, **24**, 1233–1239 (1983).
- (46) A.J. Lovinger, Ferroelectric polymers. *Science*, **220**, 1115–1121 (1983).
- (47) Y. Ahn, J.Y. Lim, S.M. Hong, J. Lee, J. Ha, H.J. Choi, and Y. Seo, Enhanced piezoelectric properties of electrospun poly(vinylidene fluoride)/multiwalled carbon nanotube composites due to high beta-phase formation in poly(vinylidene fluoride). *J. Phys. Chem. C*, **117**, 11791–11799 (2013).
- (48) J.J. Wang, H.H. Li, J.C. Liu, Y.X. Duan, S.D. Jiang, and S.K. Yan, On the alpha \rightarrow beta transition of carbon-coated highly oriented PVDF ultrathin film induced by melt recrystallization. *J. Am. Chem. Soc.*, **125**, 1496–1497 (2003).
- (49) D. Li and Y.N. Xia, Fabrication of titania nanofibers by electrospinning. *Nano Lett.*, **3**, 555–560 (2003).
- (50) D. Li, J.T. McCann, and Y.N. Xia, Electrospinning: A simple and versatile technique for producing ceramic nanofibers and nanotubes. *J. Am. Chem. Soc.*, **89**, 1861–1869 (2006).
- (51) V. Thavasi, G. Singh, and S. Ramakrishna, Electrospun nanofibers in energy and environmental applications. *Energy Environ. Sci.*, **1**, 205–221 (2008).

- (52) K. Onozuka, B. Ding, Y. Tsuge, T. Naka, M. Yamazaki, S. Sugi, S. Ohno, M. Yoshikawa, and S. Shiratori, Electrospinning processed nanofibrous TiO₂ membranes for photovoltaic applications. *Nanotechnology*, **17**, 1026–1031 (2006).
- (53) H.S. Shim, S.I. Na, S.H. Nam, H.J. Ahn, H.J. Kim, D.Y. Kim, and W.B. Kim, Efficient photovoltaic device fashioned of highly aligned multilayers of electrospun TiO₂ nanowire array with conjugated polymer. *Appl. Phys. Lett.*, **92**, 183107 (2008).
- (54) C. Kim, B.T.N. Ngoc, K.S. Yang, M. Kojima, Y.A. Kim, Y.J. Kim, M. Endo, and S.C. Yang, Self-sustained thin webs consisting of porous carbon nanofibers for supercapacitors via the electrospinning of polyacrylonitrile solutions containing zinc chloride. *Adv. Mater.*, **19**, 2341–2346 (2007).
- (55) S. Huang, W.A. Yee, W.C. Tjiu, Y. Liu, M. Kotaki, Y.C.F. Boey, J. Ma, T.X. Liu, and X.H. Lu, Electrospinning of polyvinylidene difluoride with carbon nanotubes: Synergistic effects of extensional force and interfacial interaction on crystalline structures. *Langmuir*, **24**, 13621–13626 (2008).
- (56) L. Yu and P. Cebe, Crystal polymorphism in electrospun composite nanofibers of poly(vinylidene fluoride) with nanoclay. *Polymer*, **50**, 2133–2141 (2009).
- (57) J.S. Andrew and D.R. Clarke, Enhanced ferroelectric phase content of polyvinylidene difluoride fibers with the addition of magnetic nanoparticles. *Langmuir*, **24**, 8435–8438 (2008).
- (58) S.H. Xie, J.Y. Li, R. Proksch, Y.M. Liu, Y.C. Zhou, Y.Y. Liu, Y. Ou, L.N. Lan, and Y. Qiao, Nanocrystalline multiferroic BiFeO₃ ultrafine fibers by sol–gel based electrospinning. *Appl. Phys. Lett.*, **93**, 222904 (2008).
- (59) W.W. Wu, S. Bai, M.M. Yuan, Y. Qin, Z.L. Wang, and T. Jing, Lead zirconate titanate nanowire textile nanogenerator for wearable energy-harvesting and self-powered devices. *ACS Nano*, **6**, 6231–6235 (2012).
- (60) S.V. Kalinin, E. Karapetian, and M. Kachanov, Nanoelectromechanics of piezoresponse force microscopy. *Phys. Rev. B*, **70**, 184101 (2004).
- (61) S.V. Kalinin and D.A. Bonnell, Local potential and polarization screening on ferroelectric surfaces. *Phys. Rev. B*, **63**, 125411 (2001).
- (62) S.V. Kalinin and D.A. Bonnell, Imaging mechanism of piezoresponse force microscopy of ferroelectric surfaces. *Phys. Rev. B*, **65**, 125401 (2002).
- (63) M.H. Zhao, Z.L. Wang, and S.X. Mao, Piezoelectric characterization of individual zinc oxide nanobelt probed by piezoresponse force microscope. *Nano Lett.*, **4**, 587–590 (2004).
- (64) J. Fang, H.T. Niu, H.X. Wang, X.G. Wang, and T. Lin, Enhanced mechanical energy harvesting using needleless electrospun poly(vinylidene fluoride) nanofiber webs. *Energy Environ. Sci.*, **6**, 2196–2202 (2013).
- (65) Y.R. Wang, J.M. Zheng, G.Y. Ren, P.H. Zhang, and C. Xu, A flexible piezoelectric force sensor based on PVDF fabrics. *Smart Mater. Struct.*, **20**, 045009 (2011).
- (66) G.Y. Ren, F.Y. Cai, B.Z. Li, J.M. Zheng, and C.Y. Xu, Flexible pressure sensor based on a poly(VDF-TrFE) nanofiber web. *Macromol. Mater. Eng.*, **298**, 541–546 (2013).
- (67) H. Zheng, J. Wang, S.E. Lofland, Z. Ma, L. Mohaddes-Ardabili, T. Zhao, L. Salamanca-Riba, S.R. Shinde, S.B. Ogale, F. Bai, D. Viehland, Y. Jia, D.G. Schlom, M. Wuttig, A. Roytburd, and R. Ramesh, Multiferroic BaTiO₃-CoFe₂O₄ nanostructures. *Science*, **303**, 661–663 (2004).
- (68) W. Eerenstein, N.D. Mathur, and J.F. Scott, Multiferroic and magnetoelectric materials. *Nature*, **442**, 759–765 (2006).
- (69) S.W. Cheong and M. Mostovoy, Multiferroics: A magnetic twist for ferroelectricity. *Nature Mater.*, **6**, 13–20 (2007).
- (70) R. Ramesh and N.A. Spaldin, Multiferroics: Progress and prospects in thin films. *Nature Mater.*, **6**, 21–29 (2007).
- (71) C.W. Nan, Magnetoelectric effect in composites of piezoelectric and piezomagnetic phases. *Phys. Rev. B*, **50**, 6082–6088 (1994).
- (72) K. Prashanthi, P.M. Shaibani, A. Sohrabi, T.S. Natarajan, and T. Thundat, Nanoscale magnetoelectric coupling in multiferroic BiFeO₃ nanowires. *Phys. Status Solidi RRL*, **6**, 244–246 (2012).

6

Magnetic Properties of Polymer Nanocomposites

Paolo Allia¹, Marco Sangermano¹ and Alessandro Chiolerio²

¹*Applied Science and Technology Department, Politecnico di Torino, Italy*

²*Center for Space Human Robotics, Istituto Italiano di Tecnologia, Italy*

6.1 Introduction

Inorganic nanoparticles (NPs) dispersed within polymer matrices have been exploited for a number of applications thanks to the interesting properties that result from the combination of inorganic components and polymers. Polymeric matrix nanocomposite (NC) materials containing either metallic or insulating NPs have been prepared to obtain interesting magnetic [1–4] properties for use in micro- and nanoelectronics. In addition, important contributions to fundamental studies in nanoscale physics have been made by studying those materials, such as quantum tunneling of magnetization, spin-reversal mechanism in single-domain particles, and quantum size effects [5–7], while we foresee advanced use of these materials for their magnetoresistance properties. In this case, a liquid ferrofluid containing an oligomer resin and a dispersion of magnetic NPs is made to polymerize by ultraviolet (UV) curing to form a solid film. Magnetite is a cheap material with a lower degree of toxicity when compared to other metallic ferromagnets, and it can be easily synthesized through a variety of low-cost techniques, such as the thermochemical route [8]. UV curing is also a cheap technique, particularly appealing now for what concerns coatings. Here, a UV radiation is shone on a liquid precursor, driving some chemical modifications that allow the precursor to polymerize, producing a solid polymer having tailored

physical characteristics. This process is environment-friendly, since it is solvent-free and does not require operation at higher temperatures, since the substrate is kept at room temperature. Putting together magnetic dispersoids and polymeric matrix, it is possible to control the magnetism in the NPs by modifying the matrix properties. Novel smart materials may be engineered, traducing a certain stimulus into a dramatic variation of some physical properties, such as magnetization.

6.2 Preparation of Magnetic NPs and Its Influence on the Properties of NCs

6.2.1 Top-down versus Bottom-up Approach to Synthesis

In order to prepare magnetic NCs, two different approaches must be followed: top-down approach, where magnetic NPs are preformed and dispersed in the polymer or the polymer precursor which is then polymerized; and the bottom-up approach where magnetic NPs are generated *in situ* during polymerization.

When top-down approach is used, magnetic NPs can be easily synthesized through various low-cost techniques.

Allia *et al.* [3] prepared acrylic-magnetite NCs synthesizing magnetite according to the method proposed by Sun *et al.* [9]. The achieved magnetite NP dispersion in *n*-hexane was added to an acrylic resin and was UV cured in the presence of a radical photoinitiator. The magnetization of as-received NPs was comparable with bulk magnetite, displaying the overall magnetic properties best described by the interacting superparamagnetic (ISP) model [10], indicating the presence of non-negligible long-range magnetic interactions. The dispersion of the magnetite NPs into the UV-cured acrylic matrix does not modify the ISP behavior but has important consequences on the low-temperature hysteretic properties. In particular, the coercive field is strongly reduced with increasing NP content in the polymeric matrix, a result explained by the presence of a possible compressive stress induced on the NPs by the matrix. This effect introduces an anisotropic stress that counterbalances the magnetocrystalline anisotropy. This behavior has been verified and confirmed by numerical simulation using finite element method (FEM).

More recently, magnetite-silica core-shell NPs have been synthesized and dispersed into an acrylic functionalized hyperbranched polymer (HBP), and the system was UV cross-linked [11]. The use of $\text{Fe}_3\text{O}_4@ \text{SiO}_2$ NPs for synthesizing magnetic polymeric films through an UV-induced polymerization process has proven effective. It allowed adding 10 times higher particle volume fractions with respect to the same UV-curable formulation including bare magnetite NPs. When the silica shell was covering the magnetite core, it was possible to add up to 8 vol% of NPs, reaching a complete cured system, while when bare magnetite NPs were added, the limit to get a fully cured system was only 0.7 vol%. Most important, the transparency of the UV-cured films in the visible region was highly improved in the case of the system containing core-shell structures. Magnetic measurements have shown that the system containing 8 vol% of core-shell particles has a similar magnetic behavior of the crosslinked matrix containing 0.7 vol% of bare magnetite NPs, with a

magnetization at around 1 emu/g of NCs. This result puts in evidence that the silica shell should have a little effect on the magnetic properties of magnetite core.

One main disadvantage of the top-down approach is the easy tendency of agglomeration and the consequent difficulty of homogeneous dispersion within the polymeric matrix. In this respect, *in situ* generation of NPs represents a possible alternative to design new composite materials.

In the bottom-up approach, where the metal oxide NPs are formed during crosslinking reaction, the well-known sol-gel process is often used [12]. Typically, this occurs in two steps: the first one is hydrolysis, which produces hydroxyl groups and the second one is condensation, which involves polycondensation of hydroxyl groups to form a three-dimensional network.

As an alternative to this method, there is the possibility to follow the non-hydrolytic sol-gel reaction (NHSG) to obtain very pure and crystalline metal oxide [13–15]. As well as the aqueous route, the NHSG process is divided in two steps. The first step involves the reaction of metal halide with an organic oxygen donor (i.e., alcohol, ether, etc.). The second step is the condensation. The NHSG process is potentially solvent-free, without problems with hydrophobic substances and particularly suitable for water-sensitive species. In 2013, Sangermano *et al.* [16] proposed an innovative method to produce epoxy-magnetite NCs through an NHSG process. Magnetite NPs were produced in benzyl alcohol, which can interact with the epoxy resin during UV curing via the very well-known activated monomer mechanism [17]. As precursor of the magnetite NPs Fe(III) acetylacetonate was chosen, mixed with an aliphatic epoxy resin, and cross-linked in the presence of a cationic photoinitiator.

The crosslinked composites resulted in a homogeneous distribution of the magnetite NPs, and the magnetic properties of the obtained NC were ascribed to individual, independent magnetic entities having sizes corresponding to single magnetite NPs.

6.2.2 Considerations Regarding Homogeneity and Interactions

For a number of applications, a uniform dispersion of magnetic NPs in the nonmagnetic host is a relevant issue [18]. A bad (uneven) dispersion may bring about non-optimal magnetic properties along with worsened mechanical properties. Usually, the mechanical energy introduced in the NP/polymeric fluid mixture during the dispersion process (stirring) is enough to effectively break most of the NP aggregates often found in as-prepared nanopowders, as will be shown in detail in section 6.3. Therefore, one can consider that the basic magnetic units dissolved in polymers are single magnetic NPs, or little clusters comprising a small number of them (~2–4). However, large-area uniformity of these units is often achieved with some difficulty and critically depends on the fluidity of the polymeric host during the mixing process.

Many experimental data and observations with a few exceptions point to the existence of significant fluctuations in the NP density in NC polymeric materials containing magnetic NPs, either metallic or insulating, either grown within the matrix precursor or incorporated in it by mixing [19]. These fluctuations can be related either to a specific morphology of

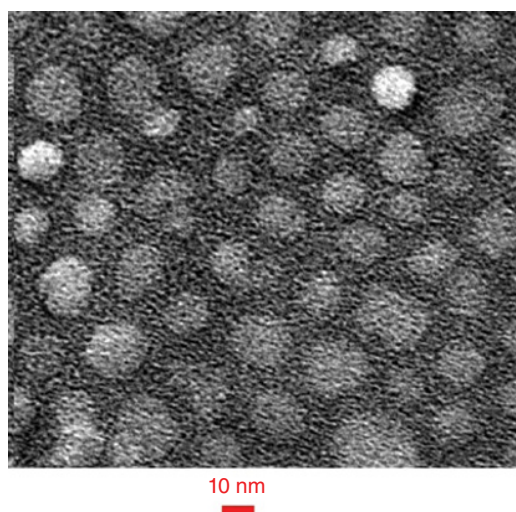


Figure 6.1 An example of spheroidal magnetite nanoparticles obtained by a wet chemical technique (see text for details)

polymeric hosts, or more generally to attractive forces among particles that act during NP growth (when applicable) or mixing. Concentration fluctuations of specific NPs can extend up to several hundreds of nanometers [20, 21] and can involve NP association or aggregation.

As a typical study case, let us consider here a magnetite nanopowder composed of 10 nm NPs obtained starting from Fe(III) acetylacetonate by a chemical route (benzyl alcohol+heating; surfactants mostly disappear after heating; see Figure 6.1). An example of “good” dispersion in an epoxy resin constituent (bisphenol A diglycidyl ether or DGEBA) is provided by Figure 6.2: on the one hand, the NPs, when dissolved with nominal concentration 4 per hundred resin (phr), appear to be evenly distributed in space. On the other hand, if the same NPs are dissolved by the same technique at a concentration as low as 0.5 phr, the result is entirely different (Figure 6.3): in this case, the NPs do form large islands comprising tens to hundreds of NPs separated by large regions of polymer where basically no magnetite is present. Inside each island, most of the NPs still keep their individuality, as shown in Figure 6.4 which is an enlargement of Figure 6.3. Possibly, in this case, the presence of a lower concentration of NPs increases the viscosity of the host fluid. As a consequence, the average interparticle distance in the 0.5 phr solution is larger than in the case of the 4 phr solution, with the obvious consequence that interparticle interactions do not decrease with reducing their concentration, as expected. In the case of uniform NP distribution, these interactions are mostly of magnetic dipolar type, while in the large islands of the 0.5 phr solution contact interactions, both electrical (van der Waals) or magnetic (exchange) cannot be excluded. The role of magnetic dipolar interactions in magnetic NCs will be thoroughly discussed in Section 6.3.

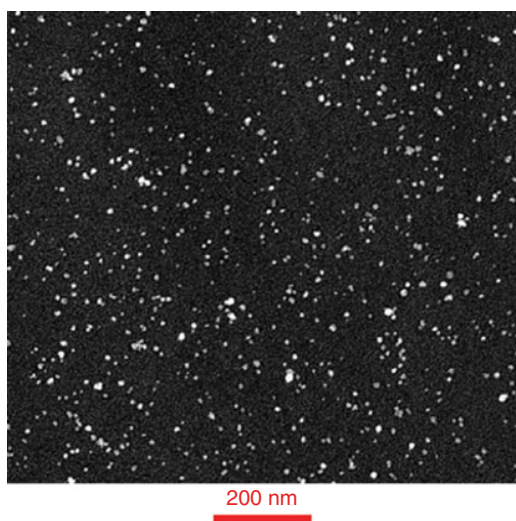


Figure 6.2 TEM image of a uniform dispersion in an epoxy resin of the magnetite nanoparticles shown in Figure 6.1 (see text for details)

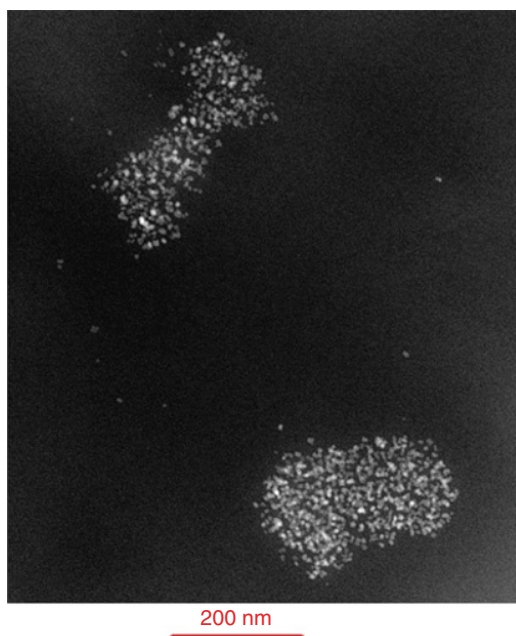


Figure 6.3 TEM image of a nonuniform, island-like dispersion in an epoxy resin of the magnetite nanoparticles shown in Figure 6.1 (see text for details)

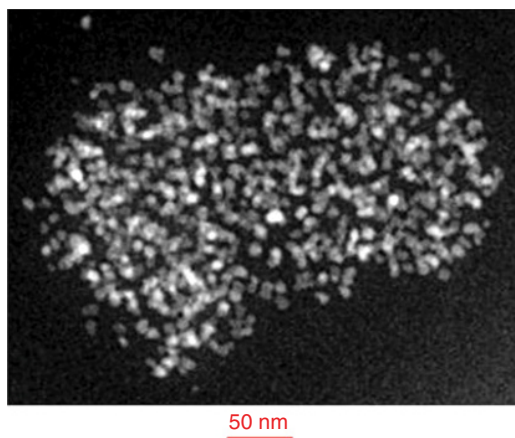


Figure 6.4 *Enlargement of Figure 6.3 showing the arrangement of magnetite nanoparticles within a single island*

6.3 An hysteretic Properties and Interparticle Interactions

NP dispersions in polymers are one of the best case studies for testing and measuring the effect of weak interparticle interactions on the magnetic properties. As known, magnetic nanopowders often contain large aggregates where the single NPs have lost their individual character to form magnetic entities much larger than the typical particle diameter, by the effect of strong interparticle magnetic interactions. This easily occurs in powders containing “bare” NPs, but it is often observed even in the presence of thin or incomplete ligand shells surrounding the individual NPs. In these cases, multiple direct contacts between adjacent NPs exist, entailing exchange or superexchange interactions; as a consequence, the magnetic exchange length becomes much larger than the average NP size, giving rise to magnetic agglomerates of NPs which respond coherently, and no longer individually, to the magnetic field [22]. In this case, huge regions of particles with nearly aligned magnetic moments exist, bearing similarities with the magnetic domains of a macroscopic ferromagnet [23]. This collective behavior is generally associated with field-cooled/zero-field-cooled (FC/ZFC) low-field magnetization curves that are almost featureless: the FC curve is basically flat, while the ZFC curve monotonically increases with increasing temperature; the two curves merge at the upper extreme of the investigated temperature range [24]. This is shown in Figure 6.5 for a 10-nm magnetite nanopowder (horizontal and bottom curves). In this case, the particle surface is surrounded by phenyl groups deriving from benzyl alcohol (BzOH), as determined by combined thermogravimetric and Fourier transform infrared spectroscopy (FTIR) analysis. However, when these materials are dissolved in a polymer, the mechanical energy introduced during stirring effectively breaks the weak bonds keeping together the NP aggregates, as shown in Figure 6.5 (top curves) for a 2.5 phr dispersion of the same NPs in an epoxy resin matrix (obtained by cationic UV-induced polymerization

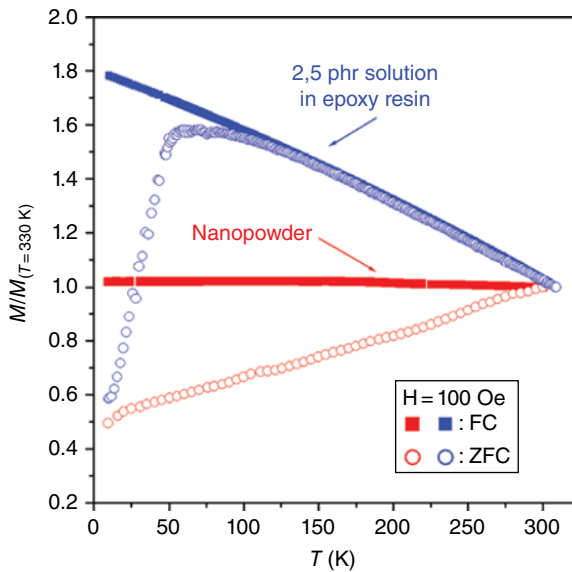


Figure 6.5 Field-cooled (FC) and zero-field-cooled magnetization curves for a magnetite nanopowder and for the corresponding nanocomposite obtained dissolving the nanopowder in epoxy resin

of cyanate ester resin). In this case, the FC/ZFC curves are typical of an NP system submitted to magnetic blocking: the ZFC curves show a rather sharp maximum located at $T \cong 70$ K; above the maximum, the FC/ZFC curves become coincident. These results are consistent with a single-particle, superparamagnetism (SPM)-like response of the NC, with a blocking temperature $T_b \cong 70$ K consistent with a size of particles of 12 nm and the magnitude of the low-temperature crystalline anisotropy in magnetite ($\sim 2 \times 10^5$ erg/cm³). The magnetic behavior of NCs above blocking temperature should be referred to as “SPM-like” because of the still non-negligible effect of interparticle interaction (strong contact interactions being ruled out in uniform dispersions (as the one shown in Figure 6.2); the most important interaction source is dipolar coupling).

Despite their being rather weak, dipolar interactions among magnetic NPs are responsible for various magnetic states at low temperatures. These are often frozen collective states, such as the super spin glass (SSG) state [25], characterized by a frozen disorder of magnetic moments, whose directions are dictated by interactions rather than by local intraparticle magnetic anisotropy. At high temperatures, where frozen states are destroyed by thermal disorder, dipolar interaction plays nevertheless a significant role, which can be figured out through ad hoc models such as the ISP model [10], which is basically a mean field approach where the argument of the Langevin function of standard SPM is modified by adding a fictive temperature T^* in the denominator (instead of adding an effective field in the numerator). Such a feature has been justified based on physical grounds. The fictive temperature T^* is defined as $T^* = N\mu^2/k_B d^3$ where N is the NP concentration, μ the mean

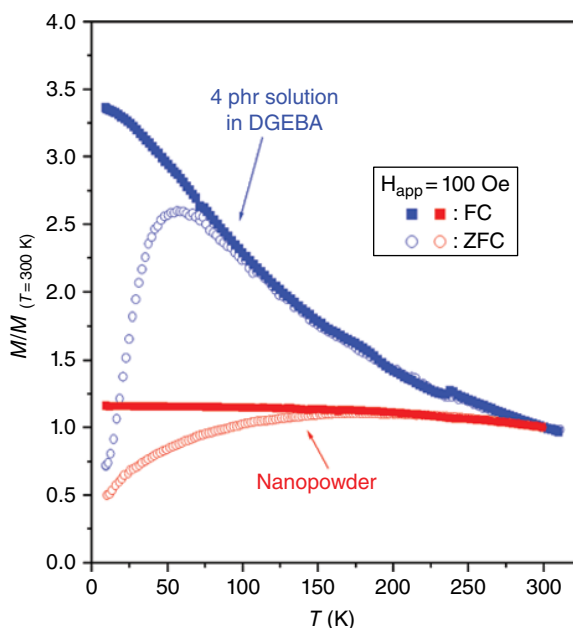


Figure 6.6 Field-cooled (FC) and zero-field-cooled magnetization curves for a magnetite nanopowder and for the corresponding nanocomposite obtained dissolving the nanopowder in a different epoxy resin constituent

magnetic moment on the NPs, and d the mean interparticle distance. This quantity is basically a measure of the strength of interparticle interactions.

It may be interesting to compare the behavior of the ratio T^*/T in nanopowders and in NCs containing the same NPs. As an example, we consider NPs of magnetite with 10–12 nm diameter obtained by a chemical route (see section 6.2.2 and Figure 6.1) and uniformly dissolved in an epoxy resin matrix (see Figure 6.2). The FC/ZFC curves shown in Figure 6.6 confirm that the nanopowder comprises strongly interacting NPs, still displaying a residual independent behavior, as evidenced by the existence of a very broad maximum in the ZFC curve (horizontal and bottom curves). The location (~180 K) and width of the ZFC curve maximum indicate a prevailing association of NPs to form aggregates having diameters of the order 20 nm, therefore containing about 10 particles, with a large distribution of sizes.

Instead, the magnetic response of the NC (top curves) is typical of a *bona fide* NP system with a narrow distribution of sizes centered at 12 nm, in very good agreement with the estimate resulting from transmission electron microscope (TEM) image analysis. As a consequence, the aggregates present on the nanopowder have been effectively broken by the mechanical energy introduced during the dispersion process. A comparable effect of mechanical action leading to the breakup of NP aggregates has been recently observed in ferrofluid inks ejected on flat surfaces through a nozzle in an ink jet device [26].

In both systems, the ISP model applies; the behavior of the fictive temperature is reported in Figure 6.7, curves 1 and 2. When $T^* < T$, the system is in the true SP phase, whereas the ISP regime occurs when $1 < T^*/T < 25$; for $T^*/T > 25$ collective frozen states are expected.

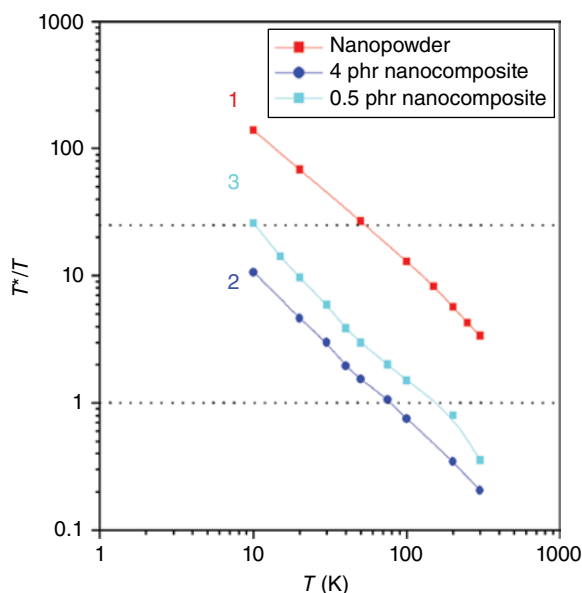


Figure 6.7 Fictive dipolar temperature ratio T^*/T as a function of measurement temperature for a magnetite nanopowder and two dispersions in epoxy resin

It can be deduced that the nanopowder is never found to be in the true SP regime, and collective states take place at a comparatively high temperature (~ 50 K); instead, the 4 phr solution in DGEBA exhibits a high-temperature SP behavior entering the ISP regime below ~ 75 K, indicating a strong reduction in the interaction strength, as expected. Interestingly enough, an NC containing less magnetite particles per unit volume (0.5 phr) exhibits a lower overall magnetic signal, as expected, but a higher T^* (see curve 3 in Figure 6.7). This result is in perfect agreement with a nonuniform distribution of NPs and the presence of islands where the interparticle distance is much closer than expected (see Figure 6.4). In this case, the values of NP density N and moment magnitude μ resulting from the ISP model analysis are not sufficient to explain the measured value of T^* . This difficulty is removed thinking that N is the *mean* density of NPs. If the NPs are confined to large islands surrounded by regions where very few or no particles at all are present, the local density N' is higher than the average value (although surface ligands prevent direct contact of adjacent magnetite cores) and the local interparticle distance $d' \cong (N')^{-3}$ smaller, correctly explaining the higher value obtained for T^* [27].

6.4 Hysteretic Properties

Despite the notable research activity in the field of magnetic NP systems, their hysteretic properties are still far from being elucidated. This situation stems from the fact that in many cases one looks for SPM or SPM-like properties, and the possible presence of a small hysteresis is merely seen as a secondary effect that can be discarded. In addition, in some

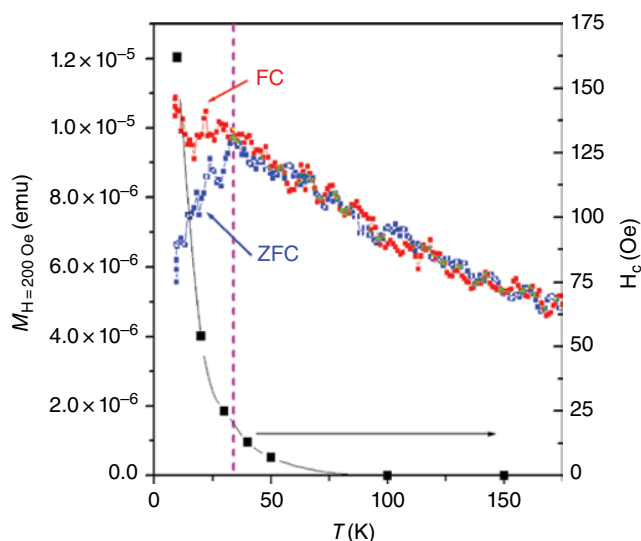


Figure 6.8 Temperature dependence of the coercive field (black symbols) and of FC/ZFC magnetization for magnetite nanoparticles dispersed in HDDA. (See insert for color representation of the figure)

nanomaterials and at some temperatures, the coercive field is so small that it cannot be easily resolved by a low-sensitivity magnetometer.

The standard explanation for the emergence of hysteretic properties involves single-particle blocking caused by intra-particle anisotropy; this directly results in the Stoner–Wohlfarth (SW) [28, 29] hysteretic response and implies the disappearance of coercivity and remanence above the blocking temperature. In many cases, however, definite hysteretic properties appear well above the estimated blocking temperature. In order to explain the occurrence of these unexpected hysteretic phenomena, it is often supposed that there exists a distribution of particle sizes so that large particles are blocked even at high temperature. According to this interpretation, the resulting magnetization curve should be a mixture of an SP (Langevin-like) anhysteretic magnetization and of an SW contribution. This naïve view is contradicted by the very shape of the hysteresis loop, which is always very different from the prediction of the SW model. Other approaches (involving both approximate analytical models [30] and simulations [31]) indicate that interparticle interaction of dipolar origin can play a major role in determining the magnetic hysteresis of NP systems.

The same picture applies to magnetic NCs also. In these systems, the common features of hysteretic properties are the following: (i) the effects (generally small) usually survive well above the blocking temperature and (ii) coercive field and magnetic remanence are often proportional to each other. As a typical example, the coercive field and magnetic remanence of 10–12 nm magnetite NPs dispersed in a photocurable resin (1,6-hexanediol diacrylate or HDDA) is shown in Figure 6.8 along with the corresponding FC/ZFC curves. In this case, the low fraction of magnetite (0.15%) results in rather noisy measurements. Although these curves

are perfectly superimposed above $T \cong 35$ K, so that there the system should be a perfect superparamagnet, the measured coercive field disappears above $T \cong 75$ K only; magnetic hysteresis therefore survives in a temperature region where FC/ZFC curve analysis would indicate a fully reversible magnetic regime. Another example is provided by 9 nm magnetite NPs dissolved in a photocured PEGDA-600 matrix with a concentration of 10 phr (Figure 6.9). Here, the blocking temperature is quite low, whilst the two curves do not perfectly superimpose above T_B , indicating some dispersion in the particle sizes. However, the coercive field stays almost constant over the whole reported temperature range; the only apparent effect of blocking on the hysteretic properties of such a sample seems to be the small but definite increase in coercive field measured at the lowest temperature ($T = 10$ K).

Therefore, in many NC systems single-particle blocking seems to be uncorrelated with the onset of hysteretic properties. This is not always true, however; as a counterexample, let us discuss the behavior of 10–12 nm magnetite NPs dissolved in epoxy resin with concentration 1 phr. The coercive field and magnetic remanence are reported in Figure 6.10 as functions of temperature. Note the close similarity between these curves. The blocking temperature $T_B = 50$ K is indicated by the vertical line. In this case, there is no high-temperature hysteresis; a nonzero coercive field emerges exactly at the blocking temperature. In other words, the considered system seems to closely behave according to the standard views than the previous ones. So far, no model has been put forward to explain why different NCs display an entirely different behavior of magnetic hysteresis as a function of temperature.

In systems where the hysteretic properties survive well above the blocking temperature, another interesting effect can be measured by performing an accurate study of the symmetrical minor loops produced by gradually lowering the value of the vertex field. In such a measurement, the temperature of the sample is kept constant and the vertex field is decreased from a high value (of the order of 15–20 kOe) corresponding to the so-called major loop [29] down to few tens of oersteds. The procedure involves (i) reaching the highest positive vertex field starting from the remanence, (ii) measuring the upper loop branch down to the negative vertex field (symmetric loop), (iii) measuring the lower loop branch and closing the loop at the positive vertex field, and (iv) reducing the positive vertex field and repeating the measurement from step (ii). In order to enhance the signal, a highly concentrated dispersion of 10-nm magnetite NPs in poly(ethylene glycol) diacrylate (PEGDA) was used (90 phr of ferrofluid in the photocurable polymer), and the measurements were performed at $T = 100$ K.

In bulk ferromagnetic materials [29] as well as in SW systems of blocked NPs, the coercive field and the magnetic remanence increase (following different laws) with increasing the vertex field until the so-called closure field is reached. The closure field is where the upper and lower branches of the major loop merge; it separates the region dominated by irreversible magnetization from the region of reversible magnetization. In standard systems, when the vertex field is higher of the closure field (i.e., is in the reversible region of the loop) neither the coercive field nor the magnetic remanence is expected to increase, and the loop width does not change any longer (major loop).

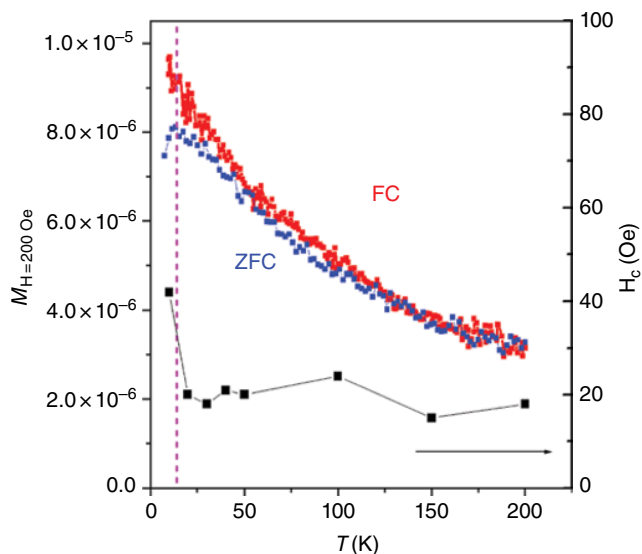


Figure 6.9 Same as in Figure 6.8 for magnetite nanoparticles dispersed in PEGDA. (See insert for color representation of the figure)

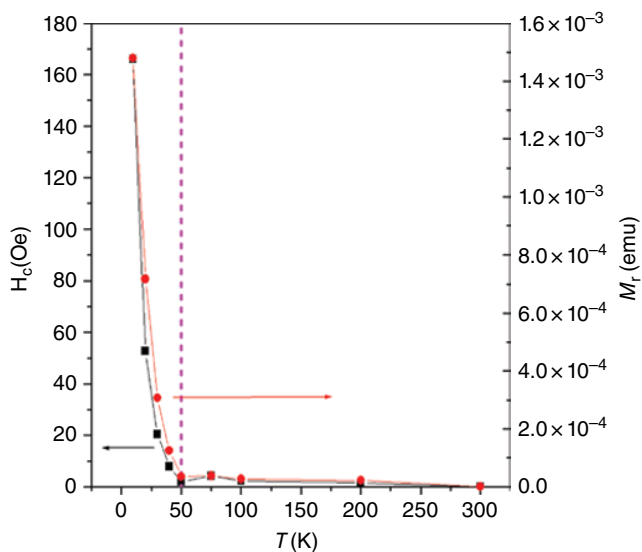


Figure 6.10 Coercive field and magnetic remanence for magnetite nanoparticles dispersed in DGEBA. The vertical dashed line indicates the blocking temperature as derived from FC/ZFC curves (not shown)

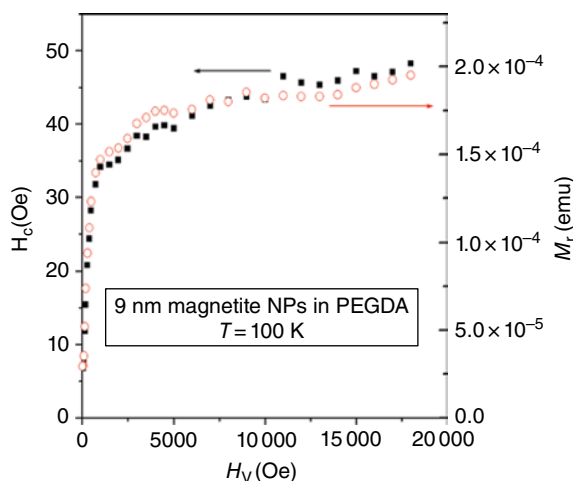


Figure 6.11 Unsaturating behavior of coercive field and magnetic remanence in a nanocomposite containing magnetite nanoparticles dissolved in PEGDA

The behavior of both coercive field and magnetic remanence as functions of the vertex field for the NC under study is shown in Figure 6.11. The steep increase at low vertex fields corresponds to the standard behavior of any hysteresis loop; however, the unsaturating behavior measured at high fields (in this case, above about 2500 Oe) is something unexpected, indicating that the notion itself of “major loop” is not directly applicable to our system, because there is no real reversible region in any magnetization loop. Note the strict relation existing between coercive field and magnetic remanence, which follow the same law of growth with increasing the vertex field. This is another feature not observed in standard ferromagnets or in SW systems.

It is possible to conclude that the present measurements provide additional incontrovertible evidence for the specificity of hysteresis phenomena in magnetic NCs; it is presumed that this behavior is related to interparticle interaction instead of intra-particle anisotropy; however, a general theory of hysteretic phenomena in magnetic NCs is unfortunately still lacking.

6.5 Nanocomposites Exhibiting Magnetoelectric Properties

NCs containing magnetic NPs in either a conducting or an insulating matrix can display various magnetoelectrical effects, ranging from magnetically induced electric polarization to magnetoresistance. Magnetoelectric properties make these materials eligible for a number of applications, as discussed in Chapter 7.

Conducting polymer NCs containing nanosized multiferroic materials such as bismuth ferrite (BFO, BiFeO_3) have been recently investigated. Multiferroics exhibit ferromagnetic and ferroelectric properties together; in Bismuth ferrite, electric polarization can be induced

by external magnetic field and magnetization can be modified by an applied electric field. Efforts are being taken to effectively induce multiferroic properties in a conducting polymer such as polyaniline (PANI) by dispersing magnetoelectric BFO NPs in it [32]. Multiferroic composite materials not requiring the presence of a polymeric matrix, such as $\text{BaTiO}_3\text{-CoFe}_2\text{O}_4$ NCs, are being actively investigated nowadays, but they fall beyond the scope of this chapter.

Giant magnetoresistance (GMR) effects, similar to the ones observed in nanogranular noble metal–transition metal alloys, for example, $\text{Cu}_{100-x}\text{Co}_x$ have been observed in conducting polymeric NCs containing Fe and/or Fe-oxide NPs after proper thermal treatment. In these materials often the resistivity exhibits a clearly nonmetallic behavior and monotonically increases with reducing T ; the conduction typically occurs via interparticle tunneling and/or hopping, and the tunneling/hopping rate displays clear spin-dependent characteristics. Usually, the measured GMR does not display particularly large values at room temperature, ranging around 1–2%; however, it can attain values up to about 10% in well-prepared samples [33]. Even in this case, an important issue is to prevent particle agglomeration and to achieve a good dispersion of NPs.

More recently, various magnetoresistance phenomena, including a very large GMR, have been observed in a number of different nonmagnetic NCs where silica NPs are embedded in a conductive polymeric matrix such as PANI [34]. In this case, the mechanism is to be ascribed to complex electronic effects (the so-called wavefunction shrinkage model).

6.6 Applications

Despite the lack of knowledge regarding the science behind the hyper-specialized field of magnetic polymer-based NCs, there is an amazingly high number of papers reporting practical applications, particularly as multifunctional smart materials, where the magnetic properties are coupled with some other characteristics, or exploited to easily produce an anisotropy in an NC where magnetic NPs align along the direction of an external magnetic field [35, 36].

Polymeric magnetite NCs have been investigated for their potential application in electrochromic devices, gas and vapor sensors, nonlinear optical systems, and photovoltaic solar cells [37]. Further, the magnetic properties of mixed iron oxides can be used in potential applications including magnetic filters, and the future generation of electronic, magnetic, and photonic devices used for information storage or magnetic imaging [38].

Polymeric magnetic composites can also be applied in an elegant and efficient way to obtain magnetic-responsive polymer materials exhibiting high amplitude magnetoresponse [39]: in Figure 6.12, the preparation route adopted by the authors and in Figure 6.13 the size distribution of the magnetic NPs within the NC have been reported.

Magnetic polymer actuators were developed by dispersing microparticles of carbonyl iron in silicone-based elastomers [40]. Such materials are characterized by a low Young's modulus (106 Pa) together with a high magnetization induced by the dispersion of the magnetic microparticles into the polymeric matrix. For these reasons, they exhibit large

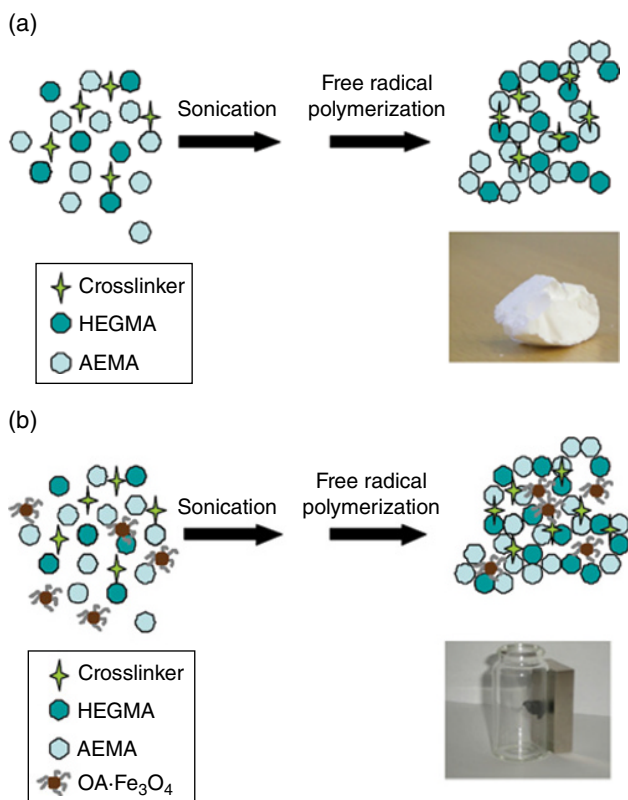


Figure 6.12 Schematic representation of the synthetic methodology: (a) pure matrix (a) and (b) magnetic NC. Papaphilippou et al. [41]. Reproduced with permission of Elsevier

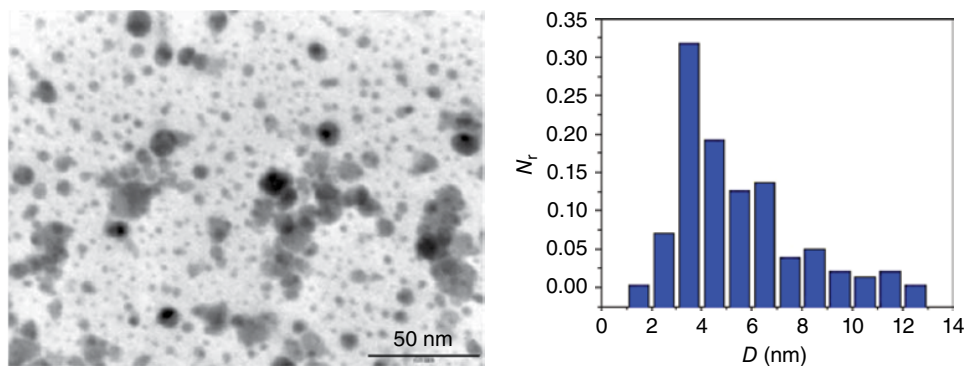


Figure 6.13 TEM image and size distribution of magnetite NPs. Papaphilippou et al. [41]. Reproduced with permission of Elsevier



Figure 6.14 Shape transition in the NC produced. Schmidt [39]. Reproduced with permission of John Wiley & Sons

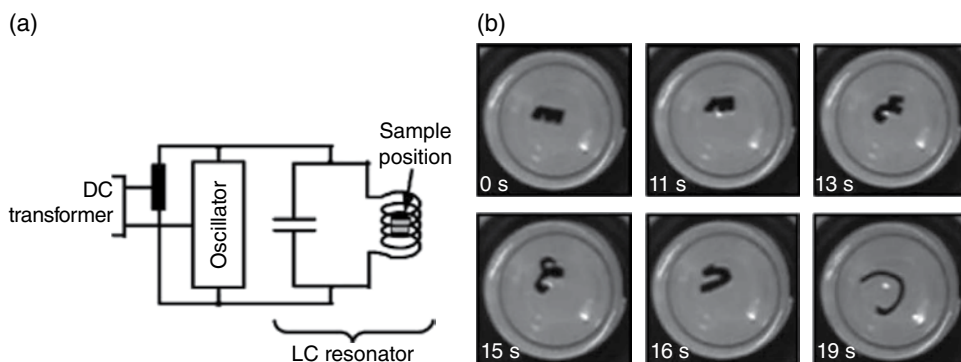


Figure 6.15 Schematic diagram of the LC resonant circuit (a) adopted to operate the shape transition in an SMP shown in (b). Schmidt [44]. Reproduced with permission of John Wiley & Sons

deformation, not only in field gradients but also in homogeneous magnetic fields. The significant variation of their tensile, compression, and shear moduli with the amplitude of the applied magnetic field makes them good candidates to design active dampers for anti-vibrating applications (e.g., in the automotive industry or to enhance the precision of rotating tools in mechanics workshops).

Hydrogels and other elastomeric materials that can be deformed in a controlled manner in homogeneous magnetic fields or gradients were successfully employed for magnetic guidance of drug delivery systems, manipulation of individual cells, and separation in complex biological media or environmental samples [41, 42].

Polymeric magnetic NCs prepared from thermoresponsive polymers can be remotely activated using alternating magnetic fields. This strategy was especially used for controlled drug delivery with injectable or implantable devices and in the area of shape-memory polymers (SMPs) [43].

Thermoplastic SMPs have been adopted for magnetic remote activation by filling them with magnetic NPs [44–46]. SMPs are capable of performing important shape changes, after the application of a programming in order to recover their original shape [47]; in Figure 6.14, an example of such capabilities is given, while a schematic of the apparatus used to produce the shape transition is shown in Figure 6.15. Generally, they are reticulated thermoplastic materials with a glass and/or melting transition temperature.

After deformation at a temperature higher than their transition temperature, the temporary shape is fixed by rapid cooling. Then, the original shape can be recovered by heating again above the transition temperature. Such materials can be useful for applications in a wide range of fields such as military defense, smart textiles, packaging, aerospace, adaptive optics, robotics, and biomedical engineering, like magnetic actuators or minimally invasive surgery devices. The thermally induced shape shifting of such materials can be triggered by exposing them to an alternating magnetic field; the heat generated by the magnetic NPs, under an alternating magnetic field, can also trigger useful phase transitions of SMPs.

Devices based on magnetically induced electric polarization such as those containing multiferroic NCs include nonvolatile memories, weak magnetic field sensors, transformers, gyrators, and microwave devices [48]. Devices based on NCs exhibiting isotropic GMR may be envisaged for use in many areas including biological detection, magnetic recording and magnetic storage, and sensors [33]. Generally speaking, devices exploiting magnetoelectrical phenomena in polymer NCs benefit from easy manipulation and cost-effective fabrication processes.

Finally, recent developments have shown a potential industrial application of magnetic NCs for oil spill recovery, where conventional technologies have failed so far. The magnetic properties are exploited for an easy recovery of a functionalized hydrophobic and oleophilic material, normally in the form of a sponge [49, 50].

References

- (1) R. D. Shull, H. M. Kerch, and J. J. Ritter, Magnetic properties of colloidal silica: Potassium silicate gel/iron nanocomposites, *J. Appl. Phys.*, **75**, 6840–6842, 1994.
- (2) B. H. Sohn, R. E. Cohen, and G. C. Papaefthymiou, Magnetic properties of iron oxide nanoclusters within microdomains of block copolymers, *J. Magn. Magn. Mater.*, **182**, 216–224, 1998.
- (3) P. Allia, P. Tiberto, M. Coisson, A. Chiolerio, F. Celegato, F. Vinai, M. Sangermano, L. Suber, and G. Marchegiani, Evidence for magnetic interactions among magnetite nanoparticles dispersed in photoreticulated PEGDA-600 matrix, *J. Nanopart. Res.*, **13**, 5615–5626, 2011.
- (4) M. Sangermano, L. Vescovo, N. Pepino, A. Chiolerio, P. Allia, P. Tiberto, M. Coisson, L. Suber, and G. Marchegiani, Photoinitiator-free UV-cured acrylic coatings containing magnetite nanoparticles, *Macromol. Chem. Phys.*, **211**, 2530–2535, 2010.
- (5) X. X. Zhang, J. M. Hernandez, J. Tejada, and R. F. Ziolo, Magnetic properties, relaxation, and quantum tunneling in CoFe_2O_4 nanoparticles embedded in potassium silicate, *Phys. Rev.*, **B54**, 4101, 1996.
- (6) D. D. Awschalom, D. P. Di Vincenzo, and J. F. Smith, Macroscopic quantum effects in nanometer-scale magnets, *Science*, **258**, 414, 1992.
- (7) G. C. Papaefthymiou, Nanometer-sized structures and the transition from the molecular to the solid state, *Phys. Rev.*, **B46**, 10366, 1992.
- (8) S. Sun, H. Zeng, D. B. Robinson, S. Raoux, P. M. Rice, S. X. Wang, and G. Li, Size-controlled synthesis of magnetite nanoparticles, *J. Am. Chem. Soc.*, **124**, 8204, 2002.
- (9) S. Z. Sun, D. B. Robinson, S. Raoux, P. M. Rice, S. X. Wang, and X. Li, Monodisperse MFe_2O_4 ($\text{M}=\text{Fe}, \text{Co}, \text{Mn}$) nanoparticles, *J. Am. Chem. Soc.*, **124**, 8204–8205, 2004.
- (10) P. Allia, M. Coisson, P. Tiberto, F. Vinai, M. Knobel, M. A. Novak, and W. C. Nunes, Magnetic properties study of iron-oxide nanoparticles/PVA ferrogels with potential biomedical applications, *Phys. Rev.* **B 64**, 1444201–12, 2001.

- (11) T. Nardi, M. Sangermano, Y. Leterrier, P. Allia, P. Tiberto, and J. E. Manson, UV-cured transparent magnetic polymer nanocomposites, *Polymer*, **54**, 4472–4479, 2013.
- (12) C. J. Brinker and G. W. Sherrer, *Sol–Gel Science: They Physics and Chemistry of Sol–Gel Processing*, Academic Press, New York, 1990.
- (13) M. Niederberger, G. Garnweitner, N. Pinna, and G. Neri, Non-aqueous routes to crystalline metal oxide nanoparticles: Formation mechanisms and applications, *Prog. Solid. State. Chem.*, **33**, 59, 2005.
- (14) M. Pinna, M. Antonietti, and M. Niederberger, A novel nonaqueous route to V_2O_5 and Nb_2O_5 nanocrystals, *Colloid Surf. A*, **250**, 211, 2004.
- (15) N. Pinna, G. Garnweitner, M. Antonietti, and M. Niederberger, Non-aqueous synthesis of high-purity metal oxide nanopowders using an ether elimination process, *Adv. Mater.*, **16**, 2196, 2004.
- (16) M. Sangermano, P. Allia, P. Tiberto, G. Barrera, F. Bondioli, N. Florini, and M. Messori, Photo-cured epoxy networks functionalized with Fe_3O_4 generated by non-hydrolytic sol–gel process, *Macromol. Chem. Phys.*, **214**, 508–516, 2013.
- (17) S. Penczek and P. Kubisa, Cationic Ring Opening Polymerization, in D. J. Brunelle Ed., *Ring-Opening Polymerization. Mechanisms, Catalysis, Structure, Utility*, Hanser, Munich, p. 13, 1993.
- (18) H. S. Khare and D. L. Burriss, A quantitative method for measuring nanocomposite dispersion, *Polymer*, **51**, 719–729, 2010.
- (19) A. C. Balasz, T. Emrik, and T. P. Russell, Nanoparticle polymer composites: Where two small worlds meet, *Science*, **314**, 1107–1110, 2006.
- (20) M. K. Corbierre, N. S. Cameron, M. Sutton, S. G. J. Mochrie, L. B. Lurio, A. Rühm, and R. B. Lennox, Polymer-stabilized gold nanoparticles and their incorporation into polymer matrices, *J. Am. Chem. Soc.*, **123**, 10411–10412, 2001.
- (21) U. Chatterjee, S. K. Jewrajka, and S. Guha, Dispersion of functionalized silver nanoparticles in polymer matrices: Stability, characterization, and physical properties, *Polym. Comp.*, **30**, 827–834, 2009.
- (22) S. Mørup, M. Fougts Hansen, and C. Frandsen, Magnetic interactions between nanoparticles, *Beilstein J. Nanotechnol.*, **1**, 182–190, 2010.
- (23) L. Del Bianco, F. Spizzo, M. Tamisari, M. Calbucci, and P. Allia, Study of the magnetic microstructure of Ni/NiO nanogranular samples above the electric percolation threshold by magnetoresistance measurements, *J. Phys. Condens. Matter.*, **24**, 306004 1–10, 2012.
- (24) M. B. Haider, R. Yang, H. Al-Brithen, C. Constantin, D. C. Ingram, A. R. Smith, G. Caruntu, and C. J. O'Connor, Room temperature ferromagnetism in CrGaN: Dependence on growth conditions in rf N-plasma molecular beam epitaxy, *J. Cryst. Growth*, **285**, 300–311, 2005.
- (25) U. Sobočan, G. Lee, H.-W. Kang, H. J. Kim, Z. Jagličič, and J. Dolinšek, The nature of magnetic state of small Fe_3O_4 nanoparticles, *J. Anal. Sci. Technol.*, **2A**, A8–A14, 2011.
- (26) P. Tiberto, G. Barrera, F. Celegato, M. Coisson, A. Chiolerio, P. Martino, P. Pandolfi, and P. Allia, Magnetic properties of jet-printer inks containing dispersed magnetite nanoparticles, *Eur. Phys. J. B*, **86**, 173 1–5, 2013.
- (27) P. Allia and P. Tiberto, Dynamic effects of dipolar interactions on the magnetic behavior of magnetite nanoparticles, *J. Nanopart. Res.*, **13**, 7277–7293, 2011.
- (28) J. M. D. Coey, *Magnetism and Magnetic Materials*, Cambridge University Press, Cambridge, UK, 2010.
- (29) G. Bertotti, *Hysteresis in Magnetism for Physicists, Materials Scientists, and Engineers*, Academic Press, New York, 1998.
- (30) P. Allia, M. Coisson, M. Knobel, P. Tiberto, and F. Vinai, Magnetic hysteresis based on dipolar interactions in granular magnetic systems, *Phys. Rev. B*, **60**, 12207–12218, 1999.
- (31) M. Vasilikaki, G. Margaritis, and K. Trohidou, Monte Carlo simulations on the magnetic behaviour of nanoparticle assemblies: Interparticle interaction effects, in P. Allia and A. Chiolerio

Eds. *Nanoparticles Featuring Electromagnetic Properties: From Science to Engineering*, Research Signpost, Trivandrum, 2012.

- (32) T. Prabhakaran and J. Hemalatha, Synthesis and characterization of magnetoelectric polymer nanocomposites, *J. Polym. Sci. B Polym. Phys.*, **46**, 2418–2422, 2008.
- (33) Z. Guo, H. Th. Hahn, H. Lin, A. B. Karki, and D. P. Young, Magnetic and magnetoresistance behaviors of particulate iron/vinyl ester resin nanocomposites, *J. Appl. Phys.*, **104**, 014314, 2008.
- (34) H. Gu, J. Guo, H. Wei, X. Zhang, J. Zhu, L. Shao, Y. Huang, N. Haldolaarachchige, D. P. Young, S. Wei, and Z. Guo, Magnetoresistive conductive polymer-tungsten trioxide nanocomposites with ultrahigh sensitivity at low magnetic field, *Polymer*, **55**, 944–950, 2014.
- (35) A. Chiolerio, S. Musso, M. Sangermano, M. Giorcelli, S. Bianco, M. Coisson, A. Priola, P. Allia, and A. Tagliaferro, *Diamond Relat. Mater.*, **17**, 1590–1595, 2008.
- (36) D. Fragouli, B. Torre, F. Villaflorida-Monteleone, A. Kostopolou, G. Nanni, A. Falqui, A. Casu, A. Lappas, R. Cingolani, and A. Athanassiou, Nanocomposite pattern-mediated magnetic interactions for localized deposition of nanomaterials, *ACS Appl. Mater. Interfaces*, **5**, 7253–7257, 2013.
- (37) Y. Long, Electrical and magnetic properties of polyaniline/Fe₃O₄ nanostructures, *Phys. B*, **370**, 121, 2005.
- (38) M. Wang, H. Singh, T. A. Hatton, and G. C. Rutledge, Field-responsive superparamagnetic composite nanofibers by electrospinning, *Polymer*, **45**, 5505, 2004.
- (39) J. Thevenot, H. Oliveira, O. Sandre, and S. Lecommandoux, Magnetic responsive polymer composite materials, *Chem. Soc. Rev.*, **42**, 7099–7116, 2013.
- (40) G. V. Stepanov, D. Y. Borin, L. R. Yu, P. V. Melenev, and N. S. Perov, Motion of ferroparticles inside the polymeric matrix in magnetoactive elastomers, *J. Phys. Condens. Matter*, **20**, 204121, 2008.
- (41) P. C. Papaphilippou, A. Pourgouris, O. Marinica, A. Taculescu, G. I. Athanasopoulos, L. Vekas, and T. Krasia-Christoforou, Fabrication and characterization of superparamagnetic and thermoresponsive hydrogels based on oleic-acid-coated Fe₃O₄ nanoparticles, hexa(ethylene glycol) methyl ether methacrylate and 2-(acetoacetoxy)ethyl methacrylate, *J. Magn. Magn. Mater.*, **323**, 557–563, 2011.
- (42) Z. Li, J. Shen, H. Ma, X. Lu, M. Shi, N. Li, and M. Ye, Preparation and characterization of sodium alginate/poly (N-isopropylacrylamide)/clay semi-IPN magnetic hydrogels, *Polym. Bull.*, **68**, 1153–1169, 2012.
- (43) N. S. Satarkar and J. Zach Hilt, Magnetic hydrogel nanocomposites for remote controlled pulsatile drug release, *Acta Biomater.*, **4**, 11–16, 2007.
- (44) A. M. Schmidt, Electromagnetic activation of shape memory polymer networks containing magnetic nanoparticles, *Macromol. Rapid Commun.*, **27**, 1168–1172, 2006.
- (45) U. N. Kumar, K. Kratz, W. Wagermaier, M. Behl, and A. Lendlein, Non-contact actuation of triple-shape effect in multiphase polymer network nanocomposites in alternating magnetic field, *J. Mater. Chem.*, **20**, 3404–3415, 2010.
- (46) U. N. Kumar, K. Kratz, M. Heuchel, M. Behl, and A. Lendlein, Shape-memory nanocomposites with magnetically adjustable apparent switching temperatures, *Adv. Mater.*, **23**, 4157–4162, 2011.
- (47) H. Meng and G. Li, A review of stimuli-responsive shape memory polymer composites, *Polymer*, **54**, 2199–2221, 2013.
- (48) F. Bai, H. Zhang, J. Li, and D. Viehland, Magnetic and magnetoelectric properties of as-deposited and annealed BaTiO₃-CoFe₂O₄ nanocomposite thin films, *J. Phys. D. Appl. Phys.*, **43**, 285002 1–7, 2010.
- (49) F. Gomes de Sousa, J. Alves Marins, C. H. M. Rodrigues, and J. C. Pinto, A magnetic composite for cleaning oil spills on water, *Macromol. Mater. Eng.*, **295**, 942–948, 2010.
- (50) N. Chen and Q. Pan, Versatile fabrication of ultralight magnetic foams and application for oil-water separation, *ACS Nano*, **8**, 6875–6883, 2013.

7

Optical Properties of Polymer Nanocomposites

Ignazio Roppolo¹, Marco Sangermano² and Alessandro Chiolerio¹

¹*Center for Space Human Robotics, Istituto Italiano di Tecnologia, Italy*

²*Applied Science and Technology Department, Politecnico di Torino, Italy*

7.1 Introduction

The aspect of a material and its interaction with light is of fundamental importance both in functional and decorative application. When light interacts with a material, there are three possible main effects: absorption, transmission, and reflection of light. These three components are directly correlated, and they depend on the nature of the material (refractive index, coefficient of absorption, surface roughness, etc.), the wavelength of the incident light, and its angle of incidence. However, there are also other effect such as scattering and light re-emission (see Figure 7.1) that are important from the technological point of view since they are the basis for many devices like LED, LASER, and up-converter.

The incorporation of nanoparticles in polymer matrices offers the possibility of substantial improvements to the optical properties of these materials with only a small amount on nanoparticles [1] since they can influence strongly the physical properties of the hosting polymeric matrices (e.g., refractive index and coefficient of absorption) but also give new characteristics to the material like light emission.

In this chapter the main trends of research in the control of the optical properties of polymeric nanocomposites, the strategies for obtaining new properties by nanoparticles incorporation, and the most important technological application as optical devices of polymeric nanocomposites will be presented.

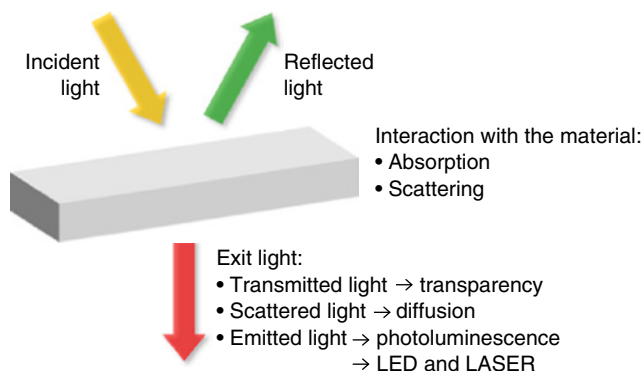


Figure 7.1 *Scheme of the possible interactions light/matter*

7.2 Photoluminescence and Related Applications

According with the IUPAC's Gold book, photoluminescence (PL) is defined as *Luminescence from direct photoexcitation of the emitting species* [2] and it consists in one of the possible physical effects resulting from the interaction of light with matter [3].

In the past several decades, there was an enormous demand for photoluminescent materials. Research on fluorescent polymers gathered great scientific attention because of their interesting properties and important application both in materials and life science [4].

Regarding the polymer world, there are two main directions for obtaining photoluminescent materials: the first one is the use of polymer that is intrinsically fluorescent having fluorescent groups (i.e., conjugated polymer) in the main chain or as pendant. Luminescent properties of different polymers were largely investigated since the 1950s [5–7]. In this frame, the latest research progress in fluorescent polymers is focused on the formation and PL of fluorescent polymers with new architecture.

The second route is the synthesis of material in which the polymeric matrix is only a host material and the luminescence behavior was given by a filler that could be either organic or inorganic. Since the formulation of polymeric mixture with luminescent pigments is a well-established procedure even in industry, in the past years the synthesis of luminescent polymeric composites, in particular nanocomposite, has gathered a great scientific attention in order to take advantage of the great potentialities of new inorganic luminescent particles that are studied all over the world.

Polymer composites presents some advantages compared to the intrinsically photoluminescent polymer. The potential use of light-emitting polymer is in fact ultimately limited by their low quantum efficiency as well as by their poor stability due to oxygen interaction [8]. Moreover even workability is not so easy: nearly all the formation processes are by casting and so involves the use of solvents, making them not environment-friendly. Finally, in order to protect the photoactive layer by the oxidation and photooxidation, often the

devices are layered, in which transparent polymeric materials surround the luminescent film preventing oxygen diffusion. This leads to an increase in the costs and complexity of the devices.

For these reasons in many applications, the use of a polymeric composite is favored. By dispersing photoluminescent fillers in a hosting polymeric matrix, it is possible to apply standard techniques of polymer processing to the development of photoactive material. Moreover, standard polymers present improved thermo-mechanical properties and a greater resistance toward the aging if compared to intrinsic photoluminescent polymers.

On the other hand, as for all the composite materials, the dispersion of the fillers and their distribution in the polymer matrix is a key challenge in order to obtain uniform properties, both optical and mechanical. Finally, for many applications, transparency is a key point. In order to obtain this property, it is necessary to embed fillers that have nanometrical (e.g., quantum dots or QDs) or molecular scale (e.g., rare-earth complexes) in a transparent polymeric matrix, thereby obtaining polymeric nanocomposites in this way.

Here, the main classes of photoluminescent nanofillers dispersed in polymeric matrices and the most relevant application of photoluminescent polymer nanocomposites will be presented.

7.2.1 Nanocomposite with Quantum Dots

QDs are semiconductor nanocrystals generally composed of atoms of elements from II–IV groups (e.g., CdSe, CdS, ZnS, and ZnSe) or III–V groups (e.g., InP and InAs) defined as particle with a dimension smaller or comparable to the exciton Bohr radius, usually between 2 and 20 nm [9]. The photoluminescent properties of the QDs arise from interaction between free photogenerated electrons and holes [10]. Light is absorbed when the energy of the exciting radiation overcomes the band-gap of the materials; in this process, electrons are promoted from the valence band to the conduction band. Light emissions arise from the recombination of free or trapped charge carriers (electrons or holes), and this mechanism is called excitonic fluorescence and is observed as a sharp peak [11]. By changing the dimension of the QDs, the emitted light can be tuned from the ultraviolet (UV) range to all the visible range up to the near-infrared (NIR) (Figure 7.2) due to the quantum effect induced by the particle size [10, 12].

One of the most important trends in the past 20 year is the dispersion of QDs in polymeric matrices. From a technological point of view, the fabrication of bulk QD/polymer nanocomposites, and in particular, thin film architectures comprising semiconductor nanoparticles and polymers, is extremely relevant. The development of optoelectronic devices, such as solar cells or light-emitting diodes, has seen its most significant improvement through the control of the quality of such hybrid thin films. In any case, in order to synthesize materials for such applications, issues concerning the poor compatibility of QDs with polymeric environments must be solved. Such problems of compatibility in fact generally lead to agglomeration of the QDs inside the polymers and, consequently, to the



Figure 7.2 Light emission of ZnS-capped CdSe excited in the UV range. Dimension of colloidal QDs increase from 2 (left) to 6 (right) nm. Chan et al. [10]. Reproduced with permission of Elsevier (See insert for color representation of the figure)

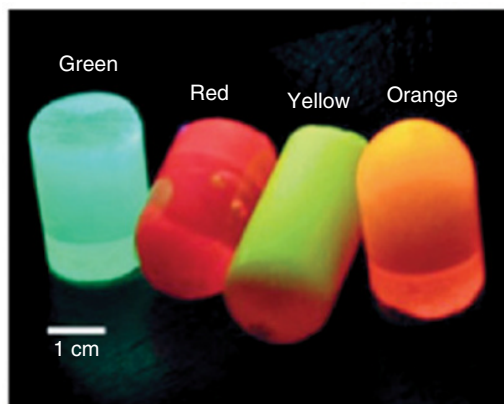


Figure 7.3 PS/QDs nanocomposites. Zhang et al. [23]. Reproduced with permission of John Wiley & Sons (See insert for color representation of the figure)

quenching of the luminescence and loss of transparency of the composite. One of the goals is therefore to establish methods to obtain transparent materials with high concentration of QDs [13].

In this frame, the main direction is to modify the surface of QDs in order to improve the solubility of QDs in polymeric matrices [14, 15], and also to tune their emission [16]. From the matrix point of view, QDs/polymer composite were prepared dispersing different types of QDs (ZnO, CdS, ZnSe, etc.) in different polymer matrices such as PE [17], PMMA [15, 18–20], polystyrene [15, 21–23] (Figure 7.3), PVA [24, 25], epoxy [26–28], polyurethanes [29, 30], and many others [31–36].

Photoluminescent nanocomposite with QDs was also synthesized via UV-curing both in radical [37–41] and cationic systems [28, 42, 43].

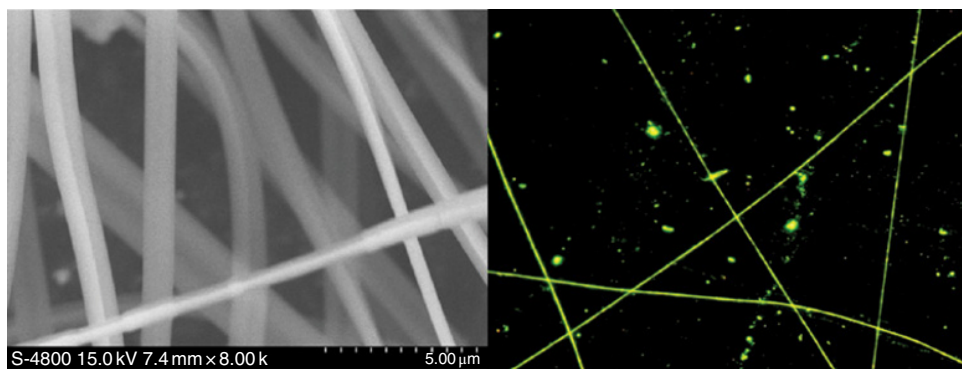


Figure 7.4 Polystyrene fibers with copper photoluminescent complexes. Li [57]. Reproduced with permission of Elsevier

7.2.2 Transition Metal Nanocomposites

Transition metal ions represent the most important class of luminescent center. Their importance could be easily represented considering that in the 1960s, the study of Cr^{3+} in Al_2O_3 crystal (ruby) was the basis of the development of solid-state laser. Transition metals are extensively used as PL active centers both in inorganic lattice and with organic complex (e.g., clusters and MOF). They have an incompletely filled d shell so their electronic configuration is d^n ($0 < n < 10$). Energy configuration diagrams of the ions that change n value as well as the effect of the crystal field were extensively studied in the literature [44–47].

Regarding transition metal particles, they are often employed in combination with conjugated polymers in order to improve the properties of OLED, as it is reported by Cheuk-Lam Ho and Wai-Yeung Wong in a recent review [48], but also in medical applications as theranostic [49]. They were also employed in other polymeric matrices as polycarbonate [50], PMMA [51–54], PE [55, 56], PS (Figure 7.4) [57–60], PDMS [48, 59, 61], and many others [62–64] most of all as oxygen sensors and as probes for the polymerization or the medium rigidity.

Regarding photopolymerized materials, there are few studies in the literature on transition metal photoluminescent composites. Recently, Gao *et al.* published an extended review on their work of photocured gold nanocomposite using the antenna effect of the gold to enhance the efficiency of solar cells [65]. In any case the main use of transition complexes in UV curable formulation was as probe of the photocuring measuring the shift of main peak of emission during the photopolymerization process [66–69]. However, recently there was an increasing interest in investigating photocurable materials containing transition metal complex for optical application [70] (Figure 7.5) and with tunable properties [71, 72].

7.2.3 Rare-Earth Polymer Nanocomposites

The last main class of photoluminescent polymer composite is the one based on rare-earth nanoparticles. Rare-earth metals, by IUPAC definition, consist in lanthanide elements plus

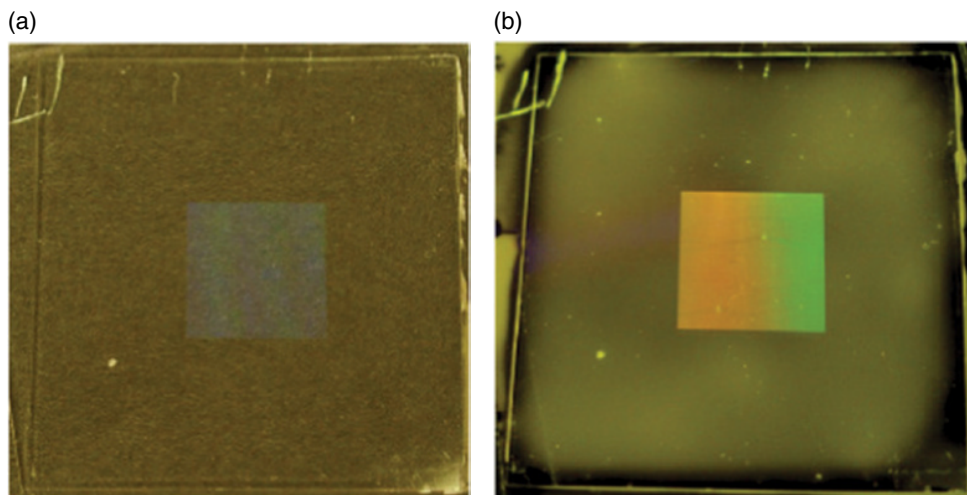


Figure 7.5 Acrylate composite film ($5\mu\text{m}$) containing copper iodide clusters ($2.5\times 2.5\text{ cm}$) on glass substrate with a square patterned area in the center (a) under ambient light and (b) under UV irradiation at 312 nm (UV lamp) at room temperature. Roppolo et al. [70]. Reproduced with permission of Royal Society of Chemistry (See insert for color representation of the figure)

scandium and yttrium [73]. In this case, the emission is due to transitions inside the 4f shell, thus intraconfigurational f–f transitions. The incomplete filled 4f shell is shielded from the surroundings by the filled $5s^2$ and $5p^6$ orbitals; therefore, the effect of the host lattice or of the surrounding organic ligands on the intra-4f transition is small but, in any case, essential. Although PL of rare-earth ions can be an efficient process, all lanthanide ions suffer from weak light absorption. Because the molar absorption coefficients ϵ of them are smaller than $10^4\text{ mol}^{-1}\text{ cm}^{-1}$, only a very low amount of radiation is absorbed by direct excitation in the 4f levels. Since the luminescence intensity is not only proportional to the luminescence quantum yield but also to the amount of radiation absorbed, low light absorption lead to weak luminescence. However, the problem of weak light absorption can be overcome by the so-called *antenna effect* (or *sensitization*) [74]. This could be achieved by dispersing in host lattices or bonding the ions with organic ligand. Because of the intense absorption bands of the inorganic matrices or organic chromophores, much more light can be absorbed and, subsequently, the excitation energy is transferred from the organic ligands to the lanthanide ion by intramolecular energy transfer [74, 75]. Thus principally nanoparticles doped with rare earths or rare-earth organic are used as filler for nanocomposites.

Many polymeric matrices were used as hosting materials: PS [76–79], PMMA [80–84], polyethylene glycol [85], PEO [86, 87], PVA [88, 89], polycarbonate [90], PDMS [91], and many more [92–97] with also particular application such as γ -ray scintillators [98], temperature sensors [99], or up-converters [100]. Some materials were even synthesized via UV-curing both in radical [101–104] (Figure 7.6) and cationic systems [105, 106] or electrospinning [107].

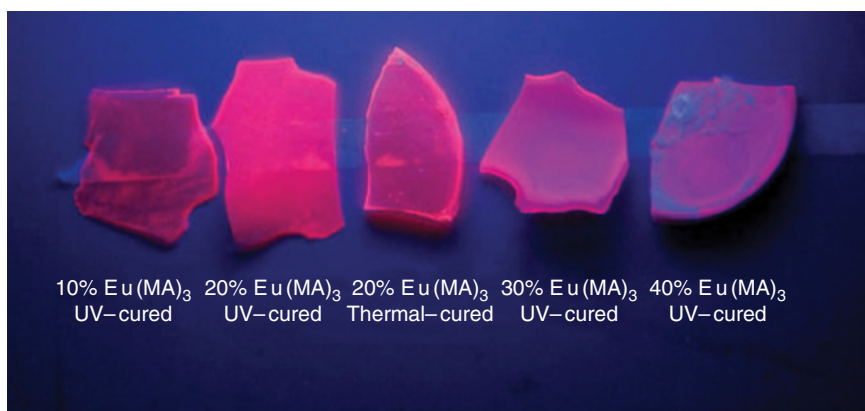


Figure 7.6 Urethanes acrylates UV and thermal cured containing Europium complexes. Zhou et al. [101]. Reproduced with permission of John Wiley & Sons (See insert for color representation of the figure)

7.3 Light Emission in Polymer Nanocomposites: From Science to Applications

As already stated in previous section, rare-earth ions have been widely used as fillers in inorganic matrices for the realization of luminescent devices, such as LEDs, LASERs, optical amplifiers, and biological fluorescent labeling. It is possible to overcome the problem of quenching from the polymeric matrix, due to a huge vibrational spectrum, by incorporating those ions in inorganic nanoparticles.

As an example in Figure 7.7, we report the flowchart of a typical synthesis for inorganic NPs of $Tb^{3+} : LaF_3$ which were then dispersed in PMMA to produce a sharp emission spectra with a typical FWHM < 5 nm, as shown in the emission spectra of Figure 7.8 [108].

A typical application for hybrid QD/phosphor nanocomposites is the realization of white light-emitting devices, WLEDs (polymers), intentionally exploiting transparency, flexibility, processability, and cost-effectiveness of the host matrices. Different approaches have been proposed for the realization of such materials, such as *in situ* polymerization [109, 110], electrostatic interaction [111, 112], physical entrapment [113], and frontal polymerization [114]; particularly interesting is its high reaction rate that prevents the easy occurrence of photooxidation, photocorrosion, and luminescence decrease. As an example, we report the typical route for the frontal polymerization synthesis of white light emitting CdS-poly (2-hydroxyethyl acrylate (HEA)-*co-N*-vinylcarbazole NVK) nanocomposites, Figure 7.9. Such materials are then blended with their compensating-color nanocomposite, to produce a broad white spectrum, and are finally positioned on top of a semiconductor LED, Figure 7.10.

As a different approach, we propose the fabrication scheme of a nanocomposite again for WLED applications, based on *N,N*-dimethylacrylamide (DMAA) matrix, containing a dispersion of ZnS nanoparticles, functionalized with 2-(2-hydroxyphenyl)-benzoxazol (BOX),

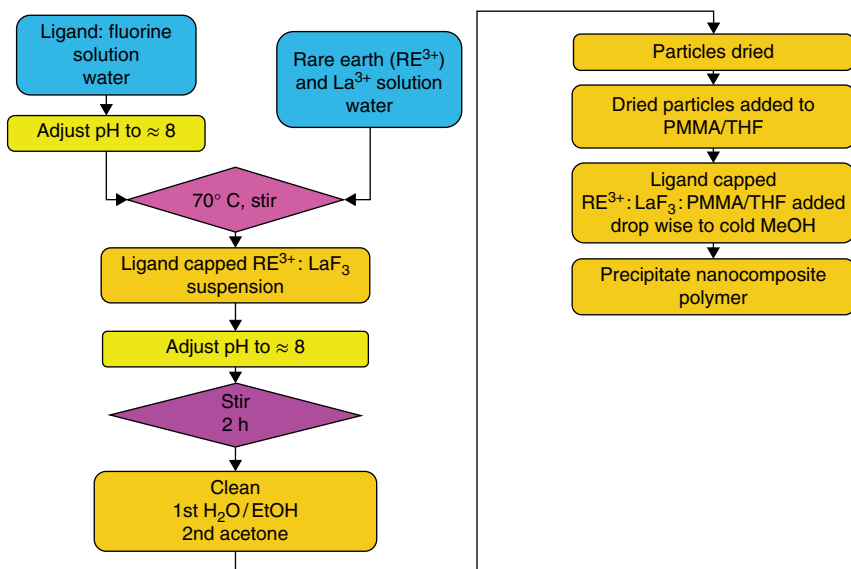


Figure 7.7 $Tb^{3+}:LaF_3$ NP synthesis flowchart. Gipson et al. [108], <http://www.hindawi.com/journals/jnt/2011/386503/>. Used under CC-BY-SA 3.0. <http://creativecommons.org/licenses/by/3.0/>

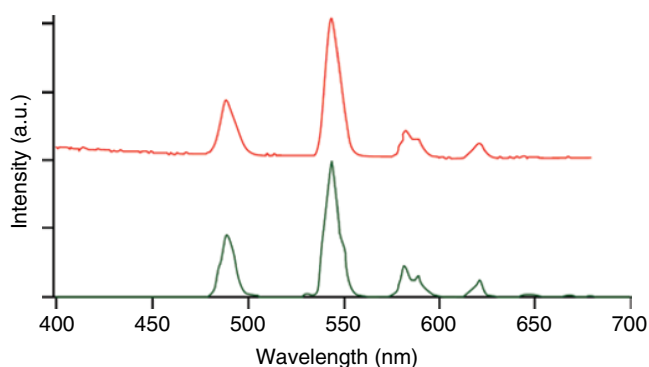


Figure 7.8 Emission spectra of $Tb^{3+}:LaF_3$ NPs in PMMA nanocomposites excited at 350 nm (top curve) and 265 nm (bottom curve) respectively; spectra are normalized to the 540 nm peak. Gipson et al. [108], <http://www.hindawi.com/journals/jnt/2011/386503/>. Used under CC-BY-SA 3.0. <http://creativecommons.org/licenses/by/3.0/>

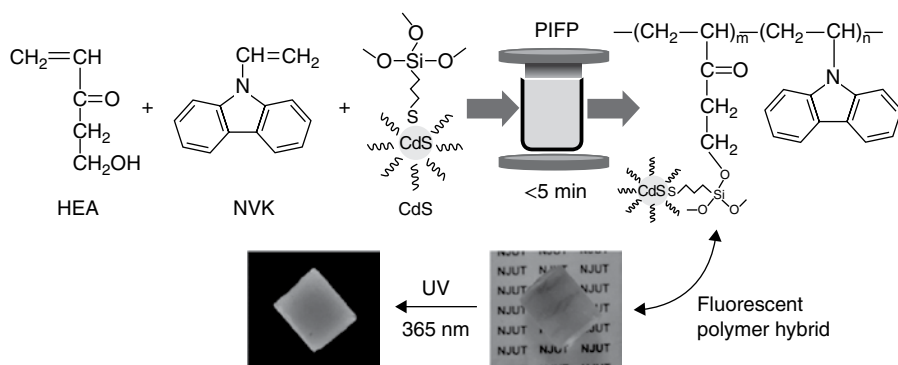


Figure 7.9 Flowchart related to the preparation of a CdS-poly(HEA-co-NVK) nanocomposite by frontal polymerization. Zhou et al. [114]. Reproduced with permission of John Wiley & Sons

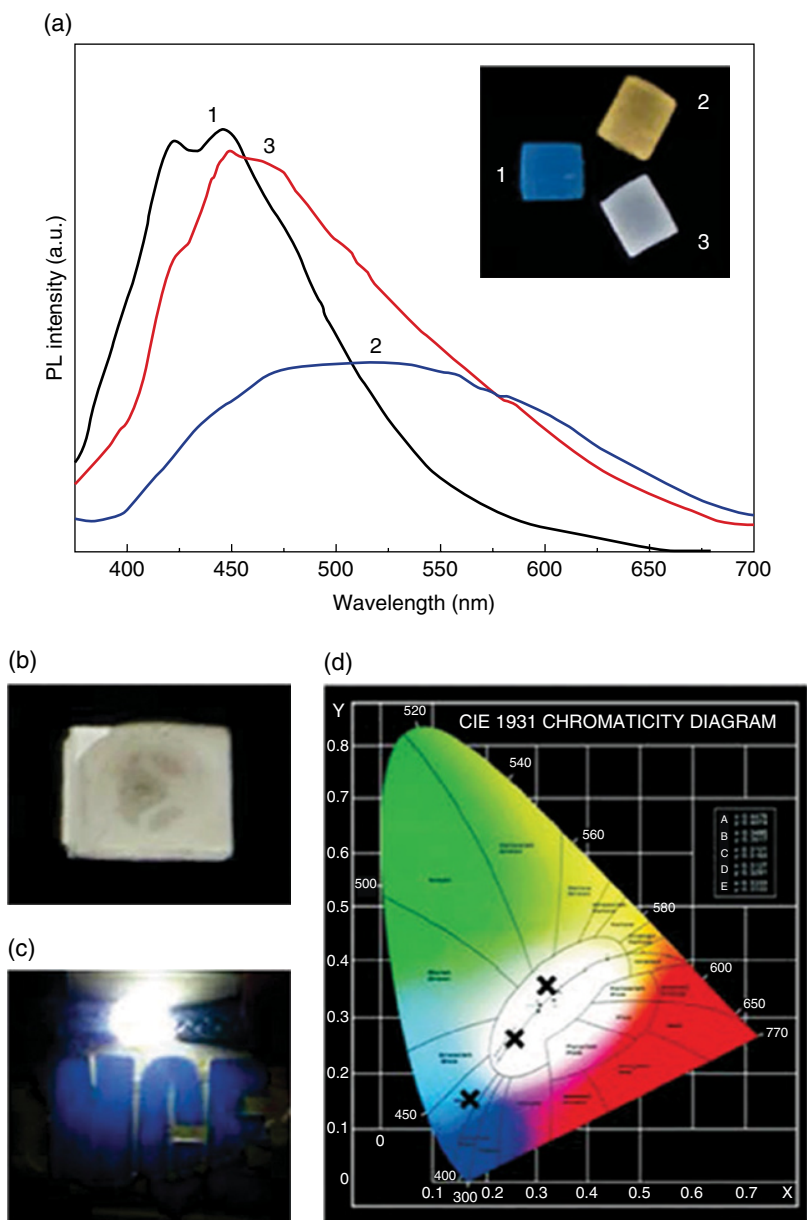


Figure 7.10 PL spectra (a), digital images of the nanocomposites (b), emitting WLED in operation (c) and chromaticity diagram of the systems based on frontally polymerized CdS-poly(HEA-co-NVK) nanocomposites (d). Zhou et al. [114]. Reproduced with permission of John Wiley & Sons (See insert for color representation of the figure)

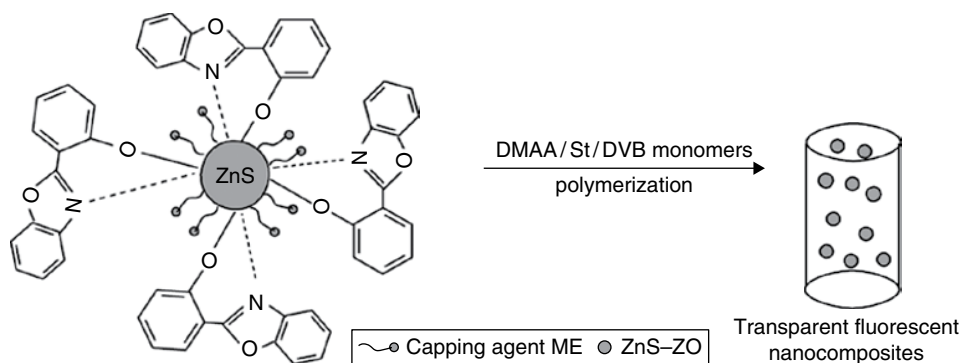


Figure 7.11 Scheme related to the preparation of a ZnS-BOX-DMAA nanocomposite by in situ bulk polymerization. Liu et al. [115]. Reproduced with permission of Elsevier

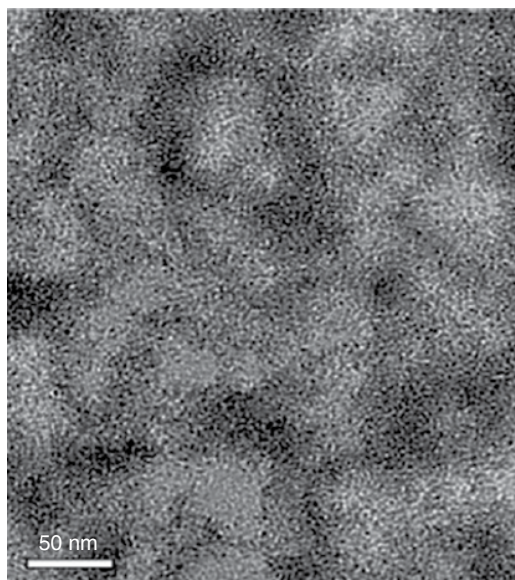


Figure 7.12 TEM image of the ZnS-BOX-DMAA nanocomposite bulk sample. Liu et al. [115]. Reproduced with permission of Elsevier

in Figure 7.11 and the relative TEM image in Figure 7.12 [115]. ZnS is a preferred choice due to its relative abundance and cost.

When the QD-incorporated polymer is used as a waveguide, it is possible to exploit interesting properties, in particular, by adding multiple materials, a broad range of visible spectrum can be guided into a patterned structure. As an example, CdS, CdTe, CdSe, and/or PbS embedded into PMMA matrix have been used and characterized, according to the experimental setup shown in Figure 7.13, to collect the waveguided spectrum of Figure 7.14,

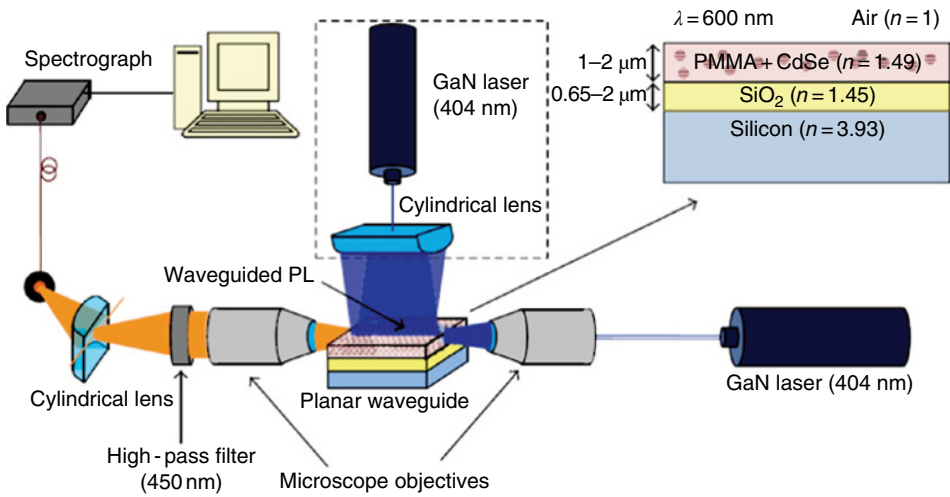


Figure 7.13 Experimental setup for the characterization of nanocomposite waveguides. Gordillo et al. [116], www.hindawi.com/journals/jnm/2012/960201. Used under CC-BY-SA 3.0 <http://creativecommons.org/licenses/by/3.0/>

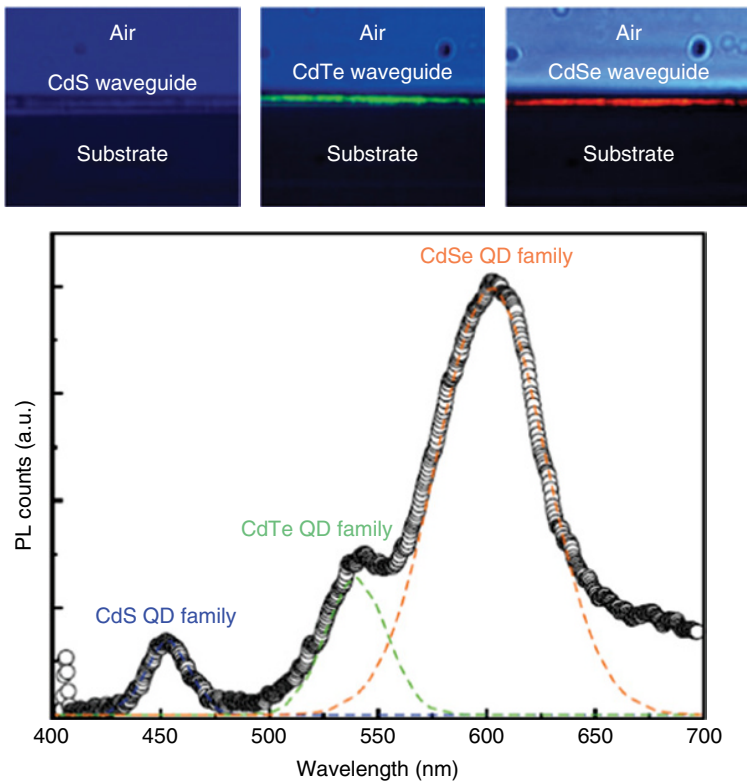


Figure 7.14 PL waveguided spectrum obtained from nanocomposite QD-PMMA thin-film waveguides. Gordillo et al. [116], www.hindawi.com/journals/jnm/2012/960201. Used under CC-BY-SA 3.0 <http://creativecommons.org/licenses/by/3.0/>

where the effect of adding CdS, CdTe, and CdSe in the same nanocomposite material is clearly visible [116].

Other interesting applications of nanocomposites are those systems where metal NPs are incorporated to quench the triplet states in organic LEDs (OLEDs). Normally, the main materials employed in device fabrication are fluorescent dyes and polymers that emit light as a result of the radiative decay of singlet excitons. The operation of LEDs generates both spin-symmetric triplets and spin-antisymmetric singlets, in the ratio of 3:1. However, the energy of triplet excitons is wasted via non-radiative processes. Furthermore long-lived triplet excitons via energy transfer produce singlet oxygens that are able to initiate oxidation processes. A possible solution is the incorporation of Au NPs, for example, where the triplet excitons are quenched by the overlap with NP optical absorption spectra. In Figure 7.15, we present the great enhancement of quantum efficiency in a blue OLED device where the poly(9,9'-dioctylfluorene) (PDOF) layer incorporates Au NPs [8].

Most interestingly, the possibility of generating coherent light from a nanocomposite material was recently explored. In particular, the experiment conceived a high refractive index filler, ZrO_2 NPs dispersed in an acrylate monomer, doped with Pyrromethene 567 laser dye [117]. Distributed feedback (DFB) resonators, which may be created inducing volume repetitions of high refractive index portions within low refractive index areas, provide the necessary light coupling to obtain a stable lasing. The periodic modulation of refractive index was produced by holographic lithography, according to the configuration shown in Figure 7.16. Resulting lasing output is shown in Figure 7.17.

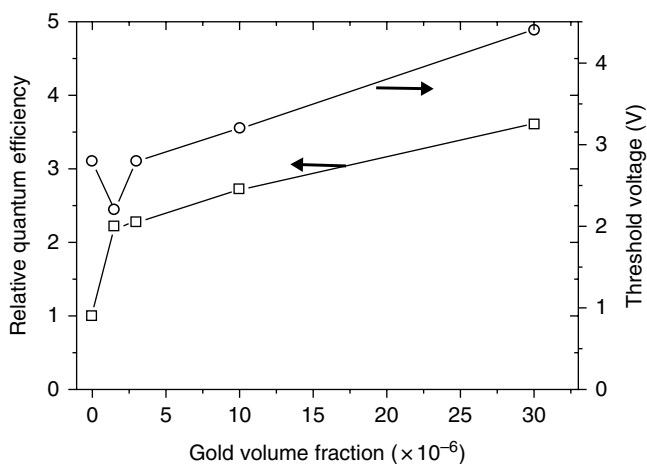


Figure 7.15 Relative quantum efficiency and threshold voltage as a function of the Au NP content in Au-DPOF OLED devices. Park et al. [8]. Reproduced with permission of American Chemical Society

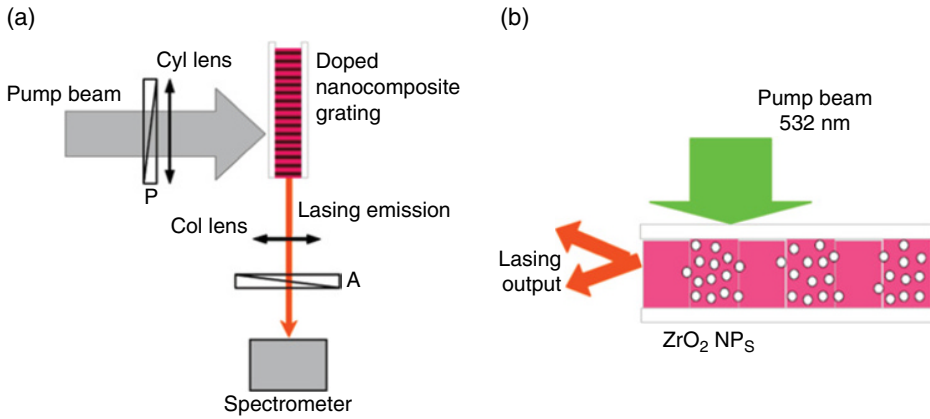


Figure 7.16 (a) Schematic representation of the lasing experiment setup and (b) nanocomposite DFB grating. Smirnova et al. [117]. Reproduced with permission of Institute of Physics

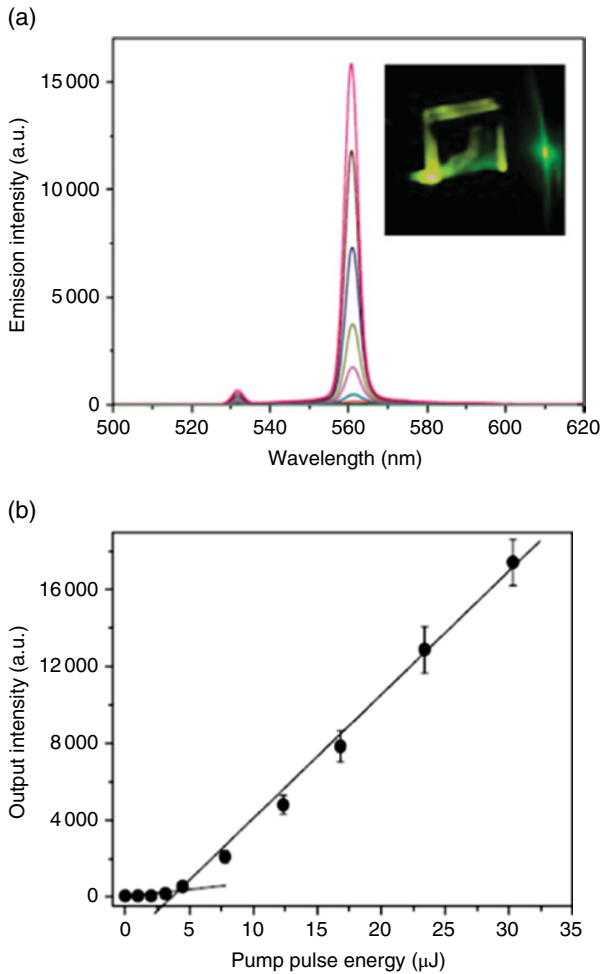


Figure 7.17 (a) Lasing emission in the nanocomposite DFB grating containing 23 wt% of ZrO_2 NPs: (b) Emission spectrum and output intensity. Smirnova et al. [117]. Reproduced with permission of Institute of Physics

7.4 Transparency and Adsorbance in Polymer Nanocomposite

Since transparency in the visible range is one of the most important polymer properties, inorganic nanoparticles were used to tune the absorption of the polymeric nanocomposites in the other spectral ranges in order to create novel materials with shielding properties [118]. In this regard, the synthesis of UV and IR shields is of particular interests for improving the outdoor stability of polymers or in coating for solar cell applications [119].

TiO₂ and ZnO are the two most important classes of nanoparticles used for creating nanocomposites because nanoparticles of these oxides absorb in the UV range but do not absorb in the visible range. Moreover, by embedding particles with a diameter lower than 40 nm, also the light scattering is negligible thus maintaining a high transparency [102].

Titanium dioxide nanoparticles were used as fillers for producing polymeric UV shield in many matrices such as polyvinylacetate [120], polyurethanes [121], epoxies [122], polyvinyl alcohol [123], and others [124, 125]. However, this metal oxide is photochemically active when it is in the anatase phase and thus can degradate the polymer matrix under UV irradiation [118]. For this reason, ZnO is preferable as nanofillers for UV shields since ZnO is a strong UV absorber but with a lower photochemical activity if compared with TiO₂.

ZnO oxide was used as active filler in polystyrene [126–128], polymethyl methacrylate [129], PVDF [130], epoxy [131], silicones [132], or polymer blends [133–135] maintaining high transparency (Figure 7.18).

Also other nanoparticles were employed in order to synthesize UV shielding properties such as indium oxide [136], iron sulfide [137], and cadmium telluride [138].

Other interesting applications, pushed by the increasing environmental and energy saving concern, regard the use of nanoparticles for synthesizing novel materials that possess selective absorption in other spectral ranges such as IR [139, 140] (see Figure 7.19) or microwaves [141].



Figure 7.18 PS/PMMA polymer blend containing 5% ZnO Nanoparticles. Ge et al. [135]. Reproduced with permission of Wiley (See insert for color representation of the figure)

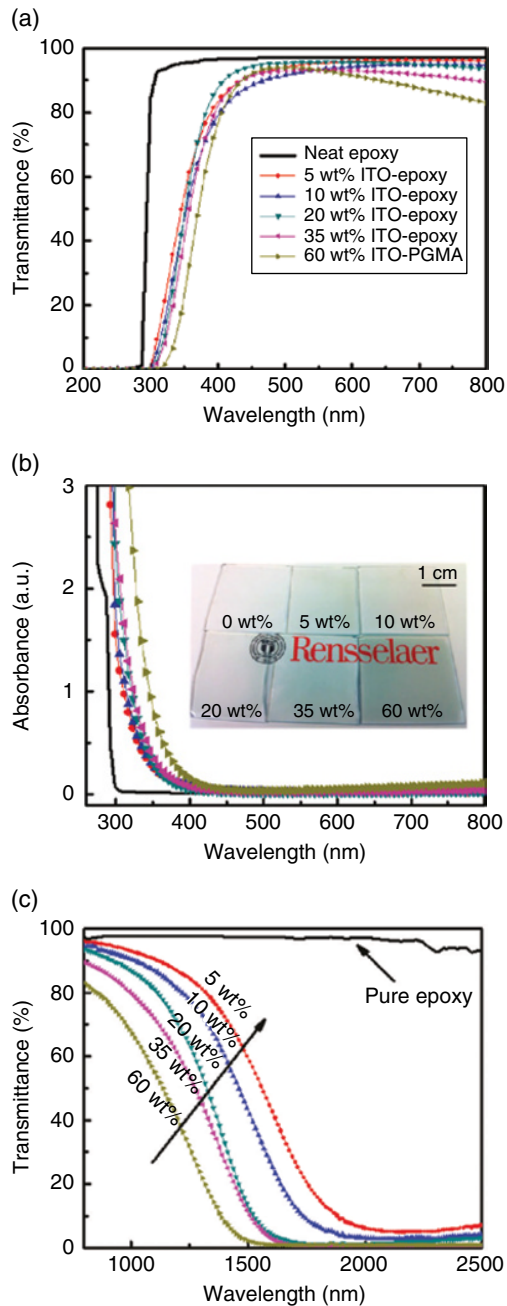


Figure 7.19 Transmittance (a) and absorbance (b) spectra in the UV-visible range of ITO/epoxy nanocomposites containing different amount of indium tin oxide (ITO) nanoparticles. (c) Near-IR spectra of ITO/epoxy nanocomposites containing different amount of ITO nanoparticles. Tao et al. [139]. Reproduced with permission of American Institute of Physics

References

- (1) Jancar J., Douglas J.F., Starr F.W., Kumar S.K., Cassagnau P., Lesser A.J., Sternstein S.S., Buehler M.J. (2010) *Polymer* **51**: 3321–3343.
- (2) Braslavsky S.E. (2007) *Pure Appl. Chem.* **79**: 293–465.
- (3) Valeur B., *Molecular Fluorescence Principles and Applications*, Wiley-VCH Verlag GmbH, Weinheim, 2002.
- (4) Yuan J., Wang S., Shan J., Peng J., Wei L., Xu X. (2010) *Int. J. Polym. Sci.* **2010**: 1–2.
- (5) Beer M. (1956) *J. Chem. Phys.* **25**: 745–750.
- (6) Brown F.H., Furst M., Kallamann H. (1959) *Discuss. Faraday Soc.* **27**: 43–56.
- (7) De Waard H., Prins W., Prins A. (1954) *Appl. Sci. Res.* **3**: 372–376.
- (8) Park J.H., Lim Y.T., Park O.O., Kim J.K., Yu J.W., Kim Y.C. (2004) *Chem. Mater.* **16**: 688–692.
- (9) Alivisatos A.P. (1996) *Science* **271**: 933–937.
- (10) Chan W.C.W., Maxwell D.J., Gao X., Bailey R.E., Han M., Nie S. (2002) *Curr. Opin. Biotechnol.* **13**: 40–46.
- (11) Chan W.C.W., Nie S.M. (1998) *Science* **281**: 2016–2018.
- (12) Guyot-Sionnest P. (2008) *C. R. Phys.* **9**: 777–787.
- (13) Tomczak N., Jančzewski D., Han M., Vancso G.J. (2009) *Prog. Polym. Sci.* **34**: 393–478.
- (14) Murakoshi K., Hosokawa H., Saito M., Wada Y., Yanagida S. (1998) *J. Colloid Interface Sci.* **203**: 225–228.
- (15) Tamborra M., Striccoli M., Comparelli R., Curri M.L., Petrella A., Agostiano A. (2004) *Nanotechnology* **15**: S240–S244.
- (16) Garreau A., Massuyeau F., Cordier S., Molard Y., Gautron E., Bertoncini P., Faulques E., Wery J., Humbert B., Bulou A., Duvail J.L. (2013) *ACS Nano* **7**: 2977–2987.
- (17) Ushakov N.M., Yurkov G.Y., Baranov D.A., Zapsis K.V., Zhuravleva M.N., Kochube V.I., Kosobudski I.D., Gubin S.P. (2006) *Opt. Spectrosc.* **101**: 248–252.
- (18) Sun D., Miyatake N., Sue H.J. (2007) *Nanotechnology* **18**: 215606.
- (19) Farmer S.C., Patten T.E. (2001) *Chem. Mater.* **13**: 3920–3926.
- (20) Khanna P.K., Singh N. (2007) *J. Lumin.* **127**: 474–482.
- (21) Wang H.Q., Wang J.H., Li Y.Q., Li X.Q., Liu T.C., Huang Z.L., Zhao Y.D. (2007) *J. Colloid Interface Sci.* **316**: 622–627.
- (22) Šajinović D., Šaponjić Z.V., Cvjetičanin N., Marinović-Cincović M., Nedeljković J.M. (2000) *Chem. Phys. Lett.* **329**: 168–172.
- (23) Zhang, H., Cui, Z., Wang, Y., Zhang, K., Ji, X., Lü, C., Yang, B., Gao, M. (2003) *Adv. Mater.* **15**: 777–780.
- (24) Tekin E., Smith P.J., Hoepfener S., van den Berg A.M.J., Susha A.S., Rogach A.L., Feldmann J., Schubert U.S. (2007) *Adv. Funct. Mater.* **17**: 23–28.
- (25) Pucci A., Boccia M., Galembeck F., de Paula Leite C.A., Tirelli N., Ruggeri G. (2008) *React. Funct. Polym.* **68**: 1144–1151.
- (26) Zou W., Du Z.J., Li H.Q., Zhang C. (2011) *Polymer* **52**: 1938–1943.
- (27) Li Y.Q., Fu S.Y., Mai Y.W. (2006) *Polymer* **47**: 2127–2132.
- (28) Sun D., Sue H.J., Miyatake N. (2008) *J. Phys. Chem. C* **112**: 16002–16010.
- (29) Cao X., Li C.M., Bao H., Bao Q., Dong H. (2007) *Chem. Mater.* **19**: 3773–3779.
- (30) Bowers II M.J., McBride J.R., Rosenthal S.J. (2005) *J. Am. Chem. Soc.* **127**: 15378–15379.
- (31) Wood V., Panzer M.J., Chen J., Bradley M.S., Halpert J.E., Bawendi M.G., Bulovic V. (2009) *Adv. Mater.* **21**: 2151–2155.
- (32) Xiong H.M., Wang Z.-D., Liu D.P., Chen J.S., Wang Y.G., Xia Y.Y. (2005) *Adv. Funct. Mater.* **15**: 1751–1756.
- (33) Firth A.V., Haggata S.W., Khanna P.K., Williams S.J., Allen J.W., Magennis S.W., Samuel I.D.W., Cole-Hamilton D.J. (2004) *J. Lumin.* **109**: 163–172.
- (34) Abdullah M., Lenggoro I.W., Okuyama K., Shi F.G. (2003) *J. Phys. Chem. B* **107**: 1957–1961.

- (35) Zhu J., Wei S., Patil R., Rutman D., Kucknoor A.S., Wang A., Guo Z. (2011) *Polymer* **52**: 1954–1962.
- (36) Mao M., Zhoun C., Shen H., Wang H., Wang S., Li L.S. (2013) *Mater. Lett.* **111**: 97–100.
- (37) Barichard A., Galstian T., Israël Y. (2010) *J. Phys. Chem. B* **114**: 14807–14814.
- (38) Li G., Ni X. (2008) *Mater. Lett.* **62**: 3066–3069.
- (39) Althues H., Pötschke P., Kim G.M., Kaskel S. (2009) *J. Nanosci. Nanotechnol.* **9**: 2739–2745.
- (40) Lü N., Lü X., Jin X., Lü C. (2007) *Polym. Int.* **56**: 138–143
- (41) Park H., Han D.C., Han D.H., Kim S.J., Lee W.E., Kwak G. (2011) *Macromolecules* **44**: 9351–9355.
- (42) Wang H., Lee K.S., Ryu J.H., Hong C.H., Cho Y.H. (2008) *Nanotechnology* **19**: 145202.
- (43) Wang H., Lee K.S., Li S., Jin L., Lee S.K., Wu Y., Cho Y.H., Cai J. (2008) *Opt. Commun.* **281**: 1588–1592.
- (44) Yam V.W.W., Lo K.K.W. (1999) *Chem. Soc. Rev.* **28**: 323–334.
- (45) Bocquet A.E., Mizokawa T., Saitoh T., Namatame H., Fujimori A. (1992) *Phys. Rev. B* **46**: 3771–3784.
- (46) de Groot F.M.F., Fuggle J.C., Thole B.T., Sawatzky G.A. (1990) *Phys. Rev. B* **42**: 5449–5468.
- (47) Dreyhsig J. (1998) *J. Phys. Chem. Solids* **59**: 31–42.
- (48) Ho C.L., Wong W.Y. (2011) *Coord. Chem. Rev.* **255**: 2469–2502.
- (49) Chen D., Luo Z., Li N., Lee J.Y., Xie J., Lu J. (2013) *Adv. Funct. Mater.* **23**: 4324–4331.
- (50) Lu X., Winnik M.A. (2001) *Chem. Mater.* **13**: 3449–3463.
- (51) Colombo M.G., Brunold T.C., Riedener T., Guedel H.U., Fortsch M., Bueg H.B. (1994) *Inorg. Chem.* **33**: 545–550.
- (52) Mills A., Thomas M. (1997) *Analyst* **122**: 63–68.
- (53) Itokazu M.K., Polo A.S., Iha N.Y.M. (2003) *J. Photochem. Photobiol. A* **160**: 27–32.
- (54) Sun W., Zhang Q., Qin L., Cheng Y., Xie Z., Lu C., Wang L. (2010) *Eur. J. Inorg. Chem.* **2010**: 4009–40917.
- (55) Pucci A., Tirelli N., Willneff E.A., Schroeder S.L.M., Galembeck F., Rugger G. (2004) *J. Mater. Chem.* **14**: 3495–3502.
- (56) Li X., Fu J., Steinhart M., Kim D.H., Knoll W. (2007) *Bull. Kor. Chem. Soc.* **28**: 1015–1019.
- (57) Li Z. (2011) *Spectrochim. Acta A* **81**: 475–480.
- (58) Hartmann P., Leiner M.J.P., Lippitsch M.E. (1995) *Anal. Chem.* **67**: 88–93.
- (59) DeRosa M.C., Mosher P.J., Yap G.P.A., Focsaneanu K.S., Crutchley R.J., Evans C.E.B. (2003) *Inorg. Chem.* **42**: 4864–4872.
- (60) Dumur F., Guillaneuf Y., Guerlin A., Wantz G., Bertin D., Miomandre F., Clavier G., Gignes D., Mayer C.R. (2011) *Macromol. Chem. Phys.* **212**: 1616–1628.
- (61) Bedlek-Anslow J.M., Hubner J.P., Carroll B.F., Schanze K.S. (2000) *Langmuir* **16**: 9137–9141.
- (62) Amaoa Y., Ishikawa Y., Okura I. (2001) *Anal. Chim. Acta* **445**: 177–182.
- (63) Ji H.F., Shen Y., Hubner J.P., Carroll B.F., Schmehl R.H., Simon J.A., Schanze K.S. (2000) *Appl. Spectrosc.* **54**: 856–863.
- (64) Lang J.M., Dreger Z.A., Drickamer H.G. (1992) *Chem. Phys. Lett.* **192**: 299–302.
- (65) Shuyan G., Kosei U., Hiroaki M. (2011) *Acc. Chem. Res.* **44**: 251–260.
- (66) Kotch T.G., Lees A.J., Fuerniss S.J., Papatomas K.I., Snyder R.W. (1993) *Inorg. Chem.* **32**: 2570–2575.
- (67) Lees A.J. (1998) *Coord. Chem. Rev.* **177**: 3–35.
- (68) Lees A.J. (1995) *Comments Inorg. Chem.* **17**: 319–346.
- (69) Rawlins K.A., Lees A.J., Fuerniss S.J., Papatomas K.I. (1996) *Chem. Mater.* **8**: 1540–1544.
- (70) Roppolo I., Celasco E., Fargues A., Garcia A., Revaux A., Dantelle G., Maroun F., Gacoin T., Boilot J.P., Sangermano M., Perruchas S. (2011) *J. Mater. Chem.* **21**: 19106–19113.
- (71) Roppolo I., Messori M., Perruchas S., Gacoin T., Boilot J.P., Sangermano M. (2012) *Macromol. Mater. Eng.* **297**: 680–688.
- (72) Roppolo I., Celasco E., Sangermano M., Garcia A., Gacoin T., Boilot J.P., Perruchas S. (2013) *J. Mater. Chem. C* **1**: 5725–5732.

- (73) Connelly N.G., Damhus T., Hartshorn R.M., Hutton A.T., *Nomenclature of Inorganic Chemistry: IUPAC Recommendations 2005*, Edited by N.G. Connelly and T. Damhus (with R.M. Hartshorn and A.T. Hutton), RSC Publishing, Cambridge, UK, 2005.
- (74) Binnemans K. (2009) *Chem. Rev.* **109**: 4283–4374.
- (75) Blasse G., Grabmaier B.C. *Luminescent Materials*, Springer-Verlag, Berlin/Heidelberg, 1994.
- (76) Haugen O., Johansen T.H. (2008) *J. Lumin.* **128**: 1479–1483.
- (77) Zhang H., Song H., Han L., Dong B., Pan G., Zhao H., Dai Q., Qin R., Qu X., Lu S. (2010) *J. Nanosci. Nanotechnol.* **10**: 2070–2076.
- (78) Diaz-Garcia M.A. (2003) *J. Polym. Sci. B Polym. Phys.* **41**: 2706–2714.
- (79) Zhang W., Gao B., Dai X. (2011) *Acta Polym. Sin.* **4**: 371–376.
- (80) Wang L.H., Wang W., Zhang W.G., Kang E.T., Huang W. (2000) *Chem. Mater.* **12**: 2212–2218.
- (81) Ding J.J., Jiu H.F., Bao J., Lu J.C., Gui W.R., Zhang Q.J., Gao C. (2005) *J. Comb. Chem.* **7**: 69–72.
- (82) Oertel A., Lengler C., Walther T., Haase M. (2009) *Chem. Mater.* **21**: 3883–3888.
- (83) Dekker R., Klunder D.J.W., Borreman A., Diemeer M.B.J., Wörhoff K., Driessen A., Stouwdam J.W., van Veggel F.C.J.M. (2004) *Appl. Phys. Lett.* **85**: 6104–6106.
- (84) Divya V., Reddy M.L.P. (2013) *J. Mater. Chem. C* **1**: 160–170.
- (85) Chen X., Yan B. (2007) *Mater. Lett.* **61**: 1707–1710.
- (86) Chigome S., Abiona A.A., Ajao J.A., Kana Kana J.B., Guerbous L., Torto N., Maaza M. (2010) *Int. J. Polym. Mater.* **59**: 863–872.
- (87) Puga M.M.S., Carlos L.D., Abrantes T.M.A., Alcacer L. (1995) *Chem. Mater.* **7**: 2316–2323.
- (88) Iovu M.S., Andries A.M., Buzurniuc S.A., Verlan V.I., Colomeico E.P., Robu S.V. (2006) *J. Optoelectron. Adv. Mater.* **8**: 257–260.
- (89) Kaur G., Dwivedi Y., Rai S.B. (2010) *Opt. Commun.* **283**: 3441–3447.
- (90) Velasco D.S., de Moura P., Medina A.N., Baesso M.L., Rubira A.F., Cremona M., Bento A.C. (2010) *J. Phys. Chem. B* **114**: 5657–5660.
- (91) Julián B., Corberán R., Cordoncillo E., Escribano P., Viana B., Sanchez C. (2004) *J. Mater. Chem.* **14**: 3337–3343.
- (92) Kumar G.A., Chen C.W., Ballato J., Riman R.E. (2007) *Chem. Mater.* **19**: 1523–1528.
- (93) Xu C.H., Jia R.P., Ouyang C.F., Wang X., Yao G.Y. (2008) *Chin. Opt. Lett.* **6**: 763–766.
- (94) Morgado J., Charas A., Fernandes J.A., Gonçalves I.S., Carlos L.D., Alcácer L. (2006) *J. Phys. D Appl. Phys.* **39**: 3582–3587.
- (95) Parra D.F., Mucciolo A., Duarte D.G., Brito H.F., Lugão A.B. (2006) *J. Appl. Polym. Sci.* **100**: 406–412.
- (96) Parra D.F., Brito H.F., Matos J.R., Carlos L.D. (2002) *J. Appl. Polym. Sci.* **83**: 2716–2726.
- (97) Kai J., Parra D.F., Brito H.F. (2008) *J. Mater. Chem.* **18**: 4549–4554.
- (98) Cai W., Chen Q., Cherepy N., Dooraghi A., Kishpaugh D., Chatzizoiannou A., Payne S., Xiang W., Pei Q. (2013) *J. Mater. Chem. C* **1**: 1970–1976.
- (99) Shen Y., Wang X., He H., Lin Y., Nan C.W. (2012) *Compos. Sci. Technol.* **72**: 1008–1011.
- (100) Anders K., Jusza A., Baran M., Lipinska L., Pyramidowicz R. (2012) *Opt. Mater.* **34**: 1964–1968.
- (101) Zhou S., Yin Y., You B., Wu L., Chen M. (2007) *Macromol. Chem. Phys.* **208**: 2677–2685.
- (102) Althues H., Simon P, Kaskel S. (2007) *J. Mater. Chem.* **17**: 758–765.
- (103) Chai R., Lian H., Hou Z., Zhang C., Peng C., Lin J. (2010) *J. Phys. Chem. C* **114**: 610–617.
- (104) Li J.Y., Sun Y.M., Zeng H., Xue W.X., Xiao Y., Yu Q. (2003) *J. Appl. Polym. Sci.* **89**: 662–667.
- (105) Sangermano M., Roppolo I., Shan G., Andrews M.P. (2009) *Prog. Org. Coat.* **65**: 431–434.
- (106) Roppolo I., Debasu M.L., Ferreira R.A.S., Rocha J., Carlos L.D., Sangermano M. (2013) *Macromol. Mater. Eng.* **298**: 181–189.
- (107) Yu H., Li T., Chen B., Wu Y., Li Y. (2013) *J. Colloid Interface Sci.* **400**: 175–180.

- (108) Gipson K., Ellerbrock B., Stevens K., Brown P., Ballato J. (2011) *J. Nanotechnol.* **2011**: 8pp.
- (109) Persano L., Camposio A., Di Benedetto F., Stabile R., Laera A.M., Piscopiello E., Tapfer L., Pisignano D. (2012) *Adv. Mater.* **24**: 5320–5326.
- (110) Shen H., Chen L., Chen S. (2009) *J. Inorg. Organomet. Polym.* **19**: 374–381.
- (111) Zhang H., Wang C., Li M., Zhang J., Lu G., Yang B. (2005) *Adv. Mater.* **17**: 853–857.
- (112) Li J., Liu B., Li J.H. (2006) *Langmuir* **22**: 528–531.
- (113) Li J., Hong X., Liu Y., Li D., Wang Y.W., Li J.H., Bai Y.B., Li T.J. (2005) *Adv. Mater.* **17**: 163–166.
- (114) Zhou J., Tang W.Q., Wang C.F., Chen L., Chen Q., Chen S. (2012) *J. Polym. Sci. A Polym. Chem.* **50**: 3736–3742.
- (115) Liu B., Liu Q., Tong C., Lu X., Lu C. (2013) *Colloids Surf. A Physicochem. Eng. Asp.* **434**: 213–219.
- (116) Gordillo H., Suarez I., Abargues R., Rodriguez-Cantò P., Albert S., Martinez-Pastor J.P. (2012) *J. Nanomater.* **2012**: 9pp.
- (117) Smirnova T.N., Sakhno O.V., Stumpe J., Kzianzou V., Schrader S. (2011) *J. Opt.* **13**: 035709.
- (118) Caseri W. (2008) *Chem. Eng. Commun.* **196**: 549–572.
- (119) Roppolo I., Shahzad N., Sacco A., Tresso E., Sangermano M. (2013) *Prog. Org. Coat.* **77**: 458–462. Doi: 10.1016/j.porgcoat.2013.11.009.
- (120) Pal M.K., Gautam J. (2013) *J. Therm. Anal. Calorim.* **111**: 689–701.
- (121) Kim H.J., Pant H.R., Kim J.H., Choi N.J., Kim C.S. (2014) *Ceram. Int.* **40**: 3023–3029.
- (122) Polizos G., Tuncer E., Sauers I., More K.L. (2011) *Polym. Eng. Sci.* **51**: 87–93.
- (123) Nussbaumer R.J., Caseri W.R., Smith P., Tervoort T. (2003) *Macromol. Mater. Eng.* **288**: 44–49.
- (124) Cui F., Liang S., Zhang, J., Han Y., Lü C., Cui T., Yang B. (2012) *Polym. Chem.* **3**: 3296–3300.
- (125) Kyprianidou-Leodidou T., Margraf P., Caseri W., Suter U.W., Walther P. (1997) *Polym. Adv. Technol.* **8**: 505–512.
- (126) Jeeju P.P., Jayalekshmi S., Chandrasekharan K., Sudheesh P. (2012) *Opt. Commun.* **285**: 5433–5439.
- (127) Jeeju P.P., Sajimol A.M., Sreevalsa V.G., Varma S.J., Jayalekshmi S. (2011) *Polym. Int.* **60**: 1263–1268.
- (128) Tu Y., Zhou L., Jin Y.Z., Gao C., Ye Z.Z., Yang Y.F., Wang Q.L. (2010) *J. Mater. Chem.* **20**: 1594–1599.
- (129) Tang E., Cheng G., Pang X., Ma X., Xing F. (2006) *Colloid Polym. Sci.* **284**: 422–428.
- (130) Indolia A.P., Gaur M.S. (2013) *J. Polym. Res.* **20**: 43, 8 pp.
- (131) Ding K.H., Wang G.L., Zhang M. (2012) *J. Appl. Polym. Sci.* **126**: 734–739.
- (132) Sun Y., Gu A., Liang G., Yuan L. (2010) *J. Appl. Polym. Sci.* **121**: 2018–2028.
- (133) Jeeju P.P., Jayalekshmi S., Chandrasekharan K., Sudheesh P. (2013) *Thin Solid Film* **531**: 378–384.
- (134) Xiong M., Gu G., You B., Wu L. (2003) *J. Appl. Polym. Sci.* **90**: 1923–1931.
- (135) Ge J., Zeng X., Tao X., Li X., Shen Z., Yun J., Chen J. (2010) *J. Appl. Polym. Sci.* **118**: 1507–1512.
- (136) Singhal A., Dubey K.A., Bhardwaj Y.K., Jain D., Choudhury S., Tyagi A.K. (2013) *RSC Adv.* **3**: 20913–20921.
- (137) Sajimol A.M., Anand P.B., Anilkumar K.M., Jayalekshmi S. (2013) *Polym. Int.* **62**: 670–675.
- (138) Jiang X., Guo Y.L., Geng Z., Huo P.F., Du Y.L., Liu Y., Zhang S.L., Wang G.B. (2012) *Mater. Lett.* **89**: 305–308.
- (139) Tao P., Viswanath A., Schadler L.S., Benicewicz B.C., Siegel R.W. (2011) *ACS Appl. Mater. Interfaces* **3**: 3638–3645.
- (140) Menning M., Oliveira P.W., Frantzen A., Schmidt H. (1999) *Thin Solid Film* **351**: 225–229.
- (141) Ma R.T., Zhao H.T., Zhang G. (2010) *Mater. Res. Bull.* **45**: 1064–1068.

8

Bismuth-Based Nanomaterials and Platforms for Sensing and Biosensing Applications

Miquel Cadevall^{1,2}, Josep Ros² and Arben Merkoçi^{1,3}

¹Catalan Institute of Nanoscience and Nanotechnology (ICN2), Campus UAB, Spain;
and The Barcelona Institute of Science and Technology, Campus UAB, Spain

²Department of Chemistry, Universitat Autònoma de Barcelona, Spain

³Institució Catalana de Recerca i Estudis Avançats (ICREA), Spain

8.1 General Properties and Applications of Bismuth

Bismuth (Bi) has been known from ancient times, although until the 18th century it was often mistaken with lead and tin, which share some similar physical properties [1–3]. Its name come from German and is related to its meaning of having the properties of antimony (*weisse masse* or *wismuth* which means “white mass”) that was translated in the mid-sixteenth century to a new Latin word *bisemutum*. It has a high electrical resistance and the thermal conductivity is lower than any other metal except mercury; considering that, Bi is sometimes called a semimetal [4]. These semimetallic properties are particularly interesting for its use as a thermoelectric material because of its low effective mass, highly anisotropic Fermi surface, and its potential to induce a semimetal/semiconductor transition with decreasing crystallite size that is typical for soft metals [5]. Among the soft metals, Bi and Pb are the most widely studied due to their thermoelectric and corrosion resistance properties, respectively.

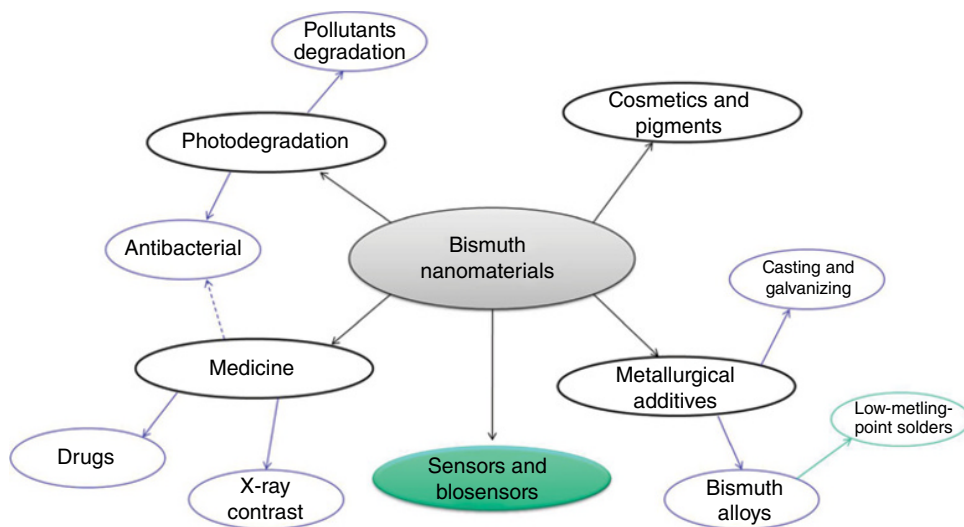


Figure 8.1 Summary of the various application fields of bismuth nanomaterials

Similar to the noble metals, a typical synthesis of bismuth nanoparticles (BiNPs) begins with the decomposition or reduction of a precursor compound, forming nuclei that then grow into nanocrystals [6]. For those nanocrystals prepared by a thermal decomposition method, often the reaction temperature has to be kept above the melting point of the metal [7]. Consequently, the “nanocrystals” remain in a liquid state throughout the entire synthesis and assume a spherical shape so as to minimize their surface area and thus the total interfacial free energy. When the reaction is quenched (typically by cooling down the solution), the liquid “nanocrystals” solidify into nanospheres with smooth surfaces.

Bi nanomaterials are being used for various applications, see Figure 8.1. Thanks to the low toxicity in comparison to heavy metals, the use of Bi in fields, such as medicine, photodegradation of organic pollutants, cosmetics, pigments, and alloys, where it replaces lead in free-machining brasses for plumbing applications is reported [8]. Historically, several Bi salts were used in medicine; as examples of that, Bi tartarate was used to treat syphilis, while Bi sodium triglycollamate has been used to treat warts, stomatitis, and upper respiratory tract infections [9–11]. Two compounds have been extensively used for gastrointestinal medication for decades. Pepto-Bismol contains Bi subsalicylate (BSS), and De-Nol contains colloidal Bi subcitrate (CBS). Other Bi compounds are used as X-ray and NMR contrast agents.

Recently, there has been intensive research in the fabrication of structured photocatalytic materials for both energetic and environmental applications, such as photocatalytic hydrogen evolution [12], degradation of organic contaminants [13], disinfection of water [14], and conversion of carbon dioxide into hydrocarbon fuels. Different Bi-based photocatalytic materials, which exhibited superior photocatalytic performance in pollutant degradation due to their special morphological structure with respect to specific surface areas, have

been fabricated by various approaches. As an example, synthetic $(\text{BiO})_2\text{CO}_3$ is found to display interesting activity in antibacterial and environmental applications [15, 16].

Besides the various applications, the use of Bi in the fabrication of sensing and biosensing platforms has shown a great interest. Its use in relation to electrochemical stripping analysis with interest for heavy metals analysis is the most significant. Electrochemical stripping techniques are particularly suitable for the determination of trace metals in samples of environmental and biological origin, due to their excellent detection limits, their sensitivity to the presence of different metal species, their capacity to perform multielement determination, and their relatively low cost. Bi-based nanomaterials, as will be shown later, play an important role in this field being the principal function its use for the surface modification of working electrodes.

8.2 BiNPs Synthesis

Various strategies for the synthesis of BiNPs have been reported since mid-1990s. As demonstrated for other metallic NPs [17, 18], following the typical approaches to synthesize nanoparticles: bottom up and top down, as will be discussed below. To summarize, BiNPs are able to be synthesized by laser ablation, electro-hydrodynamic techniques, high energy ball milling, vapor flow condensation, inverse micelles technique, high-/low-temperature chemical reduction, etc.

BiNPs can be easily obtained from bulk metallic Bi [19] by using thermal decomposition, although this method usually is not efficient enough in terms of production yield. On the other hand, reductive methods to synthesize BiNPs also have been reported. Various reducing agents and Bi precursors have been used to prepare Bi crystals. In fact, the use of an organometallic complex of Bi as a precursor for the decomposition is the most used. In addition to the decomposition of a compound or reduction of a salt precursor, nanocrystals of low-melting metals, as in the case of Bi, can be prepared by directly breaking large droplets of the molten metals under a shear force. BiNP synthesis strategies reported so far are grouped in chemical and physical methods and described in Sections 8.2.1 and 8.2.2, respectively.

8.2.1 Chemical Methods

Chemical methods employed for BiNP synthesis are based on the use of reducing agents able to reduce the Bi precursor. The distribution of the reducing agent into the synthesis medium directly affects the local variations in the rates of nucleation and growth that are directly related with the formation of polydisperse particles. To address this problem, different strategies such as the use of strong reducing agents with slow kinetics that enable homogeneous nucleation and growth have been used. Reducing agents such as ethylene-glycol [20], sodium borohydride [21], aqueous hydrazine solution [22], ethylene diamine, and, recently, sodium hyposphite [23] have been used to prepare Bi nanocrystals. The use of an organometallic complex of Bi as a precursor has been recently reported [24, 25]. In addition, photochemical activation has been used to synthesize BiNPs [26, 27]. In the following parts, these strategies are described in more detail.

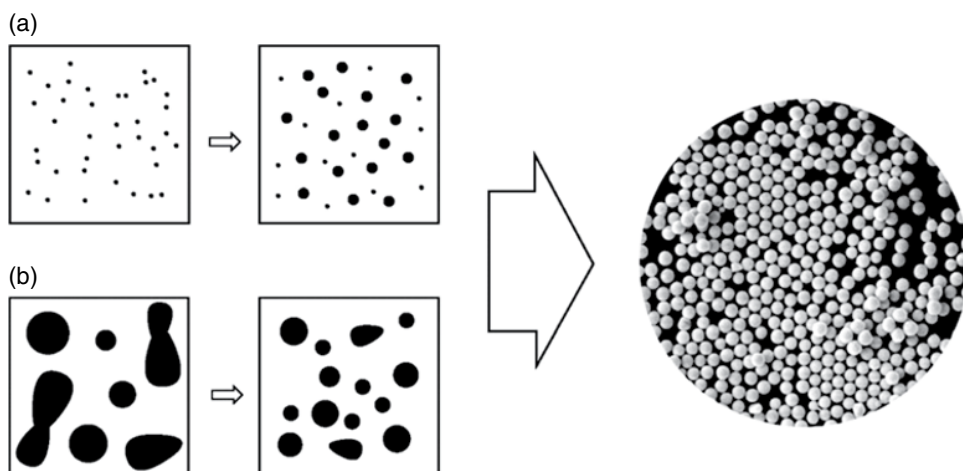


Figure 8.2 Schematic illustration of two different approaches to obtain monodispersed spherical colloids of metals with relatively low melting points: (a) the bottom-up approach, where a molecular precursor is decomposed to generate metal atoms that nucleate and grow into monodispersed colloids and (b) the top-down approach, where large drops of a metal are broken into smaller pieces and then transformed into uniform droplets by shear forces through a mechanism similar to conventional emulsification. Wang and Xia [34]. Reproduced with permission of American Physical Society

Polyol process is found to be one of the most used methodologies in the synthesis of Bi and other metallic NPs. This method of synthesis have been useful to prepare platinum [28], silver [29], gold [30], copper [31], and nickel [32] NPs with the idea to achieve NPs of different shapes and sizes [33]. The simple reagents and materials used in this technique are the main advantages. More advantages include the low cost of the reagent and the relative large productivity; nevertheless, anaerobic atmosphere and stabilizing agents are required during the synthesis. Different strategies that try to solve these drawbacks and achieve an appropriate control of the obtained nanostructure have been reported.

In 2004, Xia *et al.* reported two different solution-based approaches that allowed them to process metals with melting points below 400°C. Using both approaches, monodispersed spherical Bi colloids, in high quantities and with controlled diameters in the range of 100–600 nm can be obtained, depending on the synthesis conditions [34]. The versatility of polyol process is clearly demonstrated by the authors with Bi as an example. The production of monodispersed BiNPs was performed by either thermal decomposition of Bi acetate in boiling ethylene glycol (the bottom-up approach) or by emulsifying molten drops of Bi in boiling diethylene glycol (the top-down approach); this procedure was schematically resumed in Figure 8.2. Depending on the concentration of Bi precursor and the stirring rate, the diameters of these uniform spherical colloids could be readily varied from 100 to 600 nm. The synthetic protocols have also been extended to prepare uniform spherical colloids from other metals with relatively low melting points, and typical examples include Pb, In, Sn, Cd, and their alloys.

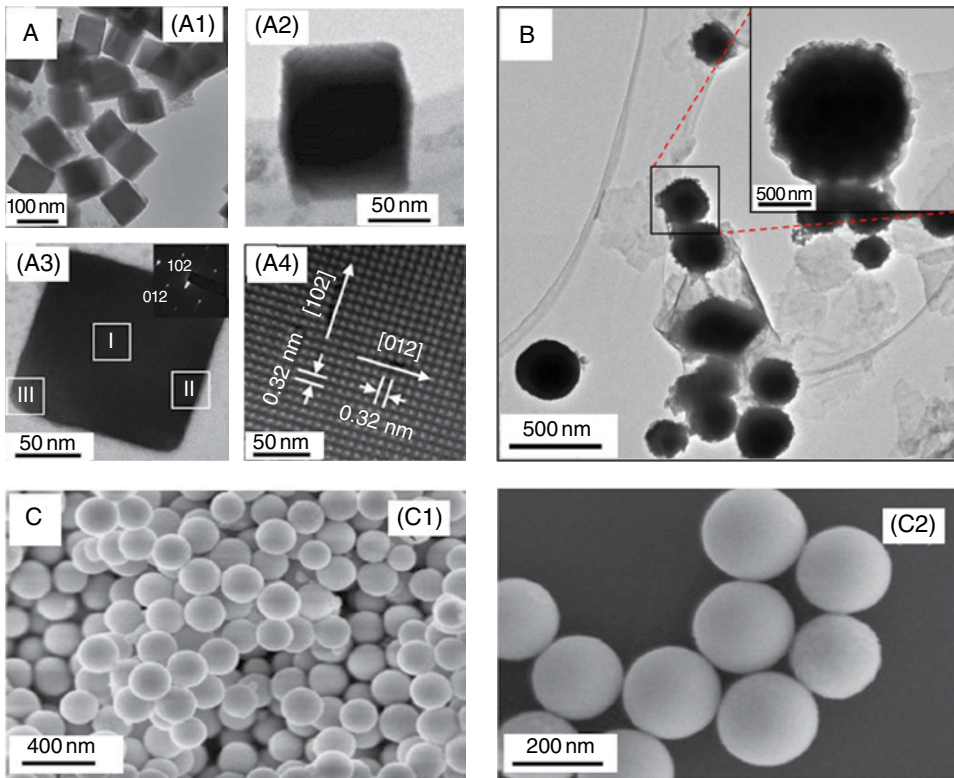


Figure 8.3 TEM images from different examples of bismuth nanostructures generated through polyol reduction in the presence of different amounts of PVP: (A) cubic (Wang *et al.* [46]. Reproduced with permission of American Chemical Society) A1, A2 and A3 show different amplified images and A4 the high resolution TEM image with the atomic planes, (B) spherical with wrinkled surface (Mayorga-Martinez *et al.* [47]. Reproduced with permission of Elsevier), and (C) spherical nanoparticles (Wu <http://www.nanoscalereslett.com/content/6/1/66>. Used under CC-BY 2.0 <http://creativecommons.org/licenses/by/2.0>) C1 and C2 show different zoom magnifications.

This methodology was improved by the addition of polymeric materials, which are usually used as stabilizers to prevent the agglomeration and precipitation. The most used polymer in this type of synthesis was polyvinyl pyrrolidone (PVP); in fact, PVP has been used for years as a capping agent in the synthesis of NPs of silver [35–37], gold [38], nickel [39, 40], copper [41], and different metal and semimetal oxide NPs [42–44]. The chain length of PVP in the synthesis can affect dramatically the prepared particles [45].

In the case of BiNPs, PVP was found to be the most critical element in the shape control. Wang *et al.* demonstrated this phenomenon while synthesizing BiNPs from sodium bismuthate (V) using different amounts of PVP [46]. BiNPs with different shapes such as sphere, triangles, and cubes were found (Figure 8.3).

Later, the synthesis of BiNPs was focused on the obtaining of spherical NPs using a simple refluxing method being PVP one of the most important ingredients. Although the

use of less oxidized states of Bi was also studied [47]. Nevertheless, the use of anionic species of Bi (III) was found to improve the synthesis. Examples include the addition of NaOH to Bi trichloride solution [48] or the use of Bi^{3+} complex with mannitol as a precursor [49].

Although PVP was found necessary as a protective agent to promote nucleation and prevent NP aggregation, the use of other polymers or surfactant offers other interesting properties. Polyethylene glycol (PEG) and cetyltrimethylammonium bromide (CTAB) are also used in the synthesis of Bi micro- and nanospheres in ethylene glycol by a simple refluxing method [50]. As a variation of the polyol process, the use of reducing agents such as hydrazine [22], sodium borohydride [51], sodium hydride [52], or potassium hydrogen phosphite was also reported [23]. The change of the reducing agent, as well as of the capping agents, plays crucial roles in the size and the stability of the particles.

Synthesis of metallic NPs by using an organometallic complex as precursor is another interesting strategy. The conditions of the decomposition of the complex and the stability of the ligand are crucial in the resultant NPs. Due to their affinity with sulfur compounds, thiol ligands are commonly used in the synthesis, for example, dodecanethiol ligands are used to synthesize disc-shaped BiNPs [21]. However, tris[bis(trimethylsilyl)amide] [53], 2-ethylhexanoate [54], and ethyl [55] ligands can also be used to functionalize the surface of BiNPs.

Bi nanoclusters can be prepared through the reduction of an aqueous Bi salt inside of AOT (dioctyl sulfosuccinate, sodium salt) reverse micelles [56]. Lin *et al.* reported for the first time a self-assembly of BiNPs, formed by reducing an organometallic Bi complex (bismuth 2-ethylhexanoate) with a hard reducing agent, lithium triethylborohydride, at high temperature. The synthesis of Bi nanocrystallites was carried out in dioctyl ether ($[\text{C}_8\text{H}_{17}\text{O}]_2$, a nonpolar solvent with high boiling point), using standard organometallic reaction procedures with anaerobic atmosphere and commercially available reagents [54].

Smaller and more homogenous NPs can be obtained from the decomposition of $\text{Bi}[\text{N}(\text{SiMe}_3)_2]_3$ [27], as shown in Figure 8.4. An example of that is the development of a simple and large-scale synthetic route for uniform-sized Bi nanocrystals with controlled particle sizes ranging from 6 to 27 nm [53]. To achieve it, the reduction of Bi thiolate with TOP is needed. The electrical and thermal conductivities of the pressed Bi nanocrystals were strongly size-dependent. Another recent synthesis is based on the thermal decomposition of ethyl-bismuth, in the presence of $\text{Na}[\text{N}(\text{SiMe}_3)_2]$, a novel low-valent precursor and PVP obtaining highly crystalline cubic NPs [55].

8.2.2 Physical Methods

Another different way to synthesize BiNPs is focused on the physical attack to different Bi species to obtain nanopowders. One of the first attempts was based upon solution dispersion of melted Bi, taking advantage of their low melting point. On the one hand, Zhao *et al.* introduced a method using paraffin oil as a solvent and capping agent [19]. On the other hand, Wang *et al.* presented a top-down approach synthesis using diethylene glycol as a solvent and PVP as a capping agent [34].

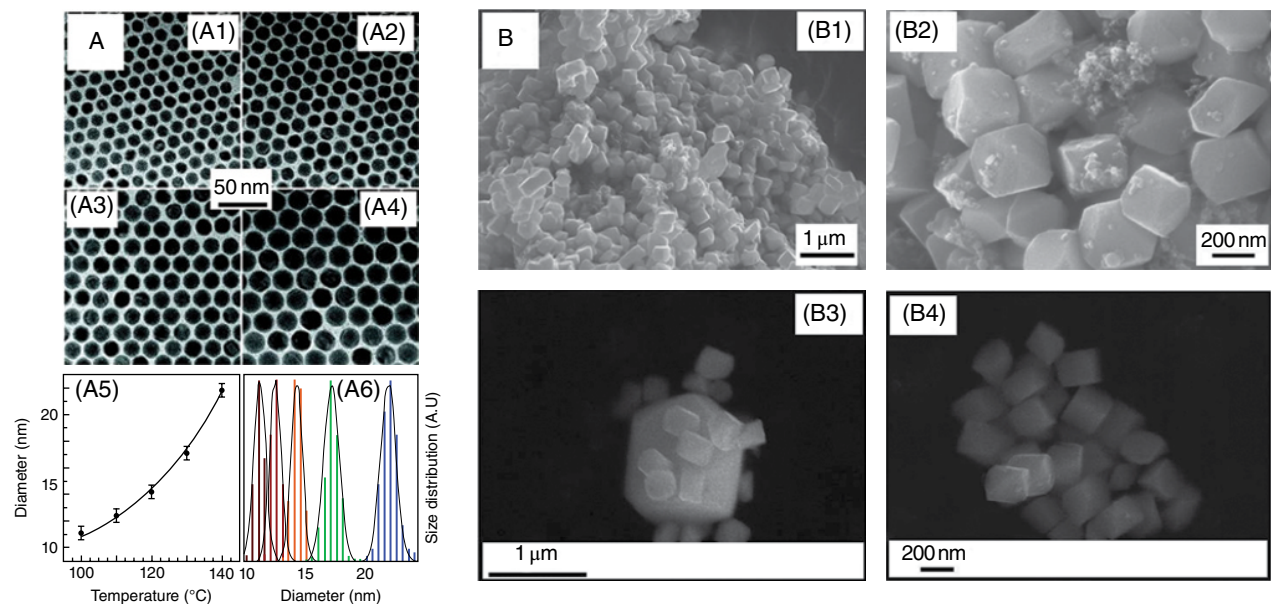


Figure 8.4 Examples of bismuth nanostructures generated by (A) a decomposition of a bismuth $\text{Bi}[\text{N}(\text{SiMe}_3)_2]_3$ compound (Yarema et al. [53]). Reproduced with permission of American Chemical Society) A1, A2, A3 and A4 show different nanoparticles obtained at 100°C, 110°C, 120°C and 130°C respectively, A5 shows a graphic with the effect of the temperature reaction in the final size nanoparticles and A6 shows the size distribution of the different synthesis conditions, and (B) thermal decomposition of the novel subvalent metal organic precursor tetraethylbismuthine Bi_2Et_4 under kinetic control at low temperatures (Schulz et al. [55]). Reproduced with permission of American Chemical Society) B1, B2, B3 and B4 show SEM images at different magnifications.

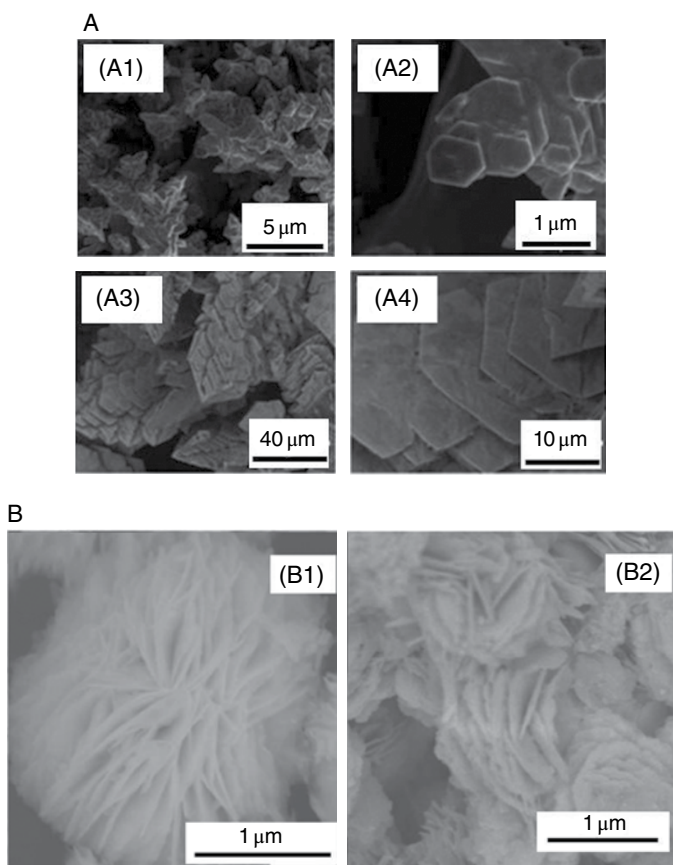


Figure 8.5 Examples of bismuth nanostructures generated by electrodeposition: (A) hexagonal discs (Ni et al. [59]. Reproduced with permission of Royal Society of Chemistry), and (B) nanoflowers (Yang et al. [57]. Reproduced with permission of Chemical Society of Japan).

Another route to obtain Bi nanostructures is by using electrochemical methods [57]. The electrochemical reduction of Bi^{3+} solutions has resulted in a plethora of interesting shapes of metal NPs such as spheres, cubes, prisms, dendrites, stars, spikes, rods, and flowers to name just a few; some of these are shown in Figure 8.5. The electrodeposition of nanostructured metals is an intense area of research interest with various important analytical applications [60]. This kind of synthesis process can be controlled by a number of electrodeposition techniques, such as cyclic voltammetry (CV), step methods such as chronoamperometry (CA), chronopotentiometry (CP), and chronocoulometry (CC), pulsed plating at a fixed or varying potential or by using AC methods.

A good way to improve the properties of Bi nanostructures obtained during electrochemical methods is to use different template techniques: the use of chemical or physical templates. The aim of chemical templating is to include in the deposition bath a ligand that

is capable of directing the growth of the material and, therefore, its properties such as shape and/or crystallography, in the same way as in chemical synthesis. The surfactants are often the same as used in chemical syntheses and are able to alter the growth kinetics at particular facets of the electrodeposited material due to their preferential adsorption at these sites. A good example of that is the use of Nafion, which was carried out by ion exchange in the Nafion film coated on the electrode surface and subsequent on-site electrochemical reduction of Bi^{3+} ions to BiNPs [61].

8.3 Bi-Based Modifications and Composites for (Bio)sensing Platforms

Historically, stripping voltammetry for heavy metal detection has been performed at mercury-based electrodes [62]. This was mainly due to the properties of this metal such as large hydrogen evolution overpotential, fast electrode kinetics, and simplified voltammetric response (associated with the formation of metal amalgam), which make its use quite advantageous [63]. Nevertheless, the toxicity of mercury has strongly limited its use for real-time/laboratory analysis due to strict environmental regulations leading to the investigation of alternative materials including noble metals (gold, platinum, iridium, and silver), Bi, and carbon-based materials (glassy carbon, carbon paste, boron-doped diamond, carbon nanotubes, and graphene). However, none of these materials, with the possible exception of Bi, can't compete with mercury in terms of potential window, sensitivity, resolution of the voltammetric responses, dynamic range, and limit of detection.

In fact, from the early 2000, Bi has emerged as a promising electrode material in electroanalysis field being with interest overall in electrochemical stripping and voltammetric-/amperometric-based sensors [47, 64–66]. It's good to remark that the interest comes from the environmental-friendly (“green”) character of Bi-based electrodes in comparison to mercury (the most used in voltammetric techniques [67–69]) and its good performance in heavy metal detection applications [70–72]. As it is well reported, Bi electrodes offer a well-defined, undistorted, and highly reproducible stripping response, excellent resolution of neighboring peaks, high hydrogen evolution, wide linear dynamic range, with signal-to-background characteristics comparable to those of common mercury electrodes [73, 74].

Different types of Bi-based sensors have been reported, but the most used configurations are based on the co-deposition (*in situ*) of Bi during electrochemical analysis and the use of Bi modified (*ex situ*) electrodes. In the following sections, some examples of Bi-based systems for both sensing and biosensing are described and discussed.

8.3.1 Chemical Sensing

The use of Bi in sensing field started on 2000 by Wang *et al.* by using Bi film electrodes or BiFEs [75]. Bi-coated carbon electrodes display an attractive stripping voltammetric performance that compares favorably with that of common mercury FEs. These BiFEs were prepared by adding 400 $\mu\text{g/l}$ (ppb) Bi^{3+} directly to the sample solution and simultaneously depositing Bi and target metals (i.e., cadmium, lead, thallium, and zinc) on the glassy-carbon or, also, carbon-fiber substrate [67, 76–79]. The use of Bi was focused on Bi

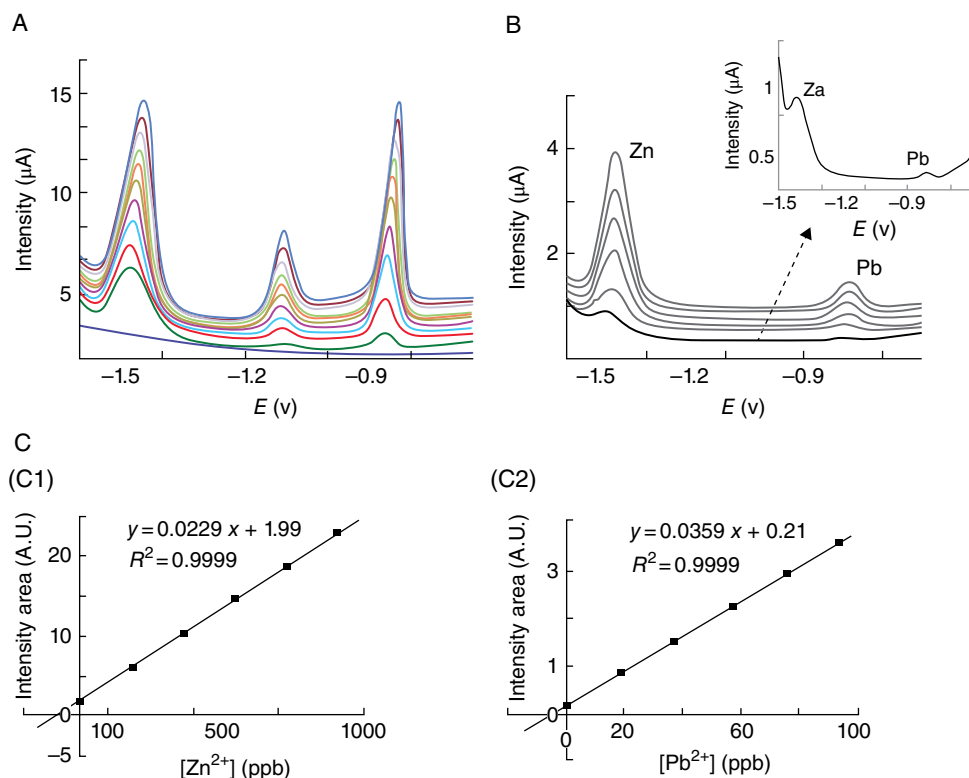


Figure 8.6 (A) Example of multielemental analysis using ex situ deposited bismuth film onto SPCE and (B) DPASV measurements in tap water samples on BiSPCE at pH 6 in 0.01 mol/l maleic–maleate buffer using an E_d of -1.50V during 120 s and t_r of 5 s; (C1) and (C2) standard addition plots for the determination of Zn^{2+} and Pb^{2+} , respectively (B and C). Serrano et al. [90]. Reproduced with permission of Springer

film-based sensors and the use of different techniques such as electrochemical stripping analysis [76, 80], electrochemical impedance spectroscopy [81], and amperometry [82]. Bi films have been normally generated by its electroplating onto electrode surfaces such as glassy carbon electrodes [83], carbon paste electrodes [84], boron-doped diamond electrodes [85, 86], gold microelectrodes [87, 88], and screen-printed carbon electrodes (SPCEs) [89, 90] (Figure 8.6).

Beside the use of Bi-film electrodes synthetic BiNPs [91] and Bi nanopowders [92–94] were also considered as modifiers of electrodes. Chang-Kyu Rhee [95, 96] reported a sensitive and conveniently usable electrode sensor for a trace analysis of heavy metal developed by using Bi nanopowder synthesized by levitational gas condensation (LGC) method. This electrode has been proven to be highly sensitive and reliable for trace analysis of heavy metals in conjunction with an anodic stripping voltammetry. The detection limits of $0.15\ \mu\text{g/l}$ for Cd and $0.07\ \mu\text{g/l}$ for Pb confirm the good performance of this sensor.

Another way to improve heavy metal sensing is the combination of Bi films or nanostructures with other nanomaterials, such as carbon nanotubes [97], graphene [98], or carbon nanofibers [99]. Hwang *et al.* describes the possibility of the Bi-CNT electrode for the determination of cadmium, lead, and zinc [77]. This Bi-CNT electrode was successfully applicable to analysis of trace metals in real environments.

Most of papers in the literature shows the capacity of Bi electrodes for cadmium, lead, and zinc sensing. However, arsenic [100, 101], antimony [102], chromium [103], mercury, thallium [104], vanadium [105], cobalt [106], nickel [107], selenium [108], and uranium [109] have also been reported as targeted analyte to be detected using Bi-based electrodes. The most commonly used electrochemical stripping analysis techniques depending on the sample and the target analyte are square-wave anodic stripping voltammetry (SWASV) [110], Osteryoung square-wave cathodic stripping voltammetry (OSWCSV) [101, 111], differential pulse anodic stripping voltammetry (DPASV) [77] and square-wave adsorptive stripping voltammetry (SWAdSV) [112]. Probably, the most frequently reported parameter by which authors evaluate the electroanalytical performance of newly developed methods is the quoted limit of detection (LOD). Table 8.1 summarizes LOD values reported by using different Bi-based electrodes while detecting various metals in different kind of samples.

Another way to generate Bi electrodes is by using Bi oxide as a precursor. In 2002, Pauliukaite *et al.* prepared a carbon-paste electrode bulk-modified with Bi_2O_3 for the determination of Cd^{2+} and Pb^{2+} ; this sensor was evaluated in synthetic solutions and real samples of river water [121].

In the field of environmental control and public health, the investigations are focused on the study of the evolution of heavy metals and other pollutants in seawater, river and lake water, drinking water, and waste water. Examples of that are the on-line lead detection [122] in tap water samples and the detection of lead and cadmium in seawater samples using SPCE modified with BiNPs (Figure 8.7).

Additionally, electrochemical methods are also used in food and health applications. Some examples are the analysis of Chinese herbal remedy samples that contain germanium contaminations [108], or propolis a honeybee product that contains lead as one of the main contaminants [123, 124]. In the second case, a BiFE plated on a modified glassy carbon electrode was prepared to determine lead and copper in raw propolis samples being a good alternative to the quality control of this kind of products [125].

Besides applications in heavy metal analysis, Bi-based sensors have been seen with interest for sulfide detection. Using BiEFs as working electrode, an indirect determination method for sulfide in water samples, based on the determination of residual Cd^{2+} after reacting with S^{2-} , is reported [126].

8.3.2 Biosensing Applications

Although the analysis of organic compounds does not represent the most important part of the research activity of Bi-based electrodes in recent years, it has been gaining presence in the literature [82]. Bi-based electrodes have been reported for the analysis of model organic compounds, pharmaceutical substances [127, 128], and pesticides [129–131] as well as in other compounds of biological relevance [132, 133].

Table 8.1 Different bismuth-based platforms used for detection of heavy metals.

Electrochemical platform	Technique	Analyte	LOD	Sample matrix	References
BiNPs/Nafion/GCE	DPASV	Pb	0.3 nM	Tap and lake water	[61]
BiFE	SWASV	Zn	6 μ M	Human serum	[113]
BiNPs/SPCE	SWASV	Pb, Cd, Zn	0.9, 1.3, 2.6 ppb	Acetate buffer	[91]
Bi nanowires	SWASV	Pb, Cd, Cu, Hg	2.5–50 ppb	Acetate buffer	[110]
Nafion-graphene/BFE	SWASV	Pb, Cd	0.1, 0.1 ppb	Lake water	[114]
MWCNTs-Nafion/BFE	DPASV	Pb, Cd	25, 40 ppt	Acetate buffer	[78]
MWCNT/BFE	SWASV	Pb, Cd, Zn	1.3, 0.7, 12 ppb	Acetate buffer	[77]
rGO/BFE	DPASV	Pb, Cd, Zn, Cu	0.55, 28, 17, 26 ppb	Acetate buffer	[98]
BiOx/SPE	CCSC	Pb, Cd	8, 16 ppb	Soil samples	[115]
BiF/SPE	SWASV	Pb, Cd, Zn	0.5, 3.9, 3.5 ppb	Tap water	[90]
BiBE	SWASV	Pb, Cd, Zn	3.2 ppb (Pb)	Acetate buffer	[116]
Bi-GECE	DPASV	Pb, Cd, Zn	23.1, 2.2, 600	Tap water, soil samples	[117]
BiFE	OSWCSV	As	0.7 ppt	Chlorhydric saline solution	[101]
BiFE	OSWCSV	Sb (III), Sb (V)	2, 2 ppt	Chlorhydric saline solution	[111]
BiFE	SWCadSV	Ge (IV)	5 ppb	Chinese herbal remedies samples	[107]
BiFE	SWAdSV	Cr (VI)	15 ppt	Acetate buffer	[118]
BiF μ E	SWAdCSV	Ni (II), Co (II)	0.06, 0.07 ppb	Ammonium buffer	[99]
BiFE	SWAdSV	Co (II)	0.09 ppb	Tap water	[119]
Bi/MWCNT/SPCE	SWASV	Hg (II)	0.09 ppb	Nitric acid solution	[120]

BiBE, Bismuth bare electrode; BiF μ E, Bismuth film microelectrode; BiFE, bismuth film electrode; BiNP/SPCE, screen-printed carbon electrode modified with bismuth nanoparticles; BiO_x, bismuth oxide; DPASV, differential normal pulse anodic stripping voltammetry; DPASV, differential pulse anodic stripping voltammetry; GCE, glassy carbon electrode; MWCNT, multiwalled carbon nanotubes; OSWCSV, Osteryoung square-wave cathodic stripping voltammetry; rGO, reduced graphene oxide; SWASV, square-wave anodic stripping voltammetry; SWCadSV, square-wave cathodic adsorptive stripping voltammetry.

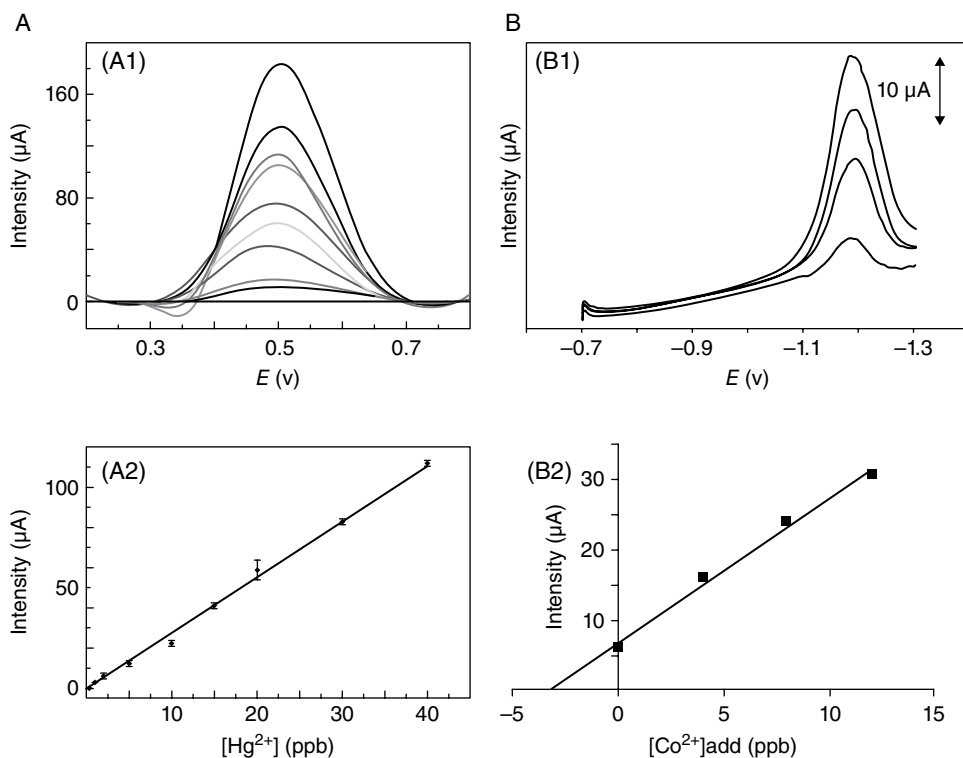


Figure 8.7 SW anodic stripping voltammograms (A1) and calibration curve (A2) for different concentrations of Hg obtained with MWCNT-modified SPBE (A) (Niu et al. [120]. Reproduced with permission of The Japan Society for Analytical Chemistry, Copyright 2011 ©) and SW voltammograms (B1) and standard addition curve for the determination of Co(II) in a certified river water sample after preconcentration for 60 s on a sputtered BiFE (B2) (Kokkinos et al. [119]. Reproduced with permission of Elsevier)

Electrocatalysis for the oxidation of carbohydrates is important in various fields, including biological fuel cells, waste water treatments, and sensors for medical and food industry applications. In particular, the electro-oxidation process of glucose at various types of platinum electrodes has been the subject of research interests for many years. In this way, a second-generation glucose biosensor was developed by using neutral red (NR) as a mediator and a BiFE as a transducer along with immobilized glucose oxidase [134]. In this work, Anik *et al.* found a very low limit of detection, 40.56 μM , showing the possibility of future applications of Bi-based platforms in other samples.

The rapid *in situ* determination of phenolic compounds and their derivatives is an important environmental challenge because of the easy penetration of such species through membranes or skins of plants, animals, and humans, with toxic side effects [135]. The development of a novel immobilization procedure including electrodeposition of mushroom tissue onto the surface of an SPCE with the aid of Bi^{3+} precursor that interacts with

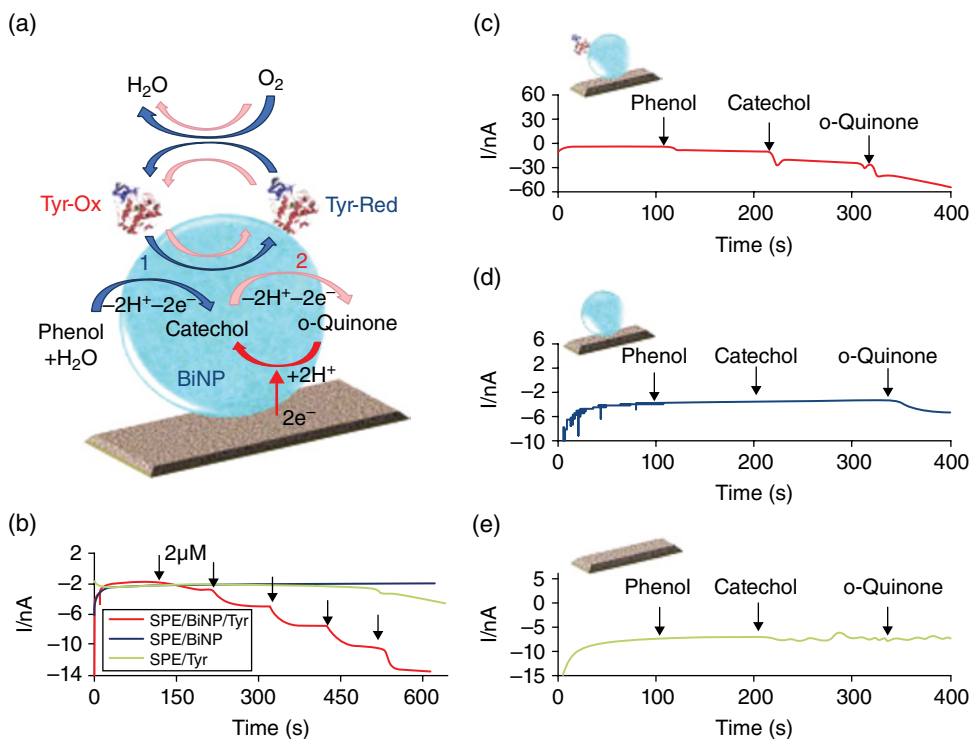


Figure 8.8 Proposed mechanism for the phenol and catechol electrocatalytic detection by using BiNP-based biosensor (a). Current–time response curves of bare SPE, SPE/BiNP, and SPE/BiNP/Tyr-modified electrodes upon successive additions of 2 μ M phenol (b). Chronoamperometric responses of SPE/BiNP/Tyr (c), SPE/BiNP (d), and SPE (e) biosensors upon successive additions of 10 μ M phenol, catechol, and o-quinone. All the experiments were carried at -200 mV, without nitrogen saturation. Mayorga-Martinez et al. [47]. Reproduced with permission of Elsevier.

the tissue and gets reduced onto the transducer surface was reported [136]. The immobilization procedure represents an *in situ* Bi and tissue deposition/entrapment without using any cross-linking agent. By this way, a disposable biosensor that gives promising results for phenol detection was obtained. This study demonstrates that this system can be with interest as a novel platform for biosensing studies and may open the door to other new configurations.

The use of BiNPs in an amperometric BiNP/Tyr-based biosensor has been also demonstrated [47]. Figure 8.8 shows the whole detection mechanism of this platform. This is achieved through BiNP/Tyr integration onto the working electrode of an SPCE by using glutaraldehyde as a cross-linking agent. The resulting BiNP/Tyr-based biosensor exhibited high sensitive response toward phenol and catechol detection with very low detection limits (26 nM for catechol and 62 nM for phenol) showing a linear response up to 100 and 71 μ M for catechol and phenol, respectively.

Another nanomaterial used is polycrystalline Bi oxide films in combination, for the first time, with polyphenol oxidase (PPO) for the development of a biosensor for determination of phenolic compounds in environmental water samples [137].

The use of Bi film is also extended in biosensing systems that involve immunoreaction assay such as interactions between IgE and anti-IgE molecules [138]. The immobilized reagents and their interaction with anti-IgE were monitored by using atomic force microscopy technique and electrochemical impedance spectroscopy.

8.4 Conclusions

The most advanced methodologies for synthesis of Bi nanostructures of different shapes and sizes based on the use of different reducing and stabilizing agents are shown. The most interesting approach is the one based on the use of ethylene glycol as both solvent and reducing agent and of the PVP as an NP protector. This versatile methodology is a good alternative for interesting applications due to the large variety of the obtained NPs. In addition, the use of electrochemical deposition methods opens up a range of new size and shape of Bi nanostructures.

Recent advances in Bi-based platforms for sensing and biosensing applications are also shown. Bi started as a promising material, basically as an alternative to mercury. During the past 15 years, scientists focused their efforts on the development of new mercury-free platforms. Nowadays, Bi can be considered as an important candidate to develop reliable non-mercury electrode. Most of the Bi-based nanostructures are used in heavy metal analysis. By using Bi-based platforms, the detection of lead, cadmium, zinc, nickel, cobalt, mercury, germanium, arsenic, chromium, and copper has been successfully achieved. Besides, the good performance in heavy metals detection Bi is also reported to be of interest for application in biosensors systems. The biocompatibility of Bi makes possible the conjugation of Bi nanostructures with enzymes and antibodies. The analysis of organic compounds, pharmaceutical substances, and pesticides as well as other compounds of biological relevance is also achieved by using Bi-based biosensors.

It's important to highlight that overall in sensing applications and especially *in situ* ones, the current electrochemical stripping technology would particularly benefit from the elimination of mercury electrodes by using Bi nanostructures.

Acknowledgments

This work was supported by MINECO (Spain, MAT2014-52485-P). ICN2 acknowledges support from the Severo Ochoa Program (MINECO, Grant SEV-2013-0295). Nanobiosensors and Bioelectronics Group acknowledges the support from Secretaria d'Universitats i Recerca del Departament d'Economia i Coneixement de la Generalitat de Catalunya (2014 SGR 260). European Union Seventh Framework Programme (FP7/2007–2013) for grant agreement n° NMP-LA-2012-280432 and n° NMP-LA-2012-280432 also is acknowledged. Miquel Cadevall thanks the Universitat Autònoma de Barcelona for the predoctoral fellowship (PIF2009).

References

- (1) G Rayner, TO Canham, *Descriptive Inorganic Chemistry*, 5th Ed., W. H. Freeman, New York, 2009.
- (2) J Barrett, *Inorganic Chemistry in Aqueous Solution*. The Royal Society of Chemistry, Cambridge, UK, 2003.
- (3) NN Greenwood, *Chemistry of the Elements*, 2nd Ed., Elsevier Butterworth-Heinemann, Oxford, 1997.
- (4) DF Shriver, *Inorganic Chemistry*, Oxford University Press, Oxford, 1999.
- (5) P Atkins, T Overton, J Rourke, M Weller, F Armstrong, *Inorganic Chemistry*, 5th Ed., Oxford University Press, Oxford, 2009.
- (6) J Krüger, P Winkler, E Lüderitz, M Lück, HU Wolf, *Bismuth, Bismuth Alloys, and Bismuth Compounds*, Ullmann's Encyclopedia of Industrial Chemistry, Wiley-VCH Verlag GmbH & Co. KGaA, Weinheim, 2000, pp. 110–133.
- (7) A Geoffrey, A Ozin, *Nanochemistry: A Chemical Approach to Nanomaterials*, 2nd Ed., Royal Society of Chemistry, Cambridge, UK, 2009.
- (8) YN Shevtsov, NF Beizel, Pb distribution in multistep bismuth refining products. *Inorganic Materials*, **1** (2), 47–51 (2011).
- (9) H Li, H Sun, Recent advances in bioinorganic chemistry of bismuth. *Current Opinion in Chemical Biology*, **16** (1–2), 74–83 (2012).
- (10) JA Salvador, SA Figueiredo, RM Pinto, SM Silvestre, Bismuth compounds in medicinal chemistry. *Future Medicinal Chemistry*, **4** (11), 1495–1523 (2012).
- (11) GG Briand, N Burford, Bismuth compounds and preparations with biological or medicinal relevance. *Chemical Reviews*, **99** (9), 2601–2658 (1999).
- (12) L Wang, W Wang, Photocatalytic hydrogen production from aqueous solutions over novel Bi_{0.5}Na_{0.5}TiO₃ microspheres. *International Journal of Hydrogen Energy*, **37** (4), 3041–3047 (2012).
- (13) J Cao, C Zhou, H Lin, B Xu, S Chen, Surface modification of *m*-BiVO₄ with wide band-gap semiconductor BiOCl to largely improve the visible light induced photocatalytic activity. *Applied Surface Science*, **284**, 263–269 (2013).
- (14) T Soltani, MH Entesari, Solar photocatalytic degradation of RB5 by ferrite bismuth nanoparticles synthesized via ultrasound. *Ultrasonics Sonochemistry*, **20** (5), 1245–1253 (2013).
- (15) Y Liu, Z Wang, B Huang, K Yang, X Zhang, X Qin, Y Dai, Preparation, electronic structure, and photocatalytic properties of Bi₂O₂CO₃ nanosheet. *Applied Surface Science*, **257** (1), 172–175 (2010).
- (16) F Dong, WK Ho, SC Lee, Z Wu, M Fu, S Zou, Y Huang, Template-free fabrication and growth mechanism of uniform (BiO)₂CO₃ hierarchical hollow microspheres with outstanding photocatalytic activities under both UV and visible light irradiation. *Journal of Materials Chemistry*, **21** (33), 12428–124236 (2011).
- (17) Y Xia, Y Xiong, B Lim, SE Skrabalak, Shape-controlled synthesis of metal nanocrystals, simple chemistry meets complex physics? *Angewandte Chemie—International Edition*, **48** (1), 60–103 (2009).
- (18) DV Goia, Preparation and formation mechanisms of uniform metallic particles in homogeneous solutions. *Journal of Materials Chemistry*, **14** (4), 451–458 (2004).
- (19) YB Zhao, KJ Zhang, HX Dang, A simple way to prepare bismuth nanoparticles. *Materials Letters*, **58** (5), 790–793 (2004).
- (20) J Li, H Fan, J Chen, L Liu, Synthesis and characterization of poly(vinyl pyrrolidone)-capped bismuth nanospheres. *Colloids and Surfaces A: Physicochemical and Engineering Aspects*, **340** (1–3), 66–69 (2009).
- (21) Y Wang, J Chen, L Chen, YB Chen, LM Wu, Shape-controlled solventless syntheses of nano bi disks and spheres. *Crystal Growth & Design*, **10** (4), 1578–1584 (2010).

- (22) D Ma, J Zhao, Y Li, X Su, S Hou, Y Zhao, X Hao, L Li, Organic molecule directed synthesis of bismuth nanostructures with varied shapes in aqueous solution and their optical characterization. *Colloids and Surfaces A—Physicochemical and Engineering Aspects*, **368** (1–3), 105–111 (2010).
- (23) D Ma, J Zhao, R Chu, S Yang, Y Zhao, X Hao, L Li, L Zhang, Y Lu, C Yu, Novel synthesis and characterization of bismuth nano/microcrystals with sodium hypophosphite as reductant. *Advanced Powder Technology*, **24** (1), 79–85 (2013).
- (24) G Carotenuto, CL Hison, F Capezzuto, M Palomba, P Perlo, P Conte, Synthesis and thermoelectric characterisation of bismuth nanoparticles. *Journal of Nanoparticle Research*, **11** (7), 1729–1738 (2009).
- (25) JS Son, K Park, MK Han, C Kang, SG Park, JH Kim, W Kim, SJ Kim, T Hyeon, Large-scale synthesis and characterization of the size-dependent thermoelectric properties of uniformly sized bismuth nanocrystals. *Angewandte Chemie—International Edition*, **50** (6), 1363–1366 (2011).
- (26) A Luz, C Feldmann, Reversible photochromic effect and electrochemical voltage driven by light-induced Bi⁰-formation. *Journal of Materials Chemistry*, **19** (43), 8107–8111 (2009).
- (27) SC Warren, AC Jackson, ZD Cater-Cyker, FJ Di Salvo, U Wiesner, Nanoparticle synthesis via the photochemical polythiol process. *Journal of the American Chemical Society*, **129** (33), 10072 (2007).
- (28) J Chen, T Herricks, M Geissler, Y Xia, Single-crystal nanowires of platinum can be synthesized by controlling the reaction rate of a polyol process. *Journal of the American Chemical Society*, **126** (35), 10854–10855 (2004).
- (29) T Yao, H Wei, Z Guoyun, W Shouxu, YT Xiaojian, T Zhihua, Z Juncheng, A new approach causing the patterns fabricated by silver nanoparticles to be conductive without sintering. *Nanotechnology*, **23** (35), 355304 (2012).
- (30) YH Lee, DW Kim, SI Shini, SG Oh, Preparation of Au colloids by polyol process using NaHCO₃ as a buffering agent. *Materials Chemistry and Physics*, **100** (1), 85–91 (2006).
- (31) J Sun, Y Jing, Y Jia, M Tillard, C Belin, Mechanism of preparing ultrafine copper powder by polyol process. *Materials Letters*, **59** (29–30), 3933–3936 (2005).
- (32) K Yu, DJ Kim, HS Chung, H Liang, Dispersed rodlike nickel powder synthesized by modified polyol process. *Materials Letters*, **57** (24–25), 3992–3997 (2003).
- (33) MB Cortie, AM McDonagh, Synthesis and optical properties of hybrid and alloy plasmonic nanoparticles. *Chemical Reviews*, **111** (6), 3713–3735 (2011).
- (34) Y Wang, Y Xia, Bottom-up and top-down approaches to the synthesis of monodispersed spherical colloids of low melting-point metals. *Nano Letters*, **4** (10), 2047–2050 (2004).
- (35) WT Cheng, YW Chih, Manipulation of silver nanostructures using supercritical fluids in the presence of polyvinylpyrrolidone and ethylene glycol. *Journal of Supercritical Fluids*, **54** (2), 272–280 (2010).
- (36) HS Shin, HJ Yang, SB Kim, MS Lee, Mechanism of growth of colloidal silver nanoparticles stabilized by polyvinyl pyrrolidone in gamma-irradiated silver nitrate solution. *Journal of Colloid Interface Science*, **274** (1), 89–94 (2004).
- (37) YZ Wang, YX L, ST Yang, GL Zhang, DM An, C Wang, Q Yang, X Chen, X Jing, Y Wei, A convenient route to polyvinyl pyrrolidone/silver nanocomposite by electrospinning. *Nanotechnology*, **17** (13), 3304–3307 (2006).
- (38) N Misra, J Biswal, A Gupta, JK Sainis, S Sabharwal, Gamma radiation induced synthesis of gold nanoparticles in aqueous polyvinyl pyrrolidone solution and its application for hydrogen peroxide estimation. *Radiation Physics and Chemistry*, **81** (2), 195–200 (2012).
- (39) JM Khurana, K Vij, Nickel nanoparticles catalyzed knoevenagel condensation of aromatic aldehydes with barbituric acids and 2-thiobarbituric acids. *Catalysis Letters*, **138** (1–2), 104–110 (2010).
- (40) D Li, S Komarneni, Microwave-assisted polyol process for synthesis of Ni nanoparticles. *Journal of the American Ceramic Society*, **89** (5), 1510–1517 (2006).

- (41) W Yu, H Xie, L Chen, Y Li, Investigation on the thermal transport properties of ethylene glycol-based nanofluids containing copper nanoparticles. *Powder Technology*, **197** (3), 218–21 (2010).
- (42) S Horiuchi, T Hanada, N Izu, I Matsubara, Electron microscopy investigations of the organization of cerium oxide nanocrystallites and polymers developed in polyvinylpyrrolidone-assisted polyol synthesis process. *Journal of Nanoparticle Research*, **14** (3), 1–10 (2012).
- (43) H Huang, QP Xie, MX Kang, B Zhang, H Zhang, J Chen, C Zhai, D Yang, B Jiang, Y Wu, Labeling transplanted mice islet with polyvinylpyrrolidone coated superparamagnetic iron oxide nanoparticles for in vivo detection by magnetic resonance imaging. *Nanotechnology*, **20** (36), 365101 (2009).
- (44) TT Tseng, WJ Tseng, Effect of polyvinylpyrrolidone on morphology and structure of In_2O_3 nanorods by hydrothermal synthesis. *Ceramics International*, **35** (7), 2837–2844 (2009).
- (45) M Tsuji, Y Nishizawa, K Matsumoto, M Kubokawa, N Miyamae, T Tsuji, Effects of chain length of polyvinylpyrrolidone for the synthesis of silver nanostructures by a microwave-polyol method. *Materials Letters*, **60** (6), 834–838 (2006).
- (46) WZ Wang, B Poudel, Y Ma, ZF Ren, Shape control of single crystalline bismuth nanostructures. *The Journal of Physical Chemistry B*, **110** (51), 25702–25706 (2006).
- (47) CC Mayorga-Martinez, M Cadevall, M Guix, J Ros, A Merkoci, Bismuth nanoparticles for phenolic compounds biosensing application. *Biosensors and Bioelectronics*, **40** (1), 57–62 (2013).
- (48) YW Wang, KS Kim, Large-scale polyol synthesis of single-crystal bismuth nanowires and the role of NaOH in the synthesis process. *Nanotechnology*, **19** (26), 265303 (2008).
- (49) J Wu, F Qin, Z Lu, HJ Yang, R Chen, Solvothermal synthesis of uniform bismuth nanospheres using poly(N-vinyl-2-pyrrolidone) as a reducing agent. *Nanoscale Research Letters*, **6**, 66 (2011).
- (50) G Cheng, J Wu, F Xiao, H Yu, Z Lu, X Yu, R Chen, Synthesis of bismuth micro- and nanospheres by a simple refluxing method. *Materials Letters*, **63** (26), 2239–2242 (2009).
- (51) YW Wang, BH Hong, KS Kim, Size control of semimetal bismuth nanoparticles and the UV-visible and IR absorption spectra. *Journal of Physical Chemistry B*, **109** (15), 7067–7072 (2005).
- (52) L Balan, R Schneider, D Billaud, Y Fort, J Ghanbaja, A new synthesis of ultrafine nanometre-sized bismuth particles. *Nanotechnology*, **15** (8), 940 (2004).
- (53) M Yarema, MV Kovalenko, G Hesser, DV Talapin, W Heiss, Highly monodisperse bismuth nanoparticles and their three-dimensional superlattices. *Journal of the American Chemical Society*, **132** (43), 15158–15159 (2010).
- (54) J Fang, KL Stokes, WL Zhou, W Wang, J Lin, Self-assembled bismuth nanocrystallites. *Chemical Communications* (18), 1872–1873 (2001).
- (55) S Schulz, S Heimann, C Woelpe, W Assenmacher, Synthesis of bismuth pseudocubes by thermal decomposition of Bi_2Et_4 . *Chemistry of Materials*, **24** (11), 2032–2039 (2012).
- (56) EE Foos, RM Stroud, AD Berry, AW Snow, JP Armistead, Synthesis of nanocrystalline bismuth in reverse micelles. *Journal of the American Chemical Society*, **122** (29), 7114–7115 (2000).
- (57) HF Yang, Y Yan, JF Li, XJ Lu, GC Xi, Q Zhang, C Wang, Low-temperature hydrothermal synthesis of bismuth nanoflowers and their application for heavy metal detection. *Chemistry Letters*, **42** (2), 150–152 (2013).
- (58) T Som, A Simo, R Fenger, GV Troppenz, R Bansen, N Pfänder, F Emmerling, J Rappich, T Boeck, K Rademann, Bismuth hexagons: facile mass synthesis, Stability and Applications. *ChemPhysChem*, **13** (8), 2162–2169 (2012).
- (59) Y Ni, Y Zhang, L Zhang, J Hong, Mass synthesis of dendritic Bi nanostructures by a facile electrodeposition route and influencing factors. *CrystEngComm*, **13**, 794–799 (2011).
- (60) BJ Plowman, SK Bhargava, AP O'Mullane, Electrochemical fabrication of metallic nanostructured electrodes for electroanalytical applications. *Analyst*, **136** (24), 5107–5119 (2012).
- (61) W Shijie, L Wenjing, K Qi, S Dazhong, P Dawei, Site synthesis of bismuth nanoparticles for electrochemical determination of lead. *Micro and Nano Letters*, **7** (12), 1260–1263 (2012).

- (62) V Beni, DWM Arrigan, Microelectrode arrays and microfabricated devices in electrochemical stripping analysis. *Current Analytical Chemistry*, **4** (3), 229–241 (2008).
- (63) G Aragay, A Puig-Font, M Cadevall, A Merkoci, A Surface. Characterizations of mercury-based electrodes with the resulting micro and nano amalgam wires and spheres formations may reveal both gained sensitivity and faced nonstability in heavy metal detection. *The Journal of Physical Chemistry C*, **114** (19), 9049–9055 (2010).
- (64) I Svancara, C Prior, SB Hocevar, J Wang, A decade with bismuth-based electrodes in electroanalysis. *Electroanalysis*, **22** (13), 1405–1420 (2010).
- (65) J Wang, Stripping analysis at bismuth electrodes: a review. *Electroanalysis*, **17** (15–16), 1341–1346 (2005).
- (66) N Serrano, A Alberich, JM Díaz-Cruz, C Ariño, M Esteban, Coating methods, modifiers and applications of bismuth screen-printed electrodes. *Trends in Analytical Chemistry*, **46**, 15–29 (2013).
- (67) O Domínguez-Renedo, MJ Gómez González, MJ Arcos-Martínez, Determination of antimony (III) in real samples by anodic stripping voltammetry using a mercury film screen-printed electrode. *Sensors*, **9** (1), 219–231 (2009).
- (68) I Palchetti, S Laschi, M Mascini, Miniaturised stripping-based carbon modified sensor for in field analysis of heavy metals. *Analytica Chimica Acta*, **530** (1), 61–67 (2005).
- (69) R Güell, G Aragay, C Fontàs, E Anticó, A Merkoçi, Sensitive and stable monitoring of lead and cadmium in seawater using screen-printed electrode and electrochemical stripping analysis. *Analytica Chimica Acta*, **627** (2), 219–224 (2008).
- (70) G Aragay, J Pons, A Merkoçi, Recent trends in macro-, micro-, and nanomaterial-based tools and strategies for heavy-metal detection. *Chemical Reviews*, **111** (5), 3433–3458 (2011).
- (71) G Aragay, A Merkoçi, Nanomaterials application in electrochemical detection of heavy metals. *Electrochimica Acta*, **84**, 49–61 (2012).
- (72) A Merkoçi, Electrochemical biosensing with nanoparticles. *FEBS Journal*, **274** (2), 310–316 (2007).
- (73) F Arduini, JQ Calvo, A Amine, G Palleschi, D Moscone, Bismuth-modified electrodes for lead detection. *Trends in Analytical Chemistry*, **29** (11), 1295–1304 (2010).
- (74) MT Castaneda, B Perez, M Pumera, M del Valle, A Merkoci, S Alegret, Sensitive stripping voltammetry of heavy metals by using a composite sensor based on a built-in bismuth precursor. *Analyst*, **130** (6), 971–976 (2005).
- (75) J Wang, J Lu, SB Hocevar, PAM Farias, B Ogorevc, Bismuth-coated carbon electrodes for anodic stripping voltammetry. *Analytical Chemistry*, **72** (14), 3218–3222 (2000).
- (76) MÁ Granado-Rico, M Olivares-Marín, E Pinilla-Gil, A novel cell design for the improved stripping voltammetric detection of Zn(II), Cd(II), and Pb(II) on commercial screen-printed strips by bismuth codeposition in stirred solutions. *Electroanalysis*, **20** (24), 2608–2613 (2008).
- (77) GH Hwang, WK Han, JS Park, SG Kang, Determination of trace metals by anodic stripping voltammetry using a bismuth-modified carbon nanotube electrode. *Talanta*, **76** (2), 301–308 (2008).
- (78) H Xu, L Zeng, S Xing, Y Xian, G Shi, L Jin, Ultrasensitive voltammetric detection of trace lead(II) and cadmium(II) using MWCNTs-nafion/bismuth composite electrodes. *Electroanalysis*, **20** (24), 2655–2662 (2008).
- (79) J Wang, J Lu, Ü Anik, SB Hocevar, B Ogorevc, Insights into the anodic stripping voltammetric behavior of bismuth film electrodes. *Analytica Chimica Acta*, **434** (1), 29–34 (2001).
- (80) SB Hocevar, J Wang, RP Deo, B Ogorevc, Potentiometric stripping analysis at bismuth-film electrode. *Electroanalysis*, **14** (2), 112–115 (2002).
- (81) R Pauliukaitė, CMA Brett, Characterization and application of bismuth-film modified carbon film electrodes. *Electroanalysis*, **17** (15–16), 1354–1359 (2005).
- (82) EA Hutton, B Ogorevc, MR Smyth, Cathodic electrochemical detection of nitrophenols at a bismuth film electrode for use in flow analysis. *Electroanalysis*, **16** (19), 1616–1621 (2004).

- (83) G Kefala, A Economou, A Voulgaropoulos, M Sofoniou, A study of bismuth-film electrodes for the detection of trace metals by anodic stripping voltammetry and their application to the determination of Pb and Zn in tapwater and human hair. *Talanta*, **61** (5), 603–610 (2003).
- (84) GU Flechsig, O Korbout, SB Hocevar, S Thongngamdee B Ogorevc, P Gründler, J Wang, Electrically heated bismuth-film electrode for voltammetric stripping measurements of trace metals. *Electroanalysis*, **14** (3), 192–196 (2002).
- (85) KE Toghil, L Xiao, GG Wildgoose, RG Compton, Electroanalytical determination of cadmium(II) and lead(II) using an antimony nanoparticle modified boron-doped diamond electrode. *Electroanalysis*, **21** (10), 1113–1138 (2009).
- (86) KE Toghil, GG Wildgoose, A Moshar, C Mulcahy, RG Compton, The fabrication and characterization of a bismuth nanoparticle modified boron doped diamond electrode and its application to the simultaneous determination of cadmium(II) and lead(II). *Electroanalysis*, **20** (16), 1731–1737 (2008).
- (87) Z Zou, A Jang, E MacKnight, PM Wu, J Do, PL Bishop, CH Ahn, Environmentally friendly disposable sensors with microfabricated on-chip planar bismuth electrode for in situ heavy metal ions measurement. *Sensors and Actuators B—Chemical*, **134** (1), 18–24 (2008).
- (88) C Kokkinos, A Economou, I Raptis, Microfabricated disposable lab-on-a-chip sensors with integrated bismuth microelectrode arrays for voltammetric determination of trace metals. *Analytica Chimica Acta*, **710**, 1–8 (2012).
- (89) N Lezi, A Economou, PA Dimovasilis, PN Trikalitis, MI Prodromidis, Disposable screen-printed sensors modified with bismuth precursor compounds for the rapid voltammetric screening of trace Pb(II) and Cd(II). *Analytica Chimica Acta*, **728**, 1–8 (2012).
- (90) N Serrano, J Díaz-Cruz, C Ariño, M Esteban, Stripping analysis of heavy metals in tap water using the bismuth film electrode. *Analytical and Bioanalytical Chemistry*, **396** (3), 1365–1369 (2010).
- (91) MÁ Granado-Rico, M Olivares-Marín, E Pinilla-Gil, Modification of carbon screen-printed electrodes by adsorption of chemically synthesized Bi nanoparticles for the voltammetric stripping detection of Zn(II), Cd(II) and Pb(II). *Talanta*, **80** (2), 631–635 (2009).
- (92) I Švancara, L Baldrianová, E Tesařová, SB Hočevár, SAA Elsuccary, A Economou, S Sotiropoulos, B Ogorevc, K Vytřas, Recent advances in anodic stripping voltammetry with bismuth-modified carbon paste electrodes. *Electroanalysis*, **18** (2), 177–185 (2006).
- (93) NA Malakhova, AA Mysik, SY Saraeva, NY Stozhko, MA Uimin, AE Ermakov, KZ Brainina, A voltammetric sensor on the basis of bismuth nanoparticles prepared by the method of gas condensation. *Journal of Analytical Chemistry*, **65** (6), 640–647 (2010).
- (94) SB Hočevár, I Švancara, K Vytřas, B Ogorevc, Novel electrode for electrochemical stripping analysis based on carbon paste modified with bismuth powder. *Electrochimica Acta*, **51** (4), 706–710 (2005).
- (95) GJ Lee, HM Lee, CK Rhee, Bismuth nano-powder electrode for trace analysis of heavy metals using anodic stripping voltammetry. *Electrochemistry Communications*, **9** (10), 2514–2518 (2007).
- (96) GJ Lee, HM Lee, CK Rhee, Effect of phase stability degradation of bismuth on sensor characteristics of nano-bismuth fixed electrode. *Talanta*, **83** (2), 682–685 (2010).
- (97) G Liu, Y Lin, Y Tu, Z Ren, Ultrasensitive voltammetric detection of trace heavy metal ions using carbon nanotube nanoelectrode array. *Analyst*, **130** (7), 1098–1101 (2005).
- (98) PK Sahoo, B Panigrahy, S Sahoo, AK Satpati, D Li, D Bahadur, In situ synthesis and properties of reduced graphene oxide/Bi nanocomposites: as an electroactive material for analysis of heavy metals. *Biosensors and Bioelectronics*, **43**, 293–296 (2013).
- (99) EA Hutton, B Ogorevc, SB Hočevár, MR Smyth, Bismuth film microelectrode for direct voltammetric measurement of trace cobalt and nickel in some simulated and real body fluid samples. *Analytica Chimica Acta*, **557** (1–2), 57–63 (2006).

- (100) DE Mays, A Hussam, Voltammetric methods for determination and speciation of inorganic arsenic in the environment—a review. *Analytica Chimica Acta*, **646** (1–2), 6–16 (2009).
- (101) L Jiajie, Y Nagaosa, Cathodic stripping voltammetric determination of As(III) with in situ plated bismuth-film electrode using the catalytic hydrogen wave. *Analytica Chimica Acta*, **593** (1), 1–6 (2007).
- (102) P Zong, J Long, Y Nagaosa, Determination of total antimony(III,V) by square-wave anodic stripping voltammetry with in situ plated bismuth-film electrode. *International Journal of Environmental Analytical Chemistry*, **91** (5), 421–430 (2011).
- (103) Q Zhang, SW Zhong, JL Su, XJ Li, H Zou, Determination of trace chromium by square-wave adsorptive cathodic stripping voltammetry at an improved bismuth film electrode. *Journal of the Electrochemical Society*, **160** (4), H237–H242 (2013).
- (104) EO Jorge, MM Neto, MM Rocha, A mercury-free electrochemical sensor for the determination of thallium(I) based on the rotating-disc bismuth film electrode. *Talanta*, **72** (4), 1392–1399 (2007).
- (105) J Wang, D Lu, Thongngamdee S, Lin Y, Sadik OA, Catalytic adsorptive stripping voltammetric measurements of trace vanadium at bismuth film electrodes. *Talanta*, **69** (4), 91491–91497 (2006).
- (106) GMS Alves, JMCS Magalhães, HMVM Soares, Simultaneous determination of nickel and cobalt using a solid bismuth vibrating electrode by adsorptive cathodic stripping voltammetry. *Electroanalysis*, **25** (5), 1247–1255 (2013).
- (107) C Kokkinos, A Economou, I Raptis, T Speliotis, Disposable lithographically fabricated bismuth microelectrode arrays for stripping voltammetric detection of trace metals. *Electrochemistry Communications*, **13** (5), 391–395 (2011).
- (108) S Zhong, J Su, L Chen, J Tong, W Jia, X Li, H Zou, Determination of total germanium in chinese herbal remedies by square-wave catalytic adsorptive cathodic stripping voltammetry at an improved bismuth film electrode, *International Journal of Electrochemistry*, **2013**, 735019 (2013).
- (109) L Lin, S Thongngamdee, J Wang, Y Lin, OA Sadik, SY Ly, Adsorptive stripping voltammetric measurements of trace uranium at the bismuth film electrode. *Analytica Chimica Acta*, **535** (1–2), 9–13 (2005).
- (110) Z Zhang, K Yu, D Bai, Z Zhu, Synthesis and electrochemical sensing toward heavy metals of bunch-like bismuth nanostructures. *Nanoscale Research Letters*, **5** (2), 398–402 (2009).
- (111) P Zong, Y Nagaosa, Determination of antimony(III) and (V) in natural water by cathodic stripping voltammetry with in-situ plated bismuth film electrode. *Microchimica Acta*, **166** (1–2), 139–144 (2009).
- (112) C Kokkinos, A Economou, I Raptis, T Speliotis, Disposable mercury-free cell-on-a-chip devices with integrated microfabricated electrodes for the determination of trace nickel(II) by adsorptive stripping voltammetry. *Analytica Chimica Acta*, **622** (1–2), 111–118 (2008).
- (113) P Jothimuthu, RA Wilson, J Herren, X Pei, W Kang, R Daniels, H Wong, F Beyette, WR Heineman, I Papautsky, Zinc detection in serum by anodic stripping voltammetry on microfabricated bismuth electrodes. *Electroanalysis*, **25** (2), 401–407 (2013).
- (114) J Li, S Guo, Y Zhai, E Wang, High-sensitivity determination of lead and cadmium based on the Nafion-graphene composite film. *Analytica Chimica Acta*, **649** (2), 196–201 (2009).
- (115) RO Kadara, IE Tohill, Development of disposable bulk-modified screen-printed electrode based on bismuth oxide for stripping chronopotentiometric analysis of lead (II) and cadmium (II) in soil and water samples. *Analytica Chimica Acta*, **623** (1), 76–81 (2008).
- (116) R Pauliukaitė, SB Hočeva, B Ogorevc, J Wang, Characterization and applications of a bismuth bulk electrode. *Electroanalysis*, **16** (9), 719–723 (2004).

- (117) Ü Anik, S Marín, M Pumera, A Merkoçi, S Alegret, Stripping voltammetry with bismuth modified graphite-epoxy composite electrodes. *Electroanalysis*, **17** (10), 881–886 (2005).
- (118) L Lin, NS Lawrence, S Thonggamdee, J Wang, Y Lin, Catalytic adsorptive stripping determination of trace chromium (VI) at the bismuth film electrode. *Talanta*, **65** (1), 144–148 (2005).
- (119) C Kokkinos, A Economou, M Koupparis, Determination of trace cobalt(II) by adsorptive stripping voltammetry on disposable microfabricated electrochemical cells with integrated planar metal-film electrodes. *Talanta*, **77** (3), 1137–1142 (2009).
- (120) X Niu, H Zhao, M Lan, Disposable screen-printed bismuth electrode modified with multi-walled carbon nanotubes for electrochemical stripping measurements. *Analytical Sciences*, **27** (12), 1237–1241 (2011).
- (121) R Pauliukaite, R Metelka, I Švancara, A Królicka, A Bobrowski, K Vytřas, E Norkus, K Kalcher, Carbon paste electrodes modified with Bi_2O_3 as sensors for the determination of Cd and Pb. *Analytical and Bioanalytical Chemistry*, **374** (6), 1155–1158 (2002).
- (122) D Pan, L Zhang, J Zhuang, T Yin, W Lu, W Qin, On-line determination of lead in tap waters at two-step prepared bismuth electrode. *International Journal of Electrochemical Science*, **6** (7), 2710–2717 (2011).
- (123) ME Conti, F Botrè, Honeybees and their products as potential bioindicators of heavy metals contamination. *Environmental Monitoring and Assessment*, **69** (3), 267–282 (2001).
- (124) S Bogdanov, Contaminants of bee products. *Apidologie*, **37** (1), 1–18 (2006).
- (125) GD Pierini, AM Granero, MS Di Nezio, ME Centurión, MA Zon, H Fernández, Development of an electroanalytical method for the determination of lead in Argentina raw propolis based on bismuth electrodes. *Microchemical Journal*, **106**, 102–106 (2013).
- (126) DQ Huang, BL Xu, J Tang, LL Yang, ZB Yang, SP Bi, Bismuth film electrodes for indirect determination of sulfide ion in water samples at trace level by anodic stripping voltammetry. *International Journal of Electrochemical Science*, **7** (4), 2860–2873 (2012).
- (127) M Bučková, P Gründler, GU Flechsig, Adsorptive stripping voltammetric detection of daunomycin at a bismuth bulk electrode. *Electroanalysis*, **17** (5–6), 440–444 (2005).
- (128) JA Rodríguez, E Barrado, Y Castrillejo, JR Santos, JLFC Lima, Validation of a tubular bismuth film amperometric detector: determination of diclofenac sodium by multisyringe flow injection analysis. *Journal of Pharmaceutical and Biomedical Analysis*, **45** (1), 47–53 (2007).
- (129) M Moreno, E Bermejo, M Chicharro, A Zapardiel, AS Arribas, Cathodic electrochemical determination of herbicides in acid media using a bismuth film electrode. *Electroanalysis*, **21** (3–5), 415–421 (2009).
- (130) AS Arribas, E Bermejo, M Chicharro, A Zapardiel, Voltammetric detection of the herbicide metamitron at a bismuth film electrode in nondeaerated solution. *Electroanalysis*, **18** (23), 2331–2336 (2006).
- (131) V Guzsvány, M Kádár, Z Papp, L Bjelica, F Gaál, K Tóth, Monitoring of photocatalytic degradation of selected neonicotinoid insecticides by cathodic voltammetry with a bismuth film electrode. *Electroanalysis*, **20** (3), 291–300 (2008).
- (132) W Zhang, H Tang, P Geng, Q Wang, L Jin, Z Wu, Amperometric method for rapid detection of *Escherichia coli* by flow injection analysis using a bismuth nano-film modified glassy carbon electrode. *Electrochemistry Communications*, **9** (4), 833–838 (2007).
- (133) S Timur, Ü Anik, α -Glucosidase based bismuth film electrode for inhibitor detection. *Analytica Chimica Acta*, **598** (1), 143–146 (2007).
- (134) Ü Anik, S Timur, M Çubukçu, A Merkoçi, The usage of a bismuth film electrode as transducer in glucose biosensing. *Microchimica Acta*, **160** (1–2), 269–273 (2008).
- (135) WY Su, SM Wang, SH Cheng, Electrochemically pretreated screen-printed carbon electrodes for the simultaneous determination of aminophenol isomers. *Journal of Electroanalytical Chemistry*, **651** (2), 166–172 (2011).

- (136) A Merkoçi, Ü Anik, S Çevik, M Çubukçu, M Guix, Bismuth film combined with screen-printed electrode as biosensing platform for phenol detection. *Electroanalysis*, **22** (13), 1429–1436 (2010).
- (137) D Shan, J Zhang, HG Xue, YC Zhang, S Cosnier, SN Ding, Polycrystalline bismuth oxide films for development of amperometric biosensor for phenolic compounds. *Biosensors and Bioelectronics*, **24** (12), 3671–3676 (2009).
- (138) Ü Anik, S Cevik, S Timur, Bismuth film electrode as sensing platform for IgE–anti-IgE interactions. *Electroanalysis*, **23** (10), 2379–2385 (2011).

9

High-Temperature-Resistant Polymer Nanocomposites

Indraneel S. Zope and Aravind Dasari

School of Materials Science & Engineering, Nanyang Technological University, Singapore

9.1 Background

High-performance/temperature-resistant polymers are a unique class of semicrystalline or amorphous polymers, primarily developed to cater specific needs in aerospace and electronic applications. Generally, they are expected to have (i) long-term durability at high temperatures (more precisely, 30000 h at 200°C, 10000 h at 250°C, 1000 h at 300°C, 10 h at 400°C, or a few minutes at 500°C), (ii) high thermal decomposition temperatures (5% mass loss should be higher than 450°C), (iii) high heat deflection temperatures (>120°C, temperature at which 10% deflection occurs under a load of 1.52 MPa), and (iv) high aromatic content and rigid segments imparting a higher glass transition temperature (>150°C) [1, 2]. Polyetheretherketone (PEEK) and polyetherketone (PEK) belong to semicrystalline group; while polysulfone (PSU), polyimide (PI), polyetherimide (PEI), and polyethersulphone (PES) are representative examples of high-temperature-resistant amorphous polymers. Chemical structures of some of these polymers are provided in Table 9.1.

Major factors that contribute to high temperature resistance include primary bond strength (see Table 9.2 [4]), molecular symmetry, intermolecular forces between

Table 9.1 Chemical structures of some representative high-performance polymers

Polymer	Structure
PES	
PI	
PEI	
PEEK	
PSU	
PPS	

Monti and Camino [3]. Reproduced with permission of Elsevier.

Table 9.2 Typical values of primary bond dissociation energies

Bond	Dissociation energy (kcal/mol)
C—C	83
C=C	145
C—S	65
C—N	73
C—Cl	81
C—O	86
C=N	147
C—H	99
C—F	102
C—B	89
Si—O	106
Si—N	104
P—O	126
P—C	138

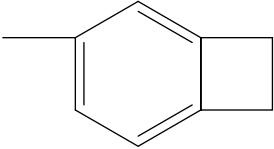
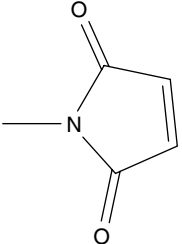
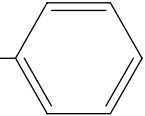
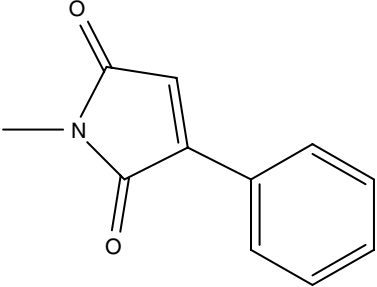
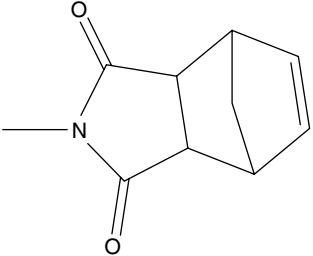
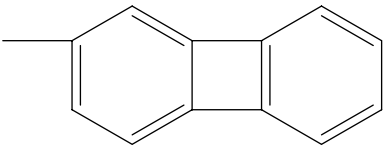
chains, cross-linking density, mechanisms of bond cleavage, and reinforcements. Difference in the bond dissociation energy between C—C (83 kcal/mol) and C=C (145 kcal/mol) or N—N (57 kcal/mol) clearly suggests why these polymers are composed predominantly of aromatic or heterocyclic rings. This presence of non-coplanar aromatic groups or hetero-aromatic groups in their backbone generally results in high softening temperatures in addition to offering resonance stabilization (~40 to 70 kcal/mol). For example, though the bond energy of N—N is low, heterocyclic polymers like poly-1,3,4-oxadiazoles containing N—N in the ring are thermally stable due to resonance stabilization [5]. It is important to note that higher primary bond strength in many systems is often compromised by chemical (or environment) attack even involving mechanisms with relatively low activation energy. Hydrolytic or oxidative cleavage reactions fall under this category. Therefore, along with high bond dissociation energies, absence of unzipping degradation reactions is required. This in fact elevates the significance of resonance stabilization along the aromatic backbone. Contrary to aromatic units, aliphatic segments are prone to oxygen attack forming radicals. Such radicals gain stability due to delocalized π electrons, resulting in inertness of these polymers even with aliphatic segments in their backbones.

Nonetheless, there are major challenges associated with these polymers like their high cost and difficulty with processing, particularly on a large scale for practical use. As a result, heteroatoms like sulfur and oxygen or groups like —COO— and —CONH— are introduced along the backbone. Their incorporation not only improved chain flexibility and processing ability, but also the compromise on thermal stability was very little [1, 6]. These heteroatoms or groups, thus, impart characteristic properties to polymers. For example, rigid units like p-phenylene and p,p'-biphenylene were found to increase the T_g and melt viscosity, but lowered solubility [6].

Apart from these, to yield high-performance/high-temperature-resistant polymers, another approach that has been commonly employed is to place latent reactive groups (terminal or pendant) on oligomers and polymers [7]. This results in cross-linking in the cured polymers, and thereby influencing many of the resultant polymer properties like T_g , solvent resistance, and modulus. Some examples of reactive end groups are given in Table 9.3. Most of the groups listed result in relatively high cross-linking density except for trifluorovinyl ether group (generally dimerizes to form perfluorocyclobutane ring) and phenylethynyl group (results in high degree of linearity in the polymer).

Further, to exploit the potential of these materials and their functionality, another approach that has been recently employed is the addition of nanoparticles. The properties that are mostly targeted include chemical resistance under aggressive conditions, performance under high temperatures, dimensional stability, coefficient of thermal expansion, and tribological properties. As there are a number of review articles and books dealing with high-performance and high-temperature polymers [1, 2, 4, 6–9], this chapter is not intended to be comprehensive but dedicated to provide an overview of the recent advancements and advantageous effect of nanoparticles in selected high-performance polymers.

Table 9.3 Representative reactive end groups for high-temperature-resistant polymers and their approximate curing temperatures

Group name	Chemical structure	Approximate curing temperature (°C)
Cyanate	$\text{—O—C}\equiv\text{N}$	200
Benzocyclobutene		220
Maleimide		230
Trifluorovinylether	$\text{—OCF}=\text{CF}_2$	250
Ethynyl	$\text{—C}\equiv\text{CH}$	250
Phenylethynyl	$\text{—C}\equiv\text{C}$ 	350
Phenylmaleimide		370
Nadimide		350
Biphenylene		350

Adapted from Ref. [7].

9.2 Representative High-Performance Polymer Nanocomposites

9.2.1 Polyethersulfone Nanocomposites

Monti and Camino [3] incorporated nanosized spherical-shaped boehmite particles (average particle size ~40 nm) to improve thermal and flammability properties of PES. Boehmite (γ -AlO(OH)) is a natural mineral of partially dehydrated aluminum hydroxide. It is similar to aluminum trihydroxide, a well-known fire retardant used in polymers, which however, starts to decompose at much lower temperature than that used for PES processing. TGA results in air showed that in the presence of 2 wt.% boehmite, onset degradation temperature ($T_{5\%}$) of PES increased by 12°C (from 502 to 514°C) (Figure 9.1). More importantly, there were no significant variations in mass loss rate profiles for PES before and after the addition of boehmite, irrespective of environment. This clearly highlights that there is no deviation in decomposition mechanism of PES even in the presence of boehmite. Further, combustion data from cone calorimeter indicated some interesting results (Table 9.4).

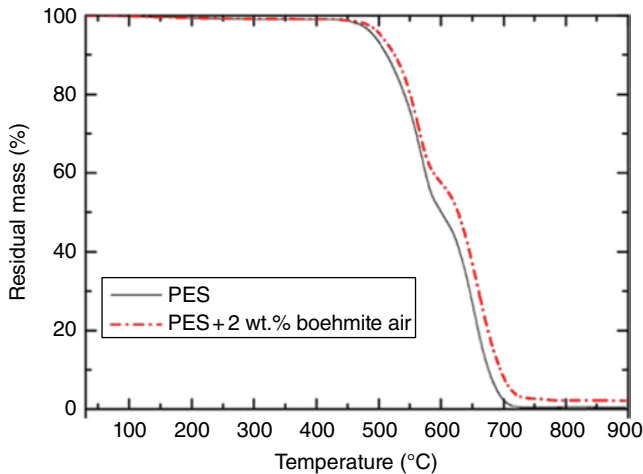


Figure 9.1 Mass loss curves for PES and PES/boehmite composite in oxidative conditions. Monti and Camino [3]. Reproduced with permission of Elsevier

Table 9.4 Cone calorimeter data of PES and PES/boehmite composite

Material	TTI (s)	pHRR (kW/m ²)	THR ^a (MJ/m ²)	TSR ^b (m ² /m ²)	EHC ^c (MJ/kg)	Residue (%)	FPI	FIGRA ^d
PES	88	226	52.9	1249	17.8	27.0	0.39	2.1
PES/2 wt.% boehmite	112	252	42.9	1488	15.9	35.4	0.45	1.7

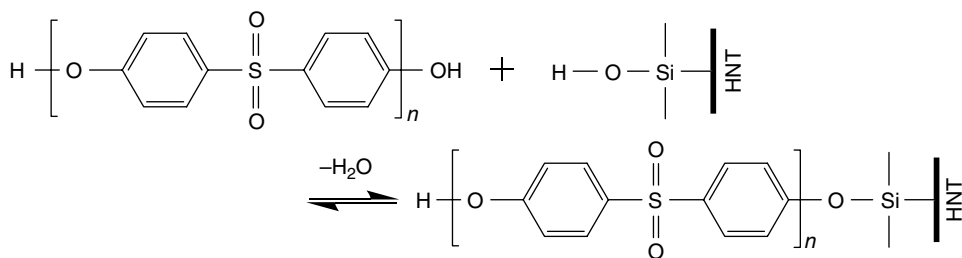
Adapted from Monti and Camino [3].

^aTotal heat released.

^bTotal smoke released.

^cEffective heat of combustion.

^dFire growth rate.



Scheme 9.1 Grafting of PES on to HNT surface via condensation reaction. Lecouvet *et al.* [11]. Reproduced with permission of Elsevier

Though the mechanisms are not clear, the incorporation of boehmite nanoparticles resulted in a remarkable 24 s increase in time-to-ignition (TTI), but peak heat release rate (pHRR) was compromised. However, the fire performance index (FPI), defined as the ratio of TTI to pHRR, was observed to be higher for nanocomposite (0.39 for neat PES and 0.45 for nanocomposite), implying that this material requires more time to reach flashover stage.

From a different perspective, it is interesting to note that boehmite exhibits size-dependent change in morphology and interfacial reactivity between 10 and 100 nm. It was noted that 100-nm-sized γ -AlOOH are fibers or rods, and they are formed by the aggregation of very small platelets (3 nm thick and 6 nm wide) with (100) lateral faces and (010) basal planes [10]. However, in between 10- and 25-nm-sized particles are diamond-shaped with (101) lateral faces. Therefore, size changes are strongly reflected in a change of the (area) ratio between the crystallographic planes. This influences the surface charge density and surface energy of these particles, subsequently effecting their reactivity in a polymer.

Lecouvet *et al.* [11] investigated the effect of addition of halloysite nanotubes (HNTs, $\text{Al}_2\text{Si}_2\text{O}_5(\text{OH})_4 \cdot 2\text{H}_2\text{O}$) to PES on its thermal stability and combustion properties. They showed that chemical affinity between terminal $-\text{OH}$ groups from PES and siloxane groups on outer surface of HNTs resulted in hydrogen bonding and in turn facilitated good dispersion. In addition, as a result of water-assisted extrusion process employed, the authors believed that PES chains were grafted onto HNTs surface through condensation reaction between Brönsted acid sites of HNTs, $\text{Si}-\text{OH}$ and $\text{Al}-\text{OH}$ and phenol groups of PES (Scheme 9.1). This was confirmed by mass loss observations between 550 and 600°C for neat HNTs and HNTs extracted from solution-mixed PES/HNT composite and melt-extruded PES/HNT composite (Figure 9.2a). Also, irrespective of the test atmosphere, the addition of HNTs to PES resulted in significant increase in degradation onset temperatures (by 20–30°C) as well as higher TTI in cone calorimeter combustion tests (see Table 9.5 and Figure 9.2b). This kind of improvement was not noted with PES if chemically inactive nanoparticles like BaTiO_3 were incorporated instead of HNTs [12]. It was noted that BaTiO_3 was unreactive with monomer and/or decomposition products. Nevertheless, in PES/HNTs systems, under oxidative conditions, higher thermal stability for intermediate carbonaceous residue highlights the formation of protective alumino-silicate frame (see later text) that delayed the oxidation of carbonaceous matter.

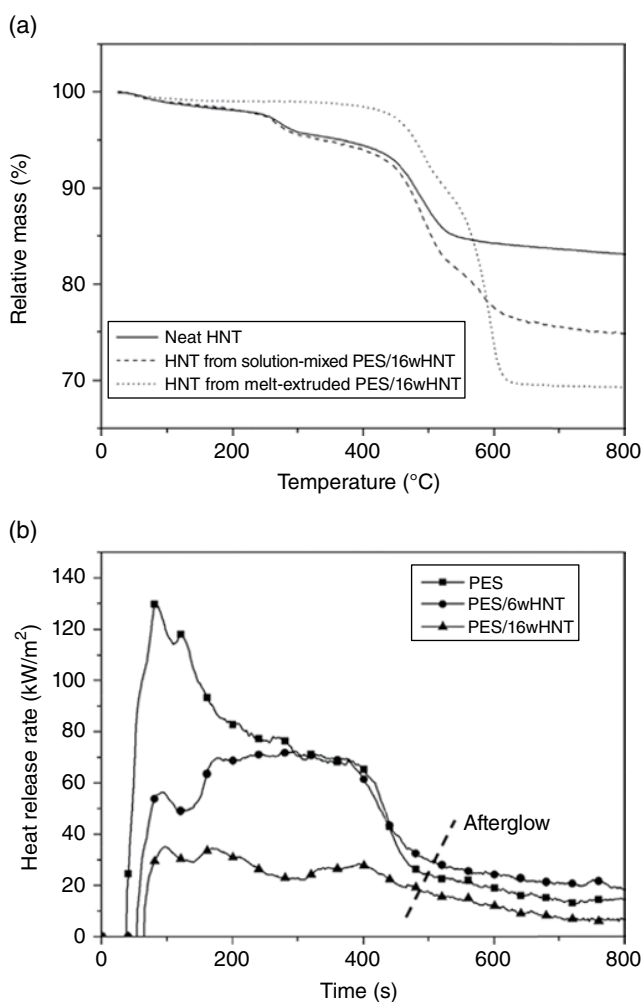


Figure 9.2 (a) Mass loss curve obtained from TGA for neat HNT, PES with HNTs extracted from solution-mixed PES/HNT composite, and HNTs extracted from solution-mixed PES... and melt-extruded PES/melt-extruded PES/HNT nanocomposite. (b) Heat release rate profiles of PES and its composites. Lecouvet et al. [11]. Reproduced with permission of Elsevier

Table 9.5 TGA data of PES and its nanocomposites in inert and oxidative conditions along with TTI values obtained from cone calorimeter

Material	TGA			Residue (%)	Cone calorimeter
	Purge gas	$T_{5\%}$ (°C)	T_p (°C)		TTI (s)
PES	N ₂	475	550	36	39
	Air	483	556, 604	0	
PES/6 wt.% HNT	N ₂	518	588	44	56
	Air	502	583, 658	6	
PES/16 wt.% HNT	N ₂	507	587	50	65
	Air	511	578, 661	15	



Figure 9.3 Cross-section picture of polyethylene terephthalate residue obtained by interrupted combustion just after TTI. Fina and Camino [13]. Reproduced with permission of Wiley (See insert for color representation of the figure)

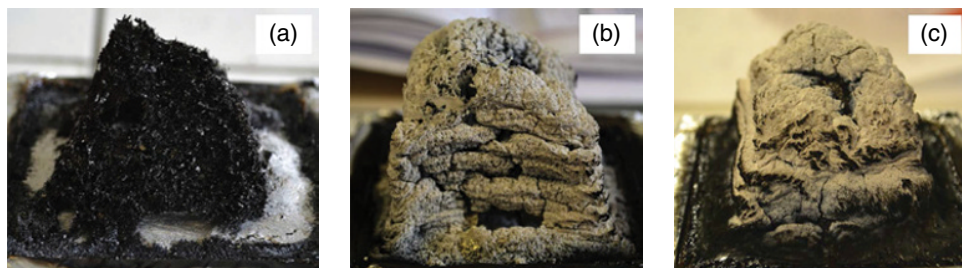


Figure 9.4 Intumescence-like behavior of residues for PES (a) and PES/HNT nanocomposites with 6 wt.% (b) and 16 wt.% HNTs (c) as obtained from cone calorimeter. Lecouvet et al. [11]. Reproduced with permission of Elsevier

Analysis of cross sections of samples (interrupted after ignition) highlighted that under external radiation, only the top exposed surface experienced thermo-oxidative degradation even for neat PES. This is in contrast to engineering polymers, for example, polyesters, where the whole cross section participates in the ignition process. An example of this is shown in Figure 9.3 [13]. It was suggested that high melt viscosity of PES system and limited thermal conductivity are the key factors. Moreover, PES by itself possesses self-extinguishing characteristics (V0 in vertical burning UL94 test) that remained unaffected in the additional presence of nanoparticles. Even under forced combustion conditions (cone calorimeter), PES showed good performance in terms of HRR values compared to other engineering polymers due to its superior thermal stability and intumescent behavior (Figure 9.4a). Interestingly, this swelling was not hindered even in the presence of nanoparticles (Figure 9.4b and c). In fact, HNTs reduced char cracking and improved structural integrity as evident in Figure 9.4b and c. This was attributed to ablative reassembling and migration of HNTs reinforcing the char structure by forming an alumino-silicate “skeleton frame,” further supporting the expanded carbonaceous char.

In another study, PES was used as an additive in carbon fiber reinforced epoxy rather than as a matrix by itself [14]. Apart from improving the impact strength of the composite, expectedly, it improved combustion properties as well. However, the extent of improvement was little (see Table 9.6) considering the amount of PES added (~20 wt.%). In a similar manner, Li *et al.* [15] embedded PES and PES/multiwalled carbon nanotube

Table 9.6 Cone analysis of epoxy and PES toughened epoxy

Material	TTI (s)	pHRR (kW/m ²)	THR (MJ/m ²)	H _c (MJ/kg)	Smoke (L)	Char (%)	FIGRA
Epoxy	33	1393	44.4	19.7	2628	2.3	26.3
Epoxy/20wt.% PES	32	1086	38.5	17.3	2401	6.2	22.0

Biswas and Kandola [14]. Reproduced with permission of Wiley.

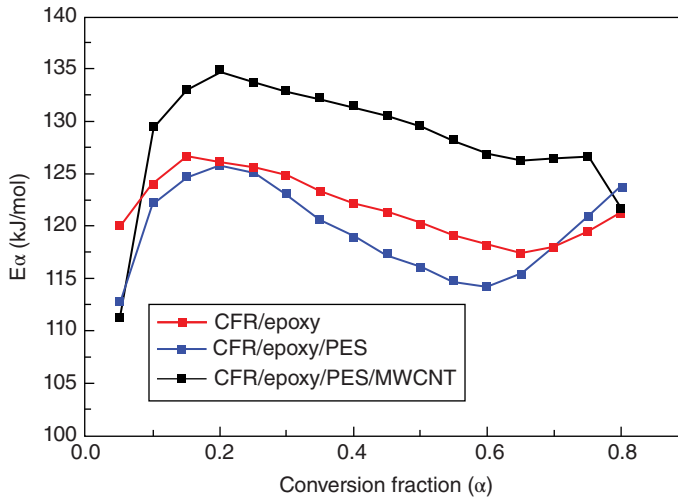
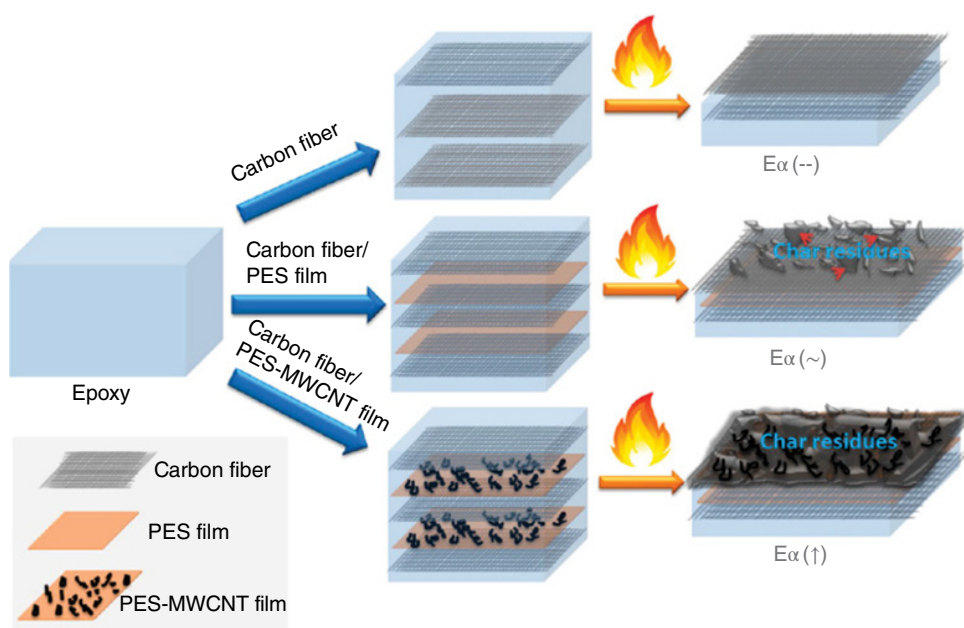


Figure 9.5 Degradation activation energies indicating effect of PES and PES/MWCNT when incorporated in carbon fiber-reinforced epoxy. Li et al. [15]. Reproduced with permission of American Chemical Society

(MWCNT) films in epoxy composites. Again, it was observed that the improvement in fire properties was minimal (particularly, pHRR values). Limiting oxygen index (LOI) values slightly improved from 32.0 in epoxy composites to 35.4 in epoxy composites with PES film and 34.8 in epoxy composite with PES/MWCNTs film. However, after analyzing thermal degradation kinetics using the Flynn–Wall–Ozawa method, it was concluded that epoxy composite and epoxy composite with PES film had similar degradation activation energies, while the introduction of MWCNTs in PES further increased activation energy as shown in Figure 9.5. It was argued that at high temperatures MWCNTs migrate to surface, carried by molten PES, to form a stable surface char (Scheme 9.2). Nevertheless, as mentioned before, the improvement in combustion properties is not significant to support the mechanism provided. In another similar study, Diez-Pascual and Naffakh [16] incorporated fullerene-like tungsten disulfide nanoparticles into structural composites (here, PPS/carbon fiber). They noted that nanoparticles improved fiber impregnation (greater wetting and lower degree of porosity) as well as delamination resistance. A marked improvement in T_g (90–118°C), heat deflection temperature (253–270°C), and coefficient of thermal



Scheme 9.2 Illustration of proposed migration of MWCNTs in molten PES toward fire-exposed surface forming a strong barrier. Li et al. [15]. Reproduced with permission of American Chemical Society

expansion ($115 \times 10^{-6}/^{\circ}\text{C}$ to $79 \times 10^{-6}/^{\circ}\text{C}$ at 120°C) was also observed with 2 wt.% of nanoparticles. In addition, degradation onset temperatures were also higher with 2 wt.% nanoparticles (from 538 to 557°C).

Moreover, due to its high aromatic content, PES shows excellent stability to γ - and e-beam radiations [17, 18]. An example of this is shown in Figure 9.6 illustrating that PES retain close to 100% of its tensile strength even after exposure to 80 kGy of radiation [18].

9.2.2 Polyimide Nanocomposites

Morgan and Putthanarat [19] explored the use of nano-fillers like carbon nanofibers, exfoliated graphite in addition to micro-sized alumina and fumed silica (FS) in PI resins. These PI composites were tested as protective coatings for carbon fiber-reinforced structures. To evaluate their thermal aging characteristics, Morgan and Putthanarat have exposed these materials to isothermal conditions at 260 and 316°C in oven with air atmosphere. Although the exact underlying mechanisms are unclear, they noted that at 260°C , the presence of fillers reduced the weight loss, whereas at 316°C , their presence accelerated the degradation (Figure 9.7). Further, based on heat release data obtained from pyrolysis combustion flow calorimeter (PCFC), the addition of CNFs and exfoliated graphite (ExG) to PI/alumina/FS micro-composite displayed impressive reductions in THR in the order of 95 and 88% (refer to Table 9.7). It was hypothesized that inorganic char residue combined with

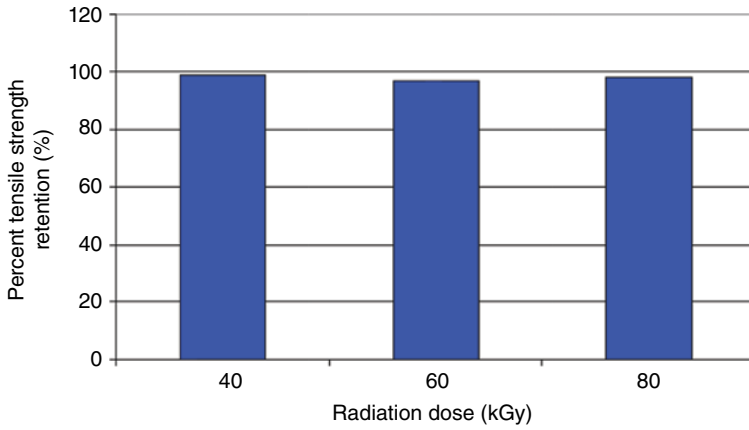


Figure 9.6 Percent retention of tensile strength of PES after exposure to different radiation doses. Sastri [18]. Reproduced with permission of Elsevier

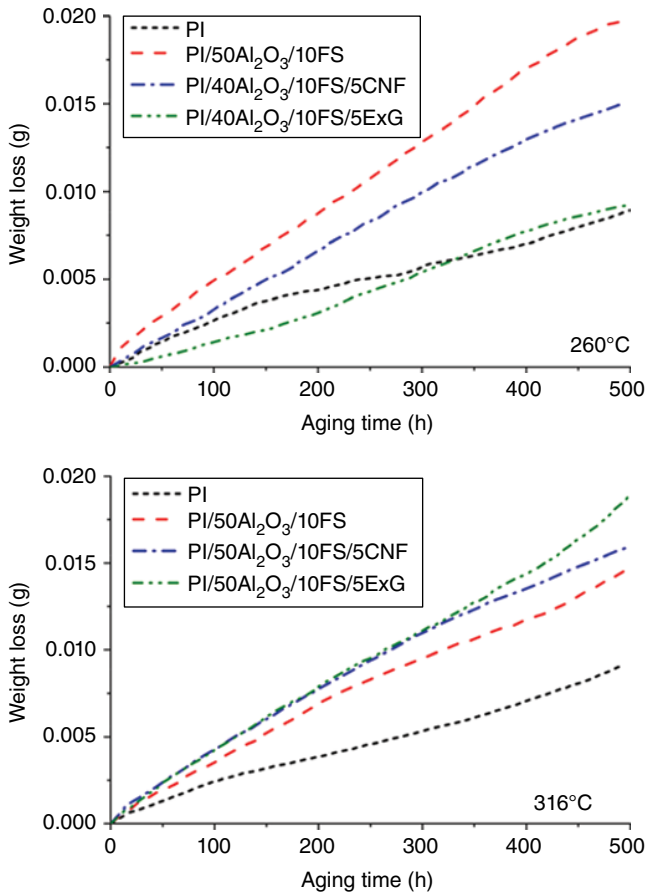


Figure 9.7 Weight loss observed with increasing aging time for PI and PI composites. Morgan and Putthanarat [19]. Reproduced with permission of Elsevier

Table 9.7 PCFC results for PI and PI composites

Material	pHRR (W/g)	THR (W/g)	% Reduction in THR	Char (%)
PI	162	13.3	—	45.7
PI/CNF	130	10.9	11.8	48.8
PI/50Al ₂ O ₃ /10FS	50	4.2	46.2	78.5
PI/40Al ₂ O ₃ /10FS/5CNF	6	0.6	95.5	87.2
PI/40Al ₂ O ₃ /10FS/5ExG	13	1.5	88.8	85.5

Morgan and Putthanarat [19]. Reproduced with permission of Elsevier.

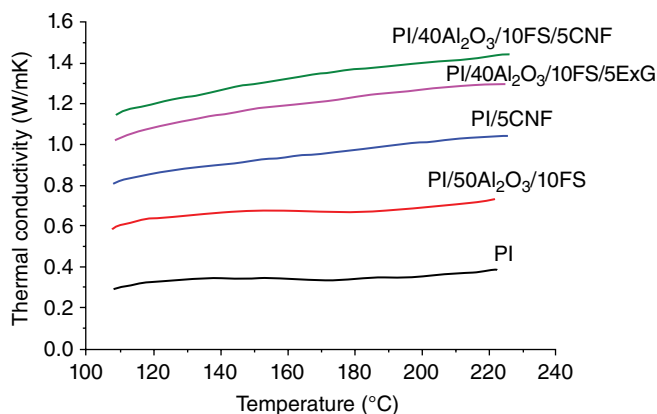


Figure 9.8 Influence of nano-fillers (CNF and ExG) on thermal conductivity of PI filled with alumina and fumed silica. Morgan and Putthanarat [19]. Reproduced with permission of Elsevier

network structure as a result of nano-fillers protect the polymer to a greater extent. These excellent PCFC results, however, could not be translated when these PI-based composites were used as protective coatings on carbon fiber-reinforced panels. Only marginal changes were observed in TTI and no noticeable changes in other combustion properties when coated panels were tested using cone calorimeter. Furthermore, thermal conductivity data of these materials clearly indicated that in the presence of nanoparticles, thermal conductivities were higher as compared to neat PI (Figure 9.8). Based on this, it was argued that application of one thin coat of this composite over carbon fiber-reinforced panel would fail to act as a thermal barrier. On the contrary, due to their higher thermal conductivities, accelerated heat transfer was expected to underneath material.

In another study, though Fan and Yang [20] cross-linked PI with octa(aminophenyl) silsesquioxane (OAPS), thermal stability of PI was not influenced (even OAPS does not seem to interfere with the degradation mechanism of PI, which was confirmed by analyzing evolved gases using TGA coupled with FTIR). Although no reasons were given for these results, it is surprising considering that LOI results showed marked improvements,

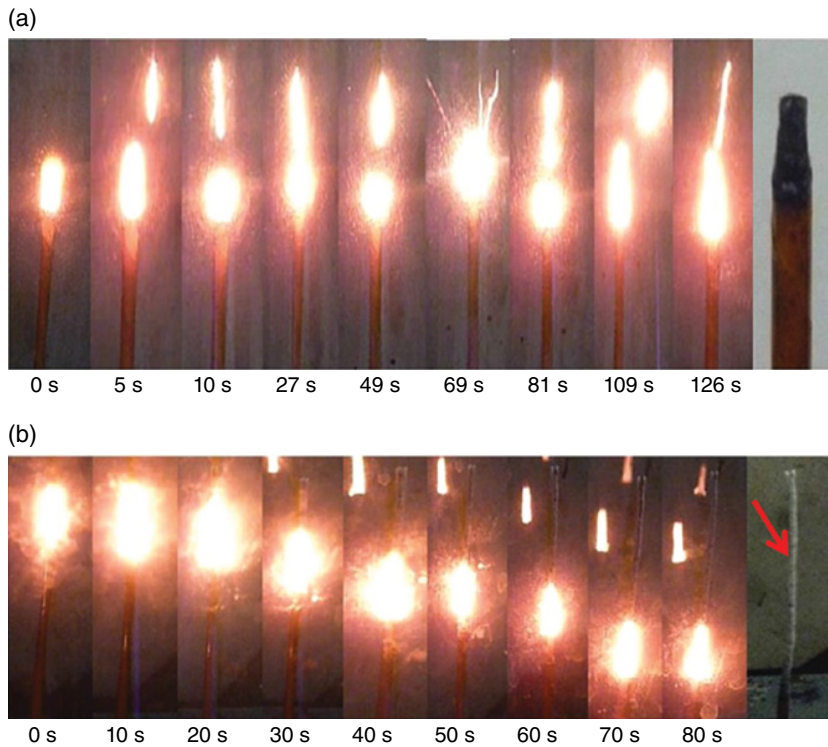


Figure 9.9 Combustion of PI (a) and PI/5.4 wt.% OAPS (b) at their respective LOI+0.5% O₂ (i.e., 47 and 57.5). Fan and Yang [20]. Reproduced with permission of American Chemical Society (See insert for color representation of the figure)

from 46.5 for neat PI to 55.5 for PI composite with 2.7 wt.% OAPS. Further, during LOI experiments, it was observed that neat PI ignites quickly and sparkled throughout the burning process (Figure 9.9a). This was absent in the case of composite (Figure 9.9b). Based on the surface morphological analysis of the char from LOI experiments (Figure 9.10), the authors suggested that sparking might be due to the coalescence of bubbles that were formed due to localized volatilization process. The coalescence released some of the flaming melt from the sample surface generating sparks. In the case of composite, it was argued that OAPS decomposition products restrain the coalescence process creating char with higher porosity and longer torturous path for volatile migration.

In another investigation, considering the importance of thermo-oxidative stability for tribological conditions, Liu *et al.* [21] synthesized PI/graphene oxide (GO) nanocomposite as a potential tribo-material under dry sliding conditions. The composite was synthesized via *in situ* polymerization of PI precursors. Although no reasons were provided, the synthesized PI/GO nanocomposite improved thermal stability over neat material (Figure 9.11). Even with reduced GO, Cao *et al.* [22] reported huge improvement in thermal stability of PI (~44°C increment in $T_{5\%}$ with 0.5 wt.% filler). Similarly, Yang *et al.* [23] observed

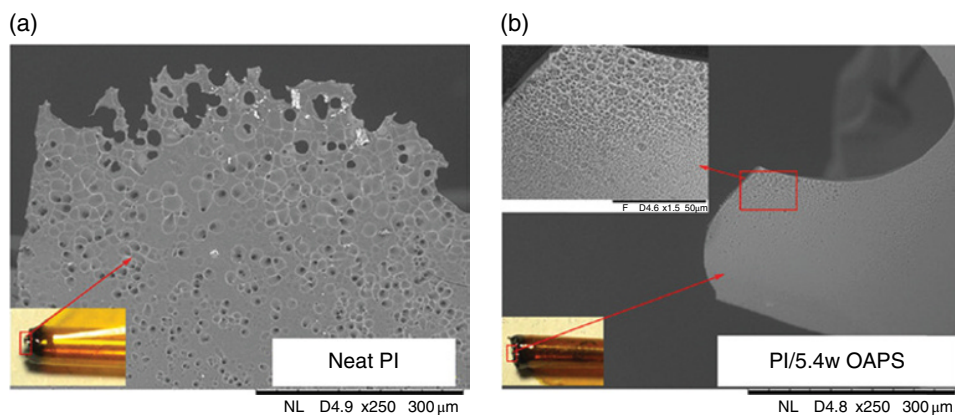


Figure 9.10 SEM micrographs of char obtained from LOI experiments: (a) neat PI and (b) PI/OAPS composite. Fan and Yang [20]. Reproduced with permission of American Chemical Society

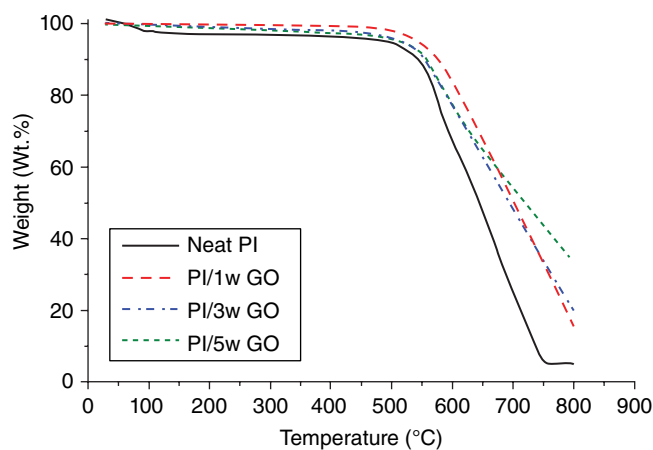


Figure 9.11 Mass loss profile for PI and PI/GO nanocomposites in oxidative conditions. Liu et al. [21]. Reproduced with permission of Springer

significant increase in thermal stability of PEEK by incorporating thermally reduced graphene (TRG) modified with PES. TGA results shown in Table 9.8 highlight the increase in $T_{5\%}$ and $T_{10\%}$ with increase in loading level of PES-TRG.

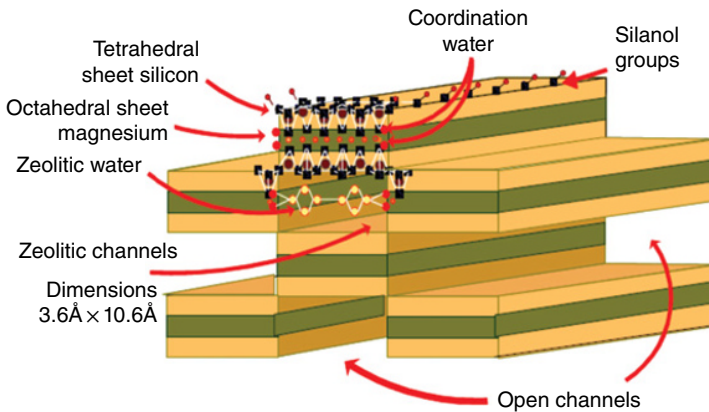
9.2.3 Polyetherimide Nanocomposites

Tabatabaei-Yezdi and Mehdipour-Ataei [24] reported the influence of sepiolite on thermal stability of PEI. Sepiolite is a hydrated magnesium silicate ($\text{Mg}_8\text{Si}_{12}\text{O}_{30}(\text{OH})_4 \cdot 12\text{H}_2\text{O}$) with needle-like morphology. These particles have an average length of 1–2 μm , width

Table 9.8 TGA data for PEEK and PEEK/PES-TRG nanocomposites

Sample	$T_{5\%}$ (°C)	$T_{10\%}$ (°C)
PEEK	575	581
PEEK/0.5 wt.% PES-TRG	582	589
PEEK/1 wt.% PES-TRG	586	596
PEEK/3 wt.% PES-TRG	599	609
PEEK/5 wt.% PES-TRG	598	608

Adapted from Ref. [23].

**Scheme 9.3** Schematic of crystal structure of sepiolite. Courtesy of Tolsa SA

approximately 10 nm, and the dimensions of open channels (along the axis of a particle) approximately $3.6 \text{ \AA} \times 10.6 \text{ \AA}$ (Scheme 9.3). The arrangement of these particles results in loosely packed and porous aggregates with an extensive capillary network. It is non-swelling and its granules do not disintegrate even when saturated with liquids. It has a surface area of $300 \text{ m}^2/\text{g}$, with a high density of silanol groups ($-\text{SiOH}$), which manifests its hydrophilicity. Under oxidative conditions, higher $T_{5\%}$ and $T_{10\%}$ were observed for PEI in the presence of sepiolite needles (Table 9.9). It was argued that sepiolite needles acted as localized cross-linking agents by forming secondary hydrogen bonds with $\text{C}=\text{O}$ in imide linkage. This was attributed to the improved thermal stability as well as T_g and CTE (Table 9.9).

In another study, Chen *et al.* [25] reported PEI nanocomposites containing bucky gels made up of MWCNTs and ionic liquid, IL (1-butyl-3-methyl imidazolium hexafluorophosphate). Due to a strong cation- π/π - π interaction of IL with MWCNT and PEI, uniform dispersion of MWCNTs was observed. Apart from drastic reduction in volumetric resistivity by 12 orders (suggesting excellent channels for electron transfer), PEI/bucky gel nanocomposite displayed significant increase in onset degradation temperatures ($T_{5\%}$) as shown in Table 9.10. Initially, with an increase in MWCNTs concentration up to 1 wt.% in bucky

Table 9.9 Glass transition temperatures (T_g), TGA results, and CTE values for PEI and PEI/sepiolite nanocomposites

Sample	T_g (°C)	$T_{5\%}$ (°C)	$T_{10\%}$ (°C)	Residue (%)	CTE (ppm/°C)
PEI	215	478	495	57.2	73
PEI/1 wt.% sepiolite	219	484	512	57.8	67
PEI/3 wt.% sepiolite	222	488	519	59.4	63
PEI/5 wt.% sepiolite	223	487	516	62.3	61

Tabatabaei-Yazdi and Mehdipour-Ataei [24]. Reproduced with permission of Wiley.

Table 9.10 Glass transition temperatures (T_g) and TGA results for PEI and PEI/IL composite filled with bucky gel containing MWCNT

Sample	$T_{5\%}$ (°C)	$T_{10\%}$ (°C)	T_g (°C)
PEI	188	488	216.9
PEI/10 wt.% IL	328	353	182.9
PEI/10 wt.% IL/0.1 wt.% MWCNTs	354	445	197.1
PEI/10 wt.% IL/0.5 wt.% MWCNTs	368	453	199.3
PEI/10 wt.% IL/1.0 wt.% MWCNTs	413	468	203.1
PEI/10 wt.% IL/2.0 wt.% MWCNTs	408	450	206.9
PEI/10 wt.% IL/5.0 wt.% MWCNTs	383	459	208.2

Chen et al. [25]. Reproduced with permission of American Chemical Society.

gel, $T_{5\%}$ and $T_{10\%}$ showed remarkable increase of 85 and 115°C, respectively. However, the authors claimed that further increase of MWCNTs in bucky gel resulted in aggregation of MWCNTs influencing the interaction between polymer chain and MWCNTs and, in turn, thermal stability.

9.3 Applications of High-Temperature Polymers and their Nanocomposites

As evident from earlier discussions, despite some potential improvements in key properties like degradation onset temperatures, HDT and CTE, with the addition of nanoparticles to high-performance/high-temperature-resistant polymers, the progress in this field is extremely slow. The depth of knowledge in many of these studies is also limited. Processing temperature conditions along with high material costs are a couple of major factors for this. Nevertheless, ongoing industrial research have led to development of various new processing friendly grades targeted toward specific applications. Table 9.11 presents list of commercial high-performance polymers and their typical applications.

Table 9.11 Applications of commercially available high-performance/high-temperature-resistant polymers

Polymer group	Trade names and manufacturer	Some representative applications
Polyimides [26–30]	Kapton®, Vespel®: DuPont Extem™, Ultem™ (polyetherimide): Sabic Torlon® (polyamide-imide): Solvay	Dielectrics in flat panel displays, protection coating on integrated circuits, and epidural catheter Sterilizable surgical appliances and window frames in aircraft interiors Low friction coatings, high temperature paints, wire enamels, bearings, and seals
Polyketones [28, 31, 32]	Victrex®: Victrex KetaSpire®, Zeniva®: Solvay; } Polyetheretherketone Vestakeep®: Evonik AvaSpire® (polyaryletherketones): Solvay Kepstan® (polyetherketoneketone): Arkema Chemical	Radiator end tank, engine cover, fuel line, alkaline battery gasket, joint replacement systems, cages in vertebral fusion therapy, heart valves and cardiac pumps, bridges, and caps in dental applications
Polyulfones [28, 33, 34]	Ultrason® PSU: BASF Udel®, Eviva™, Epispire® HTS: Solvay Ultrason® PPSU: BASF Radel®, Acudel®, Veriva®: Solvay } polyphenylsulfone Ultrason® PES: BASF Virantage®, Veradel®: Solvay } polyethersulfone Sumikaexcel™: Sumitomo Chemical	Contact lens sterilizers, battery frame cells, oil pump gears, aircraft interiors, heat exchanger parts, automotive fuses, integrated circuit sockets, coil formers, respiratory resuscitators, and artificial heart components
Polyphenylenesulfides [28, 35–38]	Durafide®: Daicel Fortron®: Celanese Ryton®: Solvay Infino® PPS: Samsung Chemical Torelina™: Toray	Burn-in sockets, surface-mount chip carriers, relays/switches, auto pump/blower housing, coolant system parts, fuel-line connectors, electric brakes/pistons, interior windows, and overhead bins in commercial aircrafts
Polyphthalamide [28, 39]	Amodel®: Solvay Vestamid® HTplus: Evonik Infino® PPA: Samsung Chemical	Stacking PCB connectors, chip carriers, 3D interconnect devices, filter systems, pump housings, and brush bristles

Acknowledgments

Aravind Dasari acknowledges the Academic Research Fund Tier-1 (RG110/14) from the Singapore's Ministry of Education and National Research Foundation's L2NIC grant (Award No.: L2NICCFP1-2013-4) for providing financial support.

References

- (1) PM Hergenrother, The use, design, synthesis, and properties of high performance/high temperature polymers: an overview. *High Performance Polymers*, **15** (2003) 345.
- (2) G Rabilloud, Heat resistant adhesives. In P Cognard (Ed.), *Handbook of Adhesives and Sealants: Vol. 2*, Elsevier Ltd., Oxford, 2006, p. 233–302.
- (3) M Monti and G Camino, Thermal and combustion behavior of polyethersulfone-boehmite nanocomposites, *Polymer Degradation and Stability*, **98** (2013) 1838.
- (4) TL Cottrell, *The strength of chemical bonds*, 2nd edition, Butterworth Scientific: London, 1978, pp. 1–310.
- (5) H Frazer and FT Wallenberger, Aromatic polyhydrazides: A new class of highly bonded, stiff polymers, *Journal of Polymer Science: Part A*, **2** (1964) 1147.
- (6) JP Critchley, GJ Knight, and WW Wright, Polymers with heterocyclic rings in the chain. In *Heat Resistant Polymers: Technologically Useful Materials*, Plenum Press, New York, 1983, pp. 185–322.
- (7) JW Connell, JG Smith Jr, PM, and Hergenrother, Oligomers and polymers containing phenylethynyl groups, *Journal of Macromolecular Science: Reviews in Macromolecular Chemistry and Physics*, **40** (2000) 207.
- (8) K Balasubramanian and M Tirumalai, High temperature polymer nanocomposites. In J Njuguna (Ed.), *Structural nanocomposites*, Springer Berlin/Heidelberg, 2013, pp. 165–186.
- (9) V Mittal, *High performance polymers and engineering plastics*, John Wiley & Sons, Inc., Hoboken, NJ, 2011, pp. 1–432.
- (10) M Auffan, J Rose, JY Bottero, GV Lowry, and JP Jolivet, Towards a definition of inorganic nanoparticles from an environmental, health and safety perspective, *Nature Nanotechnology*, **4** (2009) 634.
- (11) B Lecouvet, M Sclavons, S Bourbigot, and C Bailly, Thermal and flammability properties of polyethersulfone/halloysite nanocomposites prepared by melt compounding, *Polymer Degradation and Stability*, **98** (2013) 1993.
- (12) FJ Wang, W Li, MS Xue, JP Yao, and JS Lu, BaTiO₃-polyethersulfone nanocomposites with high dielectric constant and excellent thermal stability, *Composites Part B: Engineering*, **42** (2011) 87.
- (13) A Fina and G Camino, Ignition mechanisms in polymers and polymer nanocomposites, *Polymers for Advanced Technologies*, **22** (2011) 1147.
- (14) B Biswas and BK Kandola, The effect of chemically reactive type flame retardant additives on flammability of PES toughened epoxy resin and carbon fiber-reinforced composites, *Polymers for Advanced Technologies*, **22** (2011) 1192.
- (15) C Li, NJ Kang, SD Labrandero, J Wan, C Gonzalez, and DY Wang, Synergistic effect of carbon nanotube and polyethersulfone on flame retardancy of carbon fiber reinforced epoxy composites, *Industrial & Engineering Chemistry Research*, **53** (2014) 1040.
- (16) A Díez-Pascual and M Naffakh, Inorganic nanoparticle-modified poly(phenylene sulphide)/carbon fiber laminates: thermomechanical behavior, *Materials* **6** (2013) 3171.
- (17) Radel® Design Guide version 3.2, Advanced Polymers, Solvay.

- (18) VR Sastri, High-temperature engineering thermoplastics: polysulfones, polyimides, poly-sulfides, polyketones, liquid crystalline polymers, and fluoropolymers. In: *Plastics in Medical Devices*, Elsevier: Oxford, 2014, pp. 173–213.
- (19) AB Morgan and S Putthanasarat, Use of inorganic materials to enhance thermal stability and flammability behavior of a polyimide, *Polymer Degradation and Stability*, **96** (2011) 23.
- (20) H Fan and R Yang, Flame-retardant polyimide cross-linked with polyhedral oligomeric octa(aminophenyl)silsesquioxane, *Industrial & Engineering Chemistry Research*, **52** (2013) 2493.
- (21) H Liu, Y Li, T Wang, and Q Wang, In situ synthesis and thermal, tribological properties of thermosetting polyimide/graphene oxide nanocomposites, *Journal of Materials Science*, **47** (2012) 1867.
- (22) L Cao, Q Sun, H Wang, X, Zhang, and H Shi, Enhanced stress transfer and thermal properties of polyimide composites with covalent functionalized reduced graphene oxide. *Composites Part A: Applied Science and Manufacturing*, **68** (2015) 140.
- (23) L Yang, S Zhang, Z Chen, Y Guo, J Luan, Z Geng, and G Wang, Design and preparation of graphene/poly(ether ether ketone) composites with excellent electrical conductivity, *Journal of Materials Science*, **49** (2014) 2372.
- (24) Z Tabatabaei-Yazdi and S Mehdipour-Ataei, Poly(ether-imide) and related sepiolite nanocomposites: investigation of physical, thermal, and mechanical properties, *Polymers for Advanced Technologies*, **26** (2015) 308.
- (25) Y Chen, J Tao, L Deng, L Li, J Li, Y Yang, and NM Khashab, Polyetherimide/bucky gels nanocomposites with superior conductivity and thermal stability, *ACS Applied Materials & Interfaces*, **5** (2013) 7478.
- (26) <http://www.dupont.com/products-and-services/membranes-films/polyimide-films/brands/kapton-polyimide-film.html> (accessed on August 25, 2015).
- (27) <http://www.dupont.com/products-and-services/plastics-polymers-resins/parts-shapes/brands/vespel-polyimide.html> (accessed on August 25, 2015).
- (28) <http://www.solvay.com/en/markets-and-products/featured-products> (accessed on August 25, 2015).
- (29) <http://www.sabic-ip.com/gep/Plastics/en/ProductsAndServices/ProductLine/ultem.html> (accessed on August 24, 2015).
- (30) <http://www.sabic-ip.com/gep/Plastics/en/ProductsAndServices/ProductLine/extem.html> (accessed on August 24, 2015).
- (31) <http://www.victrex.com/en/victrex-peek> (accessed on August 25, 2015).
- (32) <http://corporate.evonik.com/en/content/product-news/pages/vestakeep-peek-industrial.aspx> (accessed on August 25, 2015).
- (33) <http://www.sumitomo-chem.co.jp/sep/english/products/pes> (accessed on August 25, 2015).
- (34) <http://www.plasticsportal.com/products/ultrason.html> (accessed on August 25, 2015).
- (35) https://www.samsungchemical.com/jsp/eng/product_intro/sm_product_infino.jsp (accessed on August 25, 2015).
- (36) <https://www.polyplastics.com/en/product/lines/durafide/app.html> (accessed on August 25, 2015).
- (37) http://www.toray.com/products/plastics/pla_005.html (accessed on August 25, 2015).
- (38) <http://www.celanese.com/engineered-materials/products/fortron-pps.aspx> (accessed on August 25, 2015).
- (39) <http://www.vestamid.com/product/vestamid/en/products-services/vestamid-htplus/pages/default.aspx> (accessed on August 25, 2015).

Index

Numbers in *italics* refer to figures; numbers in **bold** refer to tables.

- 3D image analysis, 19–23
- 3D microstructure, 7–25

- abiotic hydrolysis, 76, 82
- abiotic processes, 60
- acid hydrolysis, 32
- acrylonitrile, 70
- activated monomer mechanism, 121
- active packaging, 40–43
- ADF-STEM, 16
- adipic acid, 39
- Aegis™ CDSE, 38
- Aegis™ HFX, 38
- Aegis™ OX, 38, 41
- aerobic degradation, 61
- AFM *see* atomic force microscopy
- agar, 42
- agar/copper nanoparticles, 48
- agar nanocomposite films, 49
- AgNPs *see* silver nanoparticles
- Al₂O₃, 44
- Alcaligenes faecalis* KK314, 79
- algebraic reconstruction technique (ART), 11
 - see also* discrete ART (DART)
- aligned fibers, 96–97
- alkylamines, 2
- aluminium foil, 41
- aluminium hydroxide, 187
- amperometry, 168
- Amycolatopsis*, 71
- Amycolatopsis* sp. HT-6, 75
- α-amylase, 80
- amyloglucosidase, 80
- amylopectin, 63
- amylose, 63

- anisotropic nanocomposites, 20
- anisotropic nanofillers, 20
- antenna effect, 144
- antigen-detecting biosensors, 43
- anti-IgE molecules, 173
- antimicrobial agents, 42
- antimicrobial carriers, 42
- antimicrobial packaging, 40, 42–43
 - food packaging films, 42
- antimony, 169
- aroma emitters, 40
- aromatic polyesters, 78–79
- arsenic, 169
- ART *see* algebraic reconstruction technique
- Aspergillus fumigates*, 76
- ASTM, 60
- atomic force microscopy (AFM), 36, 173

- Bacillus megaterium*, 79
- Bacillus* strain TT96, 75
- background subtraction, 20
- back projection (BP), 11
 - see also* weighted BP (WBP)
- bacteria,
 - for degradation of polymers, 61
 - Gram-negative, 42, 44, 75
 - Gram-positive, 42, 44, 75
- bactericidal effects, 1, 33
- barium titanate fibers, 99, 103–104, 105
- barrier nanocomposites, 41
- Bayer Polymers, 38
- beer, 37, 38
- bentonite, 64
- benzyl alcohol, 121, 122, 124
- BF imaging mode, 8, 13

- BF-STEM, 16
 BF-TEM, 13, 16
 Bi-CNT electrodes, 167
 BiFES *see* Bi film electrodes
 Bi film electrodes (BiFES),
 biosensing, 169–171
 chemical sensing, 167–169
 Bi nanoparticles (BiNPs), 160
 disc-shaped, 164
 self-assembly, 164
 synthesis, 161–167
 synthetic, 168
 Bi nanopowders, 168
 BiNPs *see* bismuth nanoparticles
 BiNP/Tyr-based biosensors, 172
 biodegradability,
 assessing, 60–61
 effect of nanoclays, 48, 59, 68, 72–73, 75
 biodegradable films, 45
 biodegradable packaging, 39
 biodegradable polymers, 47–48, 57–59, 81–84
 assessing biodegradability, 60–61
 classification, 59–60
 definitions, 60
 from fossil origin, 74–81
 from mixed sources, 60
 petroleum-based, 59
 renewable resource-based, 59
 standards for, 59–61
 biodegradation, 47–48
 cellulose, 64–66
 chitosan, 64–67
 gelatin, 67
 mechanisms of, 61–63
 montmorillonite (MMT), 63–68, 72–73, 75,
 78, 80–81
 polyesters, 69–79
 polylactic acid, 71–74, 83
 polymers from natural resources, 63–74
 polysaccharides, 63–64
 polyurethanes, 80–81
 polyvinyl alcohols, 79–80
 primary degradation, 61
 proteins, 66–69
 site, 62
 ultimate, 61
 via hydrolysis, 61–63, 67, 70–74, 76, 79–83
 wheat gluten, 68–69
 bio-hybrid nanocomposite coatings, 44–45
 Biopol TM, 70
 biopolymers, 35, 39, 42, 45–46, 64, 81, 82
 biosensing, 169–173
 bismuth-based nanomaterials *see* Bi film
 electrodes (BiFES); Bi nanoparticles (BiNPs)
 bismuth ferrite, 99, 109–114, 131
 bismuth oxides, 169
 Bisphenol A diglycidyl ether (DGEBA), 122,
 127, 130
 block copolymers, 8
 boehmite, 2, 187–188
 BoneJ, 20
 boron-doped electrodes, 168
 bottles, 37–39
 BOX *see* 2-(2-hydroxyphenyl)-benzoxazol
 BP *see* back projection
 BPS Japan, 60
 breathing, 109
 bright field (BF) imaging mode, 8, 13
 bucky gels, 197
 C *see* solvent-casting, 13
 C30B *see* Cloisite 30B
 cadmium, 169
 cadmium telluride, 150
 calcium carbonate, 41, 81
 calcium hydroxide, 41
 calcium oxide, 41
 carbohydrates, electrocatalysis of, 171
 carbonated beverages, 37, 39
 carbon black (CB), 16–17
 carbon dioxide, 29
 absorbers, 40, 41
 conversion into hydrocarbon fuels, 160
 emitters, 40, 41
 retention of, 37, 39, 45
 carbon nanofibres, 169, 192
 carbon nanotubes (CNTs), 3–4
 for biosensors, 43
 for heavy metal sensing, 169
 for reinforcing electrospun fibers, 101–102
 see also multi-walled carbon nanotubes
 (MWCNTs)
 carbon paste electrodes, 168
 carboxy MC (CMC), 80
 κ-carrageenan, 49
 carrageenan biopolymer, 39
 catechol, 172, 173
 CB *see* carbon black
 CdS, 148–150
 CdSe, 19, 148–150
 CdS-poly (2-hydroxyethyl acrylate (HEA)-
 co-N-vinylcarbazole NVK), 145, 146, 147

- CdTe, 148–150
 cellobiohydrolases, 64
 cellulases, 64, 80
 cellulose, 32–33
 biodegradation, 64–66
 nanocomposites, 64–65
 nanofibers, 32
 nanofibrils, 32
 nanowhiskers, 32
 see also nanocellulose; microcellulose
 CEN, 60
 cetyltrimethylammonium bromide (CTAB), 164
Chaetomium globosum, 76
 chemical sensing, 167–169
 chemical templating, 168
 chemical vapor deposition, 44
 chemisorption, 3
 chitin, 33, 64, 65
 nanofibrils, 32, 39
 chitosan, 42, 43, 44, 45, 48
 biodegradation, 64–67
 chromium, 169
 chronoamperometry (CA), 166
 chronocoulometry (CC), 166
 chronopotentiometry (CP), 166
 clay nanoparticles, as nanofillers, 33–34
 clay nanoplatelets, 20
 Cloisite 25A, 72
 Cloisite 30B, 42, 43, 48, 68, 72, 73, 75, 77
 Cloisite Na⁺, 72
 closure field, 129
 CMC *see* carboxy MC
 CNTs *see* carbon nanotubes
 cobalt, 169
 coercive field, 128–131
 compost method, 61, 64, 65, 68, 70, 74, 79
 compressed sensing, 13
 copper nanoparticles, 33, 42
 CTAB *see* cetyltrimethylammonium bromide
 cyclic voltammetry (CV), 166

 dark field (DF) imaging mode, 8
 DART *see* discrete ART
 DAS *see* dialdehyde starch
 delamination, 35
 De-Nol, 160
 DFB resonators *see* distributed feedback (DFB)
 resonators
 DGEBA *see* Bisphenol A diglycidyl ether
 dialdehyde starch (DAS), 67
 diamond electrodes, 168

 diethylene glycol, 164
 differential pulse anodic stripping voltammetry
 (DPASV), 169
N,N-dimethylacrylamide (DMAA), 145, 148
 dioctyl ether, 164
 1,5-dioxepan-2-one (PDXO), 76
 discrete ART (DART), 13
 disinfection, of water, 160
 distributed feedback (DFB) resonators, 150, 151
 DMAA *see* *N,N*-dimethylacrylamide
 DNA-based biochips, 43
 dodecanethiol ligands, 164
 DPASV *see* differential pulse anodic stripping
 voltammetry
 drug delivery systems, 134
 Durethan, 38

 edible coatings, 45
 edible films, 45
 EDX *see* energy-dispersive X-ray spectroscopy
 EELS *see* electron energy loss spectroscopy
 EFTEM *see* energy-filtered TEM
 elastomers, 132
 electroactive clothing, 114
 electrocatalysis, 171
 electrochemical impedance spectroscopy,
 168, 173
 electrochemical methods, 166–167
 electrochemical stripping, 161, 168
 electrochromic devices, 132
 electrodeposition, 44, 166–167
 electron energy loss spectroscopy (EELS), 9, 17
 electronic coating, 44
 electronic precipitation, 44
 electron microscopy, 8
 see also transmission electron microscopy
 (TEM)
 electron tomography (ET), 7–8
 image analysis, 19–20, 21, 23–25
 “low-dose” technique, 23
 multiple-axis, 13
 3D microstructure, 7–25
 see also transmission ET
 electrospinning, 94
 fabrication of aligned fibers, 96–97
 fabrication of ferro/piezoelectric fibers, 98–99
 fabrication of fibers with reinforcements,
 100–102
 future directions, 114–115
 magnetolectric fibers, 112–114
 principle of, 95–96

- electrospun fibers, 93–115
 aligned, 96–97
 energy harvesters based on, 107
 ferro/piezoelectric, 97–99, 100, 102–103
 filled with reinforcements, 100–102
 nanogenerators based on, 106–107
 piezoelectric response, 102–104
 electrostatic interaction, 145
 endoglucanases, 64
 energy-dispersive X-ray spectroscopy (EDX), 9, 36
 energy-filtered TEM (EFTEM), 10, 17
 energy harvesters, 107
 energy harvesting materials, 93–115
 enzymes, 62, 65
 and biodegradation of gelatin, 67
 and biodegradation of polymers, 65
 and degradation of PVA, 80
 epoxies, 152
Escherichia coli, 44
 ET *see* electron tomography
 ethylene, 41
 absorbers, 40–42
 ethylene diamine, 161
 ethylene glycol, 161, 162
 ethylene vinyl alcohol copolymers, 41
 2-ethylhexanoate, 164
 exfoliated graphite (ExG), 192
 exfoliated nanocomposites, 35–36
- FC/ZFC curves *see* field-cooled/zero-field-cooled (FC/ZFC) curves
 Fe(III) acetylacetonate, 121, 122
 FEM *see* finite element method
 ferro/piezoelectric fibers,
 inorganic, 99, 100
 organic, 97–99
 FIB *see* focused ion beam (FIB) technique
 fibers,
 magnetoelectric, 112–114
 multifunctional, 109–110
see also electrospun fibers
 FIB/SEM tomography, 24–25
 fiducial markers, 11
 field-cooled/zero-field-cooled (FC/ZFC) curves,
 124–126, 128, 129, 130
 finite element method (FEM), 120
 fire performance index (FPI), 188
 flavors, 29, 40
 flexible nanogenerators, 94, 114
 flexible packaging, 39
 flexoelectric effect, 94
- fluorescent dyes, 150
 fluorescent labeling, 145
 fluorohectorite, 73
 Flynn–Wall–Ozawa method, 191
 focused ion beam (FIB) technique, 13, 18
 food additives, 45
 food contamination, 29
 food packaging, 29–50
 active, 40–43
 antimicrobial, 40, 42–43
 biodegradable, 39
 edible coating/packaging films, 45
 flexible, 39
 functions, 29
 insulating materials, 45
 intelligent, 43–44
 life cycle of, 30–31
 nanocoating, 44–45
 nylon-based materials, 38–39
 rigid packaging, 37
 types of, 36–45
 force sensors, 108–109
 Fourier transform infrared spectroscopy (FTIR),
 36, 77, 124
 FPI *see* fire performance index
 freshness indicators, 44
 Fresnel fringes, 16
 frontal polymerization, 143
 fruit, 41–42
 FTIR *see* Fourier transform infrared spectroscopy
 full width at half maximum (FWHM), 22, 23, 145
 fumed silica (FS), 192
 fungi, enzymes from, 65
Fusarium sp., 76
 FWHM *see* full width at half maximum
- gas scavengers, 37
 Gaussian blur, 19
 gelatin, 42, 67
 gelatin-based nanocomposites, 49
 generally recognized as safe (GRAS) materials, 45
 geometric confinement, 3
 germanium, 169
 giant magnetoresistance (GMR), 132, 135
 glass transition temperature, 2–3, 4
 glassy carbon electrodes, 168, 169
 gliadins, 68
 glucose oxidase, 171
 glucoses, 169
 glutaraldehyde (GA), 65, 172

- glutenins, 68
glycerin, 64
glycerol, 63
GMR *see* giant magnetoresistance
gold microelectrodes, 168
gold nanocomposites, 143
gold nanoparticles, 43
Gram-negative bacteria, 42, 44, 75
Gram-positive bacteria, 42, 44, 75
graphene, 169
graphene oxide (GO), 195
- HAADF imaging mode, 8
HAADF-STEM, 16
halloysite nanotubes (HNTs), 188, 190
HDDA *see* 1,6-hexanediol diacrylate
heavy metal detection, 167–169, 173
hectorite, 33, 78
heterocyclic polymers, 185
1,6-hexanediol diacrylate (HDDA), 128
high-angle annular DF (HAADF) imaging mode, 8
high-barrier nanocoating, 44
high-performance polymer nanocomposites, 187–198
high-temperature resistance, 183–185
high-temperature resistant polymers, 183–185, 187
 applications, 198, 199
HNTs *see* halloysite nanotubes
hot-pressing (HP), 13, 14
hydrazine, 161, 164
hydrocolloids, 45
hydrogels, 134
hydrolase enzymes, 62
hydrolysis,
 abiotic, 76, 82
 biodegradation via, 61–63, 67, 70–74, 76, 79–83
 catalytic, 62
 non-catalytic, 62
2-(2-hydroxyphenyl)-benzoxazol (BOX), 145, 148
- IgE molecules, 173
ImageJ, 20
immiscible tactoids, 35–36
immobilisation, 171–172
immunoreaction assays, 173
Imperm™, 39
indium oxide, 152
indium tin oxide (ITO), 108
ink jet device, 126
inorganic nanofillers, 32–33
- in-situ* polymerization, 35, 120, 145
insulating materials, 45
intelligent packaging, 43–44
interacting superparamagnetic model (ISP), 120, 126
intercalated nanocomposites, 35–36
interface, 2–3
ionic liquids, 197
iron oxides, 132
iron sulfide, 152
ISO 472, 60
ISP *see* interacting superparamagnetic model
- kaolin, 64
- lactic acid, 71–72
lanthanide, 143, 144
LASERs, 145
LCD *see* liquid crystal display
LDPE-coated paper, 45
lead, 169
lead zirconate titanate (PZT), 111–112
LEDs *see* light-emitting diodes
levitational gas condensation (LGC) method, 168
ligands, alkylamines, 2
light,
 absorption, 139
 emission, 145–151
 reflection, 139
 remission, 139
 scattering, 139
 transmission, 139
light-emitting diodes (LEDs), 114, 141, 145, 150
 see also organic LEDs (OLEDs)
limit of detection (LOD), 169
limiting oxygen index (LOI), 191, 194–195
liquid crystal display (LCD), 112
Listeria monocytogenes, 42
LOD *see* limit of detection, 169
- M9, 39
MA *see* maleic anhydride
magnetic field, 20
magnetic force microscopy (MFM), 112
magnetic hysteresis, 109, 114, 129–131
magnetic nanocomposites,
 anhysteretic properties, 124–127
 applications, 132–135
 hysteretic properties, 127–131
 interparticle interactions, 124–127
 preparation of magnetic nanoparticles, 120–122

- magnetic nanoparticles (NPs), 20, 119–120
 for biosensors, 43
 homogeneity and interactions, 121–122
 interparticle interactions, 124–127
 preparation of, 120–122
 synthesis, 120–121
- magnetic polymer actuators, 132
- magnetic remanence, 129–131
- magnetite, 119–130, 132, 133
- magnetoelectric (ME) fibers, 112–114
- magnetoelectric (ME) materials, 112, 114–115
- maleic anhydride (MA), 63, 75
- MC *see* methyl cellulose
- MC/MMT nanocomposites, 65, 66
- median filter, 19
- melt intercalation method, 35
- ME materials *see* magnetoelectric materials, 112
- mercury, 169
 electrodes, 167, 173
- Mesua Ferrera* L. seed oil (MFLSO), 81
- metal nanoparticles,
 antimicrobial food packaging applications, 42
 as nanofillers, 33, 34
- metal oxide nanoparticles, 121
 antimicrobial food packaging applications, 42
 for nanocoating, 44
 as nanofillers, 33, 34
- metal oxides, 152
- meta-xylylenediamine, 39
- methyl cellulose (MC), 64–65
see also carboxy MC (CMC); MC/MMT
 nanocomposites
- MFM *see* magnetic force microscopy
- MgO, 42, 44
 microbial growth, 29, 42, 44
see also antimicrobial packaging
- microbial polyesters, 31
- microcellulose, 33
- micro-composites, 2
- microwaves, 152
- “missing wedge” effect, 13, 17, 18
- MMT *see* montmorillonite
- moisture absorbers, 40
- montmorillonite (MMT), 33, 42, 48, 49
 effect on biodegradation, 63–68, 72–73, 75,
 78, 80, 81
 octadecylamine-modified (ODA-M), 78
see also organo-MMT
- multiferroic materials, 131–132, 135
- multifunctional fibers, 109–110
- multilayer nanocomposites, 37
- multiple-axis tomography, 13
- multi-walled carbon nanotubes (MWCNTs), 17,
 190–191, 197–198
- MWCNTs *see* multi-walled carbon nanotubes
- Nafion, 167
- nano-biocomposites, 59
- nanocellulose, 32–33
 crystalline 32
 paper-mulberry pulp, 39, 49
- nanoclays,
 antimicrobial activity, 42, 43
 and biodegradability, 48, 59, 68, 72–73, 75
- nanocoating,
 food packaging, 44–45
 high-barrier, 44
- nanocrystals,
 bismuth, 160, 161, 164
 quantum dots, 141
 rod-like, 32
 starch, 32
 ZnO, 44
- nanofibers,
 carbon, 169, 192
 cellulose, 49
 lead zirconate titanate, 111
 magnetoelectric, 114
 multifunctional, 109, 111
 nanocellulose, 33
- Nanofil 804, 73, 77
- nanofillers, 7
 homogenous dispersion of, 34
 inorganic, 33–34
 organic, 32–33
 and thermal stability of nanocomposites, 49
- nanogenerators, 94–95
 based on electrospun fibers, 106–107
 converting mechanical energy, 109
 flexible, 94, 114
- nanoscopic confinement, 3–5
- nanosensors, 43
- nano-SiO₂ particles, 80
- nanostructure indicators, 43
- nanotechnology, 30
- natural fibers, 67, 70
- needle-shaped nanocomposites, 18, 19
- neutral red (NR), 171
- nickel, 169
- NMR *see* nuclear magnetic resonance
- non-enzymatic catalysts, 62
- non-hydrolytic sol–gel reaction (NHSG), 121

- nuclear magnetic resonance (NMR), 36
 nylon-6, 38–39
 nylon-based materials, 38–39
 nylon-MXD6, 39, 40
 nylon-MXD6/clay nanocomposites, 39–40
- octadecylamine-modified MMT (ODA-M), 78
 ODA-M *see* octadecylamine-modified MMT
 odor absorbers, 40
 oil spill recovery, 135
 OLEDs *see* organic LEDs
 OMMT *see* organo-MMT
 optical amplifiers, 145
 organically modified layered silicate (OMLS)
 nanocomposites, 70
 organic contaminants, 160
 organic LEDs (OLEDs), 143, 150
 organic nanofillers, 32–33
 organo-MMT (OMMT), 75
 orientation techniques, 67
 Osteryoung square-wave cathodic stripping
 voltammetry (OSWCSV), 169
 OSWCSV *see* Osteryoung square-wave
 cathodic stripping voltammetry
 oxidative chain scission, 61
 oxidative cleavage, 63
 oxygen, 29
 barriers, 41
 migration through the food packaging, 37,
 39, 45
 scavengers, 40, 41
 sensors, 141
- PANI *see* polyaniline
 paraffin oil, 162
 PBAT *see* polybutylene adipate-*co*-terephthalate
 PBS *see* polybutylene succinate
 PbS, 146
 PCFC *see* pyrolysis combustion flow
 calorimeter
 PCL *see* polycaprolactone
 PDMS *see* poly(dimethyl siloxane)
 PDOF *see* poly(9,9'-dioctylfluorene)
 PDXO *see* 1,5-dioxepan-2-one
 PE, 76, 142, 143
 peak heat release rate (pHRR), 188, 191
 PEEK *see* polyetheretherketone
 PEG *see* polyethylene glycol
 PEGDA, 129, 130
 PEI *see* polyetherimide
 PEK *see* polyetherketone
Penicillium funiculosum, 76
 PEO, 144
 Pepto-Bismol, 160
 percolating networks, 24, 25
 PES *see* polyethersulphone
 pesticides, 169
 PET *see* polyethylene terephthalate
 PFM *see* piezoresponse force microscopy
 PHAs *see* polyhydroxyalkanoates
 PHB *see* polyhydroxybutyrate
 PHBV *see*
 poly(hydroxybutyrate-*co*-hydroxyvalerate)
 phenolic compounds, 171–173
 photocatalytic hydrogen evolution, 158
 photoluminescence (PL), 140–144
 defined, 140
 photoluminescent polymers, 140–144
 photovoltaic solar cells, 132
 pHRR *see* peak heat release rate
 physical vapor deposition, 44
 PI *see* polyimide
 piezoelectric effect, 94
 piezoelectric materials, 94
 piezoelectric fibers, 94–95
 piezoresponse force microscopy (PFM),
 102–104, 114
 PL *see* photoluminescence
 PLA *see* poly lactic acid
 PLA-based nanocomposites, 49
 PMMA, 142–145, 146, 148, 149
 poling, 97–98
 polyamide 6, 38
 polyaniline (PANI), 132
 polybutylene adipate-*co*-terephthalate (PBAT),
 59, 78–79
 polybutylene succinate (PBS), 48, 63, 71,
 74–75, 82, 83
 polycaprolactone (PCL), 47, 48, 59, 69, 81
 biodegradation, 76–77
 polycarbonate, 144
 poly(dimethyl siloxane) (PDMS), 24, 25, 111,
 112, 141, 142
 poly(9,9'-dioctylfluorene) (PDOF), 150
 polyesters,
 aromatic, 78–79
 biodegradation, 69–74
 from bio-derived monomers, 71–74
 from fossil origins, 74–79
 microbial, 31
 produced by microorganisms or plants,
 69–70

- polyetheretherketone (PEEK), 183, 184, 195
polyetherimide (PEI), 183, 184, 197
 nanocomposites, 196–198
polyetherketone (PEK), 183
polyethersulfone (PES), 183, 184,
 187–192, 193
 nanocomposites, 187–192
polyethylene glycol (PEG), 144, 164
polyethylene oxide, 47
polyethylene terephthalate (PET), 39, 44, 71,
 76, 111–112
polyglycolic acid, 47
polyhydroxyalkanoates (PHAs), 59, 70
 applications, 69
 biodegradability, 69–70
polyhydroxybutyrate (PHB), 47, 69–70, 76
poly(hydroxybutyrate-co-hydroxyvalerate)
 (PHBV), 69–70
polyimide (PI), 183, 184, 193, 194–195, 196
polyimide nanocomposites, 192–196
polylactic acid (PLA), 59, 63, 69, 71–74
 biodegradation, 71–74, 83
poly lactide, 47
polymer chain scission, 61, 62
polymerization,
 frontal, 145
 in-situ, 35, 120, 145
 UV-induced, 120, 124
polymer nanocomposites, 1–5, 31
 barrier properties, 31, 46
 biodegradation properties, 47–48
 characterization of films, 36
 chemical resistance properties, 46–47
 definition, 31
 high-performance, 187–198
 high-temperature-resistant, 183–199
 light emission, 145–151
 magnetic properties, 119–135
 magnetoelectric properties, 131–132
 mechanical properties, 46
 optical properties, 139–153
 preparation, 34–36
 properties, 46–50
 thermal properties, 49
 transmission ET, 13–18
 transparency and adsorbance in, 152, 153
 UV light barrier properties, 48
polymers, for preparation of nanocomposites,
 31, 32
polymethyl methacrylate, 152
polyolefins, 63
polyol process, 162, 164
poly-1,3,4-oxazadioles, 185
polyphenol oxidase (PPO), 173
polysaccharides, 63–64
polystyrene, 142, 152
polysulfone (PSU), 183, 184
poly(trimethylene terephthalate)(PTT), 60
polyurethanes (PUs), 63, 80–81, 142, 152
polyvinylacetate, 152
polyvinyl alcohols (PVA) 76, 79–80, 83–84,
 142, 144, 152
polyvinylidene fluoride (PVDF), 97–99,
 103–104, 114
 fibers with reinforcement, 100–104, 105
 use in energy harvesters, 107
 use in nanogenerators, 106–107
polyvinyl pyrrolidone (PVP), 163–164, 173
potassium hydrogen phosphite, 164
potassium hydroxide, 41
PPO *see* polyphenol oxidase
pressure sensors, 108–109
proteins, biodegradation, 66–69
Pseudomonas boreopolis, 79
Pseudomonas sp., 79
Pseudomonas vesicularis, 79
PSU *see* polysulfone
PTT *see* poly(trimethylene terephthalate)
pure culture method, 61
PUs *see* polyurethanes
PVA *see* polyvinyl alcohols
PVC, 76
PVDF *see* polyvinylidene fluoride
PVP *see* polyvinyl pyrrolidone
pyrolysis combustion flow calorimeter (PCFC),
 192, 194
Pyrrromethene 567, 150
PZT *see* lead zirconate titanate
quantum dots (QD), 141–142, 145–148, 149
 for biosensors, 43
quantum effect, 141
Radon's theory, 10, 11
rare-earth polymer nanocomposites, 143–144
rigid food packaging, 37
ripening, 41–42
rotating coating, 44
ruthenium nanoparticles, 2
saponite, 33
scandium, 144

- scanning electron microscopy (SEM), 24, 36, 96, 99, 100
see also FIB/SEM tomography
- scanning TEM (STEM), 8, 9
 applied to ET on thick samples, 24
 operating modes, 8
see also ADF-STEM; BF-STEM; HAADF STEM
- scintillators, 144
- screen-printed carbon electrodes (SPCEs), 168, 169
- selenium, 169
- self-assembling, 44
- SEM *see* scanning electron microscopy
- sensing devices, 103
- sensors, 43
 force/pressure, 108–109
 gas and vapor, 132
 temperature, 142
see also biosensors; nanosensors
- sepiolite, 73–74, 78, 196–197
- Serratia marcescens*, 65
- sewage sludge, 61
- shape-memory polymers (SMPs), 134–135
- shelf life, 29, 31, 37, 39, 40, 41
- silica,
 gel, 41
 nanoparticles, 12, 15, 17, 24, 132
 PS-grafted, 20, 22
- silicates, 16, 33–35
- silk fibroin, 71
- silsesquioxane (OAPS), 194–195
- silver nanoparticles (AgNPs),
 bactericidal effects, 1, 33
 for antimicrobial food packaging
 applications, 42, 45
 in OLEDs, 150
 and thermostability of nanocomposites, 49
- simultaneous iterative reconstruction technique (SIRT), 11, 13
- sintering, 115
- SIRT *see* simultaneous iterative reconstruction technique
- size-dependent functionality, 1
- smart packaging, 43–44
- SMPs *see* shape-memory polymers
- sodium borohydride, 161, 164
- sodium hydride, 164
- sodium hydroxide, 41
- sodium hypophosphate, 161
- soft epitaxy, 3–4
- soil burial method, 60–61
- solar cells, 19, 132, 141, 143, 152
- sol–gel process, 44, 99, 112, 114, 121
see also non-hydrolytic sol–gel reaction (NHSG)
- solubility, 1
- solution intercalation method, 35
- solvent-casting, 13, 14, 34
- soy protein films, 48
- SPECs *see* screen-printed carbon electrodes
- spin glass state (SSG), 125
- spray coating, 44
- square-wave adsorptive stripping voltammetry (SWAdSV), 169
- square-wave anodic stripping voltammetry (SWASV), 167
- SSG *see* spin glass state
- Staphylococcus aureus*, 42
- starch, 63–64, 80
- starch nanocrystals, 32
- STEM *see* scanning TEM
- Stoner–Wohlfarth (SW) response, 128
- Stoner–Wohlfarth (SW) systems, 128, 129, 131
- stripping voltammetry, 167, 168
- succinic acid, 74–75
- sulfide detection, 169
- SWASV *see* square-wave anodic stripping voltammetry
- SWdSV *see* square-wave adsorptive stripping voltammetry
- TCA *see* tricarboxylic acid
- TEM *see* transmission electron microscopy
- temperature sensors, 142
- TGA *see* thermogravimetric analysis
- thallium, 169
- thermal decomposition method, 160, 161
- thermally reduced graphene (TRG), 196
- thermocompression method, 35
- thermoformed containers, 37
- thermoform nylon *see* polyamide 6
- thermogravimetric analysis (TGA), 36, 187, 189, 196, 197, 198
- thermoplastic materials, 134
- thermoplastic proteins, 47
- thermoplastic starch (TPS), 63, 80
- thermosets, 60
- tilted tomography, 10
- time-to-ignition (TTI), 188, 194
- TiO₂-coated films, 44
- titanium nanoparticles, 42

- titanium oxide (TiO₂),
 antimicrobial food packaging applications,
 42, 44
 as ethylene absorber, 42
 nanoparticles, 41, 152
 see also TiO₂-coated films
- tomograms, 11, 13, 15
- TPS *see* thermoplastic starch
- transition metal nanocomposites, 143
- transmission electron microscopy (TEM), 7–9,
 36, 99, 100, 101, 123, 126, 133
 operating modes, 8
 see also BF-TEM; energy-filtered TEM
 (EFTEM); scanning TEM (STEM)
- transmission ET,
 application to polymer matrix
 nanocomposites, 13–18
 principles of, 10–13
- transparency, 141, 142, 152
- tricarboxylic acid (TCA), 70, 76
- Trichoderma*, 65
- tris[bis(trimethylsilyl)amide], 164
- TTI *see* time-to-ignition
- tungsten disulfide, 191
- ultramicrotomy, 18
- uranium, 167
- UV-curing, 119, 120, 121, 142, 143, 144
- UV-induced polymerization, 120, 124
- UV-light barrier materials, 48–49
- UV-light transmission, 45
- vanadium, 169
- vapor-cross linking, 67
- vegetables, 41–42
- volume calculation, 11
- Voronoi tessellation, 20, 22
- walking, 109
- watershed process, 19, 20
- waters vapor permeability, 29
- WBP *see* weighted BP
- weighted BP (WBP), 11
- wheat gluten, 68–69
- whey protein-based nanocomposite, 49
- white light-emitting devices (WLEDs),
 145, 147
- WLEDs *see* white light-emitting devices
- XRD, 36
- Young's modulus, 132
- yttrium, 144
- zinc, 169
 antimicrobial food packaging
 applications, 42
 nanoparticles, 33
- zirconia nanoparticles, 18, 19
 see also ZrO₂
- ZnO,
 antimicrobial food packaging applications,
 42, 44
 nanoparticles, 152
- ZnO-coated glass, 44
- ZnS, 145, 148
- ZrO₂, 150
 see also zirconia nanoparticles

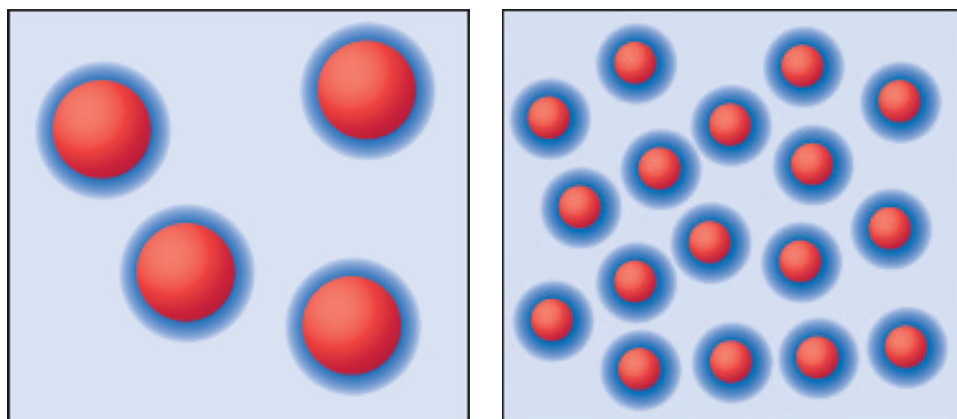


Figure 1.2 Interfacial regions in polymer micro- and nanocomposites. Particles are coloured red, interfacial regions blue and the rest is polymer matrix (in light blue). Schadler [11]. Reproduced with permission of Nature Publishing

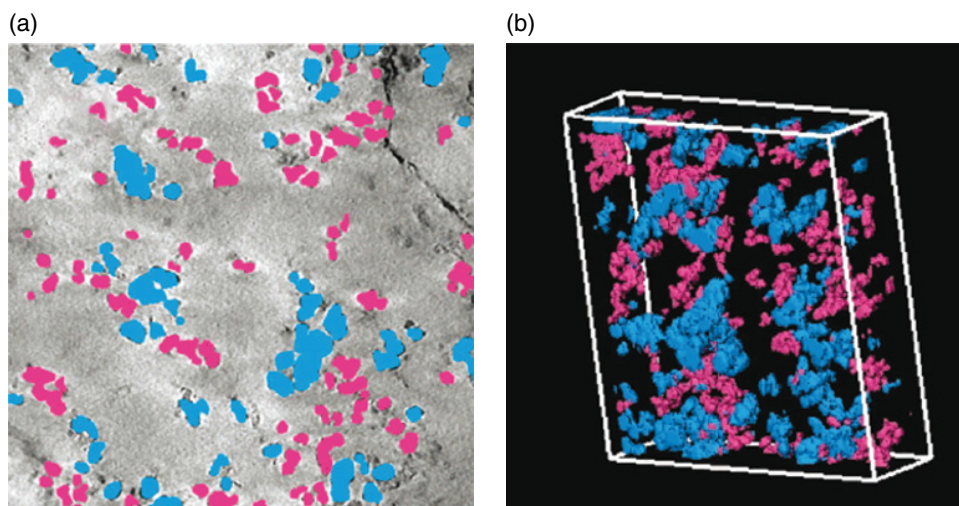


Figure 2.7 (a) Segmentation of CB (blue) and Si nanoparticles (red) in a digital slice and (b) in the 3D reconstruction of the CB-Si/natural rubber system. Box size is $726 \text{ nm} \times 726 \text{ nm} \times 107 \text{ nm}$ (EFTEM imaging, WBP reconstruction). Jinnai et al. [11]. Reproduced with permission of American Chemical Society

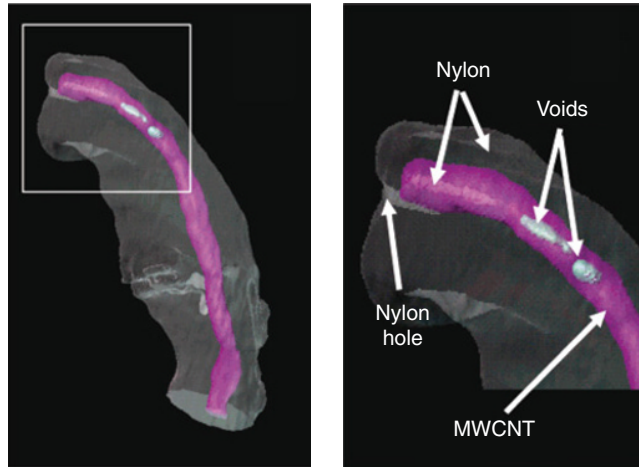


Figure 2.8 Surface render of the nanotube (purple) and nylon (gray) from the tomographic reconstruction of the plasmon ratio 28 eV/22 eV. The nylon that has filled the top end of the nanotube is shaded in light purple. A hole that occurs in the nylon can be seen just under the top end of the nanotube, and the voids within the nanotube are represented by pale green (EFTEM imaging, SIRT reconstruction). Gass et al. [39]. Reproduced with permission of American Chemical Society

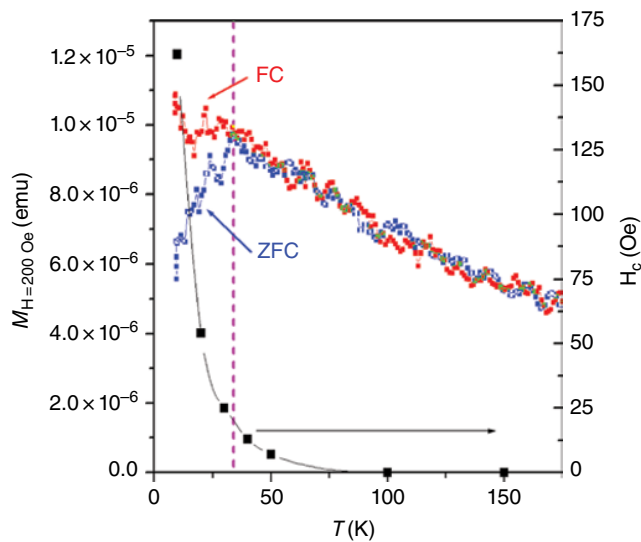


Figure 6.8 Temperature dependence of the coercive field (black symbols) and of FC/ZFC magnetization for magnetite nanoparticles dispersed in HDDA

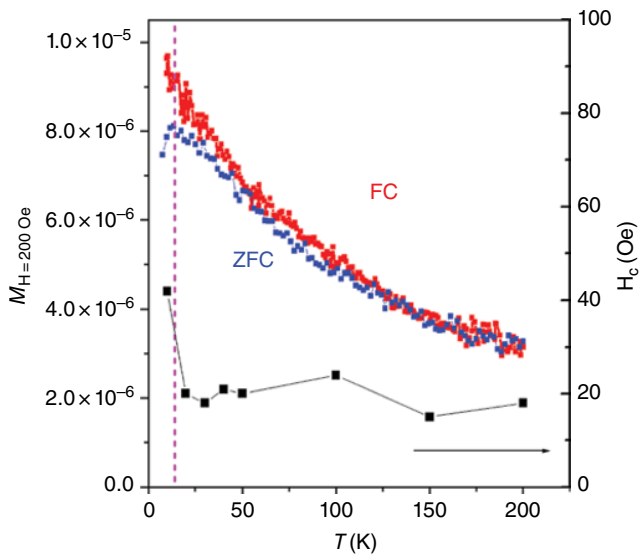


Figure 6.9 Same as in Figure 6.8 for magnetite nanoparticles dispersed in PEGDA



Figure 7.2 Light emission of ZnS-capped CdSe excited in the UV range. Dimension of colloidal QDs increase from 2 (left) to 6 (right) nm. Chan et al. [10]. Reproduced with permission of Elsevier

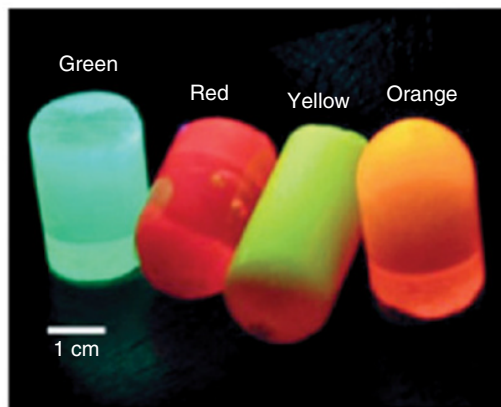


Figure 7.3 PS/QDs nanocomposites. Zhang et al. [23]. Reproduced with permission of John Wiley & Sons

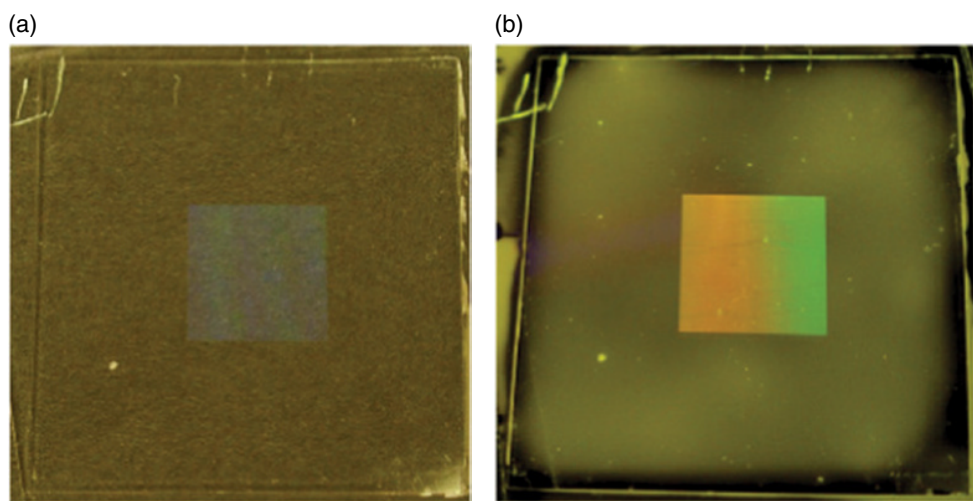


Figure 7.5 Acrylate composite film ($5\mu\text{m}$) containing copper iodide clusters ($2.5\times 2.5\text{ cm}$) on glass substrate with a square patterned area in the center (a) under ambient light and (b) under UV irradiation at 312 nm (UV lamp) at room temperature. Roppolo et al. [70]. Reproduced with permission of Royal Society of Chemistry

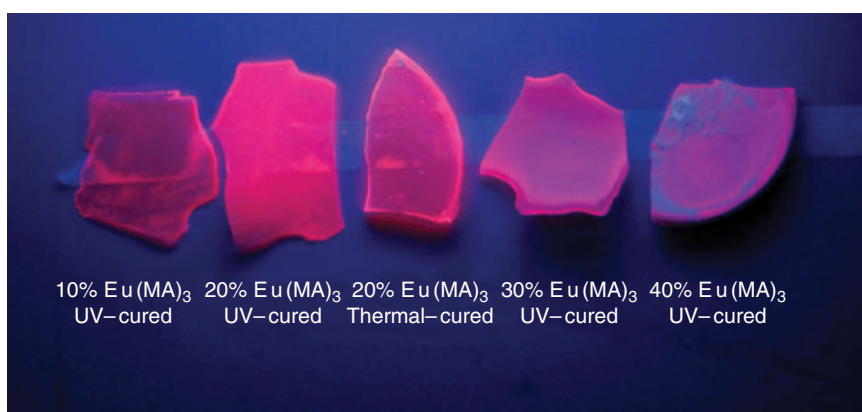


Figure 7.6 Urethanes acrylates UV and thermal cured containing Europium complexes. Zhou et al. [101]. Reproduced with permission of John Wiley & Sons

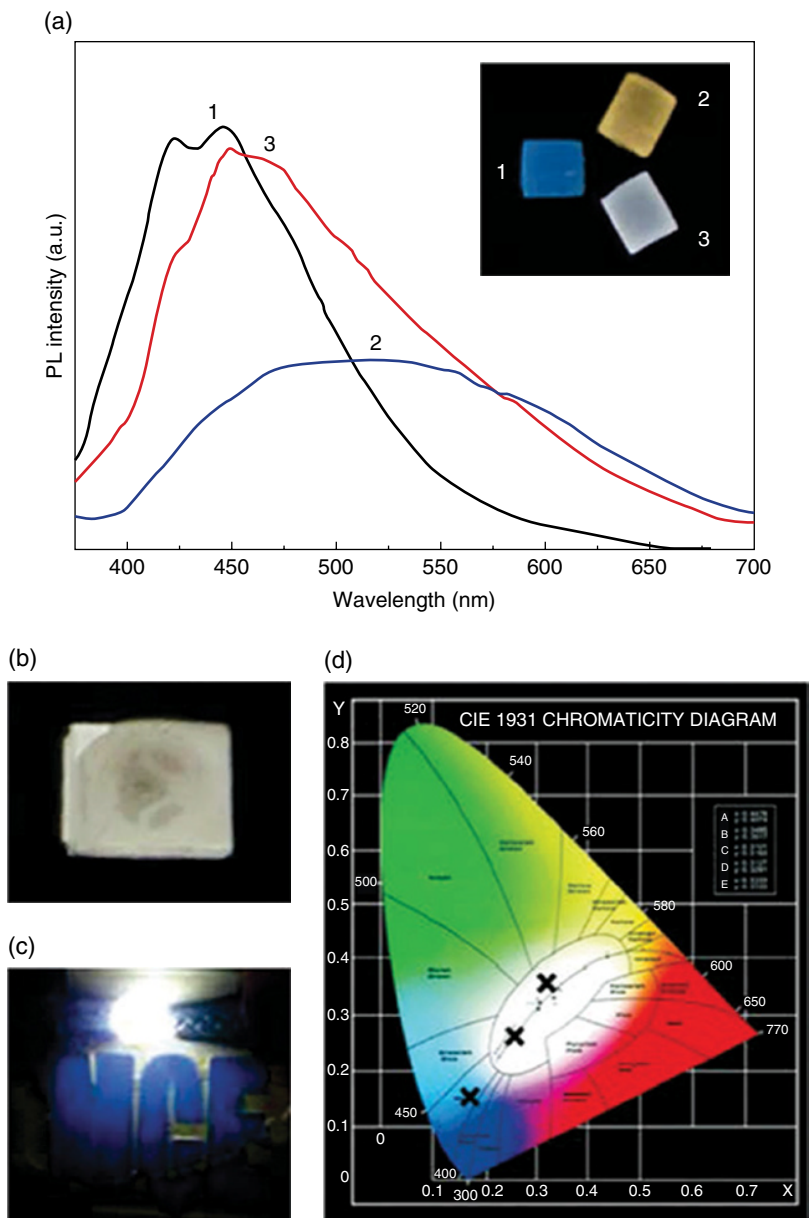


Figure 7.10 PL spectra, digital images of the nanocomposites, emitting WLED in operation and chromaticity diagram of the systems based on frontally polymerized CdS-poly(HEA-co-NVK) nanocomposites. Zhou et al. [114]. Reproduced with permission of John Wiley & Sons



Figure 7.18 PS/PMMA polymer blend containing 5% ZnO Nanoparticles. Ge et al. [135]. Reproduced with permission of Wiley

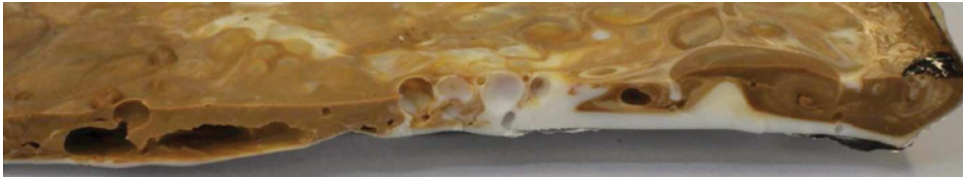
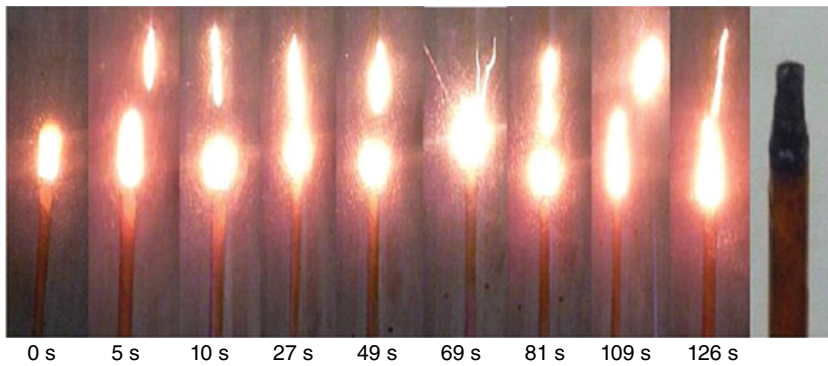


Figure 9.3 Cross-section picture of polyethylene terephthalate residue obtained by interrupted combustion just after TTI. Fina and Camino [13]. Reproduced with permission of Wiley

(a)



(b)

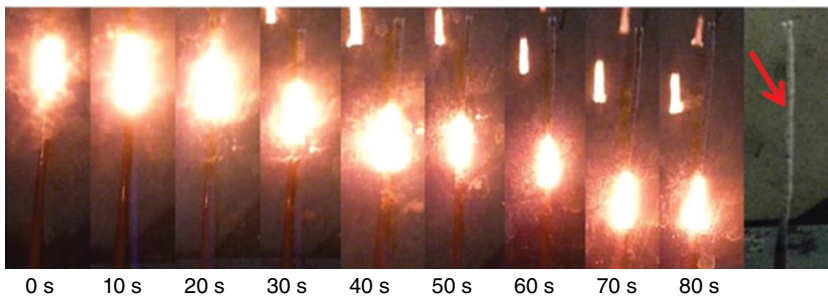


Figure 9.9 Combustion of PI (a) and PI/5.4 wt.% OAPS (b) at their respective $LOI + 0.5\% O_2$ (i.e., 47 and 57.5). Fan and Yang [20]. Reproduced with permission of American Chemical Society

WILEY END USER LICENSE AGREEMENT

Go to www.wiley.com/go/eula to access Wiley's ebook EULA.